



# SCHOOL OF ENGINEERING RESEARCH SHOWCASE 2019



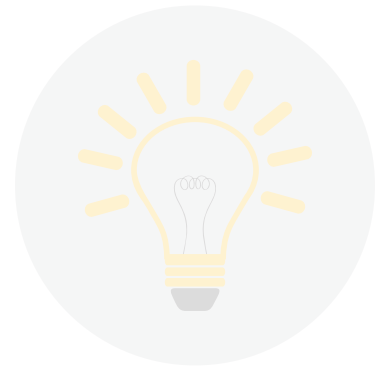
## 2018 Research Showcase Posters Table of Contents



### BIOENGINEERING

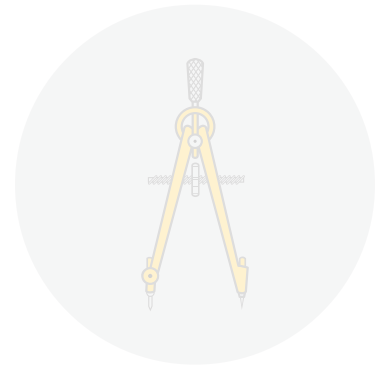
#### **28 Integration of Soft and Smart Devices for Next Generation Wearables**

Ju Young Lee: BIOE Undergraduate  
Lashan Wijayawickrama: BIOE Undergraduate  
Advisor: Dr. Emre Araci



#### **29 Integration of Microfluidic Sensors with Endoscopes for Continuous Pressure Sensing**

Tehmi den Braven: BIOE Undergraduate  
Advisor: Dr. Emre Araci

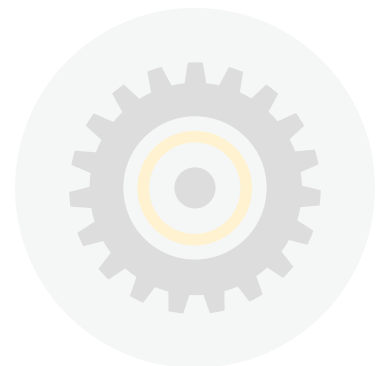


#### **30 Targeted Delivery to Neurons Using Engineered Exosomes**

David Diebold: BIOE Undergraduate  
Kyle Asano: MECH Undergraduate  
Advisor: Dr. Bill Lu

#### **32 Flow Optimization and Colloidal Stability of Microcapsules Through 3D-Printed Microneedles**

Chantell Farias: BIOE Master's Student  
Rachel Flores: BIOE Master's Student  
Natalie Ploof: BIOE Master's Student  
Advisors: Dr. Maryam Mobed-Miremadi and  
Dr. Unyoung (Ashley) Kim



### **33 Scale Optimization of Milkguard Biosensor for Detecting E. coli in Breast Milk**

Jerard Madamba: BIOE Master's Student  
Advisors: Dr. Maryam Mobed-Miremadi and  
Dr. Unyoung (Ashley) Kim

### **35 Arrhythmia Detection from ECG Signals Using Machine Learning**

Pradnya Patel: BIOE Master's Student  
Advisor: Dr. Yuling Yan

## **CIVIL, ENVIRONMENTAL AND SUSTAINABLE ENGINEERING**

### **9 Transit System Asset Management: Model-based Systems Engineering**

Alan Ng: EMGT Master's Student  
Advisor: Dr. Hisham Said

### **18 Model-Based Engineering of Smart Buildings**

Xiaopu Cheng: COEN Master's Student  
Linzhi Li: COEN Master's Student  
Advisor: Dr. Hisham Said

## **COMPUTER ENGINEERING**

### **15 Flomosys: A Low-Cost, Reliable, and Low-Power Flood Monitoring System**

Tai Groot: COEN Undergraduate  
Advisor: Dr. Behnam Dezfouli

### **17 Image Classification on IoT Edge Devices: Profiling and Modeling**

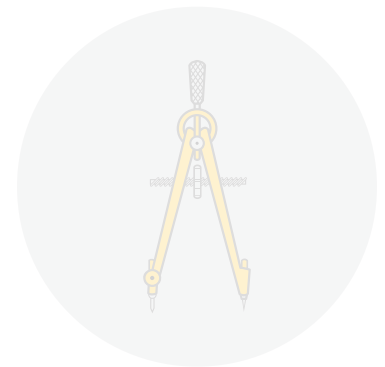
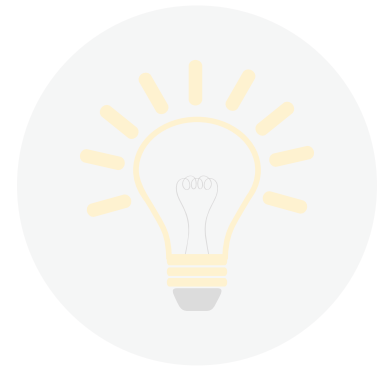
Salma Abdel Magid: COEN Master's Student  
Francesco Petrini: COEN Undergraduate  
Advisor: Dr. Behnam Dezfouli

### **24 Image Compression with Deeper Learned Transformer**

Licheng Xiao: COEN Master's Student  
Hairong Wang: COEN Master's Student  
Advisor: Dr. Nam Ling

### **25 An Efficient VM Allocation Strategy for Dynamic Cloud Service Against Co-residence Attacks**

Ruiwen Li: COEN Master's Student  
Lu Cao: COEN Ph.D. Student  
Hanxiao He: CompSci Alumnus  
Songjie Cai: COEN Alumnus  
Advisors: Dr. Yuhong Liu and Dr. Xiaojun Ruan



**26 Multilingual News Search User Behaviors –Exploring Multilingual Consumption Behaviors, Querying and Result Selection Through Crowdsourcing**

Chenjun Ling: COEN, Ph.D. Student  
Advisors: Dr. Silvia Figueira and Dr. Ben Steichen

**27 An Efficient Co-design Partitioning for WLANs on ZynqSoC**

Rami Akeela: ELEN Ph.D. Student  
Advisor: Dr. Behnam Dezfouli

**ELECTRICAL ENGINEERING**

**10 Cost Effective Camera-LIDAR Sensor Object Detection for Autonomous Vehicle Application**

Robert Christiansen: COEN Ph.D. Student  
Advisor: Dr. Sally Wood

**11 Rover Localization in Mars Helicopter Aerial Maps**

Kamak Ebadi: ELEN Ph.D. Student  
Advisor: Dr. Sally Wood

**12 Image Content Identification from CNNs with Sparse Sampling**

Allen Rush: ELEN Ph.D. Student  
Advisor: Dr. Sally Wood

**13 Selective Data Transfer from DRAMs for CNNs**

Anaam Ansuri: ELEN Ph.D. Student  
Advisor: Dr. Tokunbo Ogunfunmi

**14 Experimental Results on Using Deep Learning to Identify Agricultural Pests**

Vineet Panchbhayye: ELEN Master's Student  
Advisor: Dr. Tokunbo Ogunfunmi

**16 Model Predictive Control of a Nanogrid**

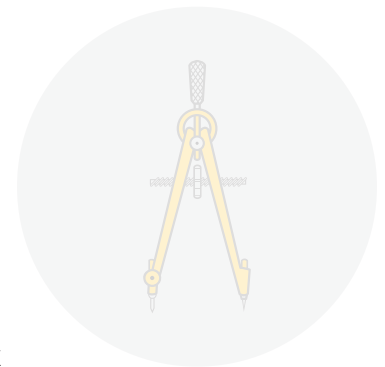
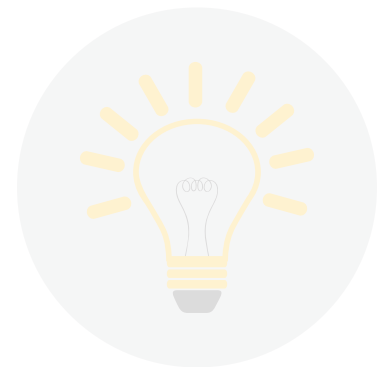
Frank Cannizzaro: ELEN Master's Student  
Ramin Vafadary: ELEN Ph.D. Student  
Advisor: Dr. Maryam Khanbaghi

**19 Design and Measurement of a Miniaturized Beam-Forming Network for a 4-Element Patch Antenna Array at 5.8 GHz**

Brian Tjahjadi: ELEN Alumnus  
Advisor: Dr. Ramesh Abhari

**20 A Highly Isolated 2x2 Printed Yagi-Uda Antenna Array for Small Form Factor Devices at 5.8 GHz**

Nivedita Parthasarathy: ELEN Ph.D. Student  
Advisor: Dr. Ramesh Abhari



## **21 Mitigation and Identification of the Cause of Radiated Emissions in an 8 Gpbs High-Speed System**

Ali Khoshnati: ELEN Ph.D. Student  
Advisor: Dr. Ramesh Abhari

## **22 Millimeter-wave 2-D Beam Steering Planar Array**

Benjamin Horwath: ELEN Ph.D. Student  
Advisor: Dr. Ramesh Abhari

## **23 A Discontinuous Charging Technique with Programmable Duty-Cycle for Switched Capacitor-Based Energy Harvesting Circuits in IoT Applications**

Sanad Kawar: ELEN Ph.D. Student  
Advisors: Dr. Shoba Krishnan and  
Dr. Khaldoun Abugharbieh

## **MECHANICAL ENGINEERING**

### **1 Molecular Dynamics Study of the Contact Behavior of FCC Metallic Substrates**

Milad Khajehvand: MECH Ph.D. Student  
Advisor: Dr. Panthea Sepehrband

### **2 Multi-robot Transport and Manipulation of Objects**

Fritz Huizengar: MECH Ph.D. Student  
Advisor: Dr. Christopher Kitts

### **3 Adaptive Navigation in 3-Dimensions with a Multirobot Virtual Structure**

Robert K. Lee: MECH Ph.D. Student  
Advisor: Dr. Christopher Kitts

### **4 Mobile Robotics Swarm Behavior Development Platform**

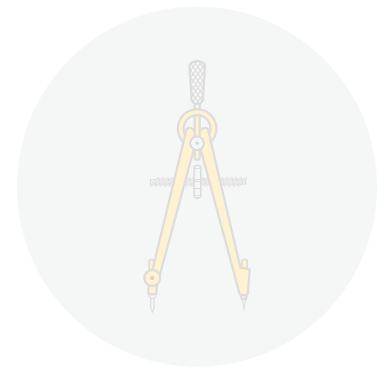
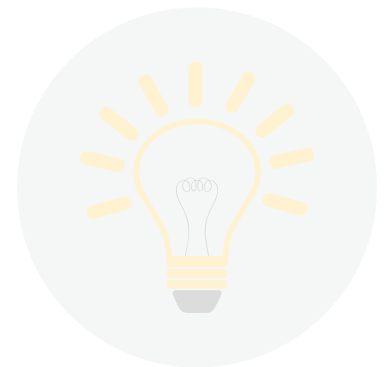
Nathan Metzger: MECH Master's Student  
Max Reese: MECH Master's Student  
Shae Hart: MECH Master's Student  
Advisor: Dr. Christopher Kitts

### **5 Stress Reduction for Crack-like Geometries in Auxetic Metamaterials**

Max Barillas: MECH Master's Student  
Dr. Luca Francesconi: MECH Post-Doctoral Research Fellow  
Advisor: Dr. Michael Taylor

### **6 Self-learning How to Swim at Low Reynolds Numbers**

Shreyes Nallan: ELEN Undergraduate  
Grant Mishler: MECH Master's Student  
Alan Tsang (BIOE Stanford University)  
Pun Wai Tong (Clinical Genomics Program, Stanford Health Care)  
Advisor: Dr. On Shun Pak



## 7 Thermoelectric Generator Integration in Wearable Devices

Joshua Vincent: BIOE Undergraduate

Advisor: Dr. Hohyun Lee

## 8 3D SPM Imaging of Ultrasonic Wedge Bonded Wire Interface

Brandon van Gogh: MECH Undergraduate

Advisor: Dr. Panthea Sepehrband

## INTERDISCIPLINARY

## 31 Comparison of Tapping Mode and Fluid Mode for Membrane Topography using Atomic Force Microscopy

Huong Chau: BIOE Undergraduate

Alex Hadsell: BIOE Undergraduate

Advisors: Dr. Maryam Mobed-Miremadi,  
Dr. Unyoung (Ashley) Kim, and Dr. Richard Barber

## 34 Effect of Anode Biofilm Immobilization in Microbial Fuel Cells for Urea Degradation

Brandon Lin: Sustainable Energy Master's Student

Advisors: Dr. Maryam Mobed-Miremadi and  
Dr. Maryam Khanbaghi

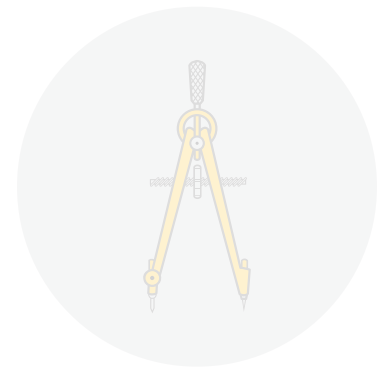
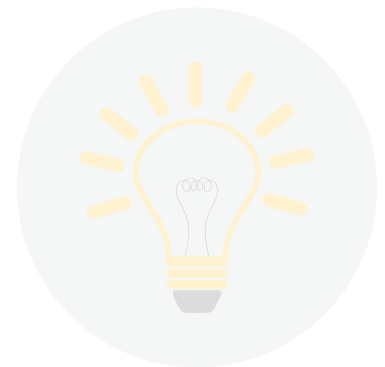
## 36 Brain Computer Interface Development for Virtual Reality Applications

Jonathan Bernal: COEN Master's Student

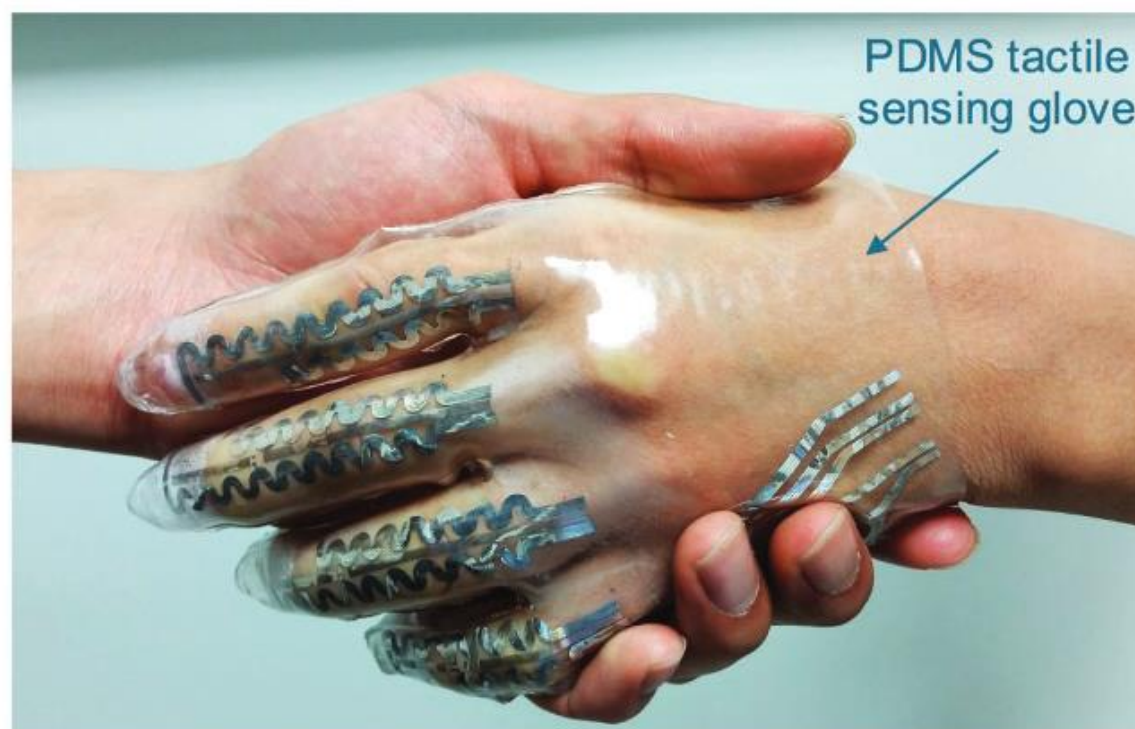
Andreas Adolfsson: COEN Ph.D. Student

Michael Breshock: BIOE Undergraduate

Advisors: Dr. Julia A. Scott and Dr. Maya Ackerman



## Microfluidics for tactile and gait monitoring



Gao et al, Adv. Mat, 2017

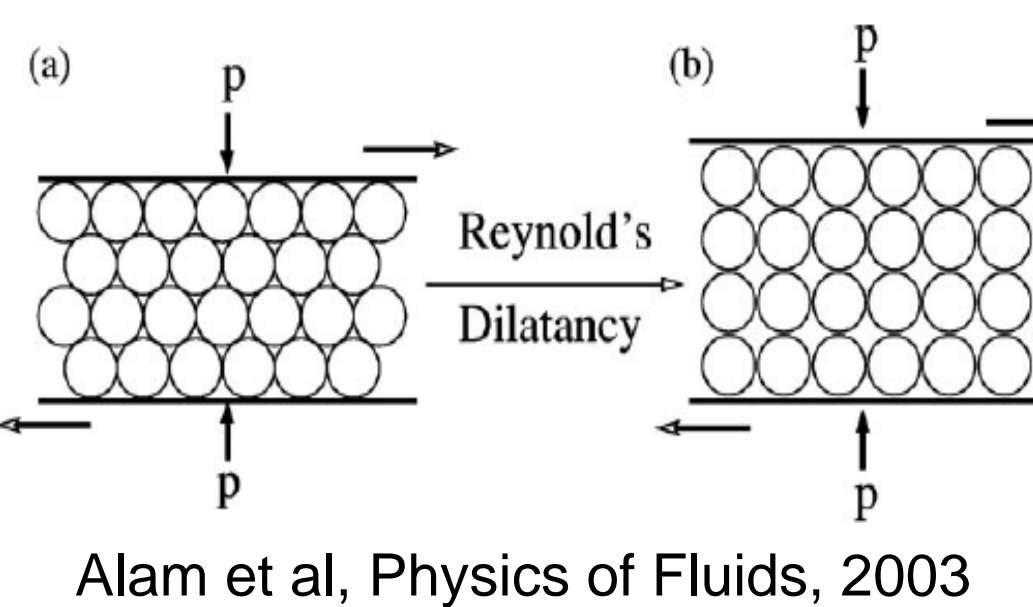
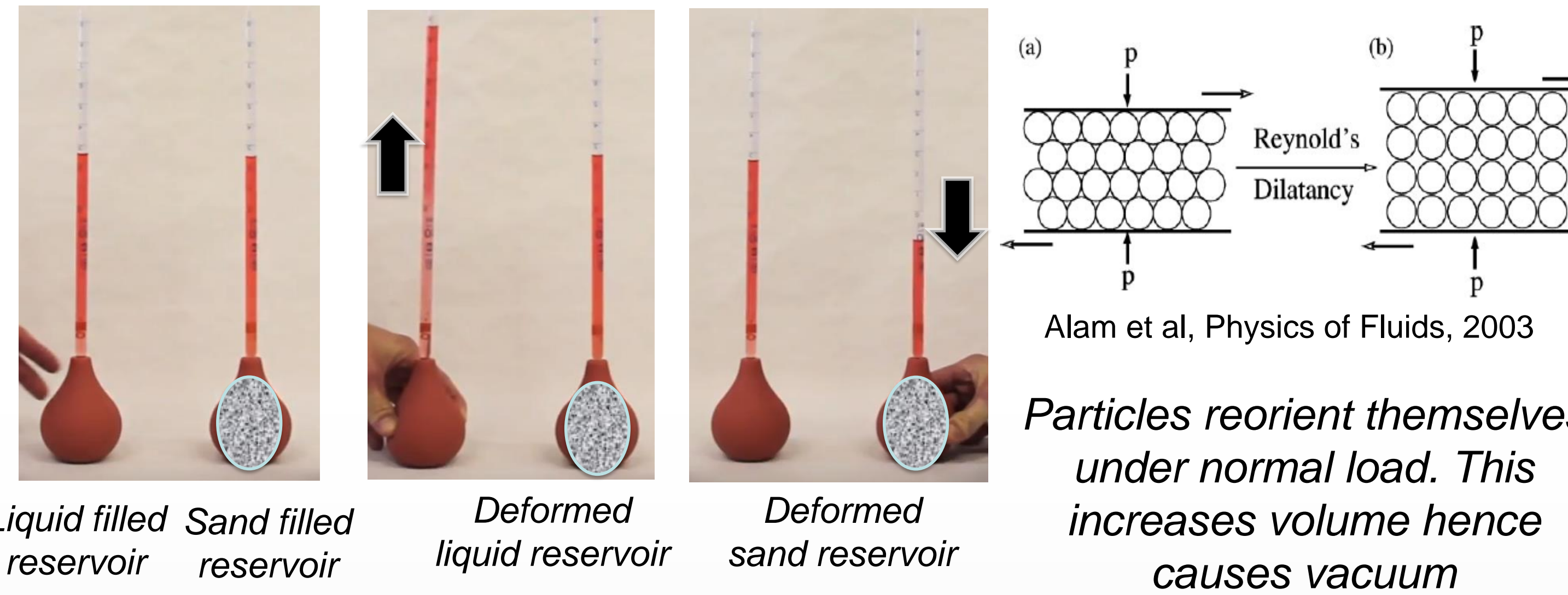
Microfluidic channels filled with liquid metals (e.g., Galinstan) or ionic solutions serve as flexible and highly sensitive sensors for at-home monitoring of physiological parameters.

The electrical resistance changes as the microfluidic channels deform according to the continuum mechanics principles.



Menguc et al, Int. J. of Robotics Res, 2014

## Reynold's dilatancy: A mechanical effect observed in granular materials



Alam et al, Physics of Fluids, 2003

Particles reorient themselves under normal load. This increases volume hence causes vacuum

## Microfluidic dilatometry is a novel technique to measure tangential uniaxial or biaxial strain

What is microfluidic dilatometry? A familiar example: mercury thermometer



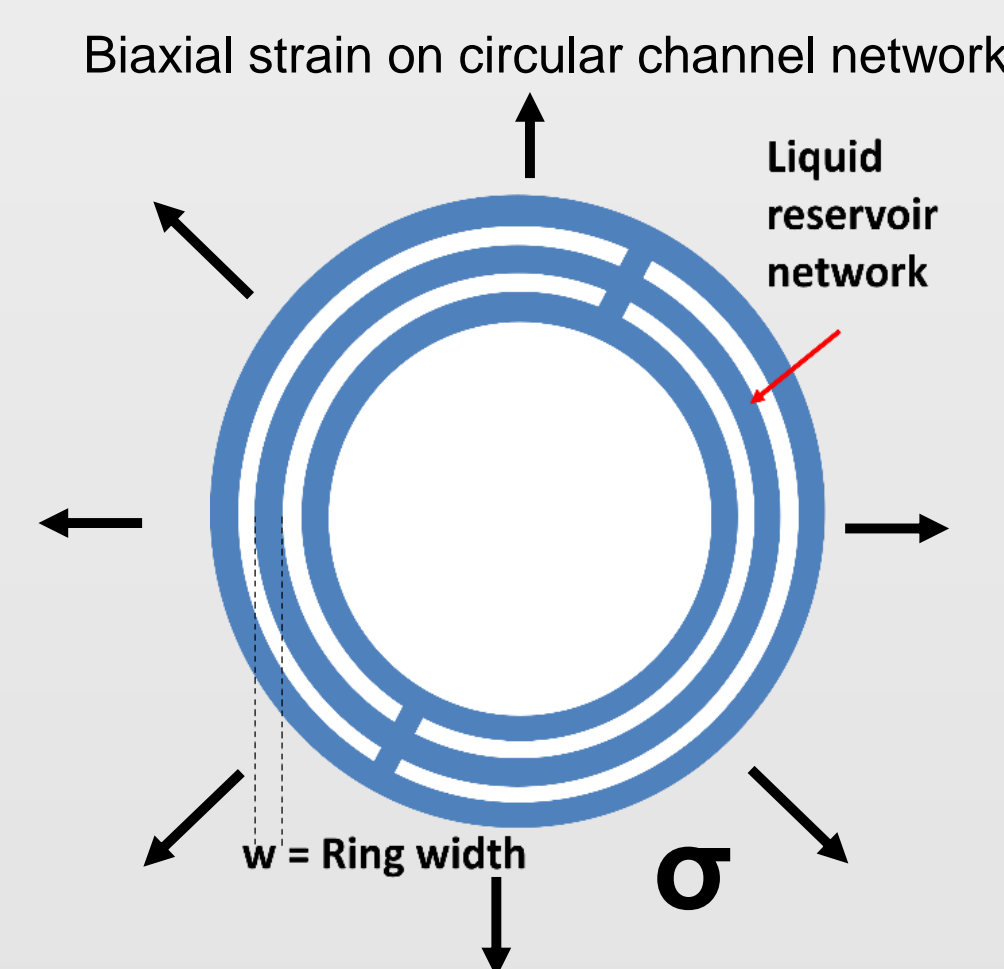
Mercury thermometer.

Volume change is used for the measurement of thermal expansion coefficient,  $T_e$ . If you know the  $T_e$ , you can make a thermometer based on dilatometry.

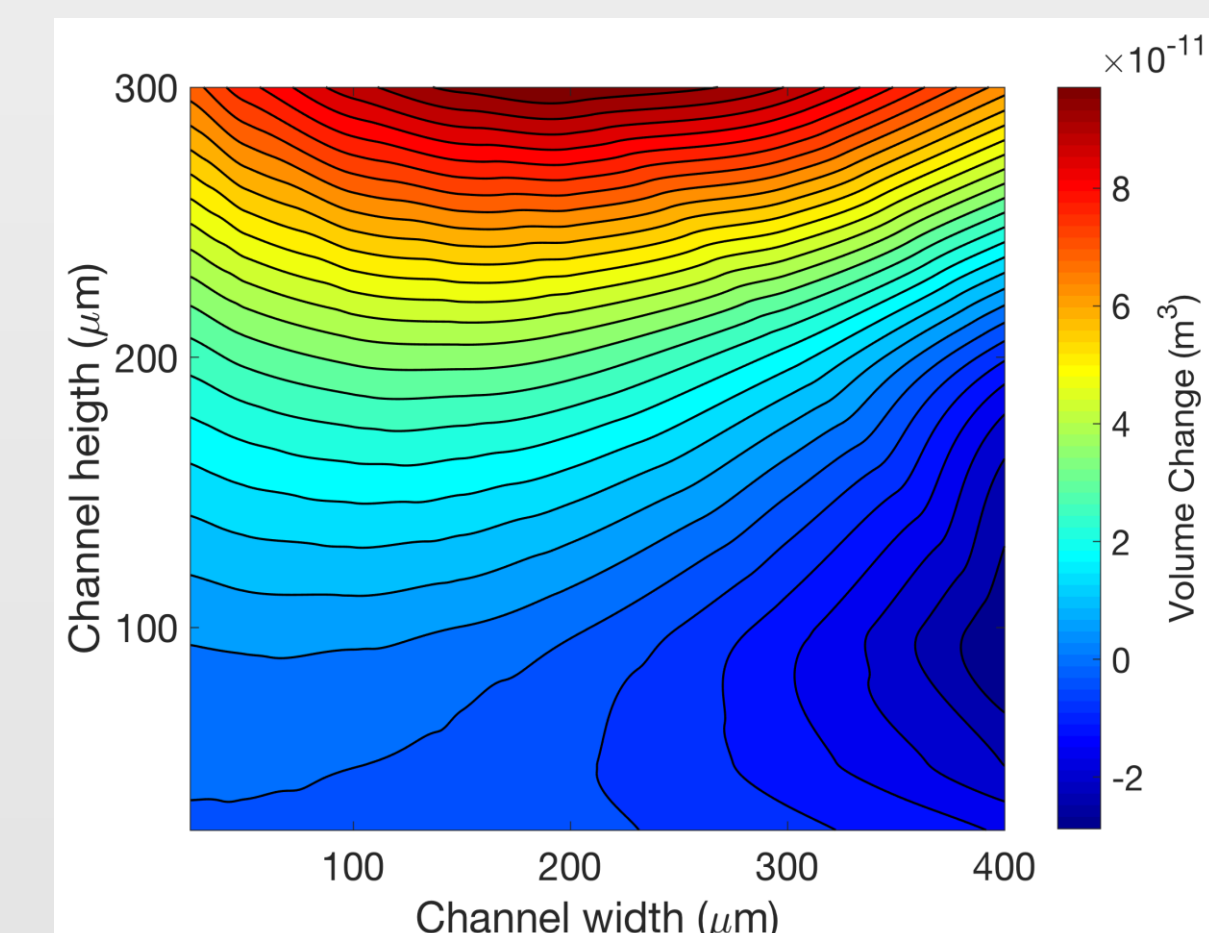
How about measuring strain?

$$\text{Volumetric strain in a solid is; } \Delta V/V_{\text{bulk}} = (1-2\nu)\epsilon$$

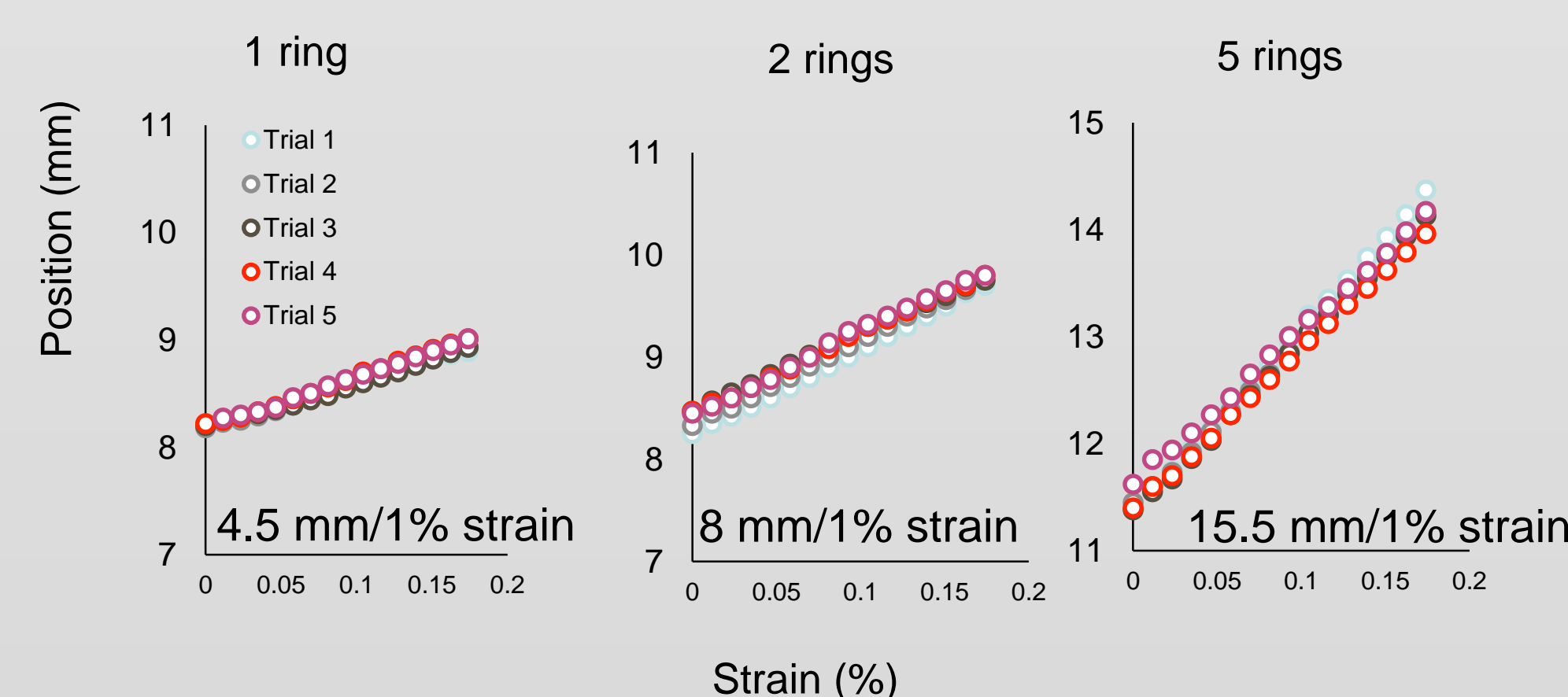
approaches zero for elastomers ( $\nu=0.49$ ); however, under stress, channels deform and volumetric strain can be increased by controlling this deformation!



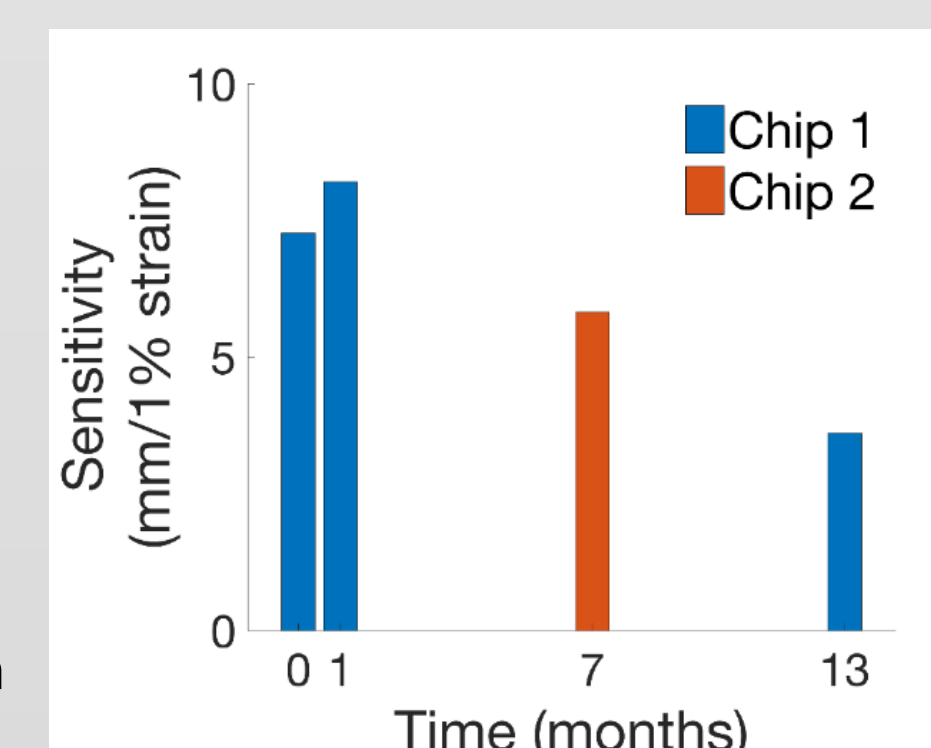
Example microfluidic network (left) and COMSOL simulation results showing the volume change for varying w and h, under biaxial stress (right)



Response of the sensor:



Lifetime of the sensor:



## Microfluidic dilatometry for strain sensing can solve the problems of existing sensors

Electrical sensing:

Dilatometric sensing:

Measures the relative resistance change	Measures the absolute volume change
High direction dependence	Low direction dependence
Affected from radial forces (motion artifacts)	Radial force effects are distinguishable
Reduced sensitivity for biaxial sensing	Increased sensitivity for biaxial sensing

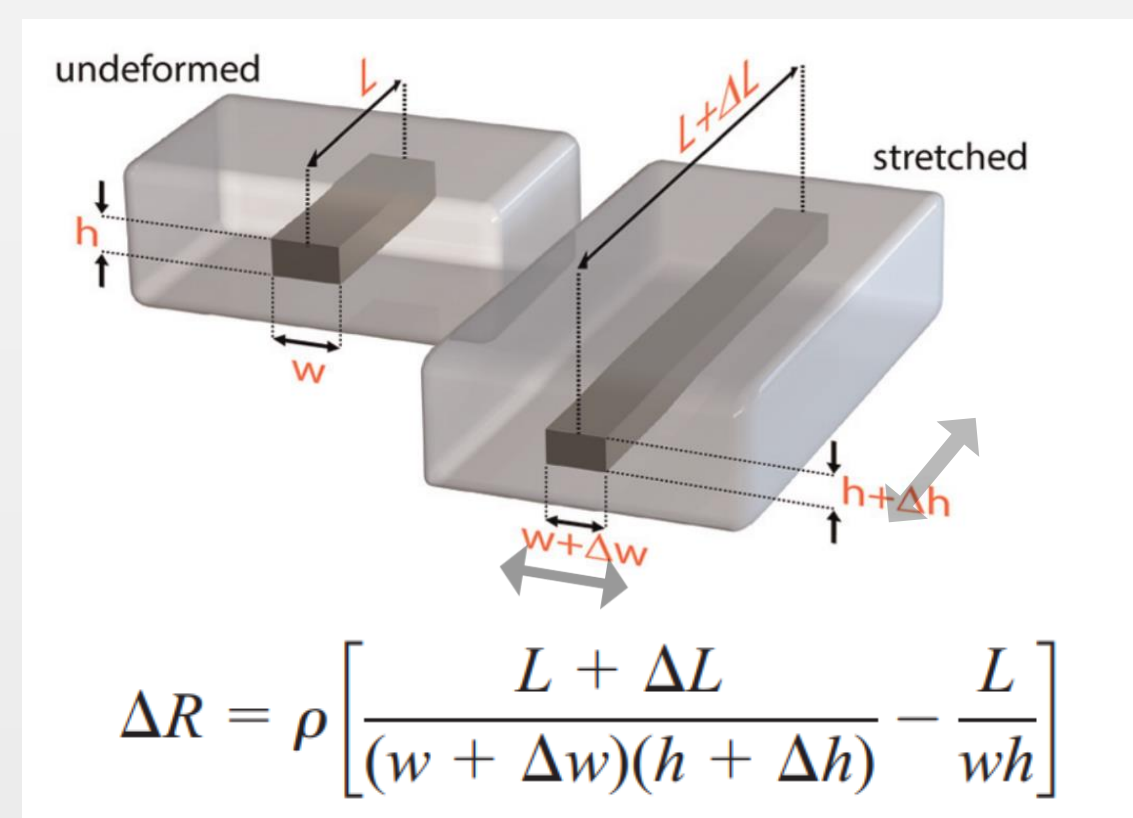
- The volume change transduced into the linear displacement: Provides ultrahigh biaxial strain sensitivity

$$\text{Sensitivity} \sim \Delta V/A \quad (A \text{ is the sensing channel cross-section})$$

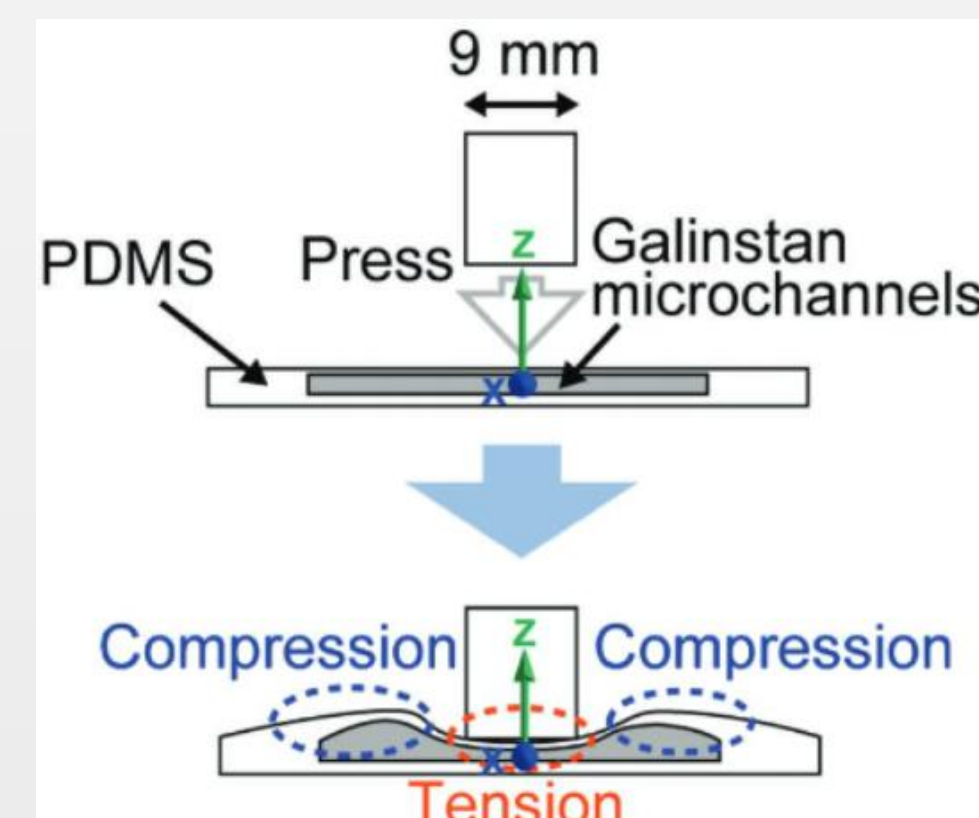
- Linear displacement visualization/detection is attractive for optical motion capture using smart devices

## Problems with existing microfluidic strain sensors

Tangential stress:



Radial stress:



1) For tangential stress: stress direction affects sensitivity:

Longitudinal stress:

$$\epsilon = \frac{\Delta L}{L}$$

$$\Delta w = -\nu \epsilon w$$

$$\Delta h = -\nu \epsilon h$$

Large sensitivity!

$\Delta R$  shows a large increase:

Transverse stress:

$$\epsilon = \frac{\Delta w}{w}$$

$$\Delta L = -\nu \epsilon L$$

$$\Delta h = -\nu \epsilon h$$

Small opposing sensitivity!

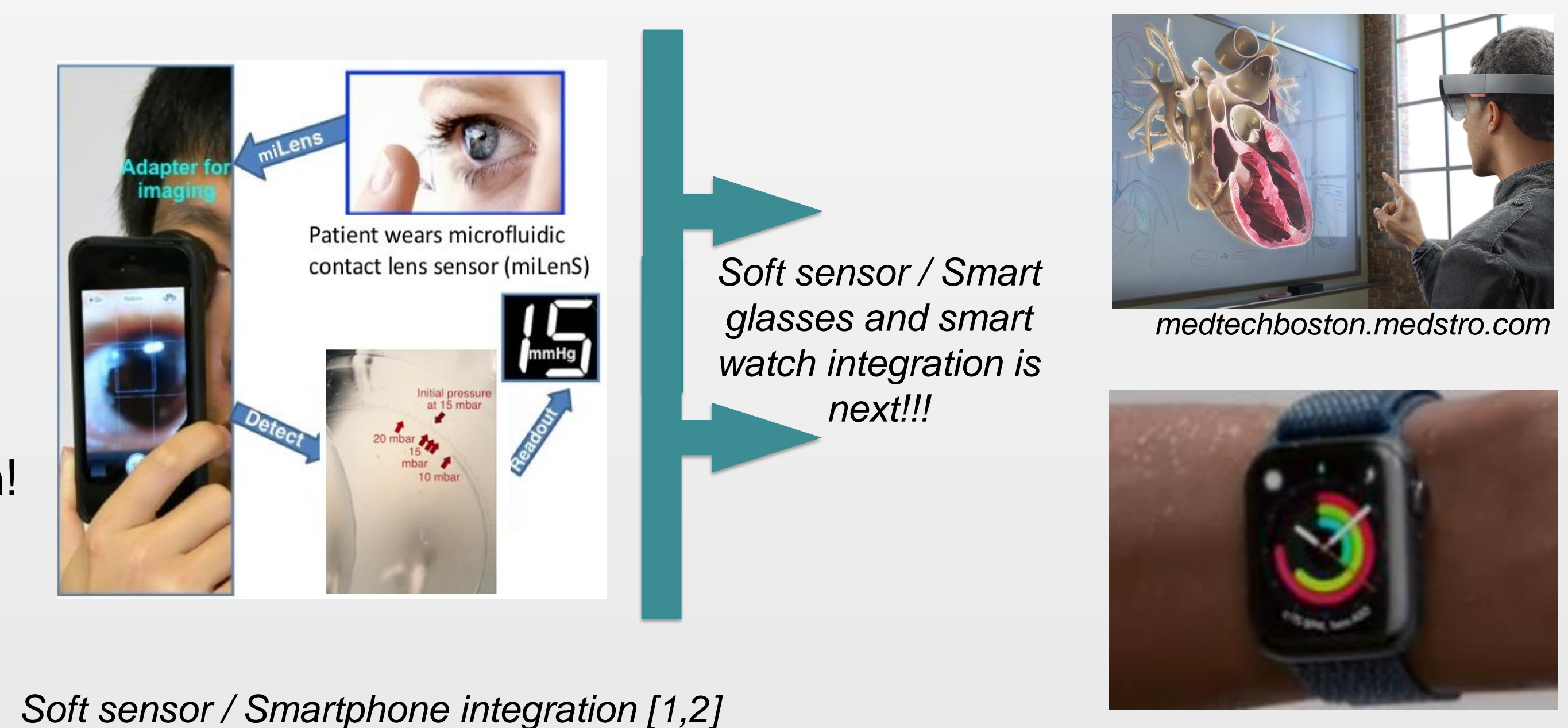
$\Delta R$  shows a small decrease:

2) The radial stress (pressure) and tangential stress are ambiguous (i.e., source of noise):

$\Delta R$  is positive for both longitudinal and radial stress. So, if both effects are present, this creates ambiguity (low signal to noise ratio)

3) Strain measurement in a large area (most biological tissue) reduces the sensitivity:

- Not suitable for biaxial tangential strain measurements
- Local strain in a large area sensor causes a small response ( $\Delta R$  is inversely proportional to the sensor width)



Soft sensor / Smartphone integration [1,2]



medtechboston.medstro.com



apple.com

## Summary / Future goals

- Microfluidic dilatometry is a novel physical transduction mechanism for precision medicine and rehabilitation engineering applications
- Suitable for biaxial sensing; ultrahigh sensitivity in wearables
- Non-linear materials and fluid dynamics models are needed in the future
- Preventing occlusion and achieving continuous measurements are the next steps

## References

- Araci I, Su B, Quake S, Mandel Y, "An implantable microfluidic device for self-monitoring of intraocular pressure", Nature Medicine, 2014
- Agaoglu S, Diep P, Martini M, KT S, Baday M, Araci I, "Ultra-sensitive microfluidic wearable strain sensor for intraocular pressure monitoring", Lab on a chip, 2018

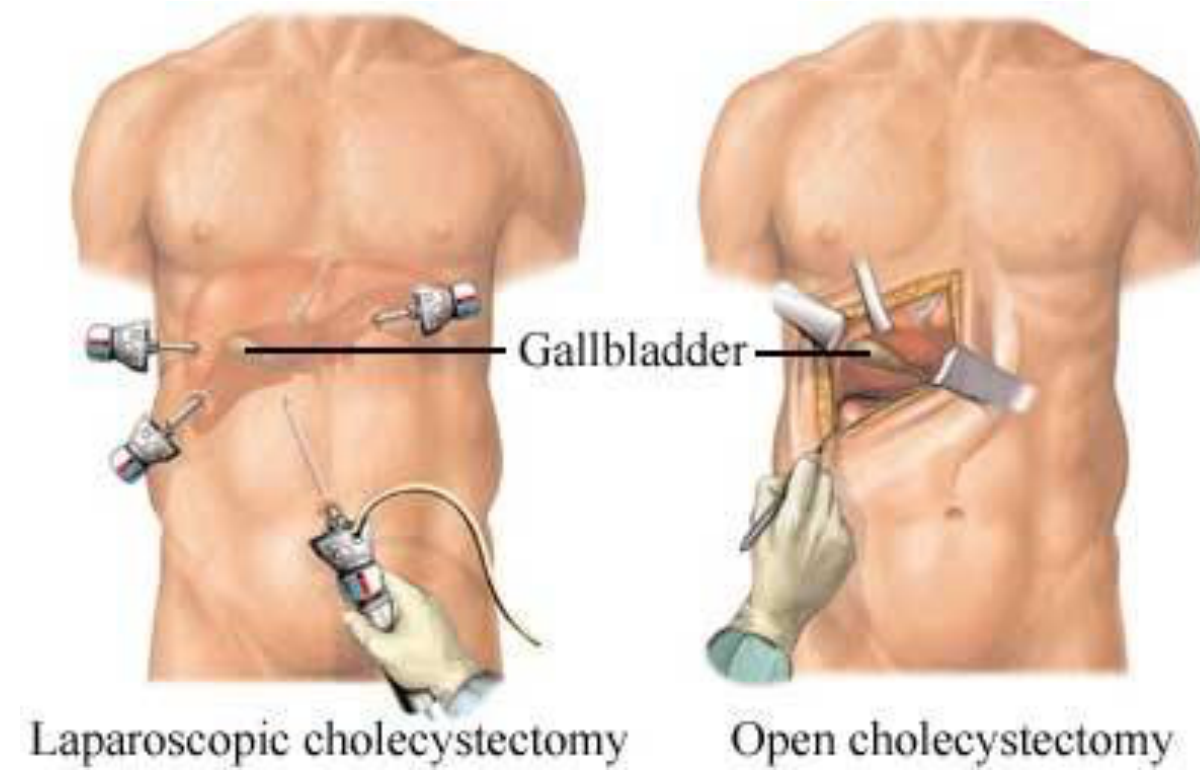
\*This study is supported by School of Engineering, SCU

## Introduction and Motivation

- **Endoscopes**
  - Eliminate need for large incisions
  - Viewed through eyepiece or projected onto monitor [1]
- **Minimally invasive surgery**
  - Irrigating fluids distend body cavities
  - If fluid pressure > venous pressure, **excess absorption of fluid** can occur [2]
  - Increasingly used every year [3]

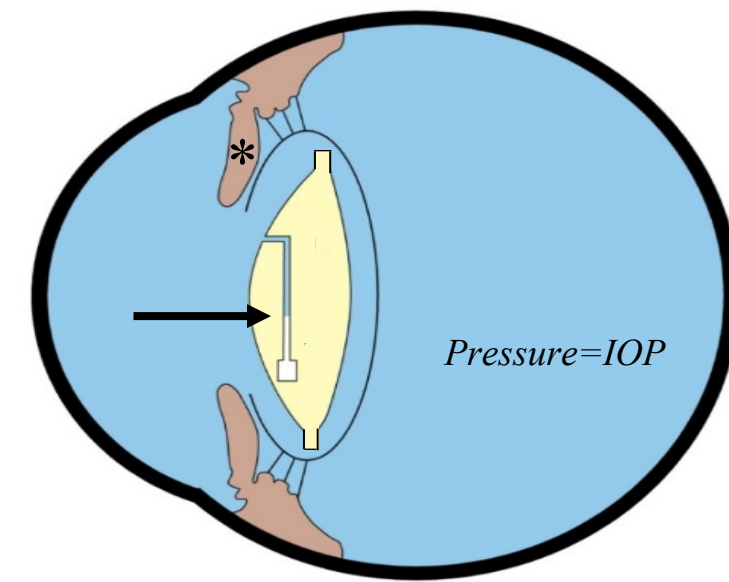


<https://www.microscopemaster.com/endoscopes.html>

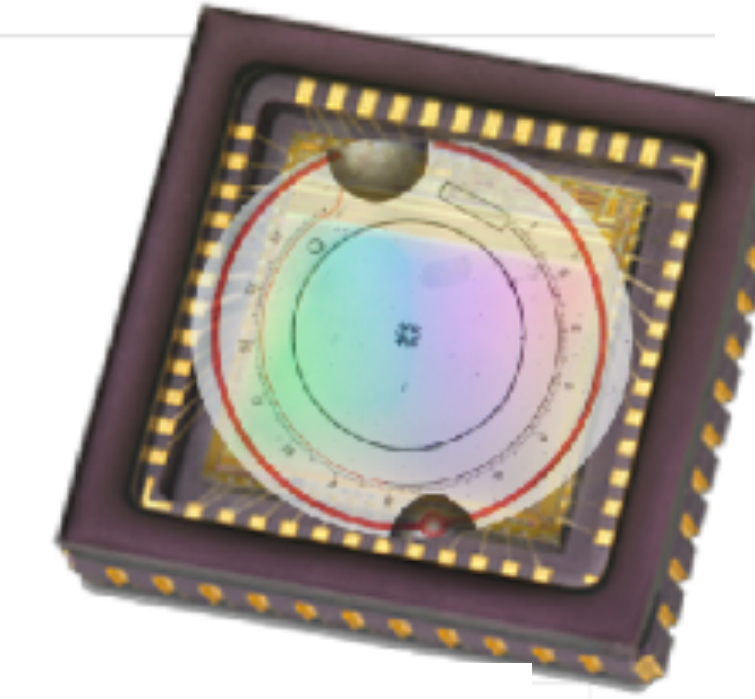


Laparoscopic cholecystectomy Open cholecystectomy  
<https://www.policymed.com/2014/10/minimally-invasive-surgery-educating-surgeons-through-proctorships.html>

- **Passive pressure sensors**
  - Accurate “true fluid pressure” monitoring using soft microfluidic device technology.
  - Eliminate need for electrical connections
  - **Demonstrated for intraocular pressure measurement [4]**



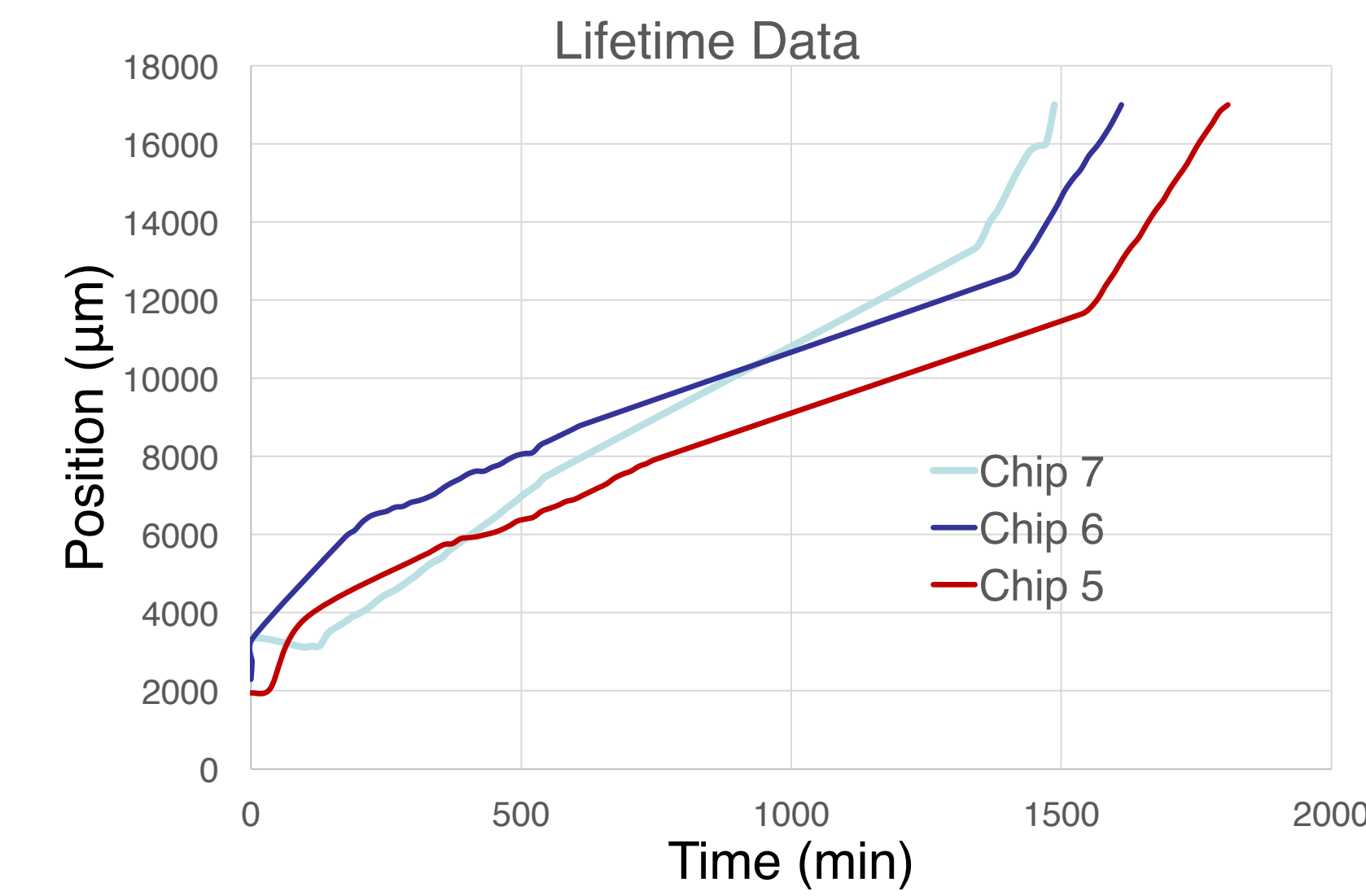
Schematic of the IOL sensor in the eye



Conceptual representation of the endoscopic pressure sensor

**Our goal is to successfully integrate a pressure sensor with a CCD camera for continuous pressure sensing during endoscopic surgery.**

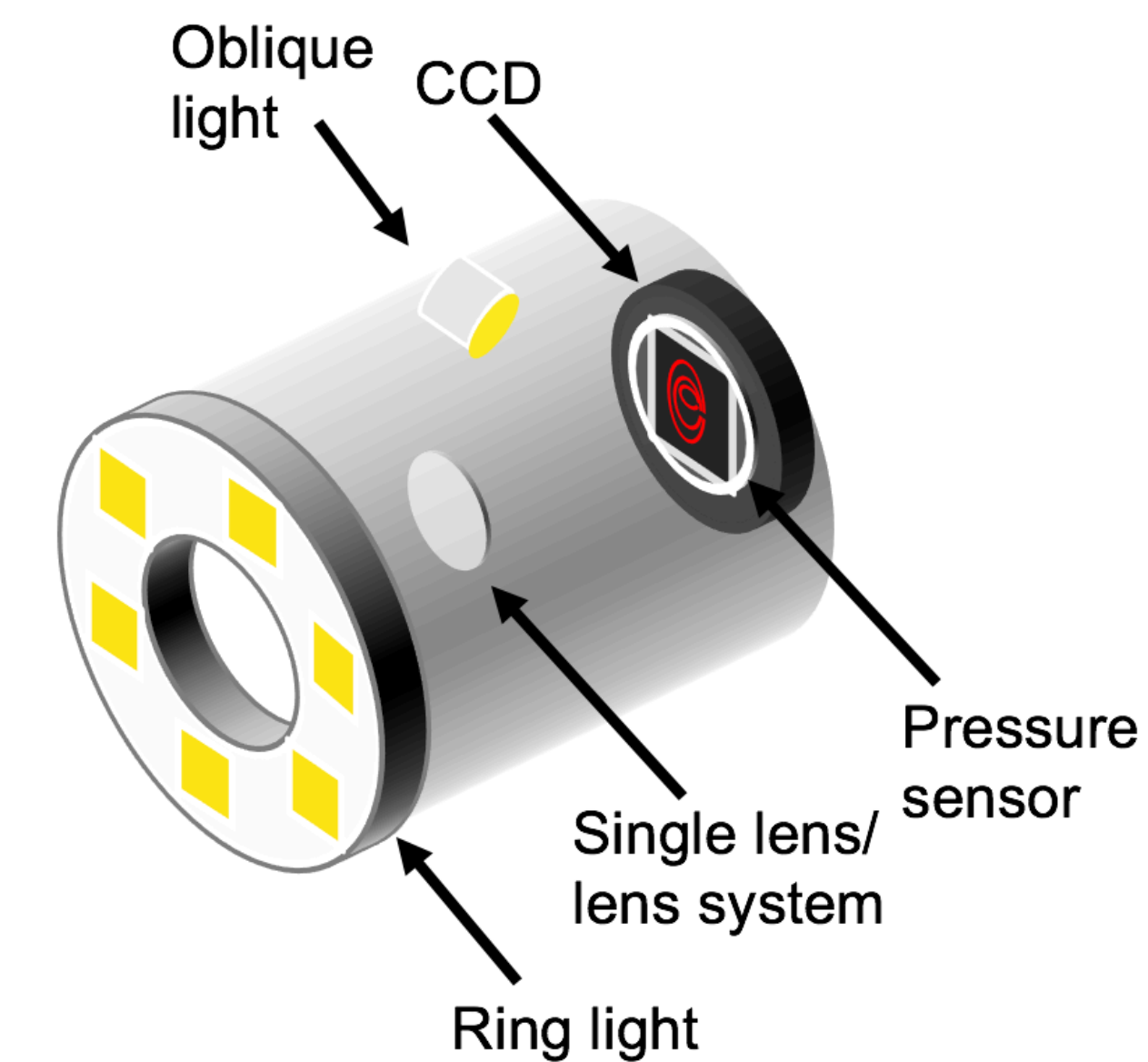
## Sensor Characterization Shows a Lifetime of Over 24 Hours



The chips have an average lifetime of about 26 hours. The miniaturized sensor limits the lifetime, however 26 hours is sufficient for endoscopy applications.

## Conclusion and Future Plans

These results show the potential for a sensor/CCD integration with a variety of applications. Creation of a prototype with both background and inner illumination is needed, along with a standardization of pressure sensor sensitivity. The next step would be to test the prototype inside an *in vivo* environment.



Once this prototype is finished, a future goal would be to create a system in which pressure may be continuously monitored while preserving the entire field of view.

## Design and Methods

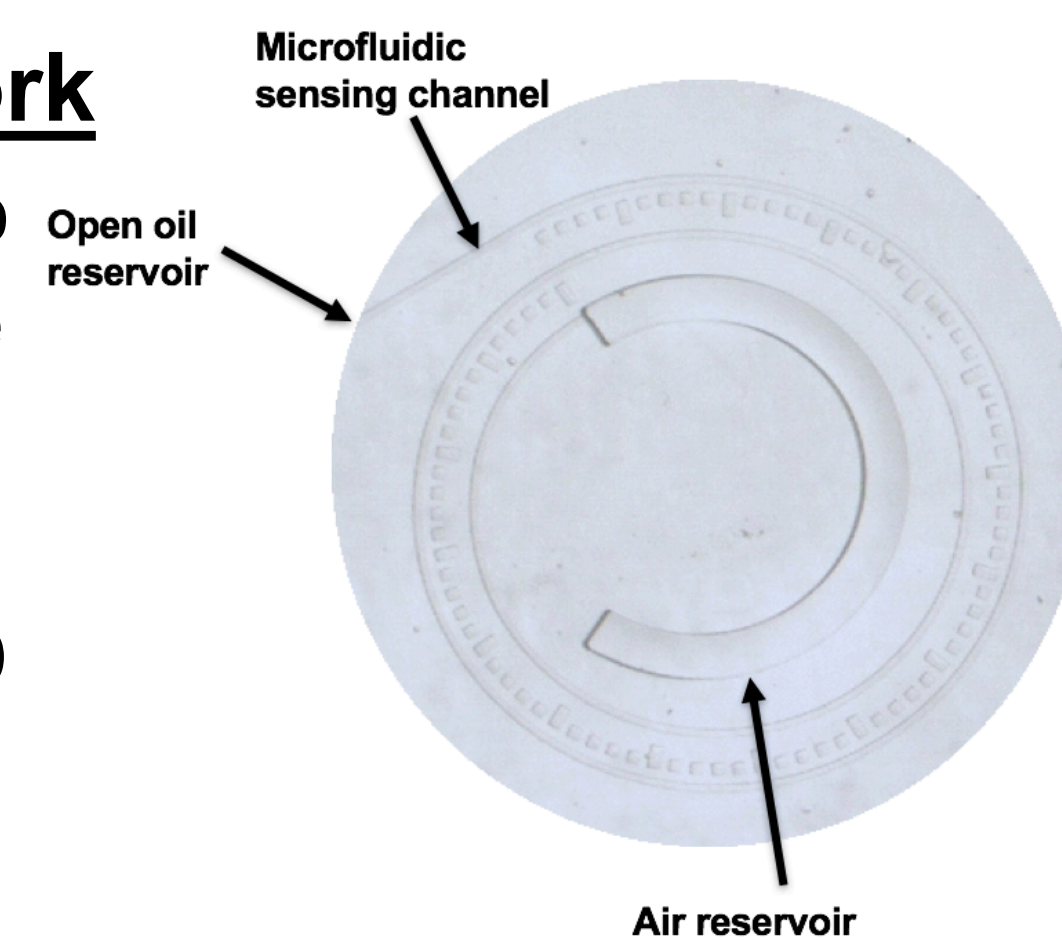
A direct integration **approach** was taken, which involved placement of a pressure sensor directly onto the CCD.

### New Sensor Design

- Entire sensing channel visible on CCD → within 3 mm x 3 mm area
- Must take into account:
  - Decrease in length of sensing channel → lower lifetime
  - Smaller air reservoir → lower sensitivity

### How They Work

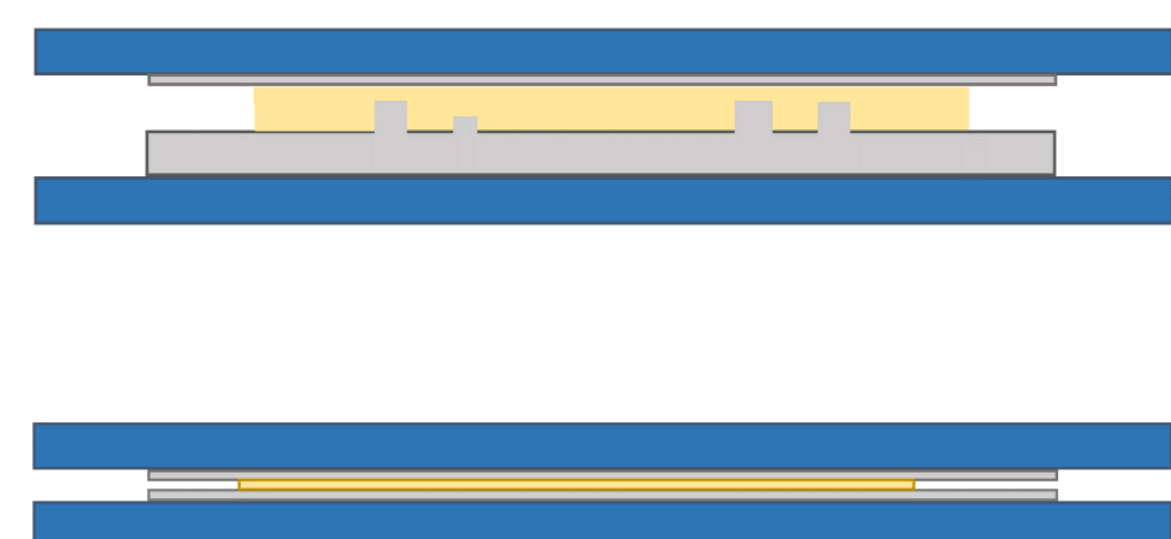
- Changes in fluid pressure converted into gas/liquid interface movement inside the microfluidic channel
- The movement of gas/liquid interface is illuminated and viewed through the CCD camera



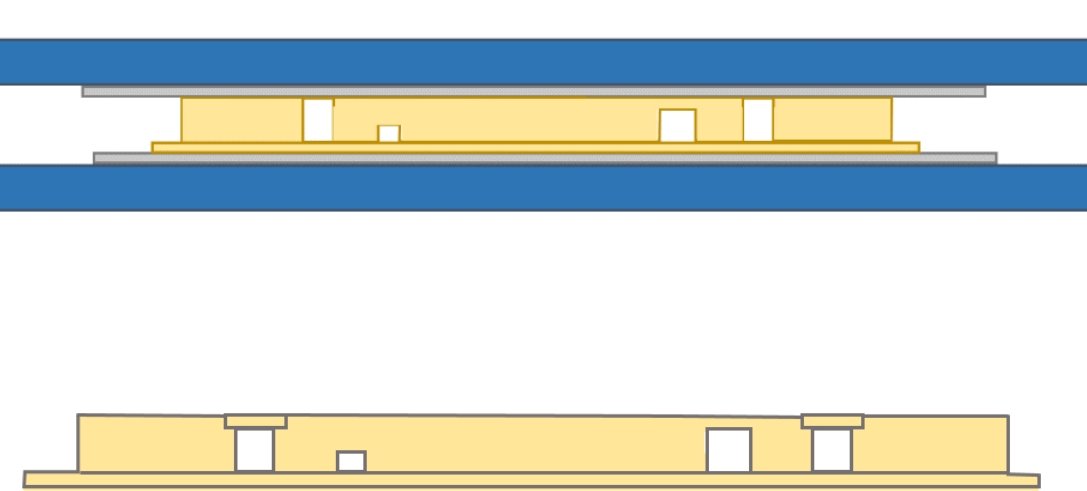
### Sensor Fabrication Process

#### Top Layer

UV curable NOA 65 exposed to UV light for 1 min. 30 seconds



Plasma treated for 60 seconds  
 Pressure for 15 minutes



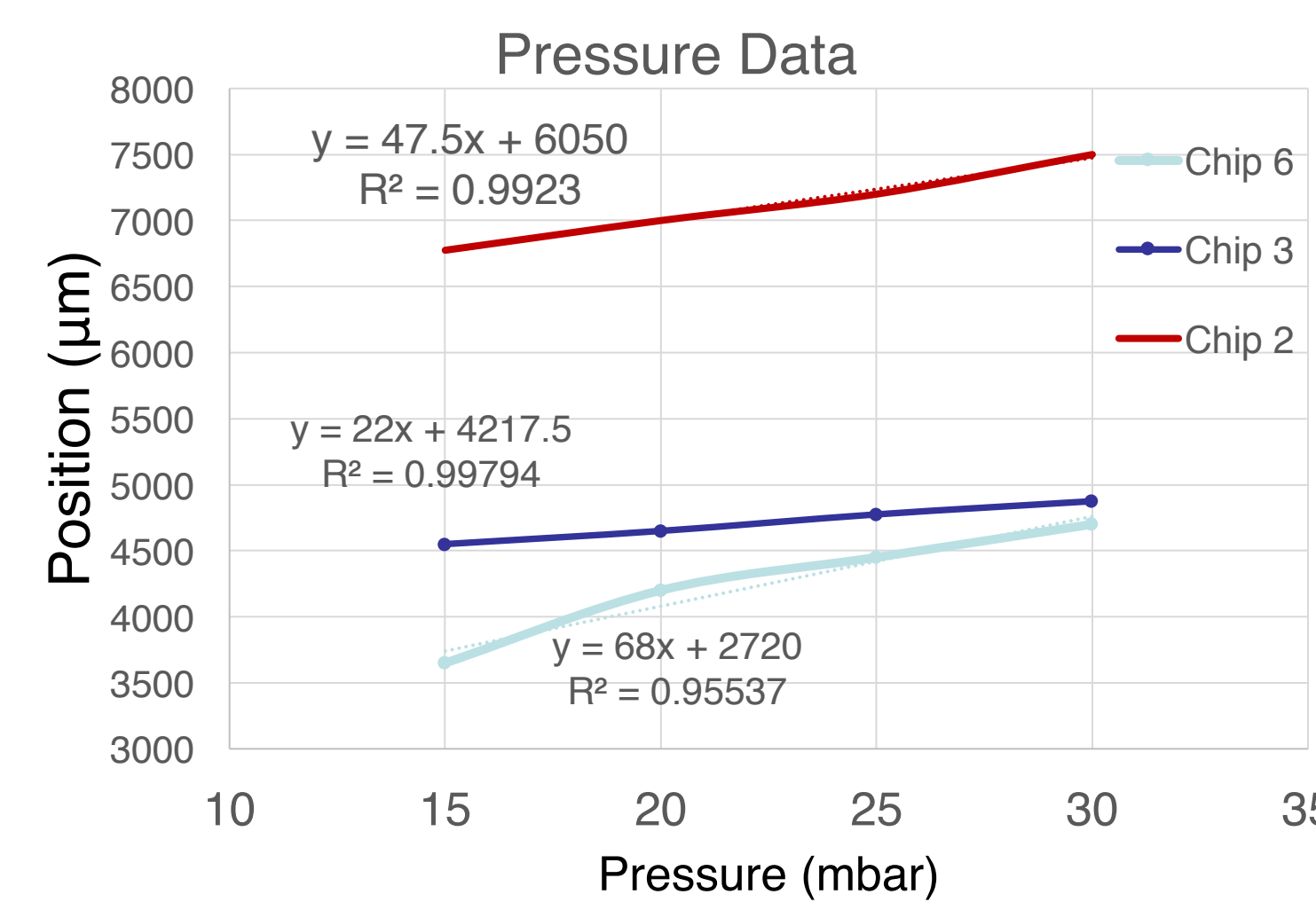
Fill with oil

#### Bottom Layer

NOA 65 UV cured for 1 min. 30 seconds  
 Surface treated to add amine groups for 10 minutes

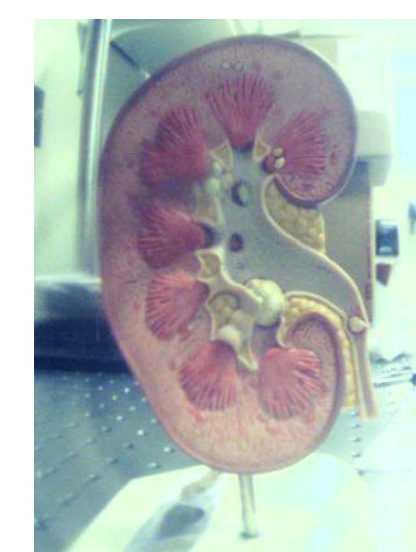
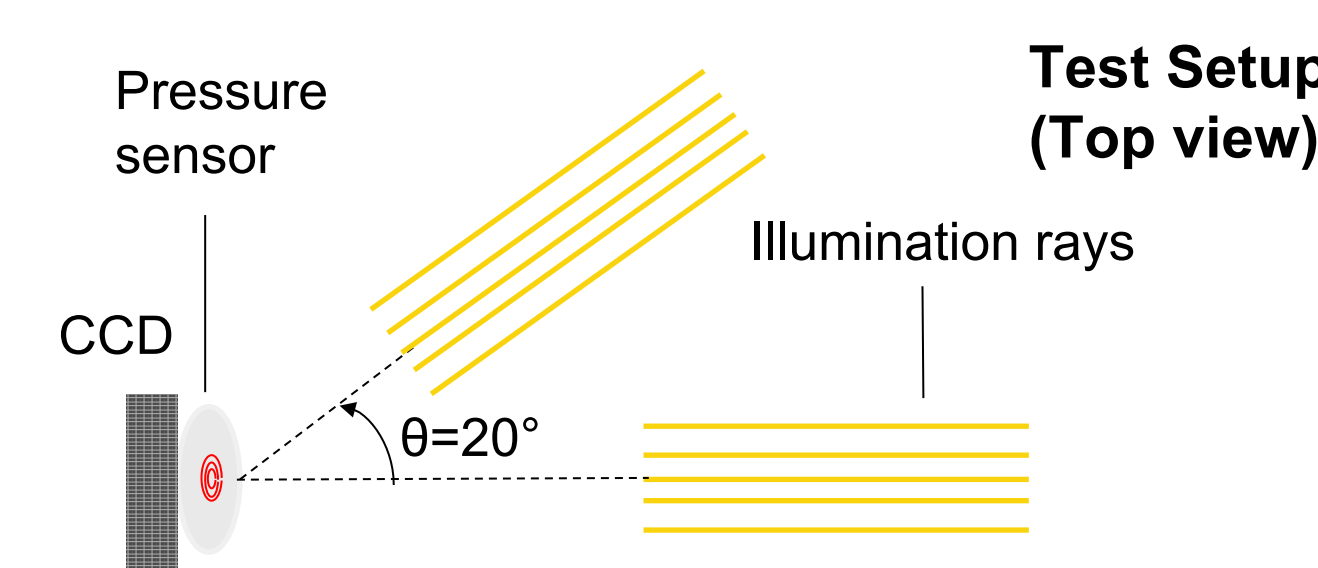
## Pressure Sensitivity

The pressure sensors show approx. linear sensitivity to changes in pressure. Each pressure sensor must be calibrated to determine its sensitivity (in µm/mbar).



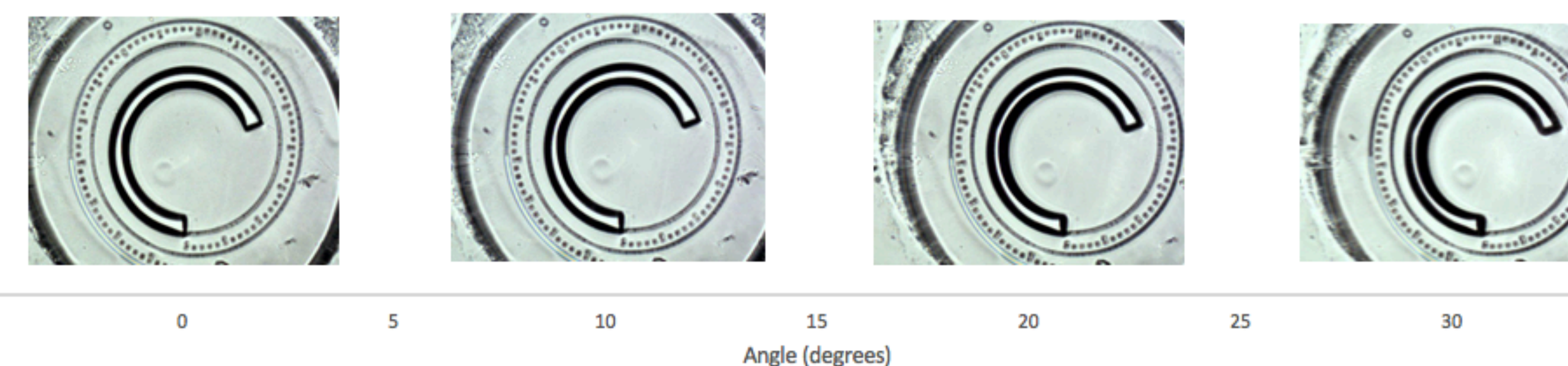
## Angle of Illumination

Variation in angle of illumination tested to determine if oblique illumination would be viable (to avoid placing a light in the direct line of imaging).



An objective lens system with a focal length of 12.5 mm was used to image this kidney model. It was used to test an optical setup for the prototype.

### Illumination angle (θ) testing



As seen by the angle testing results, an oblique angle of illumination would result in good visualization of the pressure sensor.

## References

1. Hahn, R. (2006). Fluid absorption in endoscopic surgery. *British Journal of Anaesthesia*, 96(1), 8-20. doi:10.1093/bja/aei279
2. Cheng, D., Wang, Y., Yu, L., & Liu, X. (2014). Optical design and evaluation of a 4 mm cost-effective ultra-high-definition arthroscope. *Biomedical Optics Express*, 5(8), 2697. doi:10.1364/boe.5.002697
3. Tsui, C., Klein, R., & Garabrant, M. (2013). Minimally invasive surgery: National trends in adoption and future directions for hospital strategy. *Surgical Endoscopy*, 27(7), 2253-2257. doi:10.1007/s00464-013-2973-9
4. Araci, I. E., Su, B., Quake, S. R., & Mandel, Y. (2014). An implantable microfluidic device for self-monitoring of intraocular pressure. *Nature Medicine*, 20(9), 1074-1078. doi:10.1038/nm.3621

## Acknowledgements

The author would like to thank the Kuehler Undergraduate Research Program from Santa Clara University for financial support, along with Dr. Emre Araci for his mentorship.

# Targeted Delivery to Neurons Using Engineered Exosomes



David Diebold | Kyle Asano | Biao Lu | Santa Clara University | Department of Bioengineering

## Abstract

The brain and central nervous system have been notoriously difficult to treat with therapeutics due to the blood-brain barrier. Exosomes, however, can easily pass through this barrier. By loading therapeutics into exosomes, drugs could be delivered more easily to treat neural diseases like brain tumors.

Exosomes are cell-derived nanovesicles that can be modified with engineered surface proteins. We hypothesize that we could manufacture engineered exosomes that have enhanced neuron-specific delivery in living human cells.

These protein constructs use VSVG as a scaffold and target with RVG (viral protein) or NCAM (human protein).

We have shown that the desired engineered exosomes have been produced, characterized, and re-uptaken by human cells. Tests are currently being run to determine how readily these exosomes are absorbed into a variety of human cell types, including neural cells. Then, quantitative analysis can be done to determine if this uptake occurs preferentially in neural cells.

## Approach: Surface Engineering

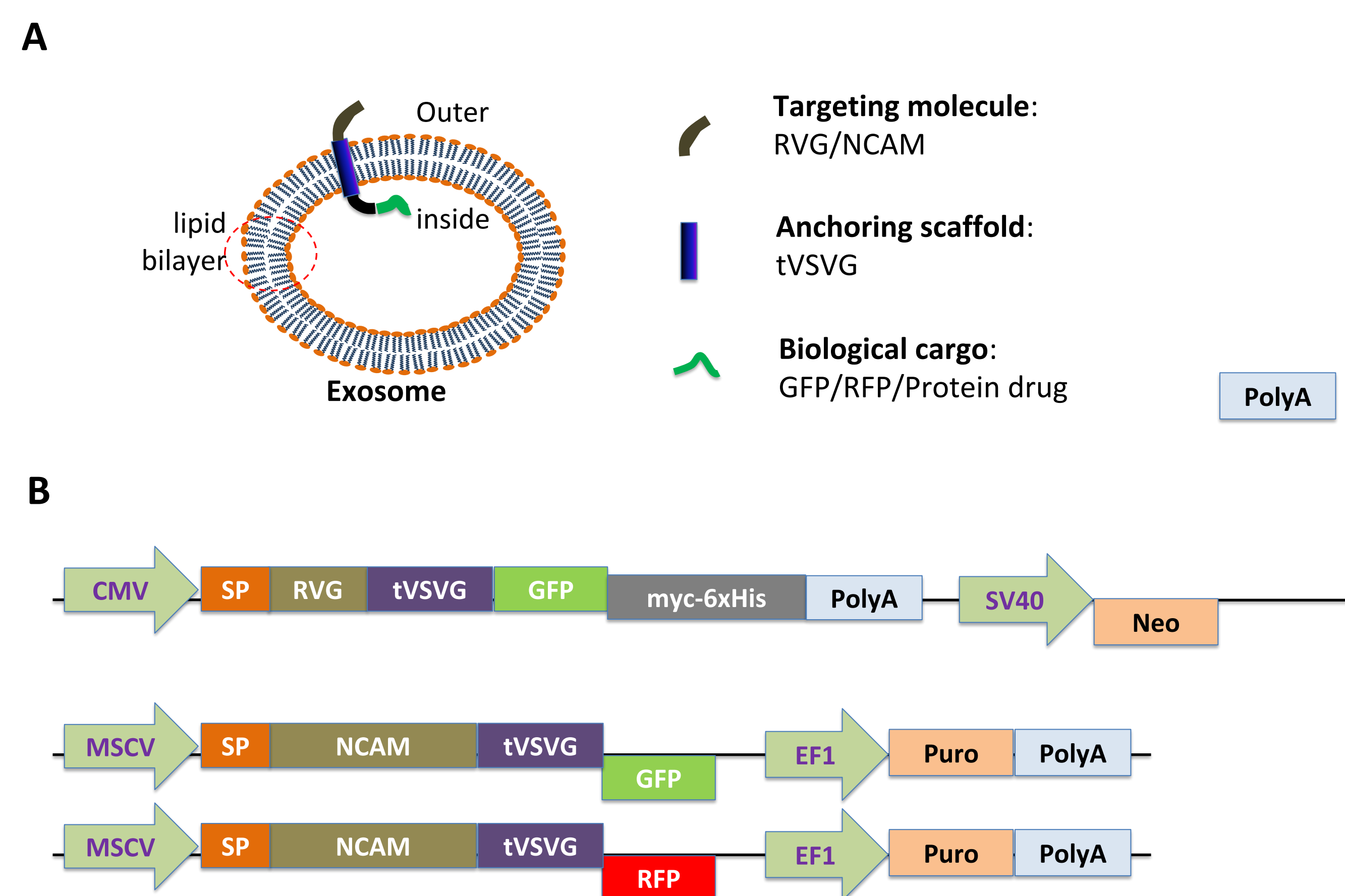


**Figure 1: Design and construction of dual-tagged reporter protein for exosome tracking and capture**  
**(A)** Vector design for VSVG fusion proteins. Fluorescent (GFP, RFP) and NCAM/RVG genes were attached as shown. **(B)** The schematic of dual loaded exosomes showing VSVG transmembrane protein, GFP or RFP reporters, and NCAM/RVG -tag.

## Results

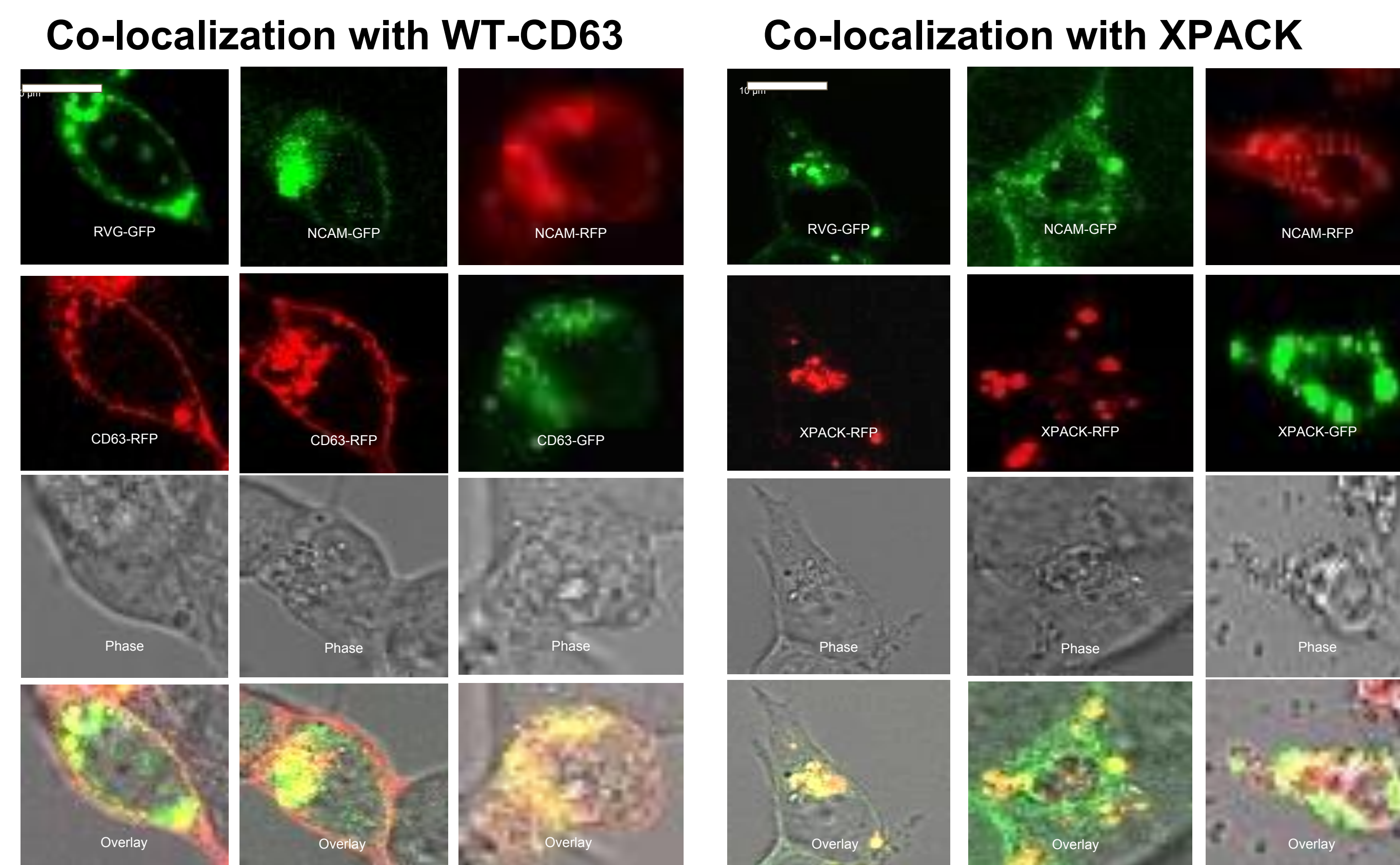


**Figure 2: Colocalization of tracking molecules with exosome markers**  
 HEK293 cells were co-transfected with our RVG-VSVG-GFP, NCAM-VSVG-GFP, or NCAM-VSVG-RFP and known exosomal markers XPACK, and WT-CD63. After 48 hours incubation time, exosomes were observed to be colocalized in subcellular punctations.

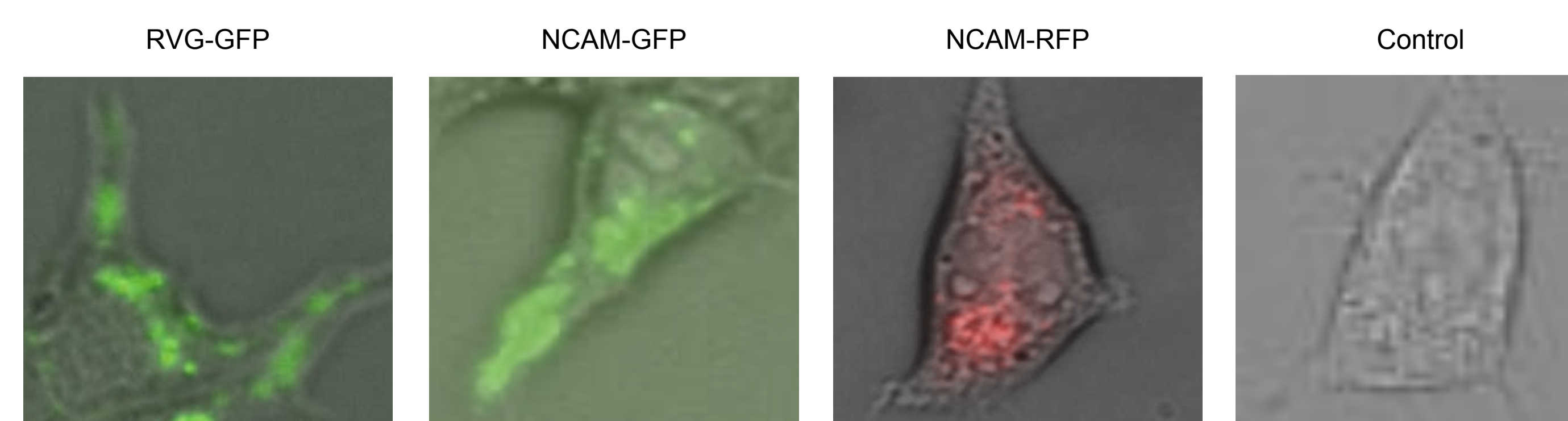


**Figure 3: Modified Exosome Stable Cell Lines (HEK293)**  
 HEK 293 cells were transfected to produce modified exosomes containing our three constructs along with a toxin resistance. We then introduced the toxin to remove all unmodified cells.

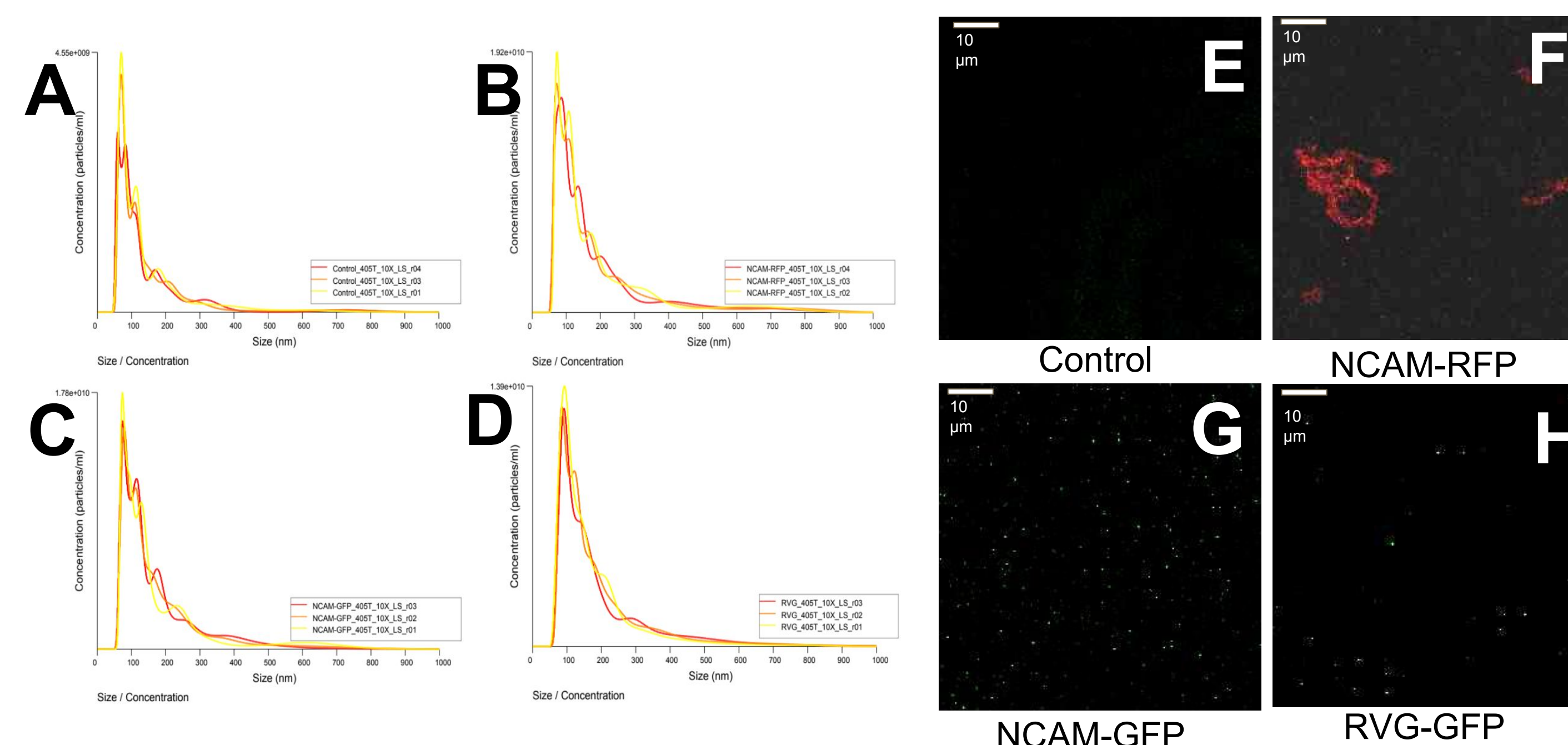


**Figure 4: Characterization of exosomes released from producer cells**  
 Isolated exosomes were analyzed with Nanoparticle Tracking Analysis (A-D) (Nanosight) indicating similar size distributions between our construct modifications and unmodified HEK293 exosomes. The images on the left (E-H) show the exosomes suspended in phosphate buffered saline (PBS).

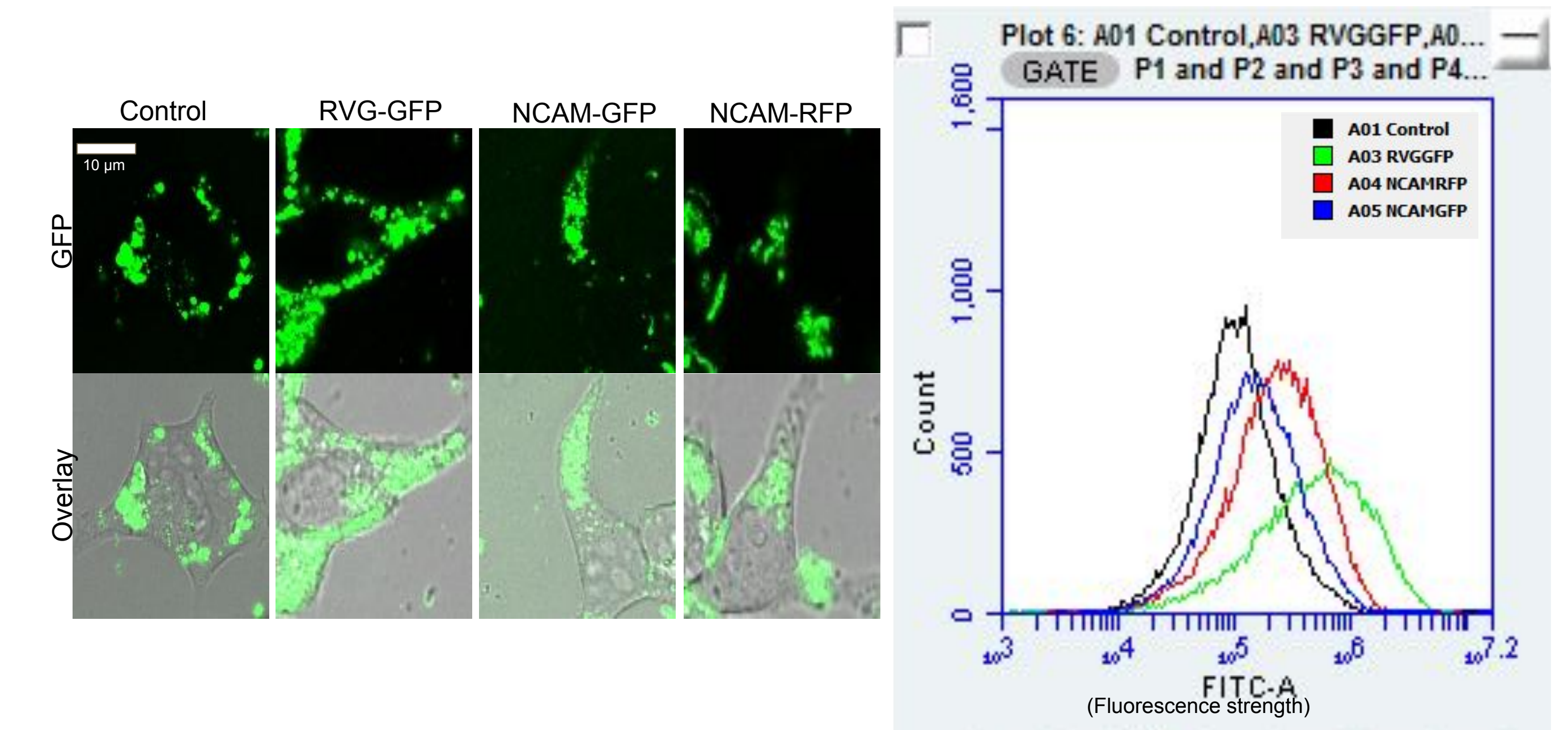


**Figure 5: Uptake of Modified Exosomes to HEK293 cells (72 hr)**  
 An uptake assay with RVG-VSVG-GFP, NCAM-VSVG-GFP, NCAM-VSVG-GFP modified exosomes in HEK293 cells was performed in serum-free Ultra-Culture (Gibco). All exosomes were stained using EXOglow. A FACS analysis was done to compare the relative strength of fluorescence coming from these cells.

## Summary & Future Studies

So far, we have successfully designed, produced, and harvested from human cells. We have had them characterized, and we were able to confirm re-uptake by human cells.

Currently, experiments focus on confirming that these engineered exosomes will be uptaken in a variety of cell types. Preliminary data affirms exosomes being uptaken in NEURO2A (a type of mouse neural cell) and U87 (cell type used in brain cancer research) cell types.

We will further test more cell types to confirm if engineered exosomes are preferentially uptaken by neural cells with positive markers. If our hypothesis is correct, these engineered exosomes may be used to deliver drugs to targeted cells in the brain. Delivering drugs through exosomes may allow easy passage through the blood-brain barrier and lower the likelihood of an immune response to medication.

## References

- Tkach, M., & Théry, C. (2016). Communication by Extracellular Vesicles: Where We Are and Where We Need to Go. *Cell*, 164(6), 1226-1232. doi:10.1016/j.cell.2016.01.043
- Meyer, C., Losacco, J., Stickney, Z., Li, L., Marriott, G., Lu, B. (2017). *International Journal of Nanomedicine*. 12:3153-3170
- Hassuna, N., Monk, P. N., Moseley, G. W., & Partridge, L. J. (2009). Strategies for targeting tetraspanin proteins: Potential therapeutic applications in microbial infections. *BioDrugs*, 23(6), 341-359. http://doi.org/10.2165/11315650-000000000-00000
- Stickney, Z., Losacco, J., McDevitt, S., Zhang, Z., & Lu, B. (2016). Development of Exosome Surface Display Technology in Living Human Cells. *Biochemical and Biophysical Research Communications*, 472(1), 53-59. http://doi.org/10.1016/j.bbrc.2016.02.058



Chantell Farias, Rachel Flores, Natalie Ploof, Dr. Maryam Mobed-Miremadi, Dr. Unyoung Kim  
Department of Bioengineering

## INTRODUCTION

Due to the growing need for minimally invasive drug delivery systems for therapeutics, hollow microneedle (MN) arrays have been designed and fabricated by stereolithography (SLA). This biodevice has been designed to extrude alginate microcapsules into which epithelial cells have been seeded for regenerative medicine applications.

To enable flowrate optimization for therapeutic administration, we will change the aspect ratio. In this study, the operating flowrate of 12 mL/min associated with reliable jetting of the bolus microcapsule suspension exceeded 40 times the therapeutic value of 0.3 mL/min<sup>[1]</sup>. Microcapsule administration at lower flowrates led to nozzle blockage induced by aggregation. Colloidal stability can be inferred by surface coating of microcapsules with a polyelectrolyte (modifying the surface charge) and changing the ionic strength of the media<sup>[2]</sup>. A consequence of increased distance between capsules due to electrostatic repulsion may have a lower particle density, resulting in decreased payload. This drawback could be overcome by fabricating smaller alginate structures using well established methodologies<sup>[3]</sup>.

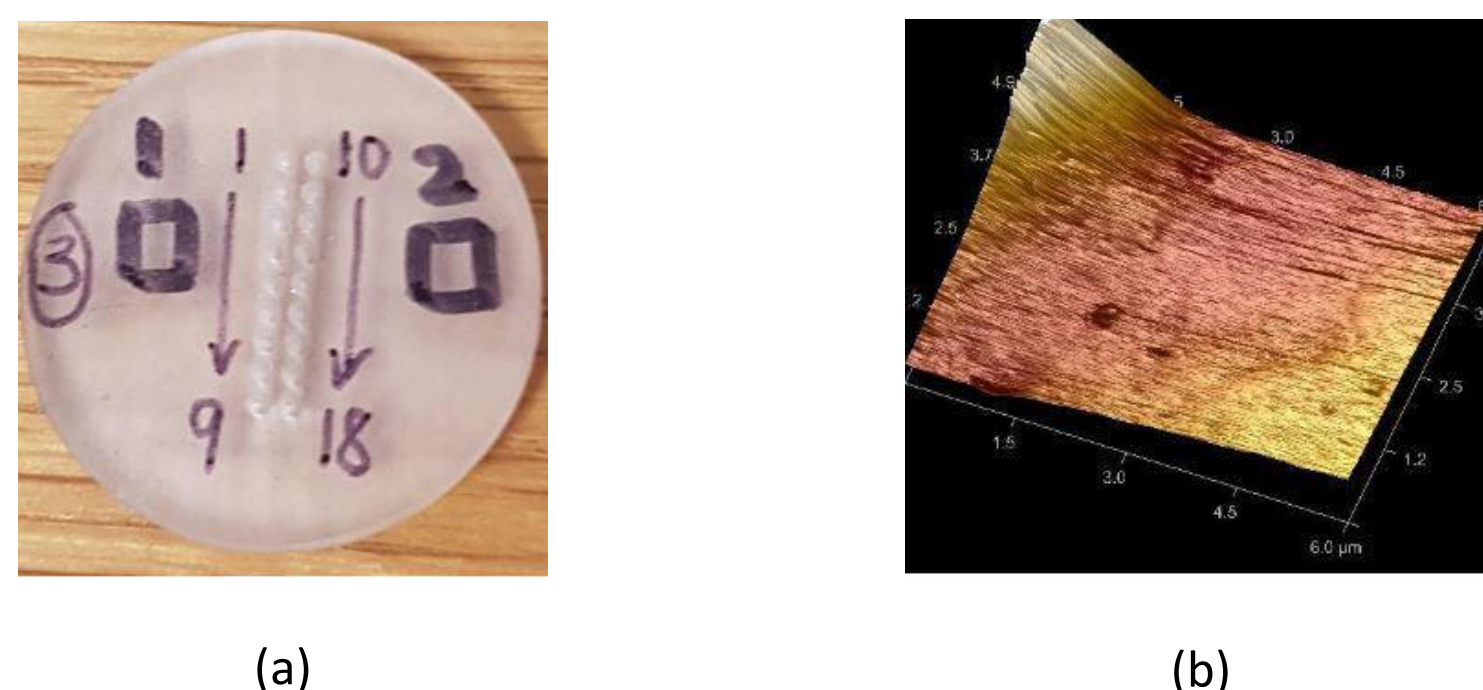


**Figure 1:** Atomic Force Microscopy (AFM) measurements: (a) Labeled custom-printed part designed for surface roughness measurements; (b) 3D structure of the regions geared towards exposure to skin surface utilized for RMS determination [4].

## OBJECTIVES

- To optimize the colloidal stability of the microcapsule suspension to be extruded in order to prevent flocculation during extrusion
- To measure the impact of the aforementioned optimization on human hepatocellular carcinoma (HepG2) cell viability

## METHODS

### 1. 3D Printing

- Change in the aspect ratio
  - height increased to 750 $\mu$ m

### 2. Flow Optimization

- Navier Stokes equation

$$\rho \frac{\partial u}{\partial t} + \rho(u \cdot \nabla)u = \nabla \cdot [-pI + \mu(\nabla u + (\nabla u)^T)] + F$$

$$\rho \nabla \cdot (u) = 0$$

- Drag Force and Shear Stress

$$F_D = \frac{1}{\tau_p} m_p (u - v) \quad \tau_p = \frac{\rho_p d_p^2}{18\mu}$$

### 3. DLVO Theory

- Provides theory on colloidal stability by summing attractive and repulsive forces on particle
- Determines distance between colloid particles

$$V_T(h) = \frac{4\pi\epsilon_0 a_1 a_2}{a_1 + a_2} [(\psi_1 + \psi_2)^2 \ln(1 + \exp(-kh))] - \frac{Aa_1 a_2}{6(a_1 + a_2)h} f(p)$$

- Can alter the electric double layer to ensure that particles repel enough to not flocculate
- Model using COMSOL Multiphysics

### 4. Cell Viability Tests

- Determine cell viability under following conditions:
  - Alginate encapsulation
  - Microneedle exposure
  - Extrusion
- Invitrogen™ LIVE/DEAD™ Viability/Cytotoxicity Kit
  - Dead - red (ex/em ~495nm/~635nm)
  - Live - green (ex/em ~495nm/~515nm)
- Determine dye diffusivity

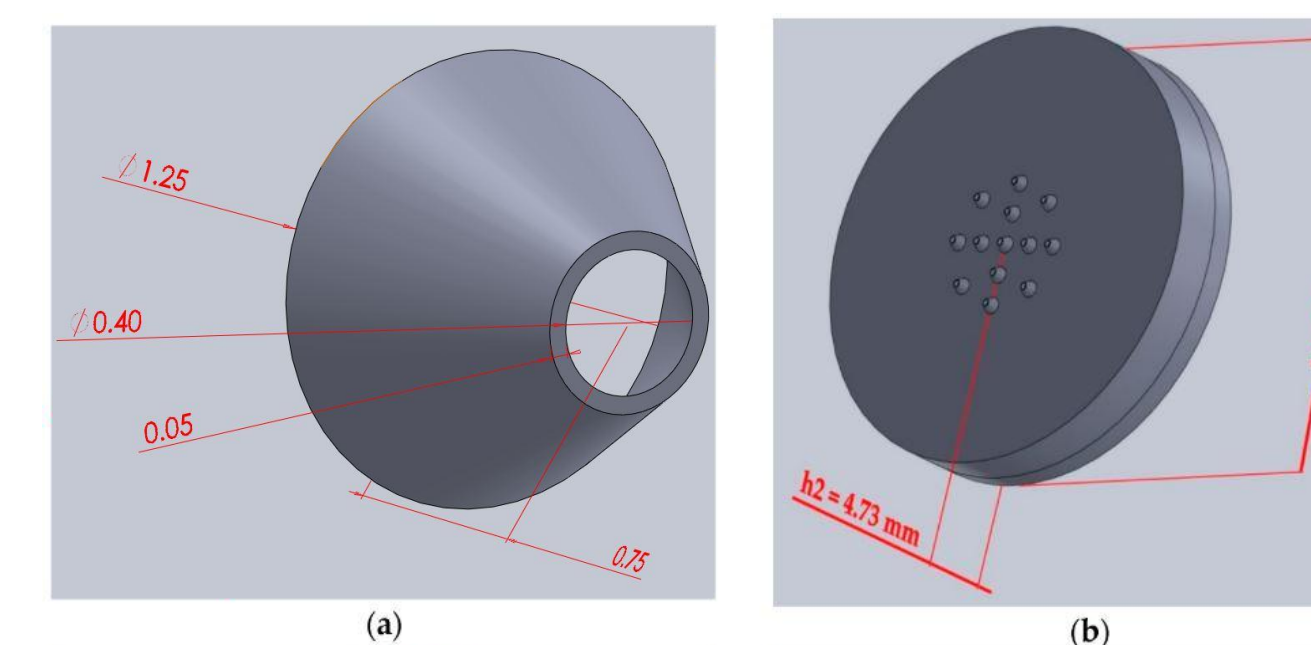
$$\frac{\partial c_i}{\partial t} + \nabla \cdot (-D_i \nabla c_i) = R_i$$

$$N_i = -D_i \nabla_i$$

## RESULTS

### 1. 3D Printing

**Figure 2:** SolidWorks 2018 drawings. (a) microneedle dimensions; (b) microneedle array; [4].



### 2. Flow Optimization

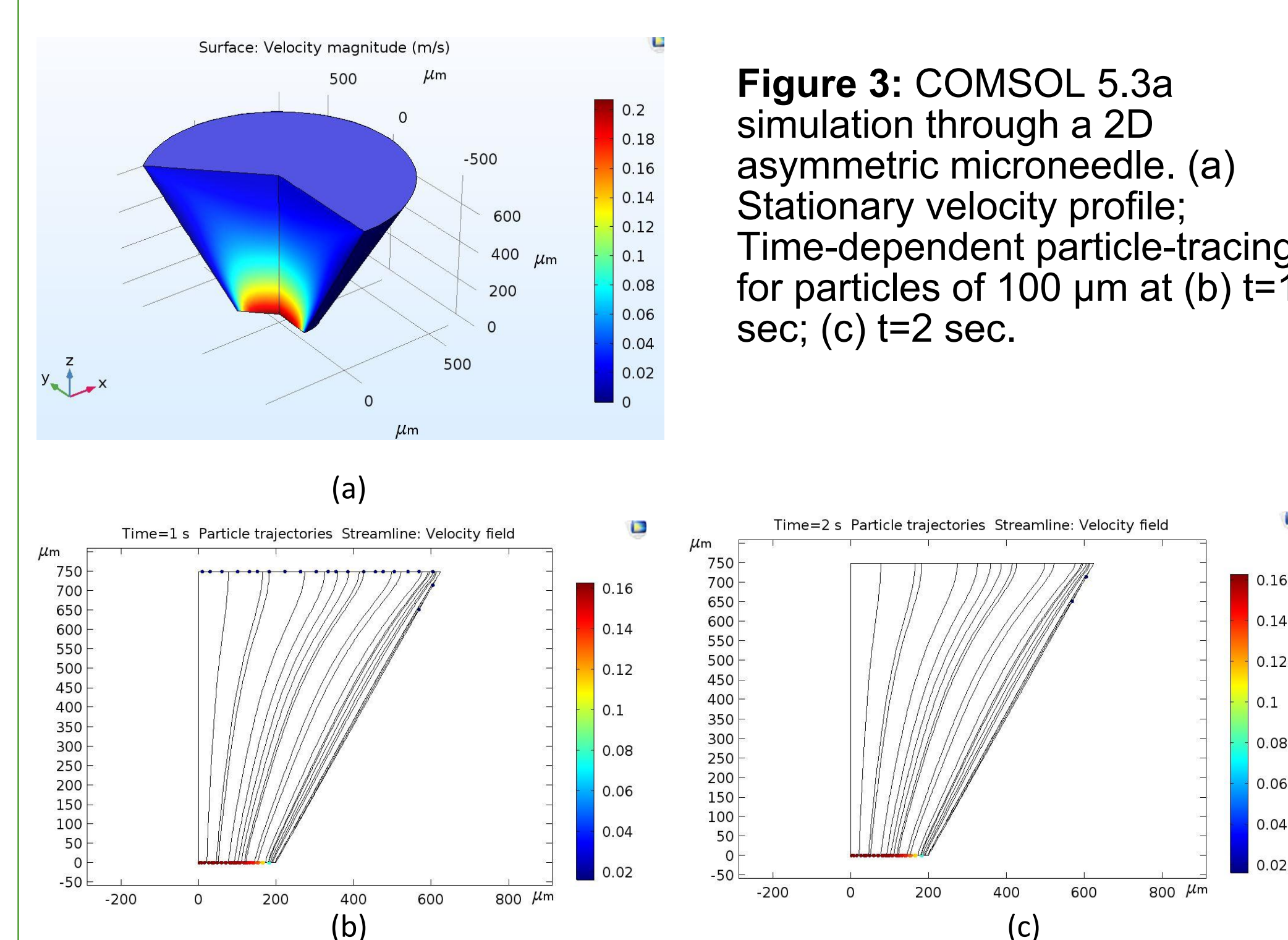


**Figure 3:** COMSOL 5.3a simulation through a 2D asymmetric microneedle. (a) Stationary velocity profile; (b) Time-dependent particle-tracing for particles of 100  $\mu$ m at (b) t=1 sec; (c) t=2 sec.

### 3. Sample Potential Energy Plot

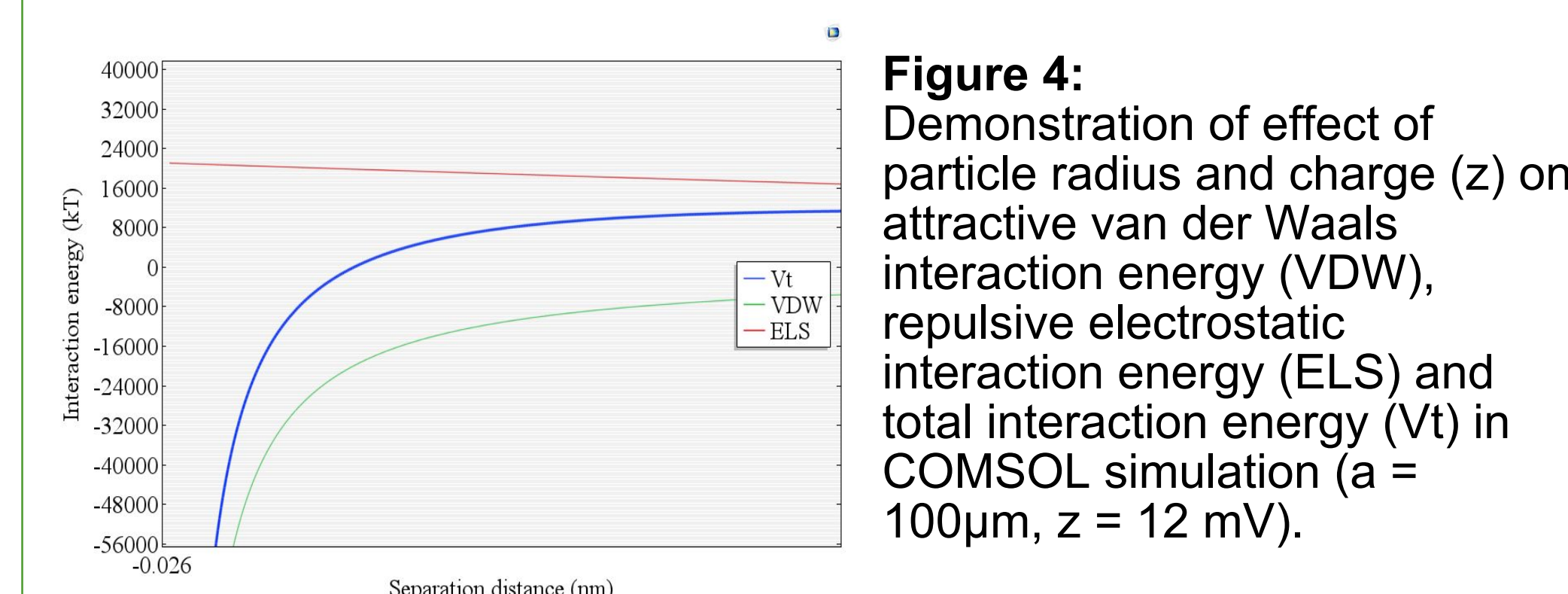


**Figure 4:** Demonstration of effect of particle radius and charge (z) on attractive van der Waals interaction energy (VDW), repulsive electrostatic interaction energy (ELS) and total interaction energy (Vt) in COMSOL simulation (a = 100  $\mu$ m, z = 12 mV).

### 4. Cell Viability Tests

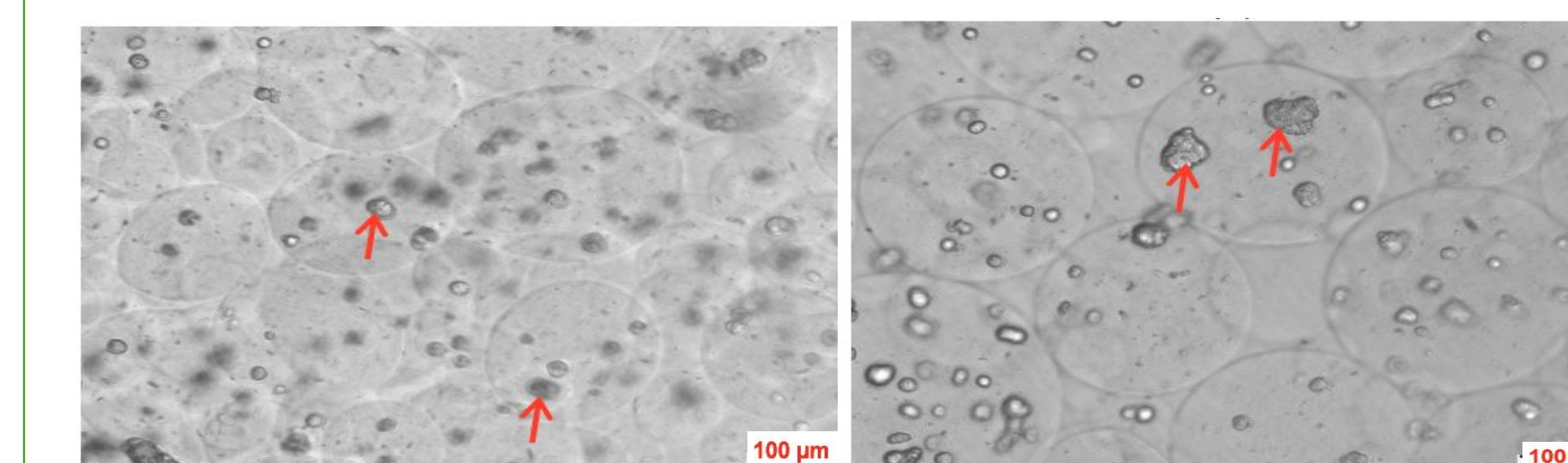


**Figure 5:** Alginates encapsulated HepG2 pre and post extrusion. Figures (a) (left) & (b) (right) at 24 hrs post fabrication.

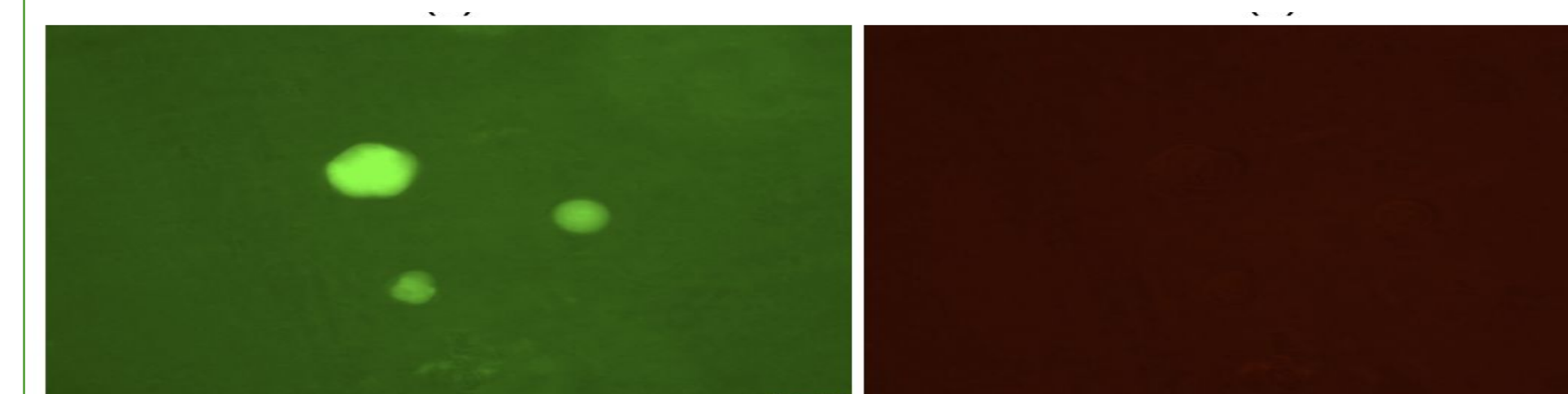


**Figure 6:** Live cells labeled with calcein AM and fluorescein green. Dead cells labeled using ethidium-homodimer 1 and fluorescence red. Figures (a) (left) and (b) (right) at 24 hrs post fabrication.

## CONCLUSION & NEXT STEPS

In this bench scale study a custom 3D-printed Hollow Microneedle biodevice comprised of a reservoir chamber and an array of conical microneedles (13 conical frusta, d = 400  $\mu$ m, D = 1000  $\mu$ m, H = 750  $\mu$ m) was fabricated using the sustainable low cost method of SLA. This microneedle platform may be customized for delivery of a broad variety of tunable scaffold properties and it should not be limited to alginate. Using SLA and the proprietary methacrylate-based Formlabs Clear photoresin®, the rate limiting factor is improvement of printing resolution, which in turn governs flow optimization and painless administration, the former being addressed in this research effort. Results of the initial simulation and experimental viability tests validate the research objectives. Simulation efforts will be concentrated on merging the flow and electrostatic physics. Viability optimization and additional flow experimentation will be carried out in parallel.

## REFERENCES

- Gupta, J.; Park, S.S.; Bondy, B.; Felner, E.I.; Prausnitz, M.R. Infusion Pressure and Pain During Microneedle Injection into Skin of Human Subjects. *Biomaterials* 2011, 32, 6823–6831.
- Harrison, R.G.; Todd, P.W.; Rudge, S.R.; Petrides, D. *Bioseparations Science and Engineering*, 1st ed.; Oxford University Press: Oxford, UK, 2002; ISBN 0195123409.
- Mobed-Miremadi, M. High-Throughput Methods for Miniaturization of Implantable Artificial Cells. In *Selected Topics in Nanomedicine*; Chang, T.M.S., Ed.; World Scientific Publishing: Singapore, 2013; pp. 411–427. ISBN 9789814472852.
- Farias, C.; Lyman, R.; Hemingway, C.; Chau, H.; Mahacek, A.; Bouzos, E.; Mobed-Miremadi, M. Three-Dimensional (3D) Printed Microneedles for Microencapsulated Cell Extrusion. *Bioengineering* 2018, 5, 59.

## ACKNOWLEDGEMENTS

The authors would like to acknowledge the support of the Department of Bioengineering. The authors would also like to acknowledge the support of the SCU Center for Nanostructures and the SCU Maker Lab where the prototype surface characterization and 3D printing were conducted, respectively.

Jerard Madamba, Dr. Maryam Mobed-Miremadi, Dr. Ashley Kim

## INTRODUCTION

Breast milk is the standard for infant nutrition. However, many mothers are unable to breastfeed for various reasons and must rely on donated milk to feed their infants. The Milkguard biosensor is designed to be a low cost and rapid alternative for testing for contamination in donated breast milk. The current sensor is able to detect higher concentrations of bacteria over long periods of time.

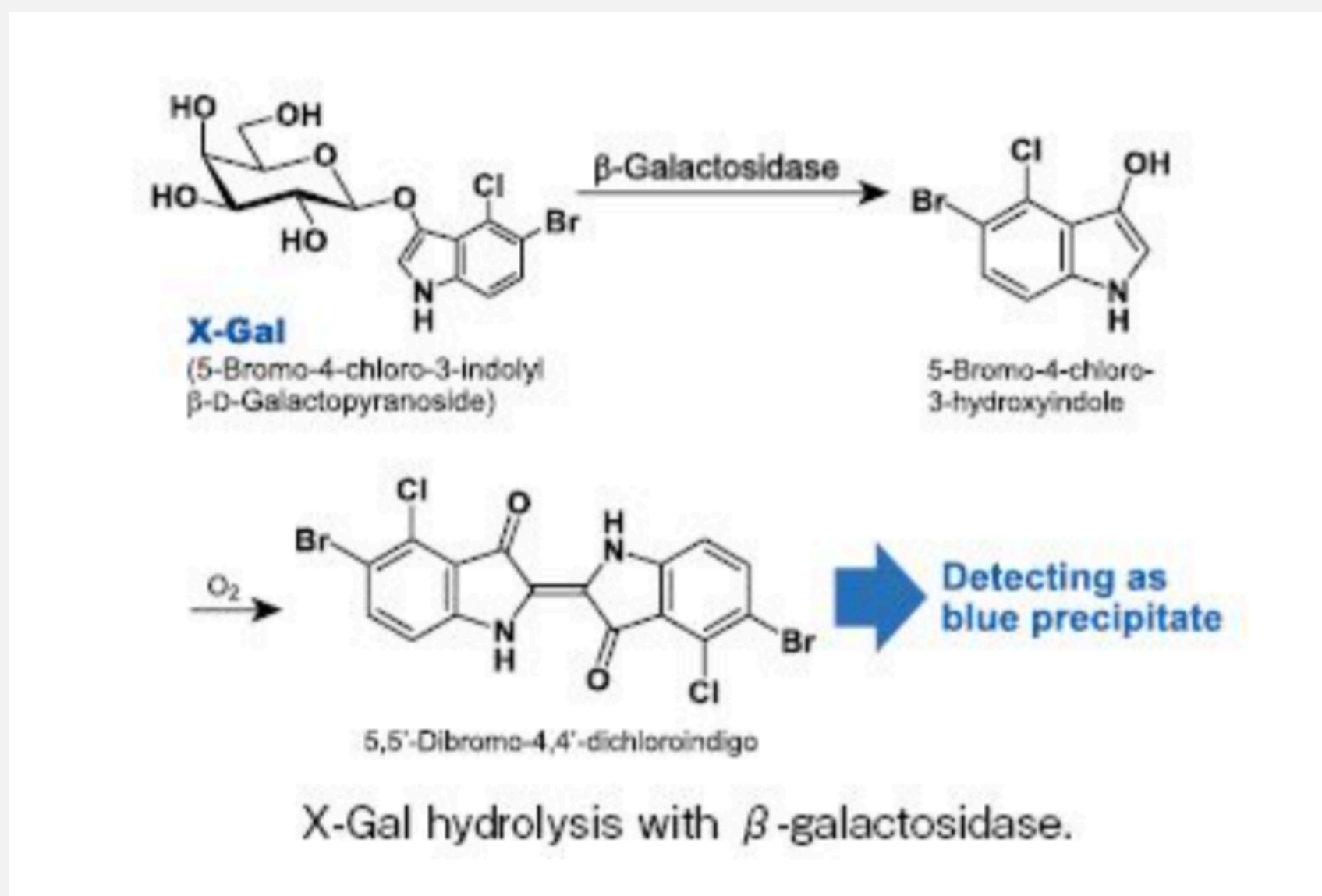


Figure 1. X-Gal hydrolysis as a method of detection

The current sensor has difficulties in detecting lower concentrations of bacteria in a practical timeframe via X-Gal hydrolysis. Modeling reaction kinetics between  $\beta$ -galactosidase and X-Gal in bulk and in solution can inform future optimizations of the biosensor. Size optimizations by downscaling the sensor size is one proposed method.

## OBJECTIVES

1. Model substrate diffusion and enzyme kinetics of the  $\beta$ -galactosidase and X-Gal reaction in the reaction space and obtain relevant system-specific reaction constants.
2. Optimize sensor reaction time by scale optimization, specifically by reducing sensor diameter by 10-fold.

## METHODS

1. *E. coli* (Strain SCU-104) is induced with human breast milk and lysed to isolate  $\beta$ -galactosidase.
2. X-Gal is incorporated into dissolved alginate. This mixture is then crosslinked using  $\text{CaCl}_2$ , to create the sensor.
3. Both the  $\beta$ -galactosidase lysate and the alginate-based sensor are allowed to incubate together in a reaction tube or well for up to 8 hours at approximately  $37^\circ\text{C}$
4. Reaction mixtures are colorimetrically assessed for  $\beta$ -galactosidase activity, signifying *E. coli* presence.

## Equations:

Fick's 2<sup>nd</sup> Law of Diffusion + reaction term

$$\frac{\partial[S]}{\partial t} = \nabla^2[S] + R_i \quad (1)$$

Substituting Michaelis-Menten kinetics:

$$\frac{\partial[S]}{\partial t} = D_e \left( \frac{\partial^2[S]}{\partial r^2} + \frac{2}{r} \frac{d[S]}{dr} \right) - \frac{v_m''[S]}{K_m + [S]} \quad (2)$$

$$\text{Assuming } \bar{S} = \frac{[S]}{[S_s]}, \quad \bar{r} = \frac{r}{R}, \quad \beta = \frac{K_m}{[S_s]}$$

$$\frac{d^2\bar{S}}{d\bar{r}^2} + \frac{2}{\bar{r}} \frac{d\bar{S}}{d\bar{r}} = \phi^2 \frac{\bar{S}}{1 + \bar{S}/\beta} \quad (3)$$

$$\text{where } \phi = R \sqrt{\frac{v_m''/K_m}{D_e}} \quad (4)$$

$\phi$ : Thiele modulus

Reaction rate per unit volume:

$$r_s = \eta \frac{v_m''[S]}{K_m + [S]} \quad (5)$$

Where  $\eta = f(\phi)$

## RESULTS

### Assay

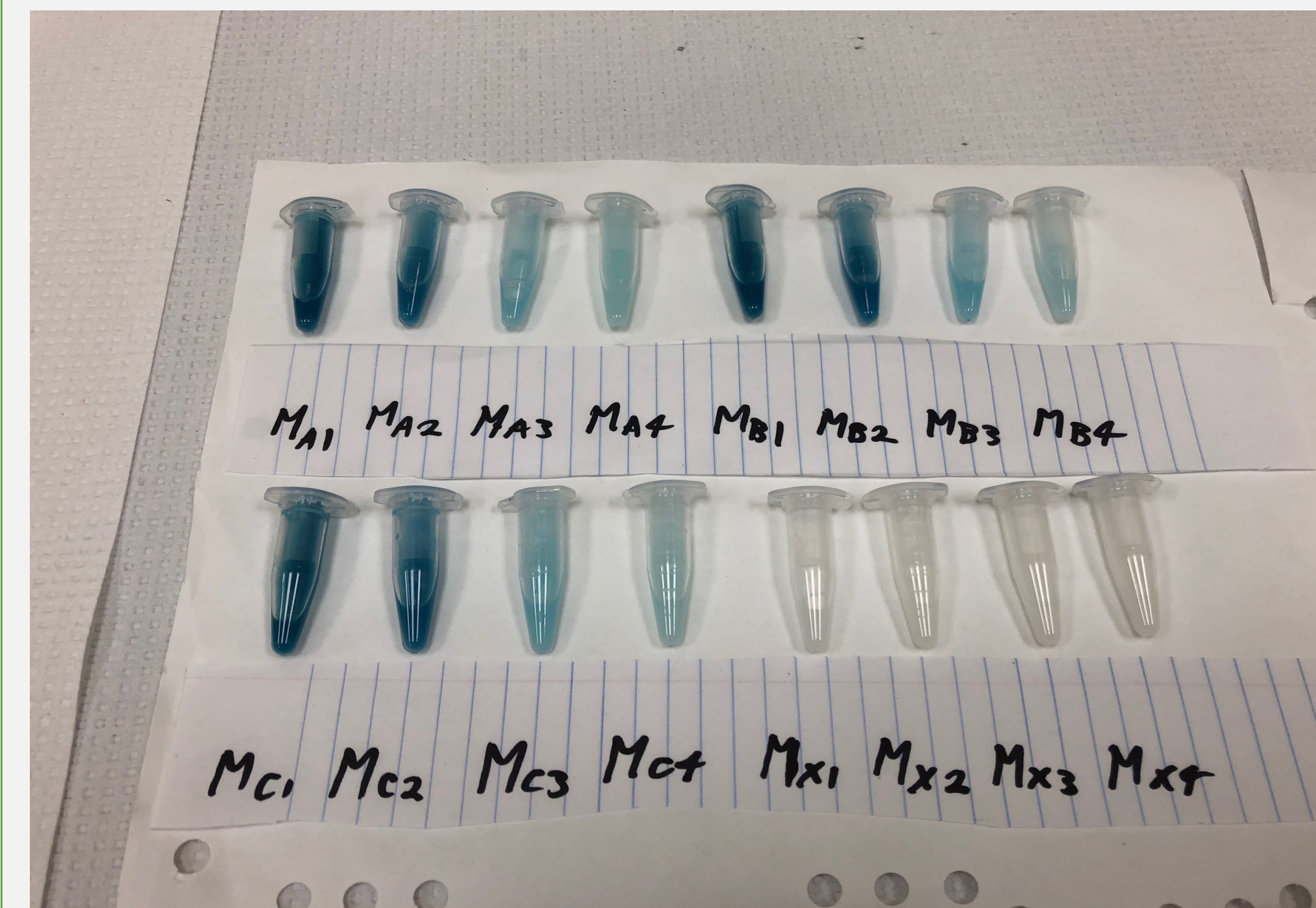


Figure 2. Sensor response after 8 hours of incubation. Darker blue color indicates higher concentration of *E. coli*.

### Model

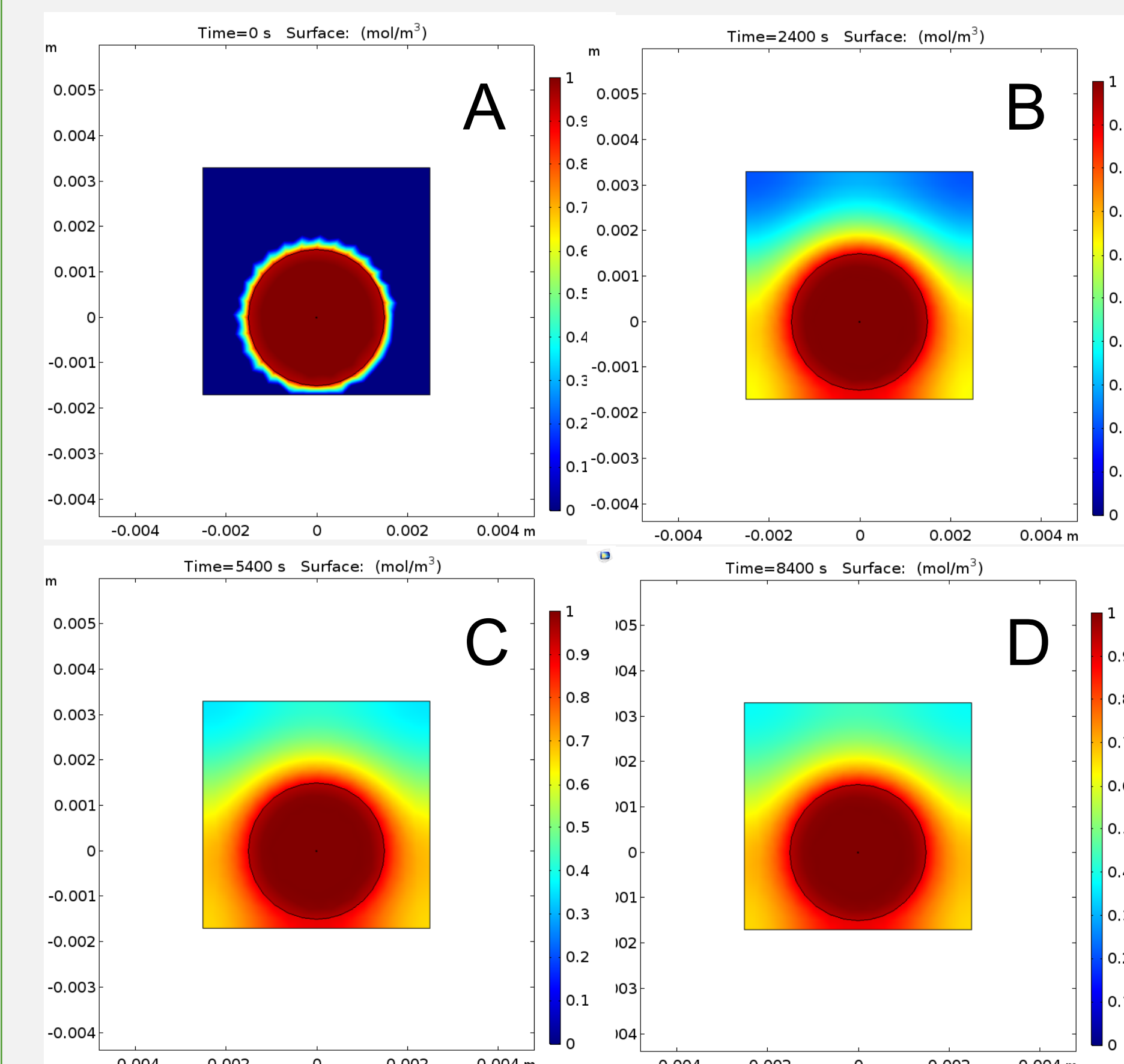


Figure 3. COMSOL 5.3 model of substrate diffusion and enzyme reaction. Color gradient represents substrate concentration at (A) 0 seconds, (B) 2400 seconds, (C) 5400 seconds, (D) 8400 seconds.

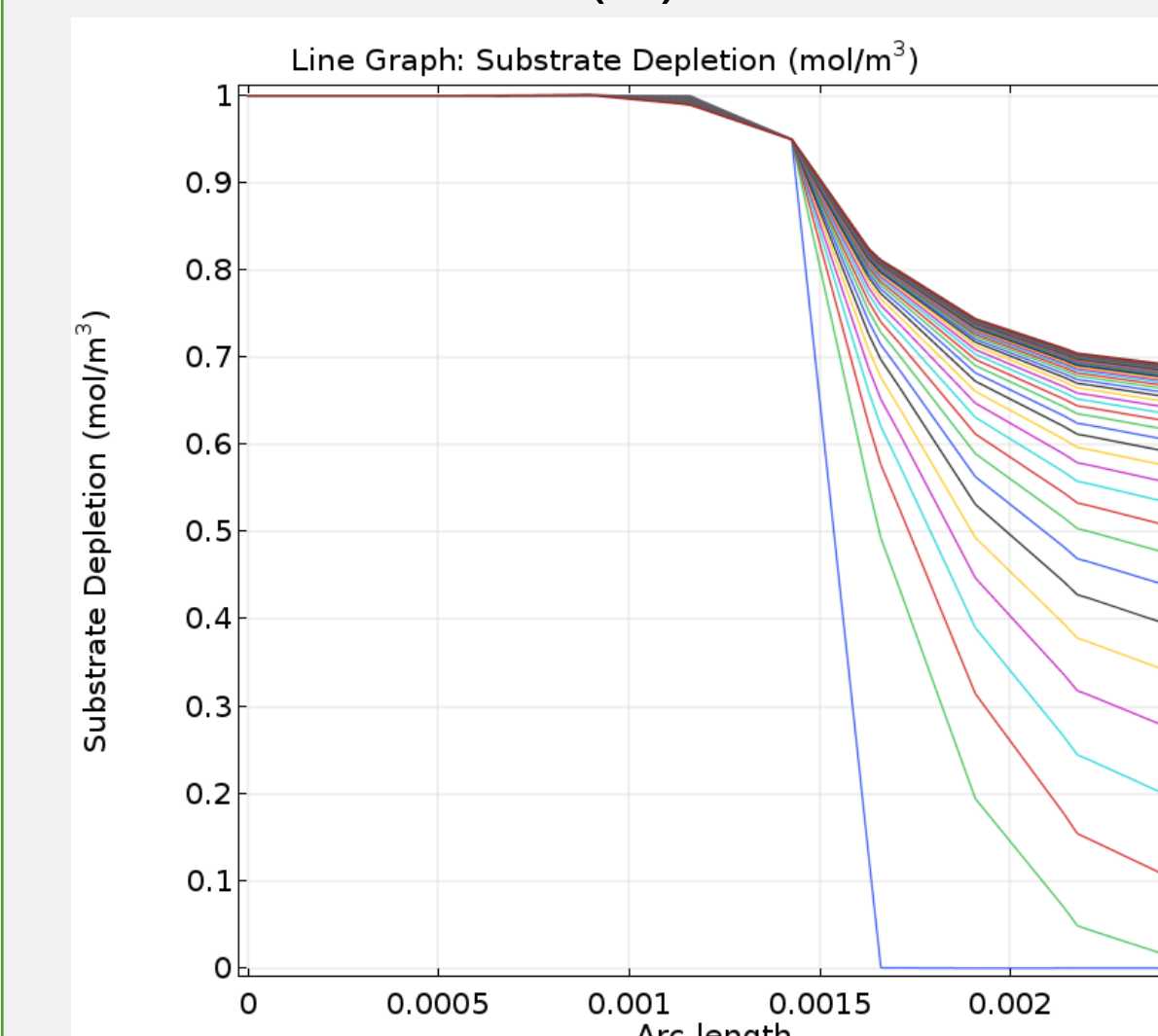


Figure 4. COMSOL 5.3 model showing substrate depletion over profile of reaction container.

## CONCLUSIONS

Preliminary results indicate the reaction is diffusion-limited. Future efforts will encompass effectiveness factor determination at a constant radius before miniaturization.

## FURTHER STUDIES

Future studies may examine further size and/or sensor modifications to increase sensor response times and sensor sensitivity. Key optimizations may include reducing  $R$  as given by Equations 1-4, increasing capsule diffusivity,  $D_e$ , or catalyzing the enzymatic reaction to yield a faster reaction rate. Investigation into capsule manufacturing materials and or techniques may allow for physical optimization of the sensor.

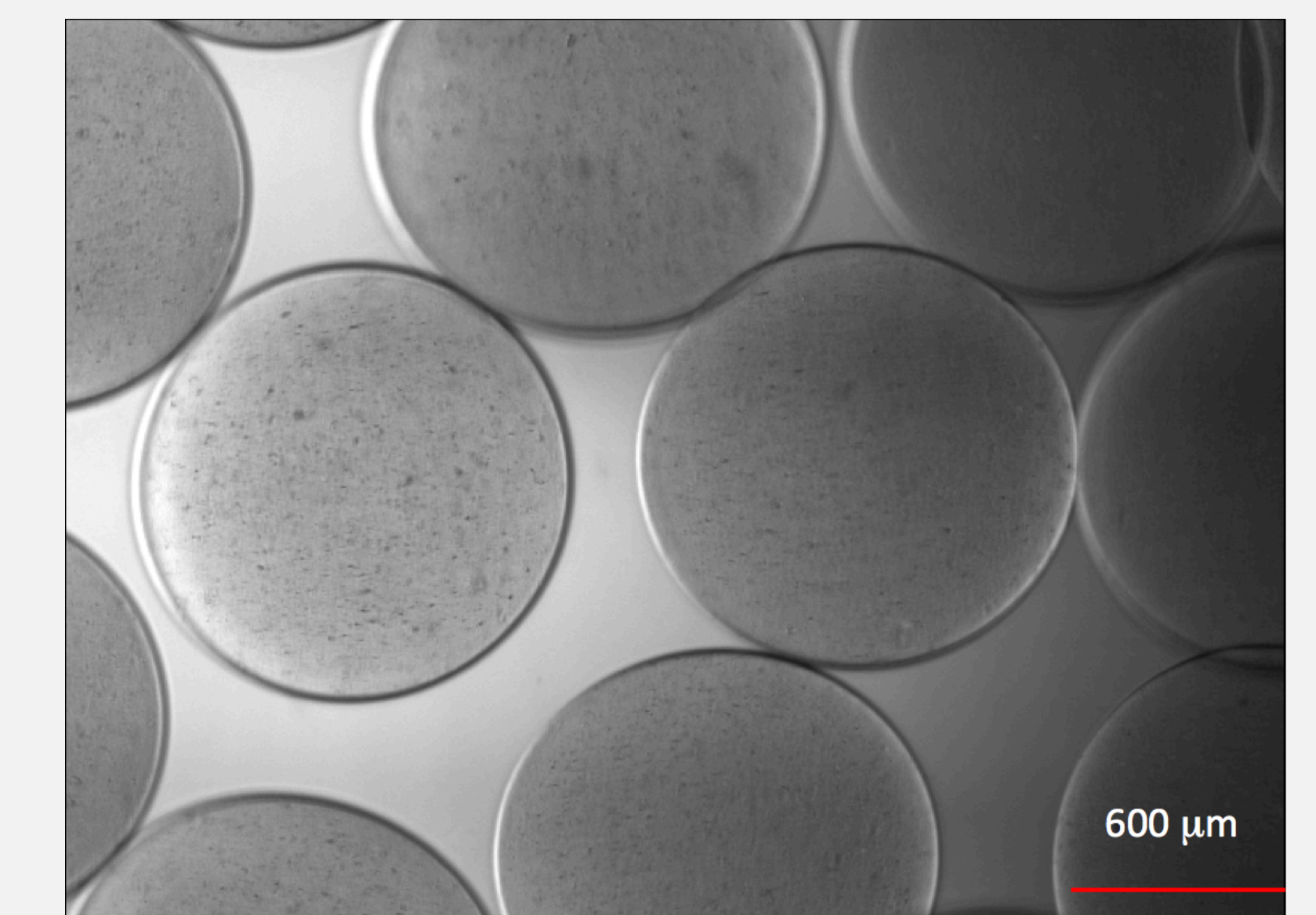


Figure 5. Phase contrast microscopy of proposed alginate capsules for sensor

## ACKNOWLEDGEMENTS

We would like to thank Nicholas Kikuchi, Maggie May, and Matt Zweber for their foundational work on this project.



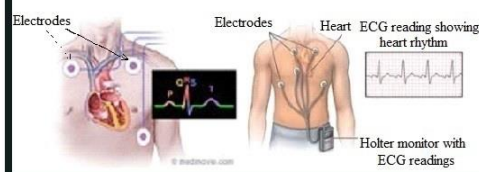
# Arrhythmia Detection from ECG Signals Using Machine Learning



Pradnya Patel, Master's Student | Dr. Yuling Yan, Advisor  
DEPARTMENT OF BIOENGINEERING, SANTA CLARA UNIVERSITY

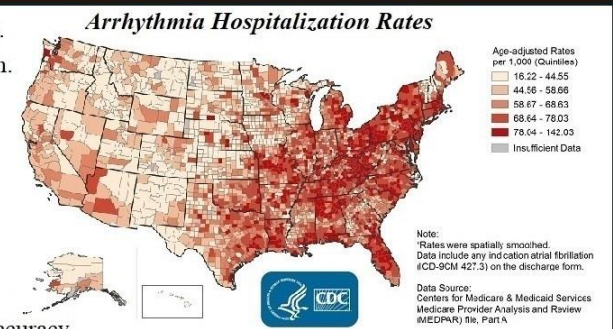
## INTRODUCTION

- Electrocardiography (ECG) measures the electric activities of the heart.
  - Wearables like apple watch also measures ECG.
  - 12-lead ECG, is a non-invasive diagnostic test.
  - ECG produces tracing/reading consisting of several P-QRS-T wave complexes that recur with each heartbeat.
- Arrhythmia is an abnormal heart rhythm
  - Types of arrhythmia addressed:
    - Bradycardia (Heart Rate is too slow)
    - Tachycardia (Heart Rate is too fast)
    - Atrial Fibrillation
      - Atrial rate 350-400 bpm
      - P waves absent
      - Rhythm for Ventricular is irregular
    - Atrial Flutter
      - Atrial rate 250-350 bpm
      - P waves absent
      - Rhythm for Ventricular can be irregular
- Measuring ECG has become easier with wearable technology.
  - This combined with advancement in machine learning and computational power, presents more perspective for our research.
  - Stanford scientists developed an algorithm that diagnoses arrhythmias with cardiologist-level accuracy.
  - The Apple watch 4 ECG is 98% accurate at detection of Afib.
  - The withings move fitness watch has ECG for \$130.



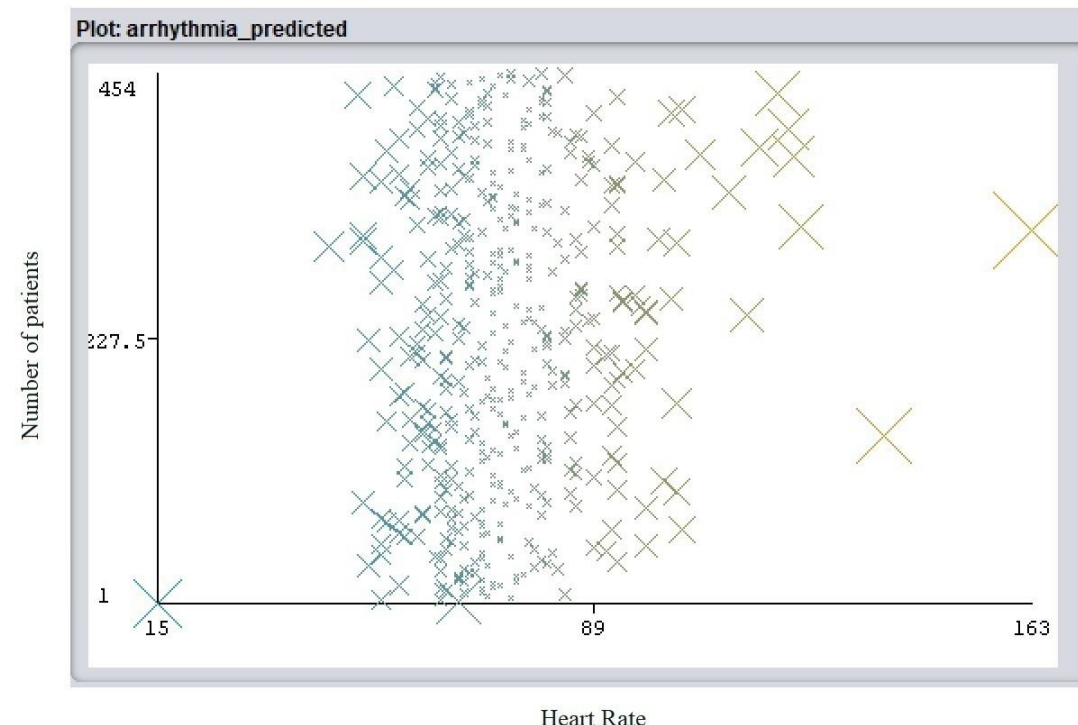
## MOTIVATION

- ~2.7-6.1 million people in the United States suffer from arrhythmia.
- This number is expected to increase, with aging of current population.
- < 750,000 hospitalizations occur each year.
- Costs the United States about \$6 billion each year.
- ~130,000 deaths each year.
- The death rate has been rising for more than two decades.
- Irregularity in heartbeat may be harmless or life threatening.
- Hence both accurate detection of presence as well as classification of arrhythmia are important.
- We aim to detect arrhythmia in early stages with cardiologist-level accuracy.
- This especially is useful in regions where medical facilities are not readily available.



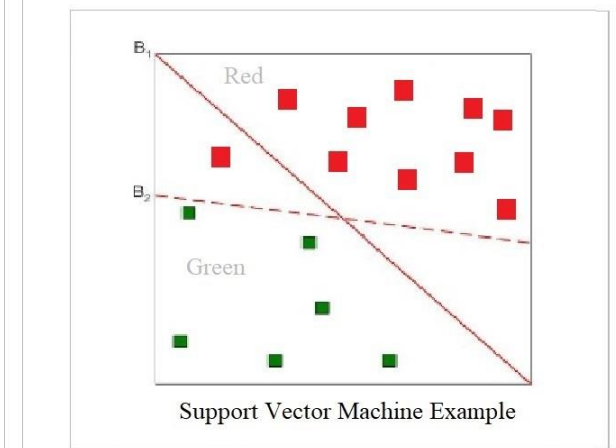
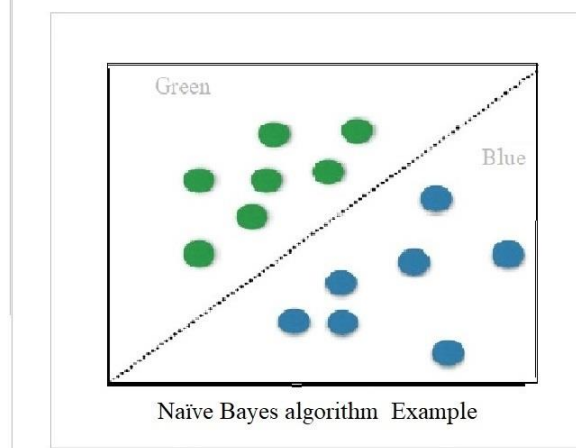
## RESEARCH DESIGN

- MIT-BIH Arrhythmia Database is used for the research.
- Tool used is WEKA, Waikato Environment for Knowledge Analysis.
- WEKA is a suite of machine learning software written in Java, developed at the University of Waikato, New Zealand.
- The dataset is divided into 75% - 25% for training set and test set respectively.
- In this preliminary study, our dataset contains ECG signals representing both normal rhythm and arrhythmia.
- The following figure shows the classification results:

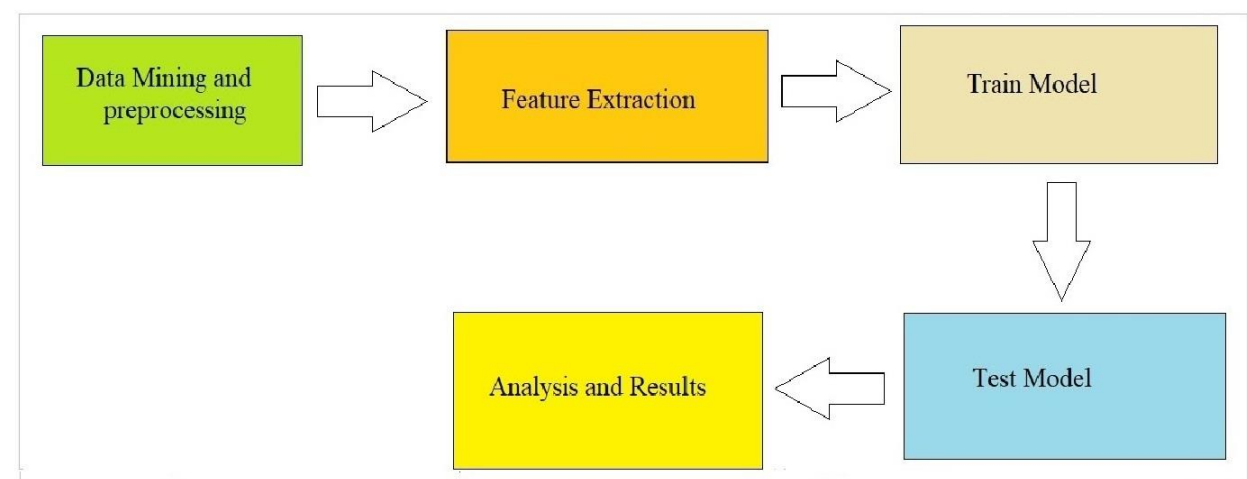


## METHOD

- Naïve Bayes assigns class labels from the data, representing it as vectors of feature values.
  - Each feature value is independent of other feature value and while classifying algorithm does not consider any correlation between them.
  - In the following figure, an example of Naïve Bayes algorithm is shown.
  - In this example, the colored balls are classified using the feature - color.
- SVM uses hyperplane or hyperplanes in high dimensional space for classification.
  - In the following figure, an example of Support Vector Machine algorithm is shown.
  - In this example, the colored squares are classified using two hyperplanes- B<sub>1</sub> and B<sub>2</sub>
  - The Hyperplane B<sub>1</sub> does not completely classify red and green squares, this classification is done by hyperplane B<sub>2</sub>.



- For detection of arrhythmia the following equations were followed:  
 If (Heart\_beat >= 60 & Heart\_beat < 100) & (PR >= 0.12 & PR <= 0.2) & (QRS >= 0.06 & QRS < 0.12)  
  
 If (Heart\_beat >= 100) & (PR >= 0.12 & PR <= 0.2) & (QRS >= 0.06 & QRS < 0.12)  
  
 If (Heart\_beat < 60) & (PR >= 0.12 & PR <= 0.2) & (QRS >= 0.06 & QRS < 0.12)
- The algorithm in this paper combines two classifier algorithms, Support Vector Machine and Naïve Bayes Algorithm.
- Then the performance is compared with other algorithms.
- The following diagram gives the overview of the steps followed:



## RELATED RESEARCH

- Groundbreaking research, "Cardiologist-Level Arrhythmia Detection with Convolutional Neural Networks" was published by Stanford scientists in 2017.
- They developed an algorithm that diagnoses 14 types of arrhythmia and the algorithm was tested against 6 cardiologists.
- A 34-layer convolutional neural network (CNN) is built to detect arrhythmias in arbitrary length ECG time-series.
- Inspired by this work, we aim to develop an arrhythmia classifier with cardiologist-level accuracy.
- Our research focuses on the classification of four special types of arrhythmia: Bradycardia, Tachycardia, Atrial Fibrillation (AFib) and Atrial Flutter.

## PRELIMINARY RESULTS

- The proposed algorithm outperforms several standard algorithms including SVM, Naïve Bayes, and Random Tree.
- The results obtained from our algorithm in comparisons with standard algorithms are listed in the table below.

Algorithm	Training Set	Testing Set	Whole Set
Naïve Bayes	95.92	95.96	96.71
SVM	98.81	99.02	98.84
Random Tree	100	98.81	98.88
Algorithm addressed in this paper	100	99.96	99.93

## CONCLUSION

- We developed a new classification algorithm that combines SVM and Naïve Bayes methods.
- Our preliminary results showed that the proposed algorithm successfully classified the four types of arrhythmia: Bradycardia, Tachycardia, Atrial Fibrillation (AFib) and Atrial Flutter with high accuracy and outperformed standard methods including SVM, Naïve Bayes, and Random Tree.

## FUTURE WORK

- Apply Short Time Fourier Transform to classify arrhythmia into more categories.
- Apply our classification algorithm to different datasets.
- Embed our algorithm in wearables.
- Explore more types of arrhythmia.
- After obtaining a larger dataset, we will explore the use of deep neural network methods in the classification of various types of arrhythmia.

## REFERENCES

- Isin, Ali, and Selen Ozdalili. "Cardiac arrhythmia detection using deep learning." *Procedia Computer Science* 120 (2017): 268-275.
- Rajpurkar, Pranav, et al. "Cardiologist-level arrhythmia detection with convolutional neural networks." *arXiv preprint arXiv:1707.01836* (2017).
- Soman, Thara, and Patrick O. Bobbie. "Classification of arrhythmia using machine learning techniques." *WSEAS Transactions on computers* 4.6 (2005): 548-552.
- Assodiky, Hilmy, Iwan Syarif, and Tessa Badriyah. "Deep learning algorithm for arrhythmia detection." *Knowledge Creation and Intelligent Computing (IES-KCIC), 2017 International Electronics Symposium on. IEEE, 2017.*
- Polat, Kemal, and Salih Güneş. "Detection of ECG Arrhythmia using a differential expert system approach based on principal component analysis and least square support vector machine." *Applied Mathematics and Computation* 186.1 (2007): 898-906.
- Budzianowski, Jan, et al. "Predictors of atrial fibrillation early recurrence following cryoballoon ablation of pulmonary veins using statistical assessment and machine learning algorithms." *Heart and vessels* (2018): 1-8.
- Rizwan, Muhammed, Bradley M. Whitaker, and David V. Anderson. "AF detection from ECG recordings using feature selection, sparse coding, and ensemble learning." *Physiological measurement* 39.12 (2018): 124007.

# Transit System Asset Management: Model-based Systems Engineering

Alan J. Ng | Dr. Hisham Said | Department of Civil Engineering | Department of Engineering Management and Leadership

## Abstract

The goal of this study was to analyze Santa Clara Valley Transportation Authority's (VTA) Light Rail System using a model-based systems engineering and geographical mapping approach to develop a system model. This model captures the VTA system-of-systems and their interdependencies, which will be valuable in cordoning and optimizing the asset management and repair effort. The preliminary study will be useful for VTA's effort to maintain this critical infrastructure system.

## Background

The United States started its renaissance of electrified rail system well over thirty years ago in almost every major metropolitan area. As the electrified rail system expanded around the city, so did the economy and neighborhoods along the light rail system; dubbing the term transit-oriented development. However, most of these transit infrastructure systems are approaching their end of useful life, and require disruptive and costly maintenance and renovation. Light rail systems are interconnected and any one system element failure will render light rail service inoperable to revenue service. Currently, an ad-hoc and informal decision-making process is used to determine the annual maintenance and renovation projects. This inefficient asset management approach is due to the lack of system asset data and tools to coordinate and optimize the life-cycle system actions related to its interconnected sub-systems.

## Study Methodology

As a proof of concept, the initial phase will only focus on "rail system elements" including major disciplines: Traction Power Substations (TPSS), Overhead Contact System (OCS), Tracks, and Signals/Communication. A model-based systems engineering (MBSE) tool, called Visual Paradigm (VP), was used to model these subsystems using the Systems Modeling Language (SysML). A draft system model was developed and is synchronized to a data model that can be used as the database schema for a GIS-based Asset Management tool.

## Envisioned Benefits

- Determine if it is more economical to only replace contact wire or replace all overhead contact system to the pole.
- Determine the cost to only replace contact wire or all OCS to the pole, factoring in the cost of mobilization and revenue impact.
- Determine if it is advised to do minor rehabilitation to reduce cost, and rehabilitate the same segment again a few years later.
- Determine if all disciplines' rehabilitation elements or having separate discipline-specific rehabilitation projects are more economical.

## VTA Light Rail System Overview

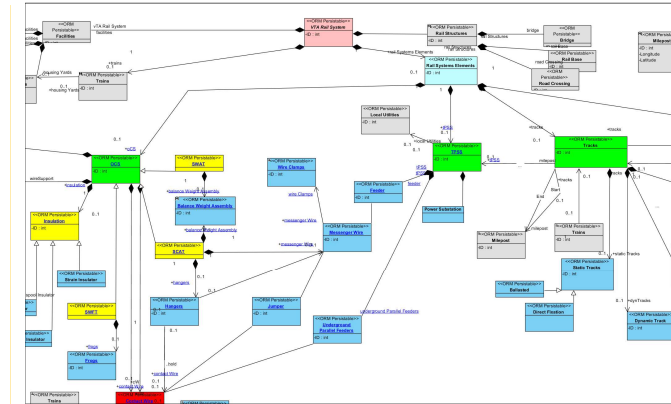
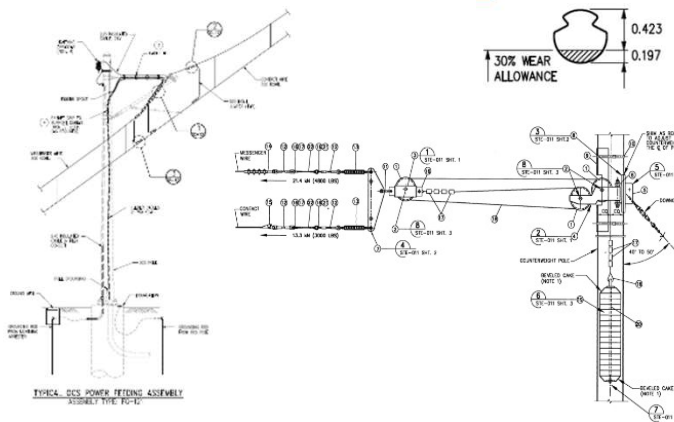
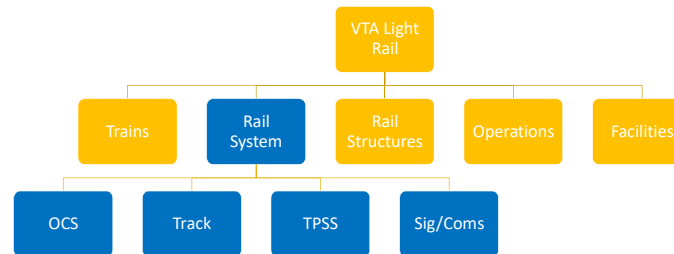


- 42.2 Miles Length of Line
- 81.6 Miles of Track
- 1 Light Rail Maintenance Yard
- 61 Passenger Stations
- 99 Light Rail Trains
- 20 Light Rail Park and Ride Lots



## Systems Model

A systems model was developed using VP and is being updated to represent all light rail elements' interdependencies and relationships. This required light rail discipline experts to assist on creating the complete model. As a proof of concept, the first phase of this research focused on the "rail system" package, which includes TPSS, OCS, tracks, and signal/communication.

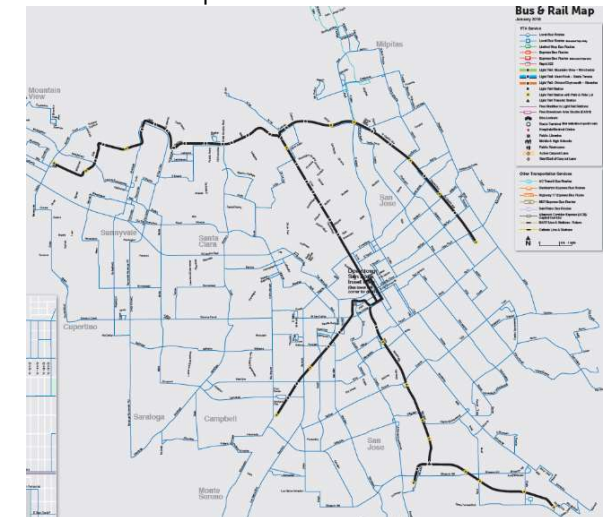


A screenshot of the system model included in the VP tool is shown above. The model is large and cannot be shown here in detail. However, you can scan this QR code to open the published model on your browser.



## Future Research: GIS Model and Spatial Analysis

All light rail relevant systems, subsystems, and components will be mapped using Geographical Information System (GIS). The first phase of this research will focus on the oldest segment, Guadalupe Line, to record system elements. Spatial analysis algorithms will be developed to represent the dependencies between the rail sub-systems and prioritization rules for selecting the maintenance and rehabilitation work with minimal cost and service disruptions.



## Problem Statement

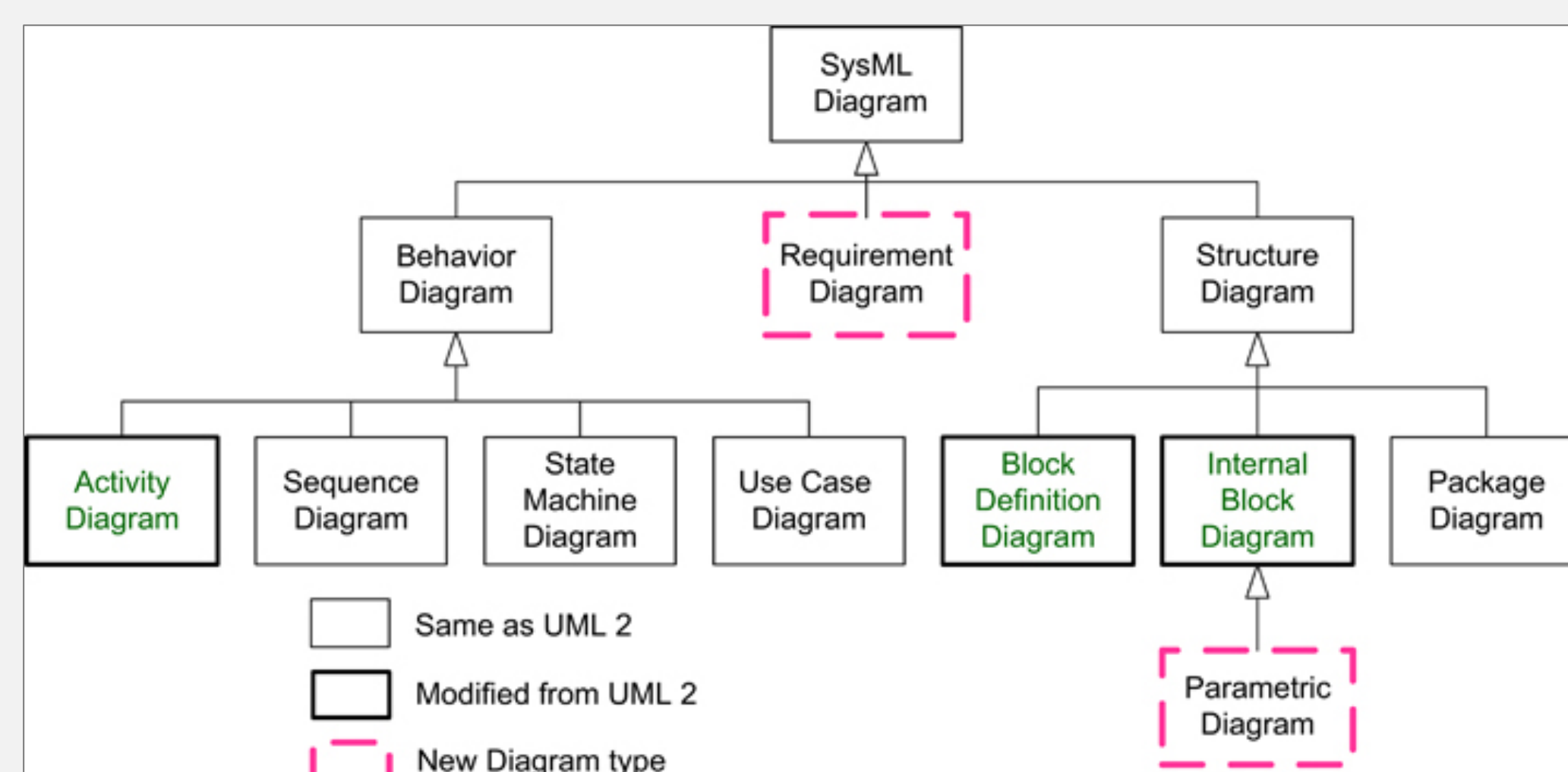
Recently there has been a huge growth in IoT (Internet of things) applications in the control and automation of smart buildings. Automation is not a new concept in buildings and facility management, but IoT expands the real-time intelligence capabilities of conventional automation systems. However, smart building developers, designers and builders are challenged with the lack of smart building standards, absence of common understanding of smart building user requirements and interoperability between the systems and their communication protocols. With all these existing challenges, it is imperative to develop new approaches for modeling, specifying, and communicating smart building designs.

## Research Objectives

The objective of this research is to **develop a model-based engineering framework for smart buildings to capture their generic requirements, systems, and behaviors.** This model-based systems engineering framework can be foundational in the future for knowledge engineering, semantics analysis, and early conceptual design.

## Methodology

The framework was developed using the systems modeling language (SysML), which is a special profile of the unified modeling language (UML). Both languages were developed by the Object Management Group (OMG).

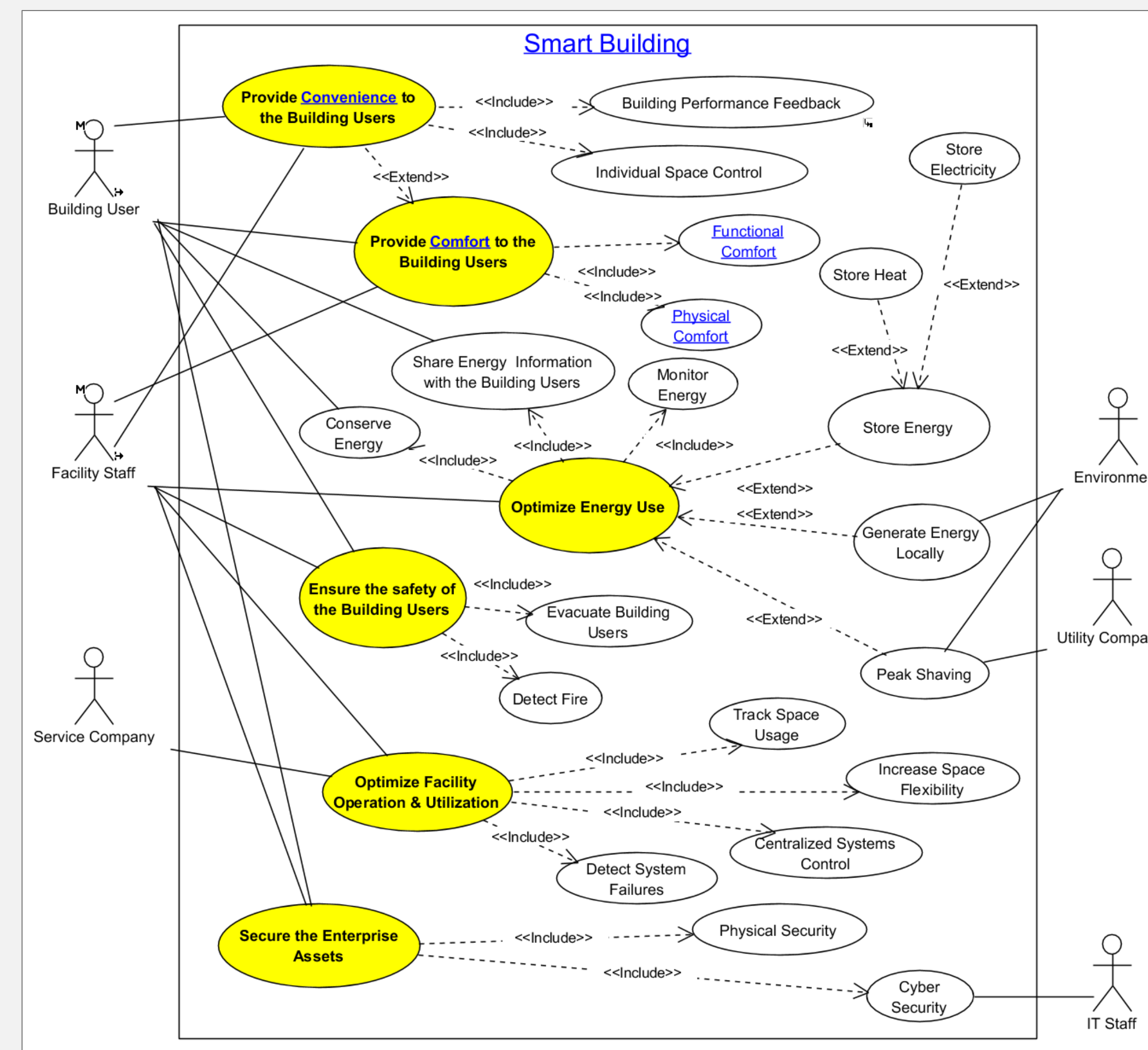


## Framework Components

Component	SysML Diagram
Use and Design Specification	Requirements Diagram
System Architecture	Block Definition Diagram
System Behavior	Use Case & Activity Diagrams
Definitions	Glossary Table

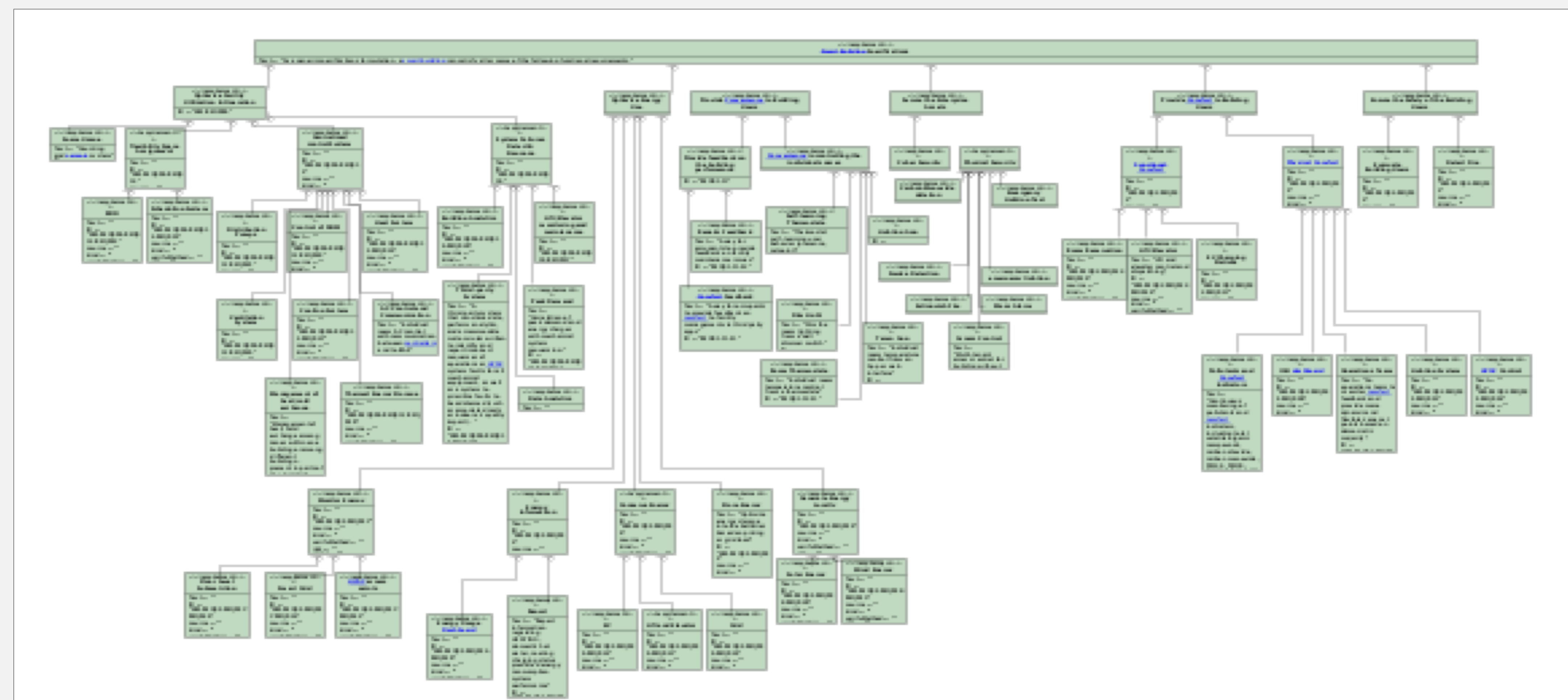
### Use Case Diagram

6 main use cases, and they include 20 sub use cases. The use cases help to clarify some of the requirements.



### Requirement Diagram

The performance requirements are outlined in a 3-level hierarchical representation. Total requirements are 71.

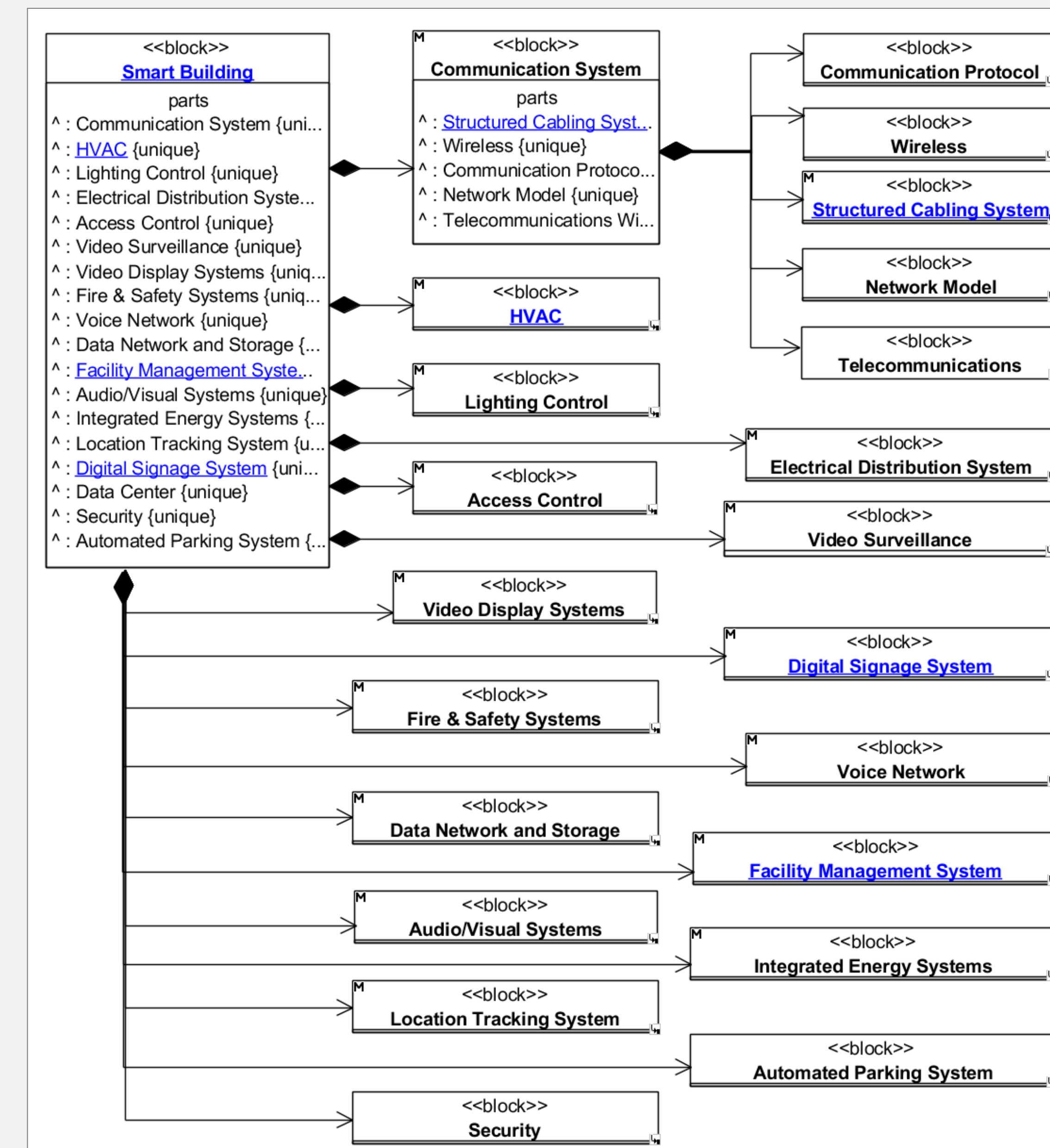


The framework is being continuously expanded and updated. It is large and cannot be shown entirely in this poster. Please scan this QR code to view it on your mobile device.



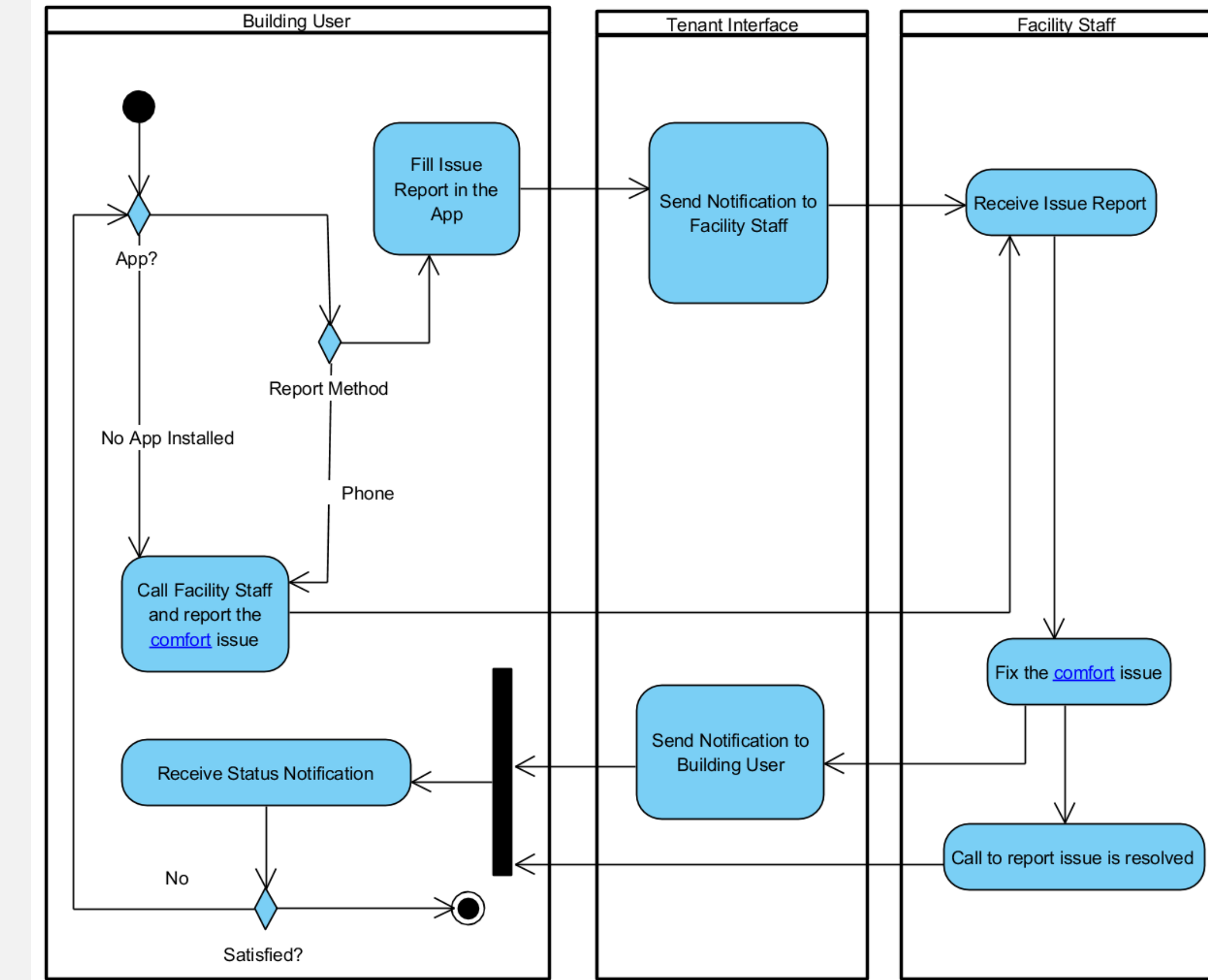
### Block Definition Diagram

17 building systems are modeled in this framework. Each system is modeled using a sub block definition diagram, totaling 26 Diagrams and 730 blocks.



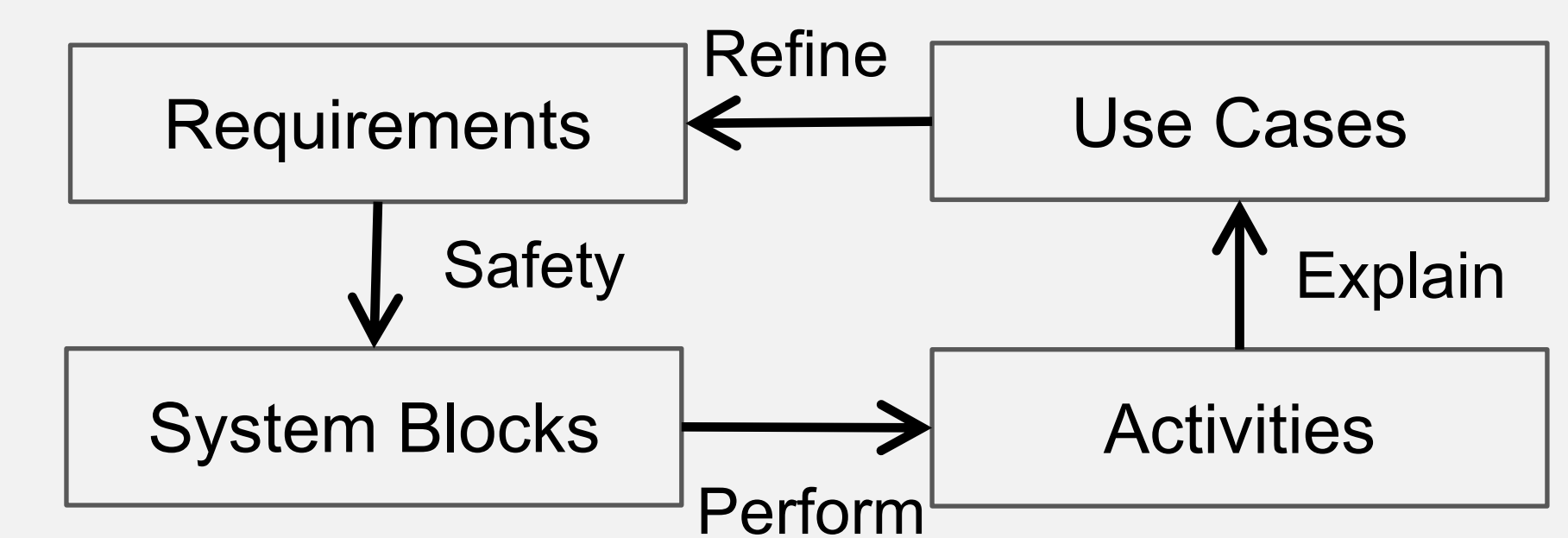
## Activity Diagram

Each use case is detailed and explained using an activity diagram that shows the flow of actions and their responsibility to the different system blocks.



## Framework Dependencies

SysML allows modeling the dependencies between the different framework components and diagrams. They are critical for performing change impact and failure analyses.



## Future Works

- Building Information Modeling (BIM)
- Conceptual Design Simulations
- Reliability Analysis
- Performance-based Specifications

## Research Support

The researchers appreciate the financial support from the Latimer Energy Lab of SCU's School of Engineering and ELECTRI International Research Foundation.



# Flomosys: A Low-Cost, Reliable, and Low-Power Flood Monitoring System

Tai Groot and Behnam Dezfouli  
Internet of Things Research Lab, Santa Clara University

## Problem

- Since 2000, the US has spent **over \$107 billion** on the damages caused by floods.
- During the past seventeen years, annual damage costs have continued to increase.
- In 2017 alone, the US spent \$60.7 billion on floods, which accounts for 57% of the cumulative 17-year total.
- **In 2017, San Jose suffered a flooding of the Coyote Creek which amounted to around \$100 million in total damage and displaced 14,000 residents.**

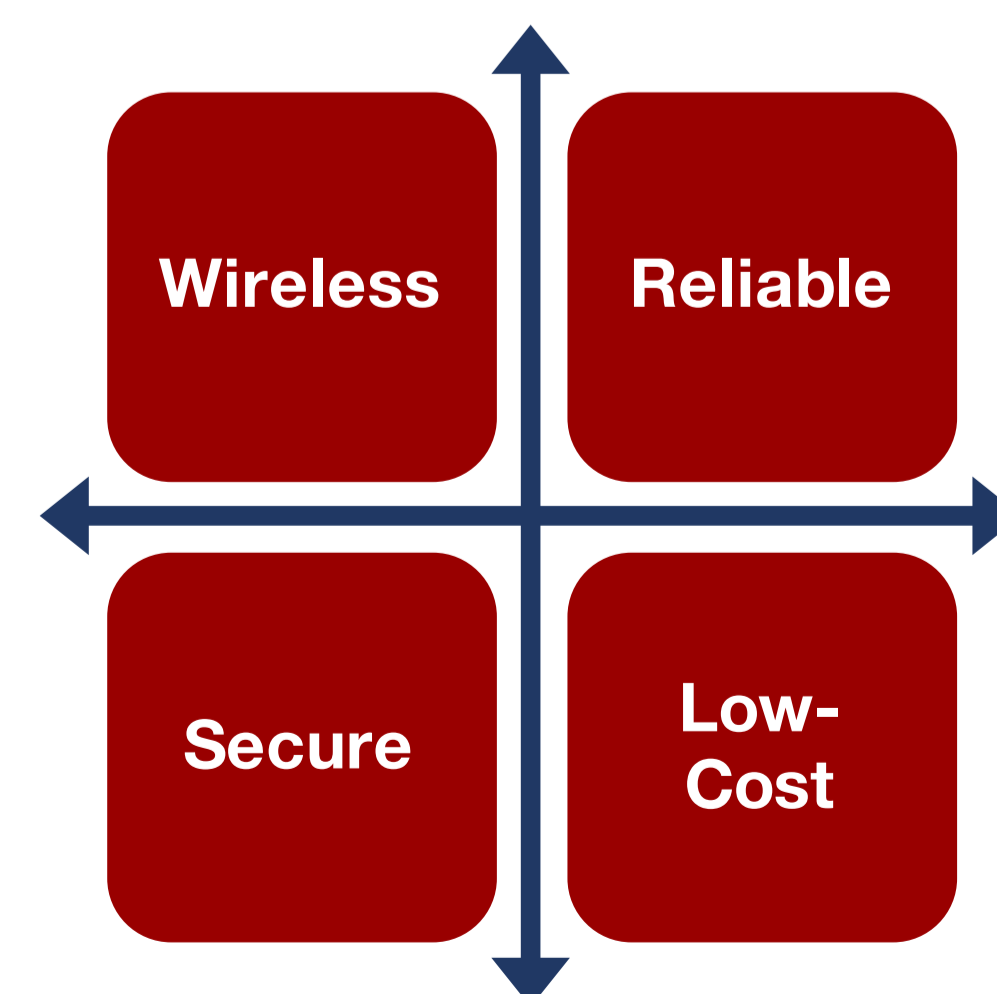


In February 2017, San Jose was forced to close entrances to Highway 101 due to flooding. Some drivers (including professors at SCU) unexpectedly found themselves without a way to get to work, as many of the usual detours were closed as well.



Santa Clara Valley needs a reliable and economical way to warn its citizens ahead of time about this growing safety issue.

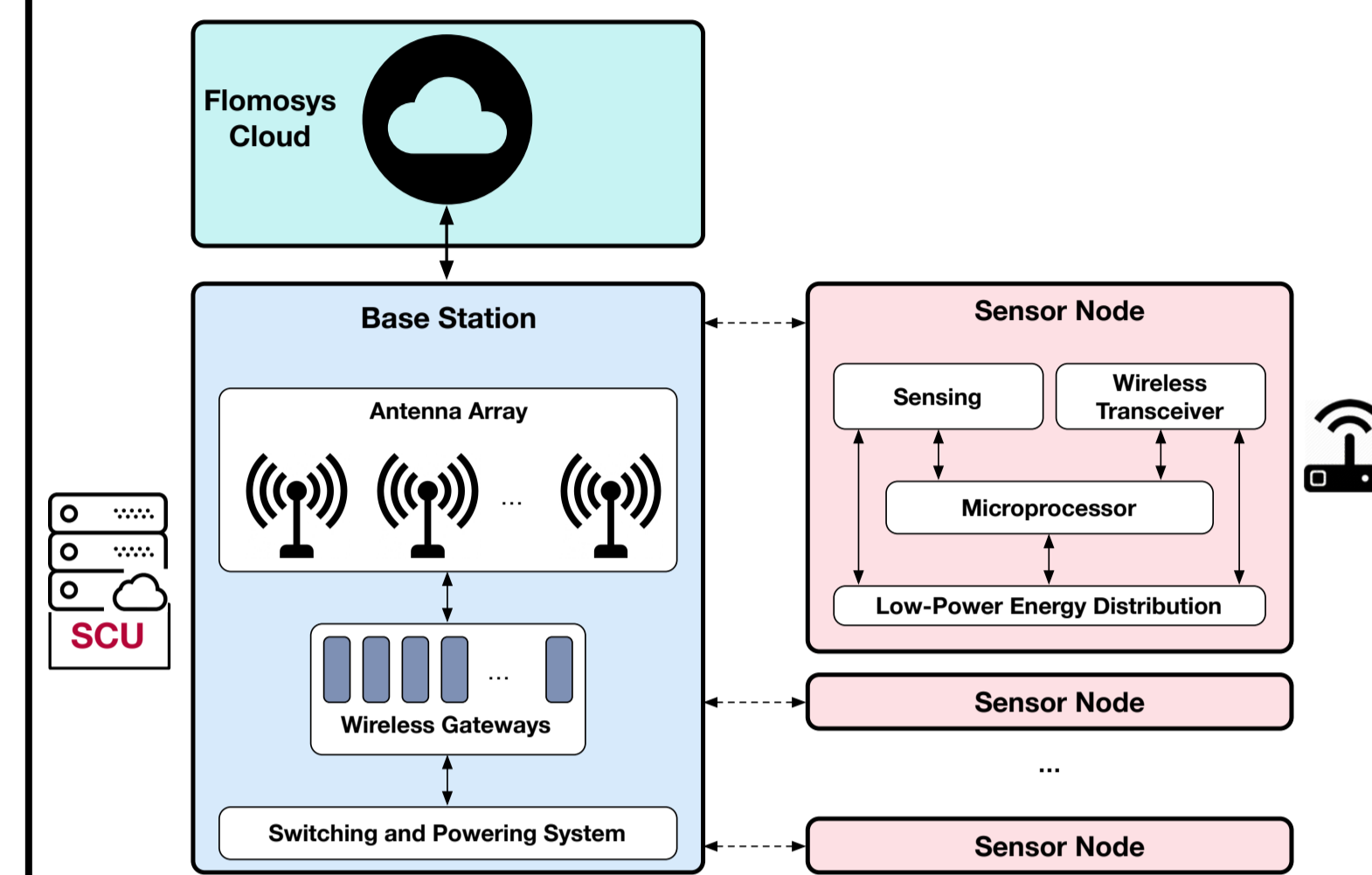
Commissioned by the City of San Jose and Santa Clara Valley Water District, **SIOTLAB** designed and implemented the **Flomosys** solution.



The right picture shows the salient features of **Flomosys**.

We had to consider various factors, such as the lack of Internet connectivity and electricity.

## System Overview

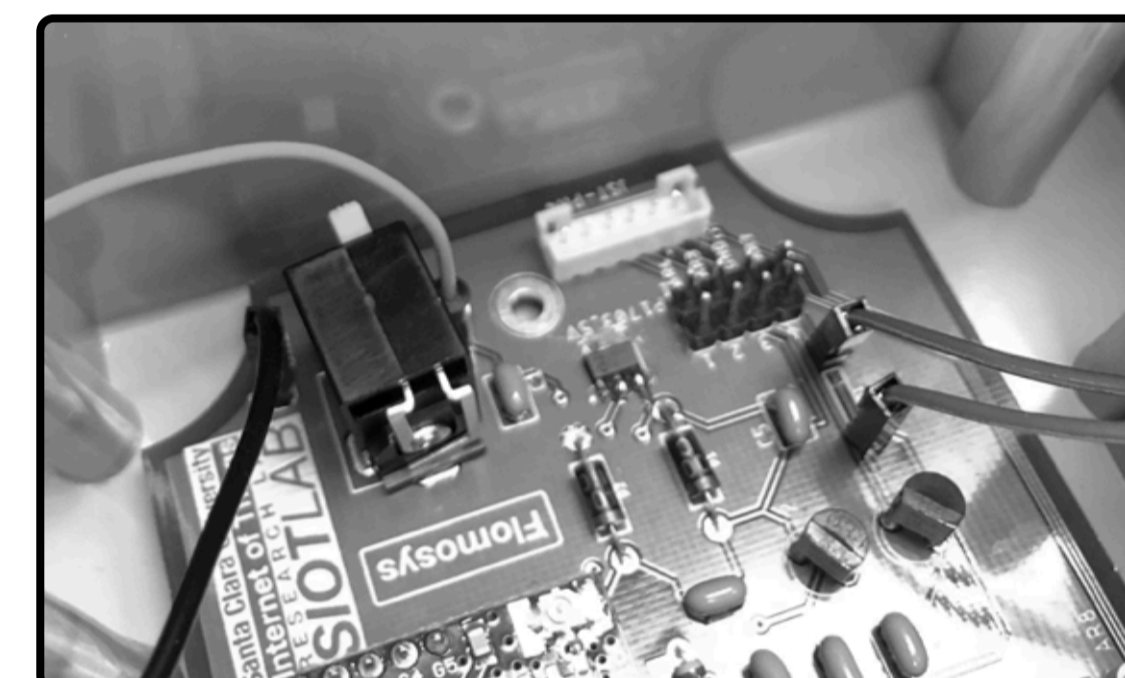


The **Flomosys** system consists of three major components: Sensor Nodes, Base Stations, and a Cloud Application.

Sensor Nodes are deployed out in the field, under the bridges designated by the City of San Jose and Santa Clara Valley Water District. They communicate with Base Stations through a sub-GHz wireless technology that offers low-power, reliable, and long-range links.

Data is then forwarded to the Cloud Application, where it is processed and delivered to the interested parties.

## Sensor Nodes



On the left is a photo of the Sensor Node, and the picture below is the enclosure that is mounted on-site.

Sensing Distance	10 meters (32.8 foot)
Accuracy	1 cm (0.393701 inch)



Each Sensor Node has an on-board ultrasound distance measurement sensor, which is used to measure water height and detect anomalies.

The system must be able to sustain itself on an energy-harvesting solution, such as a solar panel.

- A Very Low-Power Hardware Design
- ~5000 Lines of Code Carefully Engineered to Ensure Energy Efficiency

Energy Usage: 30 uA

## Base Station and Cloud Application

Right: The base station is composed of an array of receivers each connected to its own antenna mounted on top of SCU's Swig Residence Hall, marked by the red rectangle in the photo below.

Multiple Gateways can receive from one Sensor Node

Reliability: 99.9%

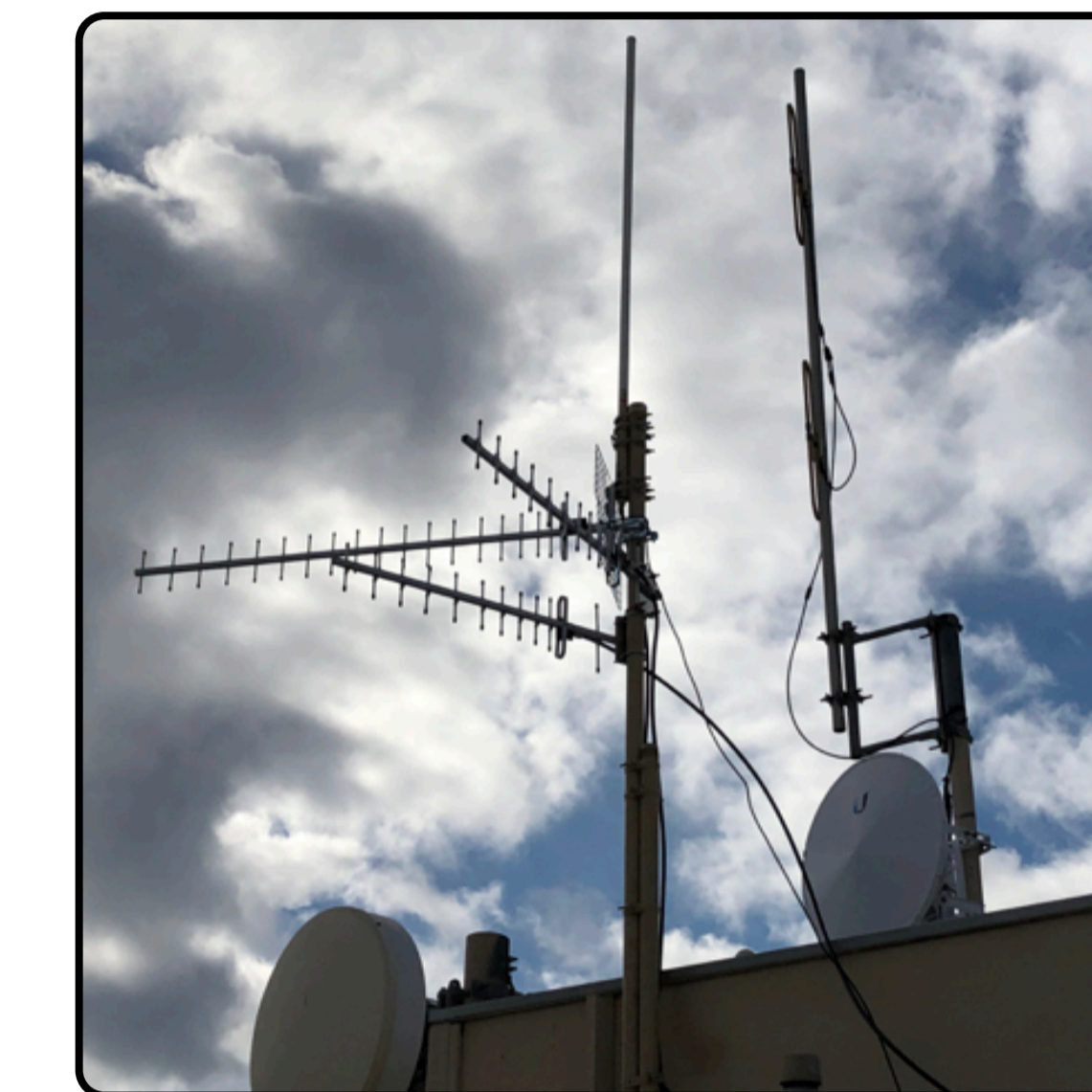
The receivers forward the data to the Cloud Application, which aggregates data across all the Sensor Nodes and detects anomalies.



## Technologies and Novelties

- Low-Power Hardware Design
- Long-Range and Reliable Wireless
- Cloud-Based Management
- Novel Security Algorithm
- Gateway Arrays and High Reliability

## Results

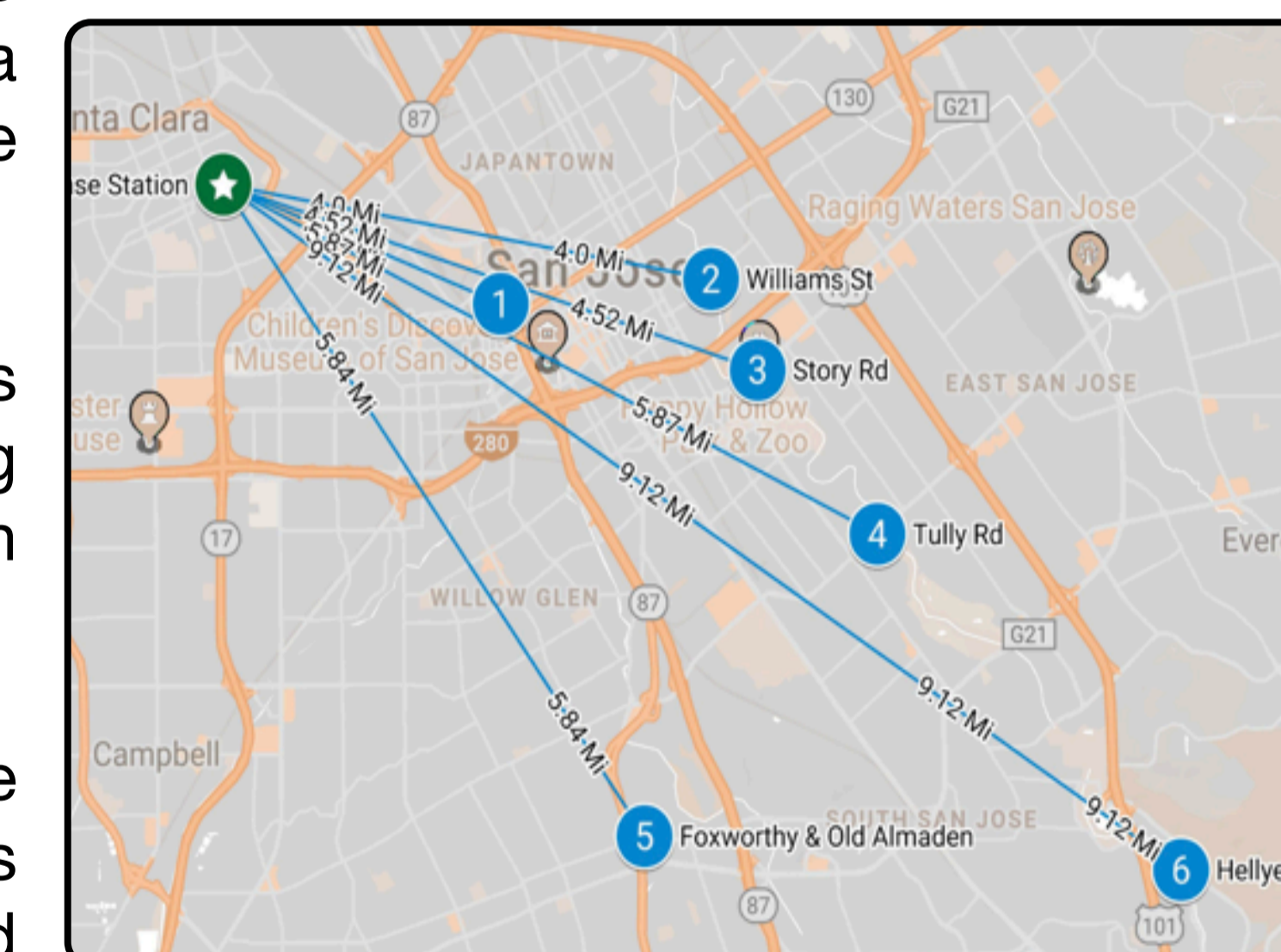


Our antenna array currently is composed of 3 directional antennas and one omnidirectional antenna to provide coverage across the Valley.

We have tested **Flomosys** at 6 different bridges in Santa Clara Valley, as marked by the blue pins.

The Base Station, which is installed on the roof of the Swig Residence Hall, is shown in green for reference.

The distances between the base station and the nodes is demonstrated by the annotated blue lines.



## Credits



A big thank you to all those who contributed to this project!

# Image Classification on IoT Edge Devices: Profiling and Modeling

Salma Abdel Magid, Francesco Petrini, and Behnam Dezfouli  
Internet of Things Research Lab, Santa Clara University

## Problem

Researchers at Gartner estimate that there will be **20 billion IoT devices** connected to the internet by 2020. The burgeoning of such devices has sparked many efforts into researching the optimal device design.

Since IoT devices are resource-constrained, we must utilize their limited resources in an efficient manner. Some popular applications of IoT include autonomous vehicles, surgical devices, security cameras, obstacle detection for the visually-impaired, rescue drones, and authentication systems. Most of these applications utilize machine learning. Here we focus on IoT applications which use a specific type of machine learning: supervised image classification. **We study how several factors of these algorithms affect the energy consumption on IoT edge devices.**

## Methodology

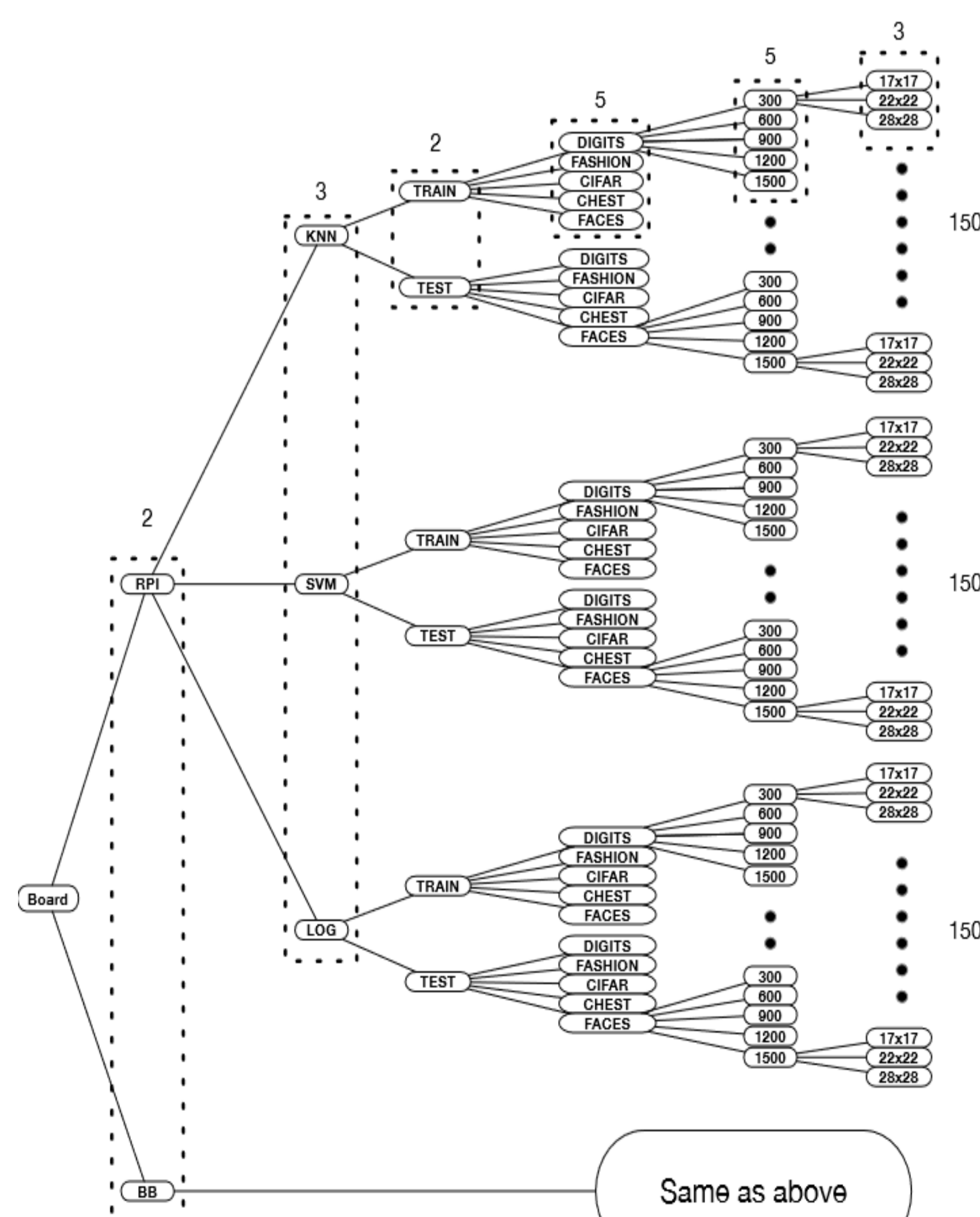
**Hardware:** 1.2GHz quad-core Raspberry Pi 3 w/ 1GB RAM & a 1GHz AM3358 BeagleBone Black Wireless

**ML Algorithms:** SVM, k-NN, & logistic regression

**Datasets:** MNIST Digits, MNIST Fashion, CIFAR10, Chest X-Ray, Faces in the Wild

**Factors Manipulated:** image resolution & dataset size

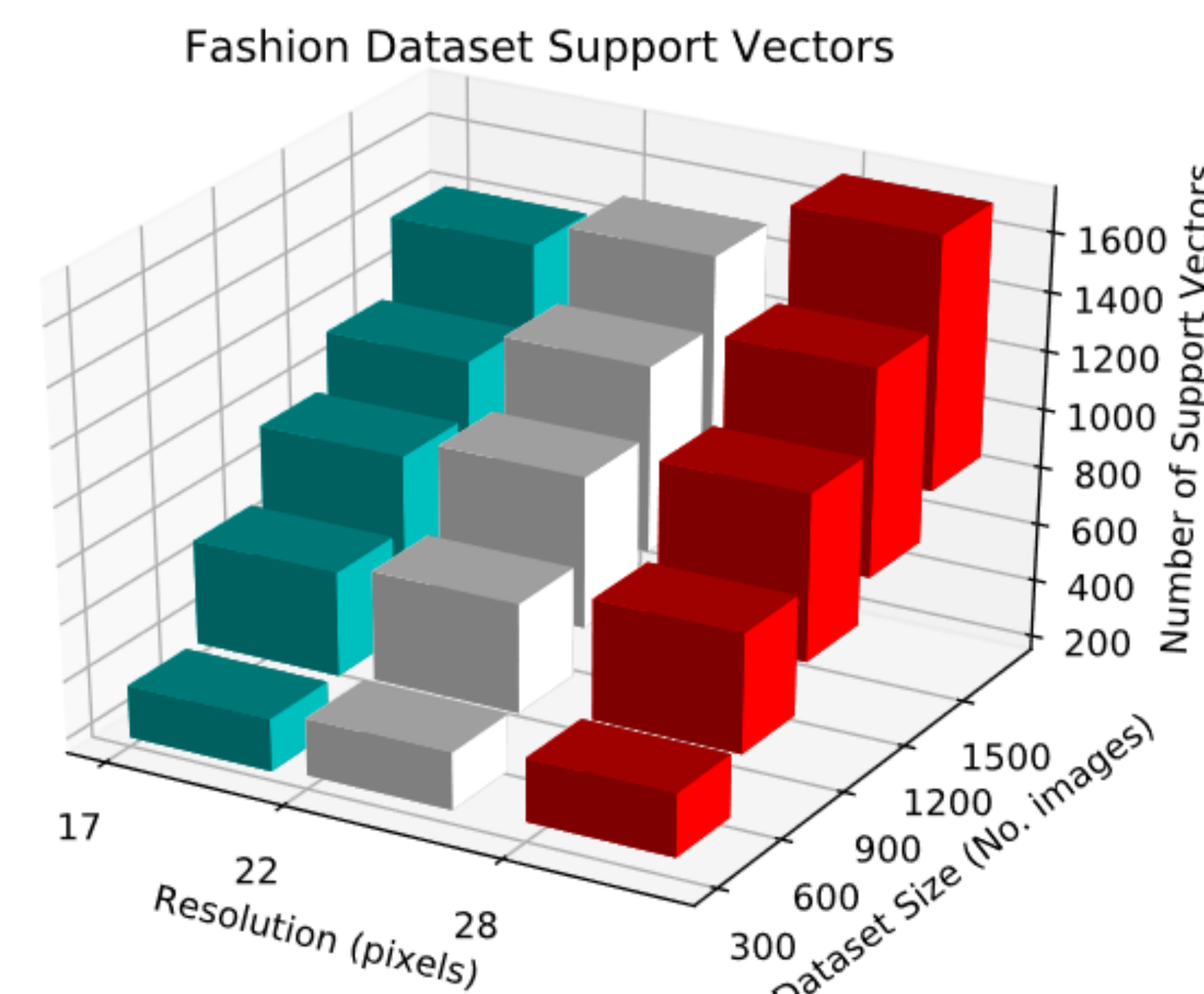
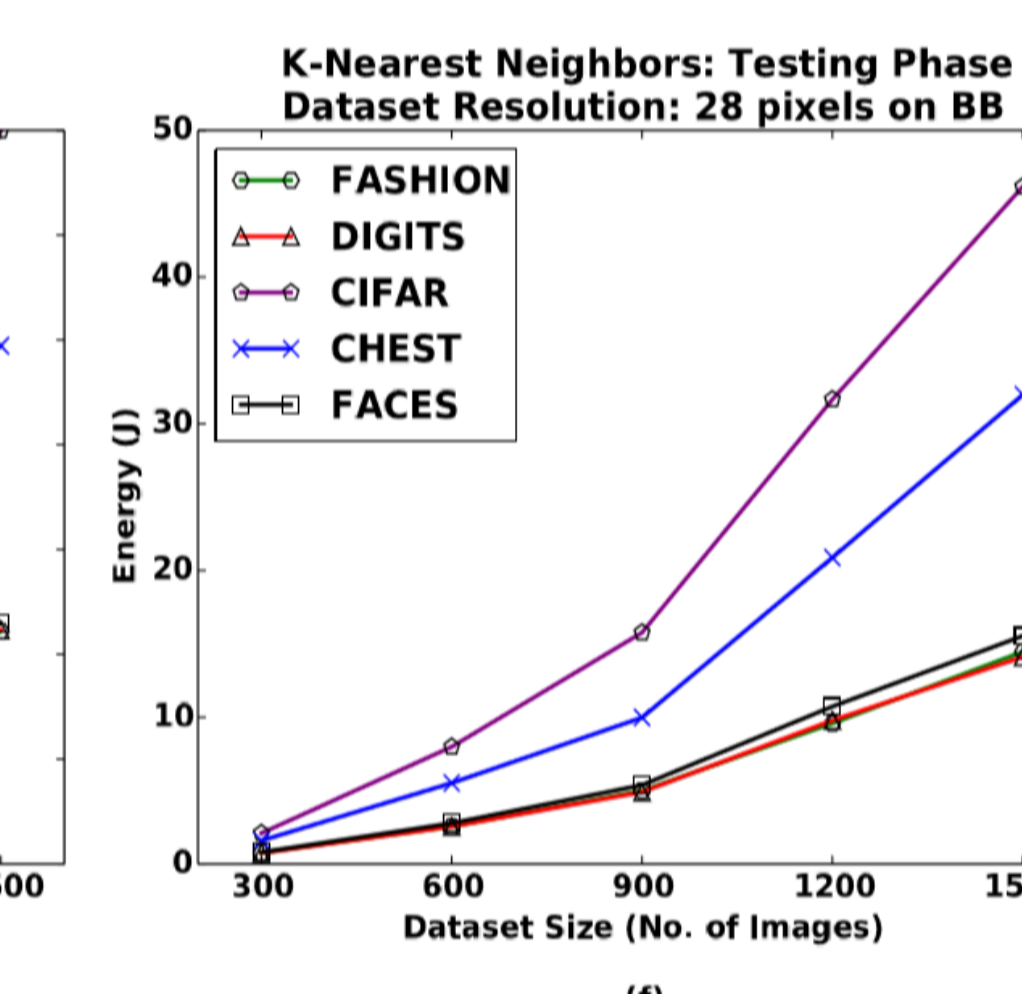
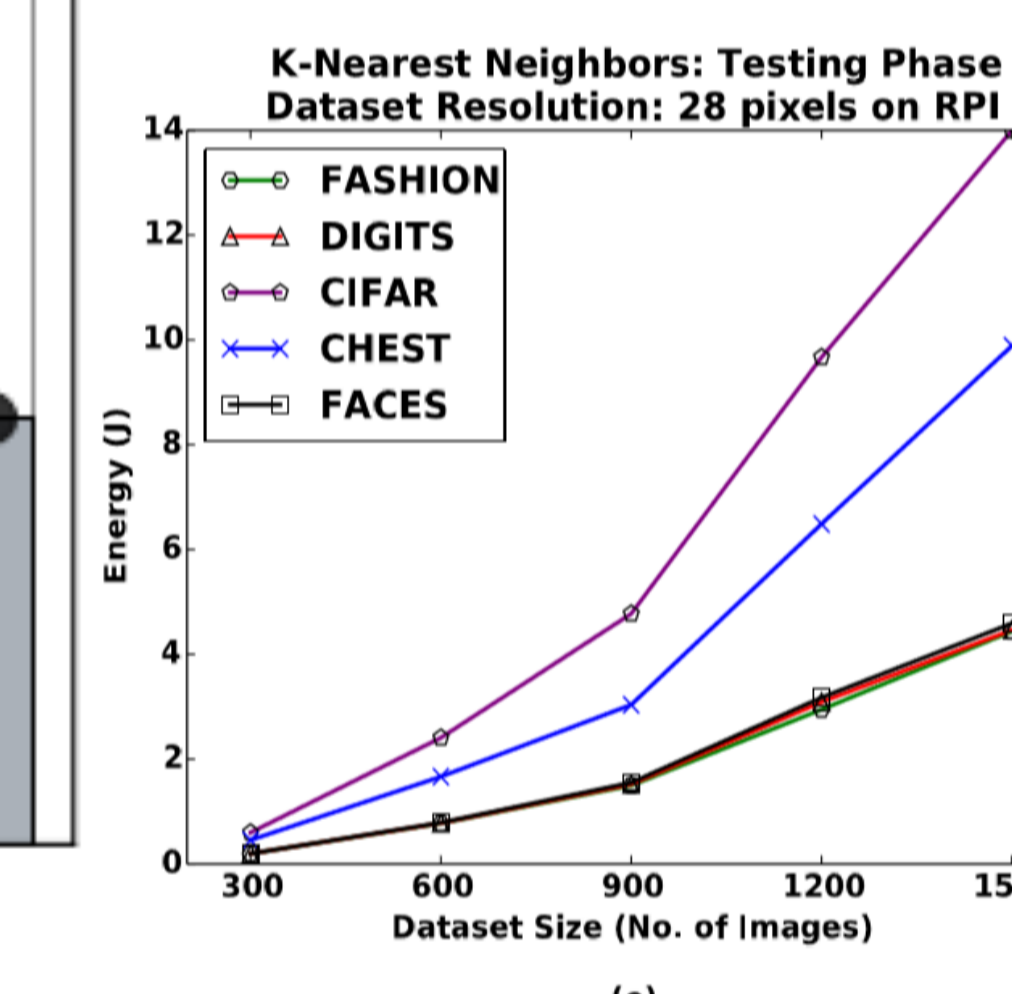
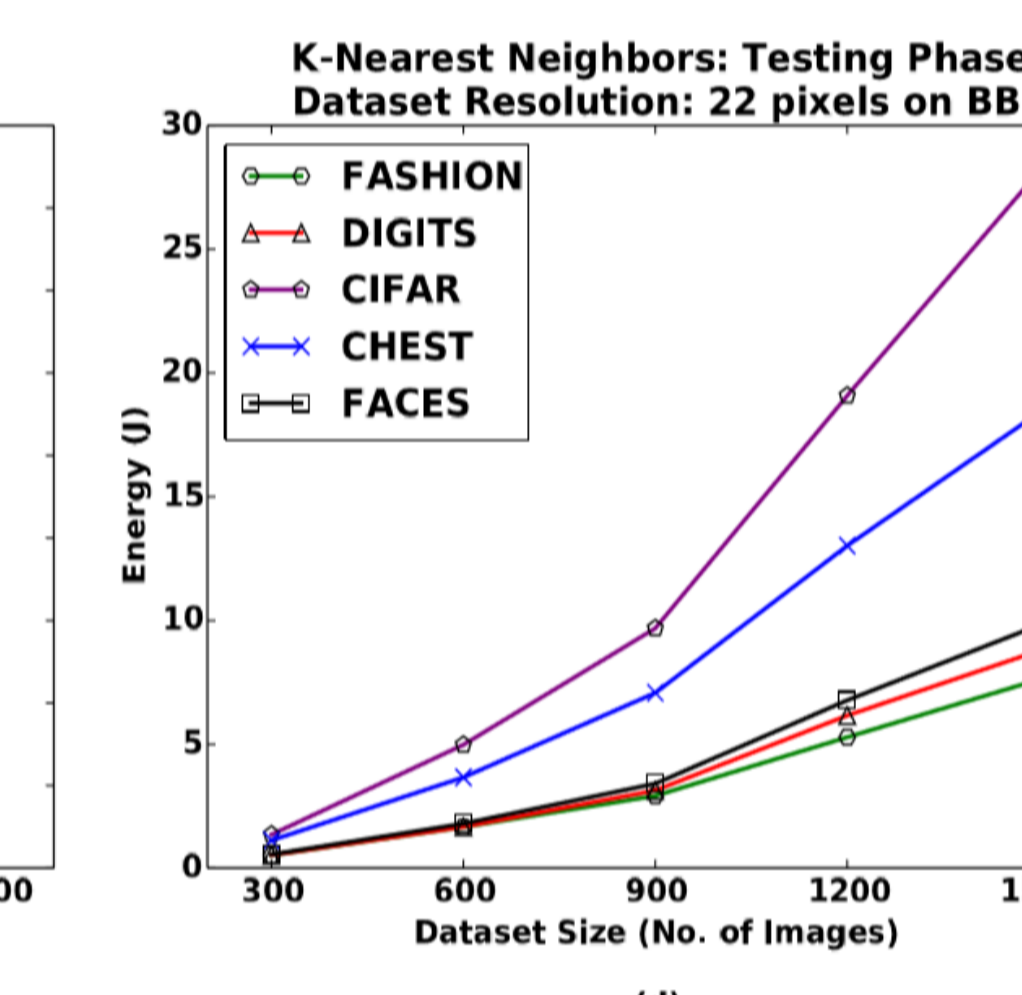
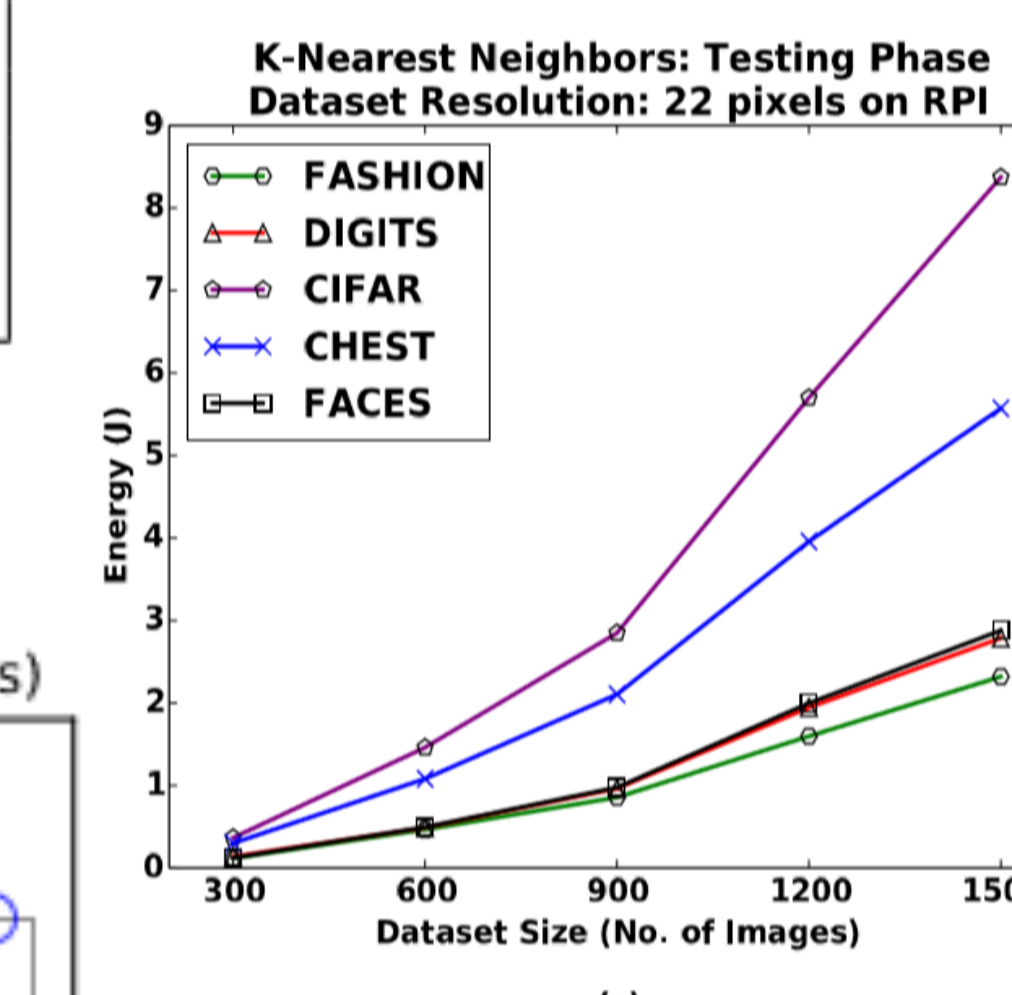
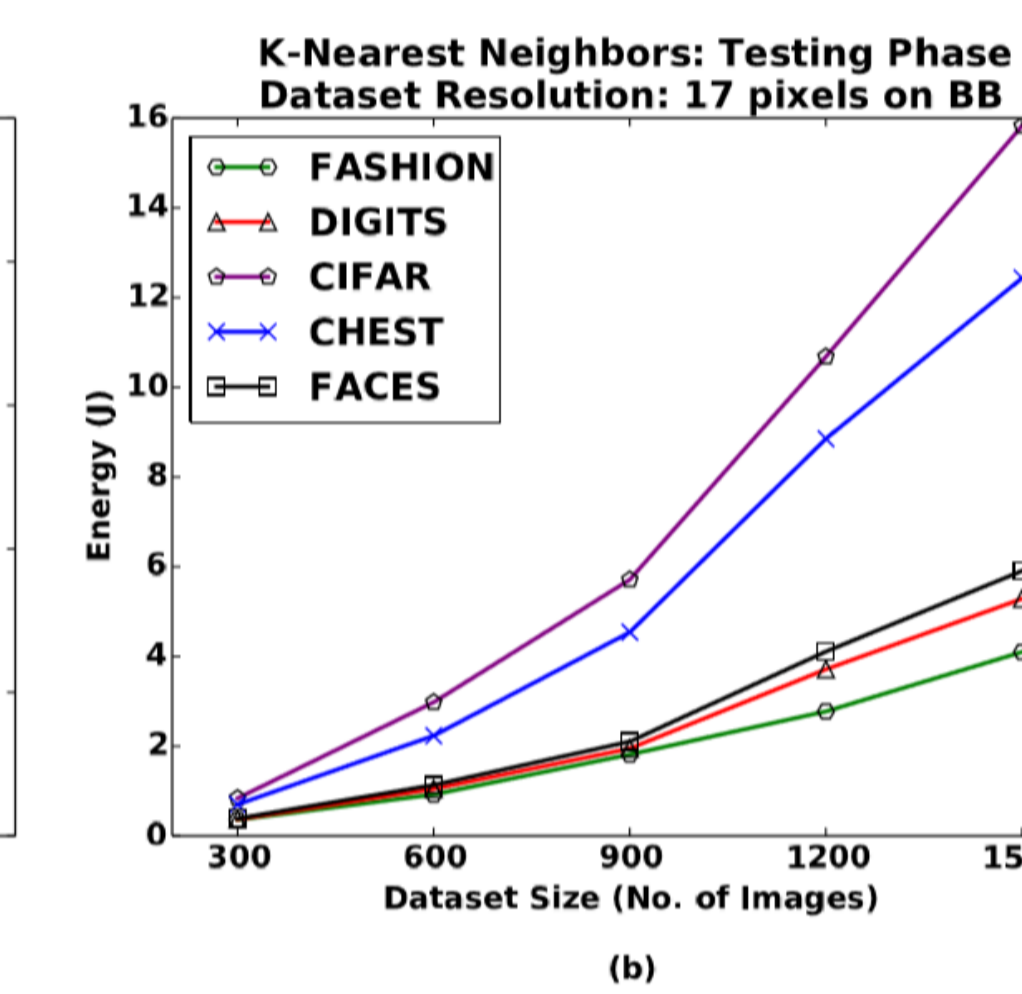
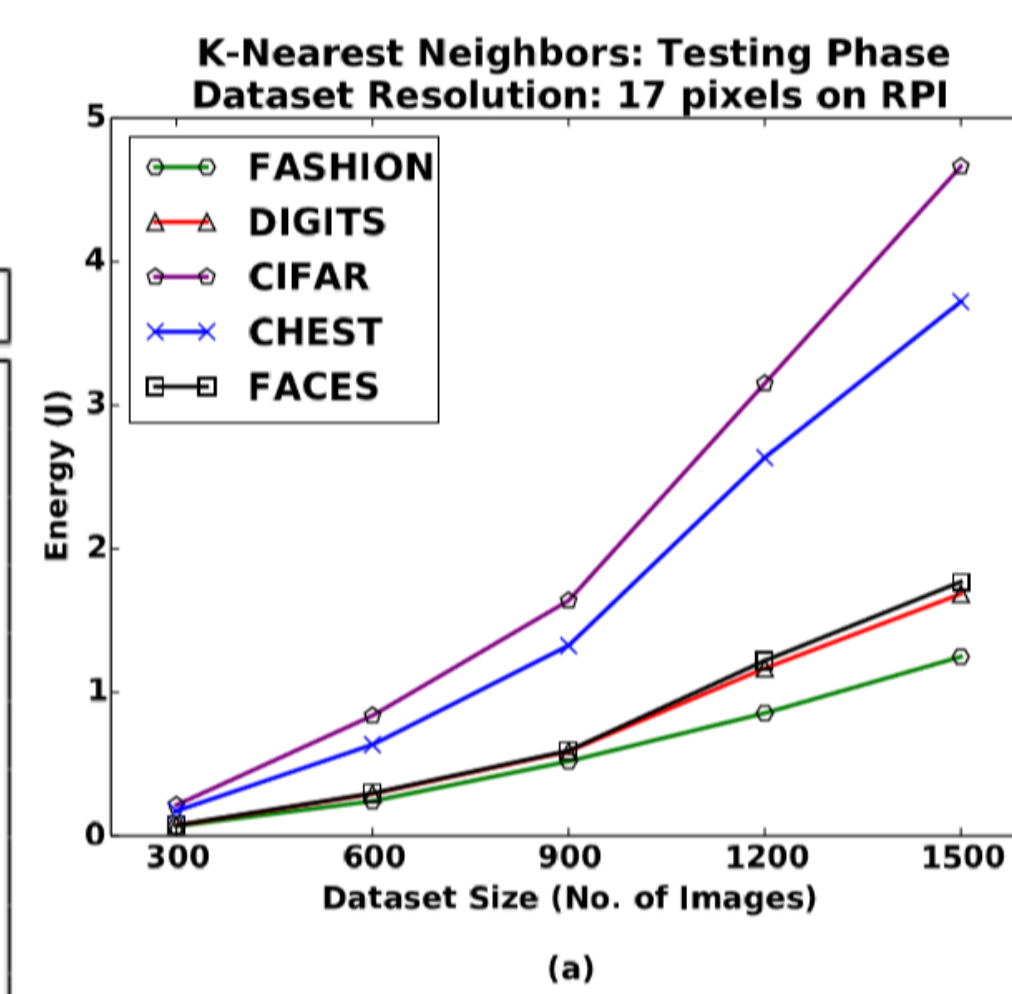
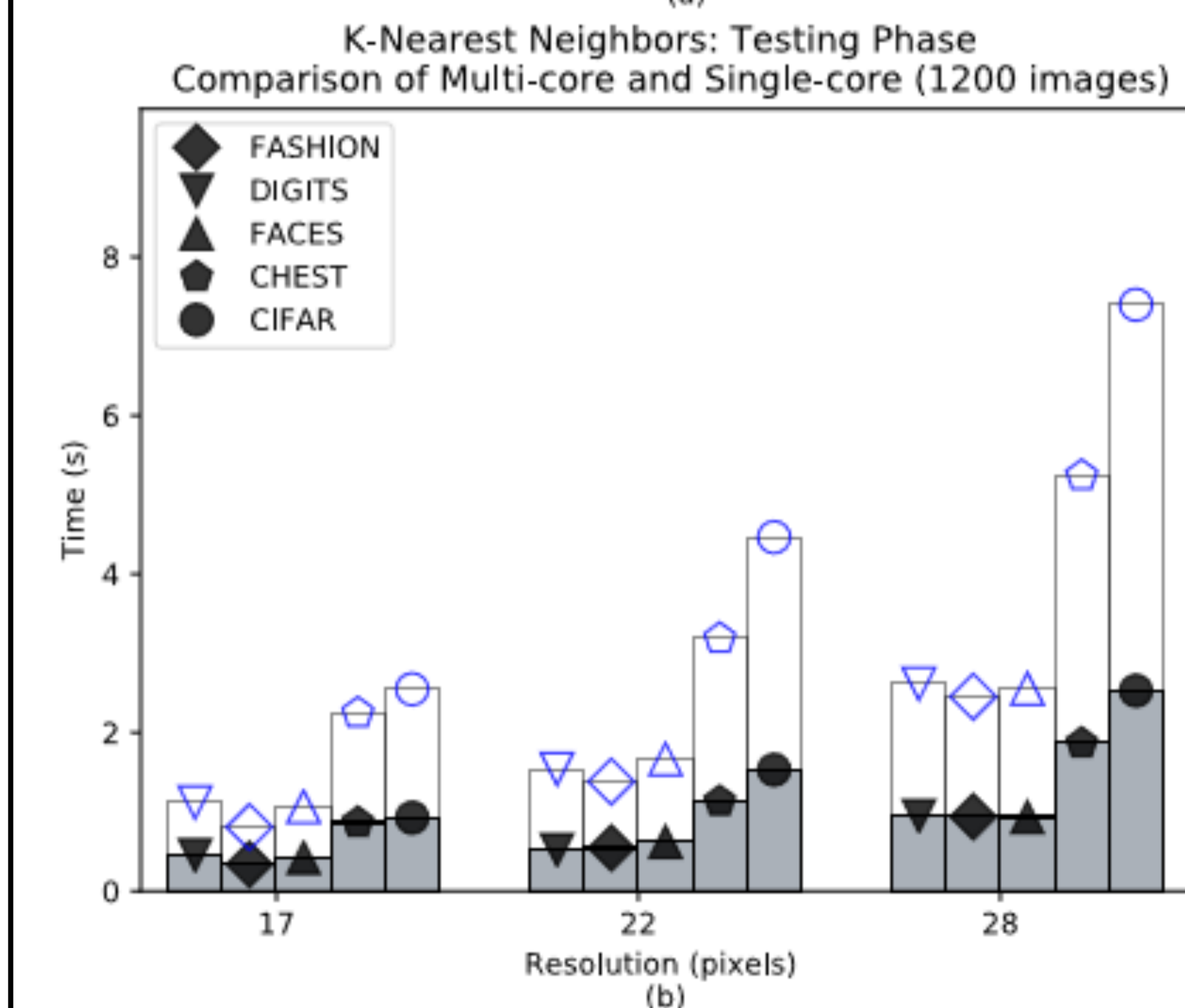
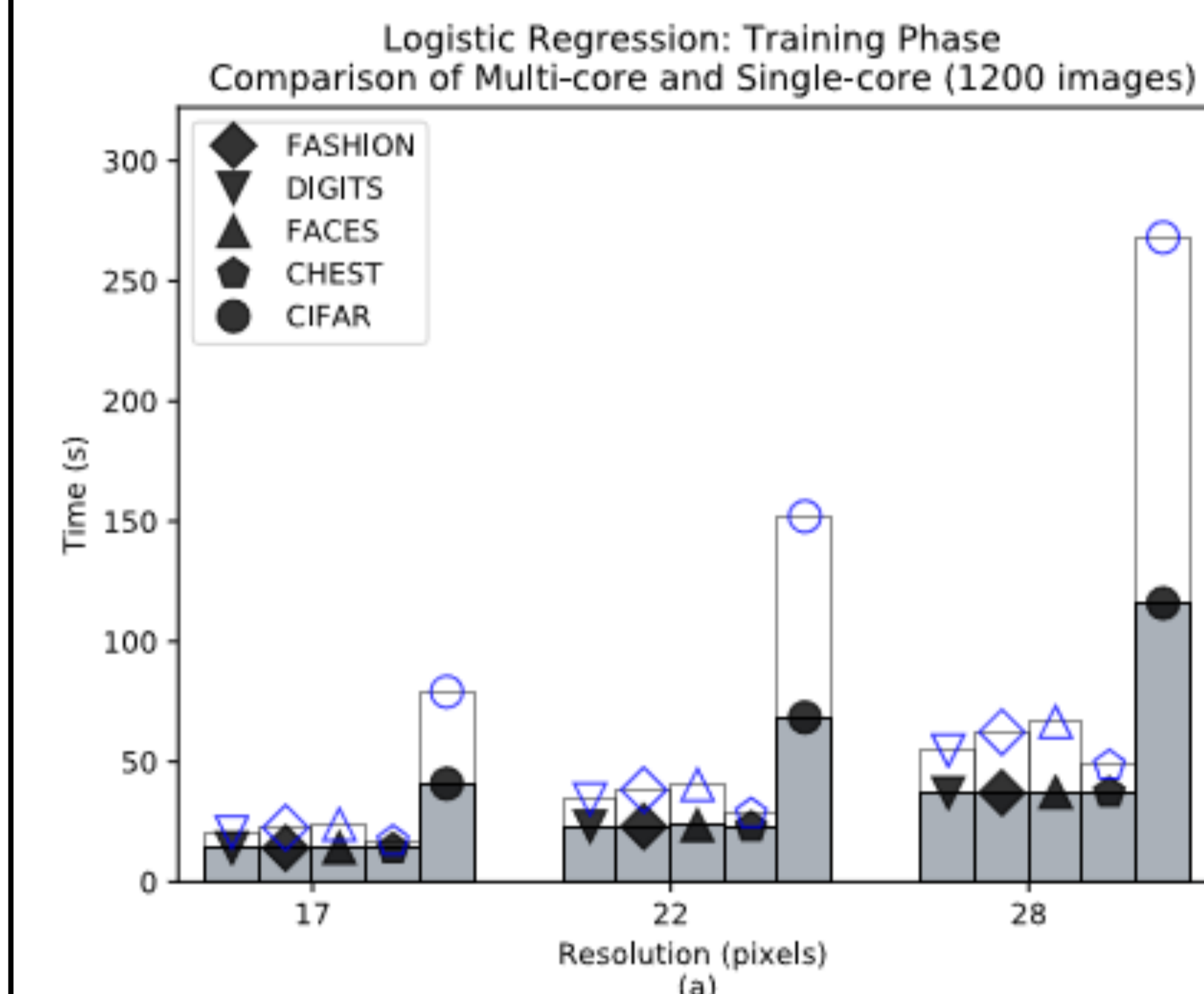
**Testing:** Each board, dataset, size, image resolution, and ML algorithm combination tested 5 times each for a total of 2250 experiments



## Results

TABLE V  
The percent change in time and accuracy when varying between 17x17 and 28x28 image resolutions on the RPI platform. The dataset size is constant.

Algorithm	Dataset	$\Delta t_{300}$	$\Delta a_{300}$	$\Delta t_{1500}$	$\Delta a_{1500}$
k-NN	DIGITS	137%	0%	243%	-4.80%
k-NN	CHEST	173%	-7.4%	1.72%	1.48%
k-NN	FASHION	200%	0%	244%	1.85%
k-NN	FACES	160%	0%	164%	0%
k-NN	CIFAR	179%	-12.5%	199%	-23.89%
SVM	DIGITS	226%	-4.16%	224%	2.11%
SVM	CHEST	200%	0%	203%	-0.69%
SVM	FASHION	226%	-10%	218%	-4.1%
SVM	FACES	154%	0%	136%	5.31%
SVM	CIFAR	206%	-25%	233%	-14%
LOG	DIGITS	170%	0%	188%	-0.71%
LOG	CHEST	209%	7.69%	289%	0.69%
LOG	FASHION	184%	-17.64%	202%	-4.13%
LOG	FACES	207%	0%	221%	0%
LOG	CIFAR	236%	14.29%	324%	-28.85%



## Predicting Energy Consumption

Our experimentation provided us with a sizable amount of data that can be used to model and predict the energy consumption. **We utilize and compare the performance in terms of prediction accuracy of three statistical analysis techniques: random forest, linear regression, and Gaussian process.**

TABLE IX  
 $R^2$  comparison

ML Model	Flowers	CALTECH-256	Original Datasets
Linear Regression	0.34	0.30	-0.15
Gaussian Process	0.5	0.63	0.49
Random Forest	0.79	0.95	0.74

TABLE X  
RMSE comparison

Algorithm	Phase	Dataset	RMSE	Range	N_RMSE
KNN	Train	O	0.162	4.409	0.036
KNN	Train	F	8.518	11.55	0.737
KNN	Train	C	8.400	11.91	0.705
KNN	Test	O	1.389	14.14	0.098
KNN	Test	F	5.464	45.28	0.120
KNN	Test	C	4.989	44.43	0.112
SVM	Train	O	27.508	196.81	0.139
SVM	Train	F	30.980	348.01	0.089
SVM	Train	C	26.509	334.57	0.079
SVM	Test	O	1.561	12.53	0.124
SVM	Test	F	5.004	30.19	0.165
SVM	Test	C	4.399	28.92	0.152
LOG	Train	O	170.54	1305	0.130
LOG	Train	F	181.08	776.67	0.233
LOG	Train	C	157.74	1117.46	0.141
LOG	Test	O	0.021	0.248	0.086
LOG	Test	F	4.465	6.476	0.689
LOG	Test	C	4.379	6.241	0.701

Linear regression performed the worst, with the lowest R-squared value across both validation datasets and our original testing set. This table also demonstrates the poor performance exhibited by the Gaussian process model across all datasets.

R-squared can be interpreted as the percent of the variation in y that is explained by the variation in the predictor x. **A value of 1 for R-squared indicates all of the data points fall perfectly on the regression line** which means the predictor x (features such as image size, resolution, etc.) accounts for all of the variation in y.

## Acknowledgements

This research has been partially supported by the Santa Clara Valley Water District (grant# SCWD02) and Latimer Energy Lab.

# Image Compression with Deeper Learned Transformer

Authors: Licheng Xiao, M.S. CSE, Computer Engineering, lxiao@scu.edu | Hairong Wang, M.S. CSE, Computer Engineering, hwang1@scu.edu

Faculty Research Advisor: Nam Ling, Chair, Department of Computer Engineering

## Background

Balle et al (2017) presented a non-linear transformer for end-to-end image compression, which outperforms image compression standard JPEG2000, but not as good as BPG (better portable graphics), the state-of-the-art image compression standard using traditional methods the same as intra frame coding in the latest video coding standard H.265.

## Objectives

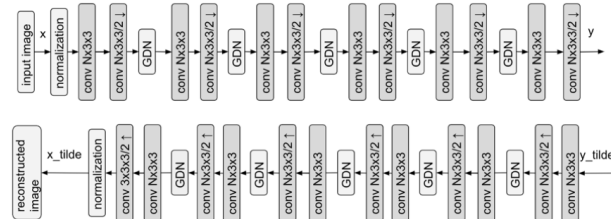
To improve Balle's model to outperform BPG.

## Research Design

First, we use a deeper variational autoencoder as learned transformer with more parameters and smaller convolutional kernels.

GDN (generalized divisive normalization) is for Gaussianizing image densities.

Second, we train models with more iterations, from 1 million to 10 million.



Unlike BPG, which use a discrete cosine transform (DCT)-like linear transform on transform units (TUs) of size 4x4, 8x8, 16x16 or 32x32 to get image frequencies distribution, followed by a quantization that can be adjusted with quantization parameter (QP), our approach uses a non-linear transform implemented as a deep neural network on patch size of 256x256, to get image frequencies distribution, followed by a uniform scalar quantization.

## Experimental Results

Our approach outperforms BPG(RGB 4:4:4) in all three major metrics, i.e. bpp (bit per pixel), PSNR (Peak Signal-to-Noise Ratio) and MS-SSIM (Multi-Scale Structural Similarity) index.

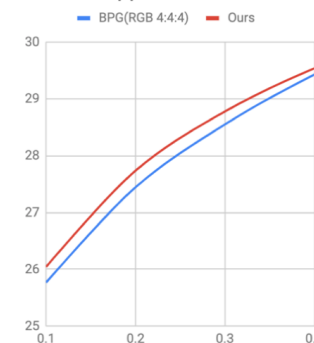
Test images consist of all 24 images from Kodak Lossless True Color Image Suite. All three metrics, i.e. bpp, PSNR and MS-SSIM are calculated by the average value of 24 test images.

For BPG, we use RGB color domain with 4:4:4 chroma format, compression level = 9 (highest), and the quantization parameter (QP) = 48, 46, 43, 42, 41 respectively.

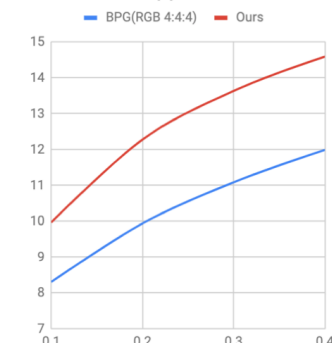
For our learned transformer, we set  $\lambda$  to 0.0001, 0.0005, 0.005, 0.05, 0.5 respectively.

The MS-SSIM is rescaled to  $-10 \log_{10}(1 - MS\_SSIM)$ , the same as Balle's research.

PSNR vs bpp



MS-SSIM vs bpp



Original



BPG (RGB 4:4:4), bpp = 0.835



Ours, bpp = 0.561

## Conclusion & Future Plan

We achieved our goal to outperform BPG (RGB 4:4:4).

In the future, we plan to modify the model to compress in YCbCr 4:2:0 format, and outperform BPG (YCbCr 4:2:0).



## Background

Cloud computing has become popular in both business and personal services. IaaS, or Infrastructure as a Service in cloud computing, is a service model that grants multiple users' access to a shared pool of physical resources in a dynamic way. Such dynamic resource sharing among disparate users provides the foundation of cloud computing by enabling tremendous advantages, such as the huge data storage and processing capability, scalability, and dramatic reduction in businesses costs. However, the infrastructure resource sharing among multiple tenants also raises new security challenges. Co-residence attack has been recognized as an efficient attack over the cloud infrastructure through which the attackers are able to sniff sensitive information from or negatively influence the performance of other tenants located on the same host.

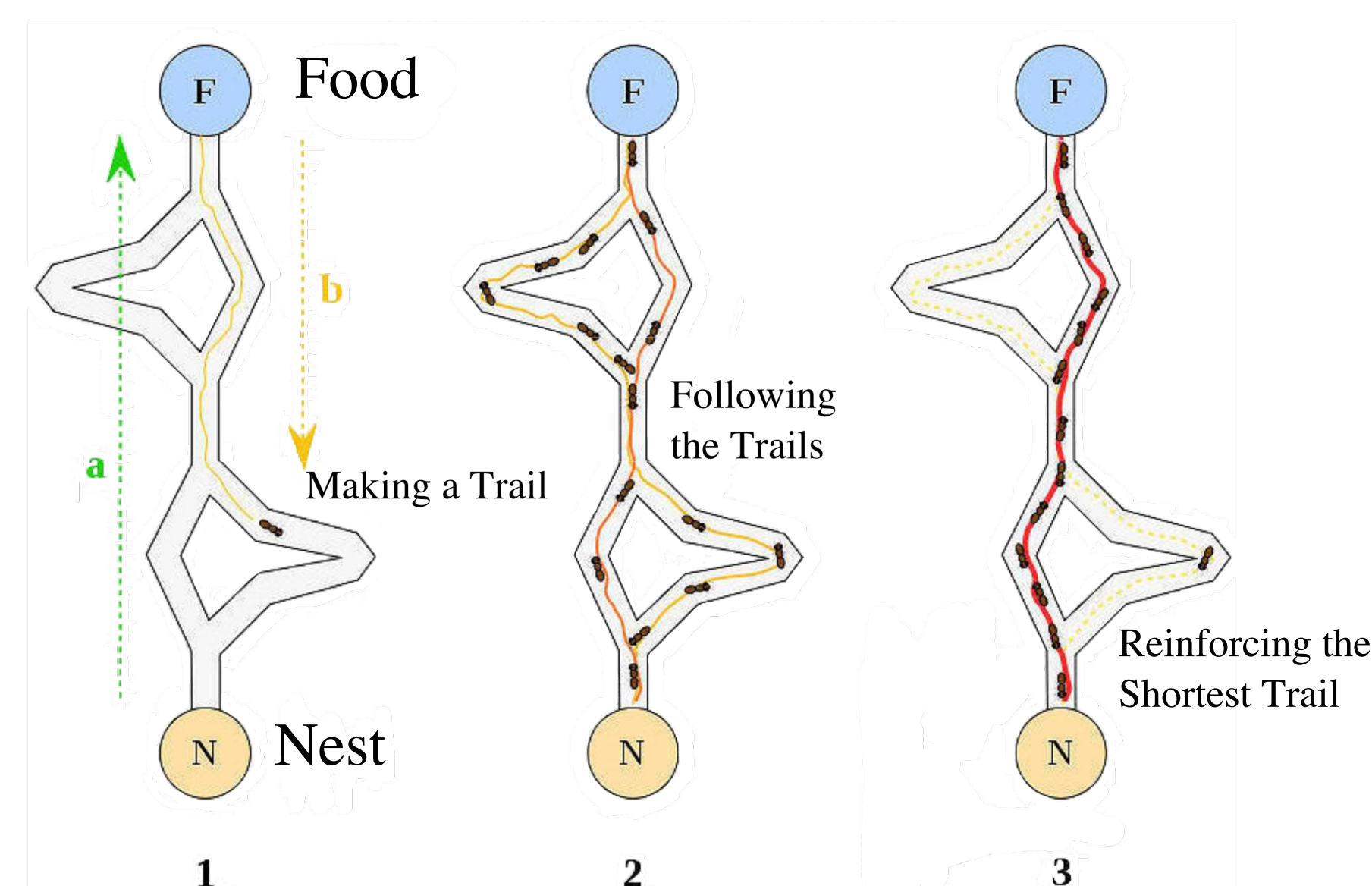
## Objective

We proposed a secure, workload-balanced, and energy efficient Virtual Machine (VM) allocation strategy to defend against co-residence attacks. Specifically, we modeled the VM allocation problem as an optimization problem where the goal is to minimize the security risks introduced by the co-residence of VMs from multiple users, the overall power consumption, and the unbalanced workload among different physical servers. As the optimization problem is NP-hard, we apply the Ant Colony Optimization (ACO) algorithm, an evolutionary algorithm that mimics the biological behaviors of ants, to find the optimal solution for our VM allocation strategy.

## Ant Colony Optimization

Ant Colony Optimization is inspired by natural ant activities. It integrates both heuristic information and randomness to find the optimized solution to a problem.

- \* Ants make random trails at the beginning and leave pheromone.
- \* More ants choose the trail with more pheromone.
- \* The shortest trail stands out.



## Research Design

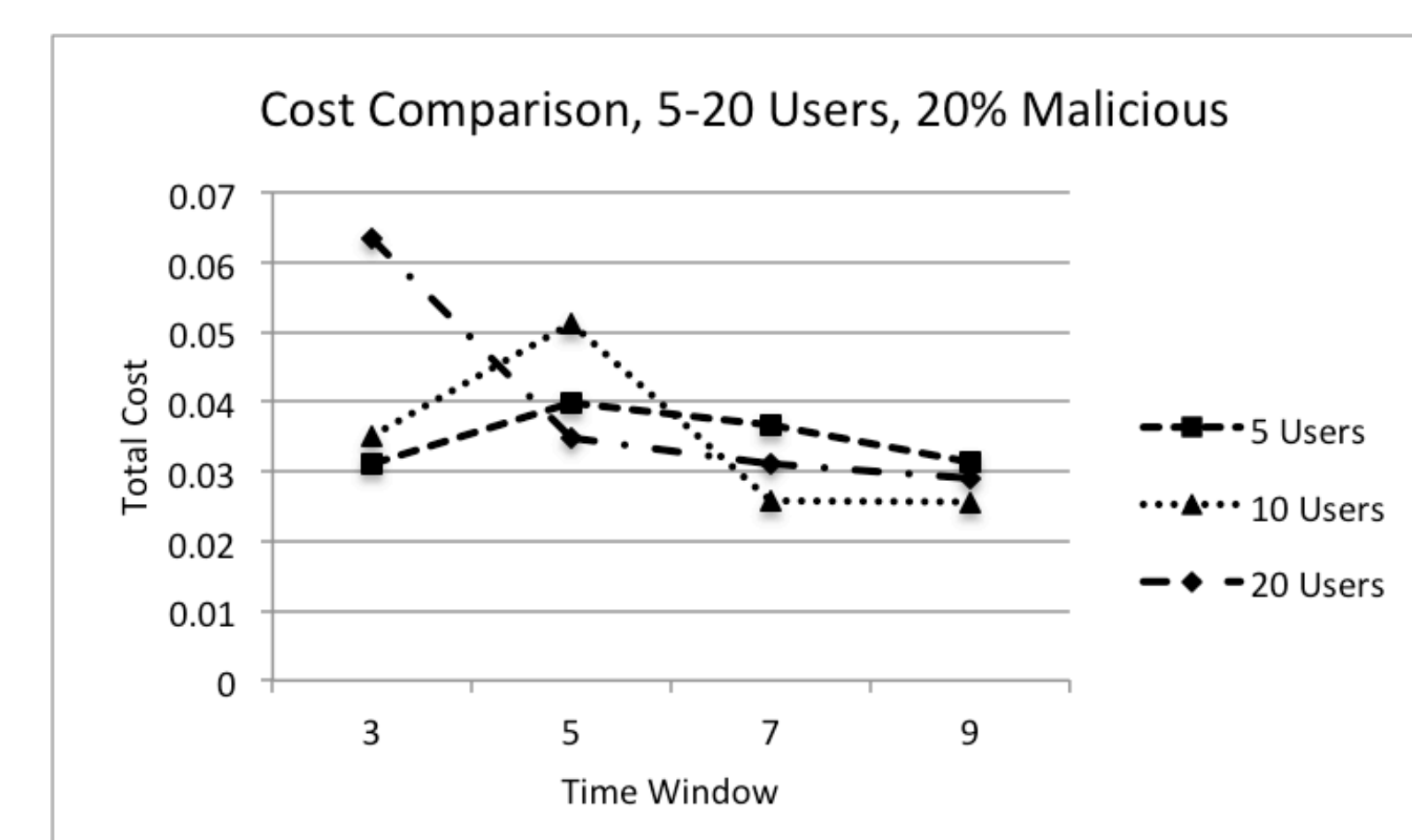
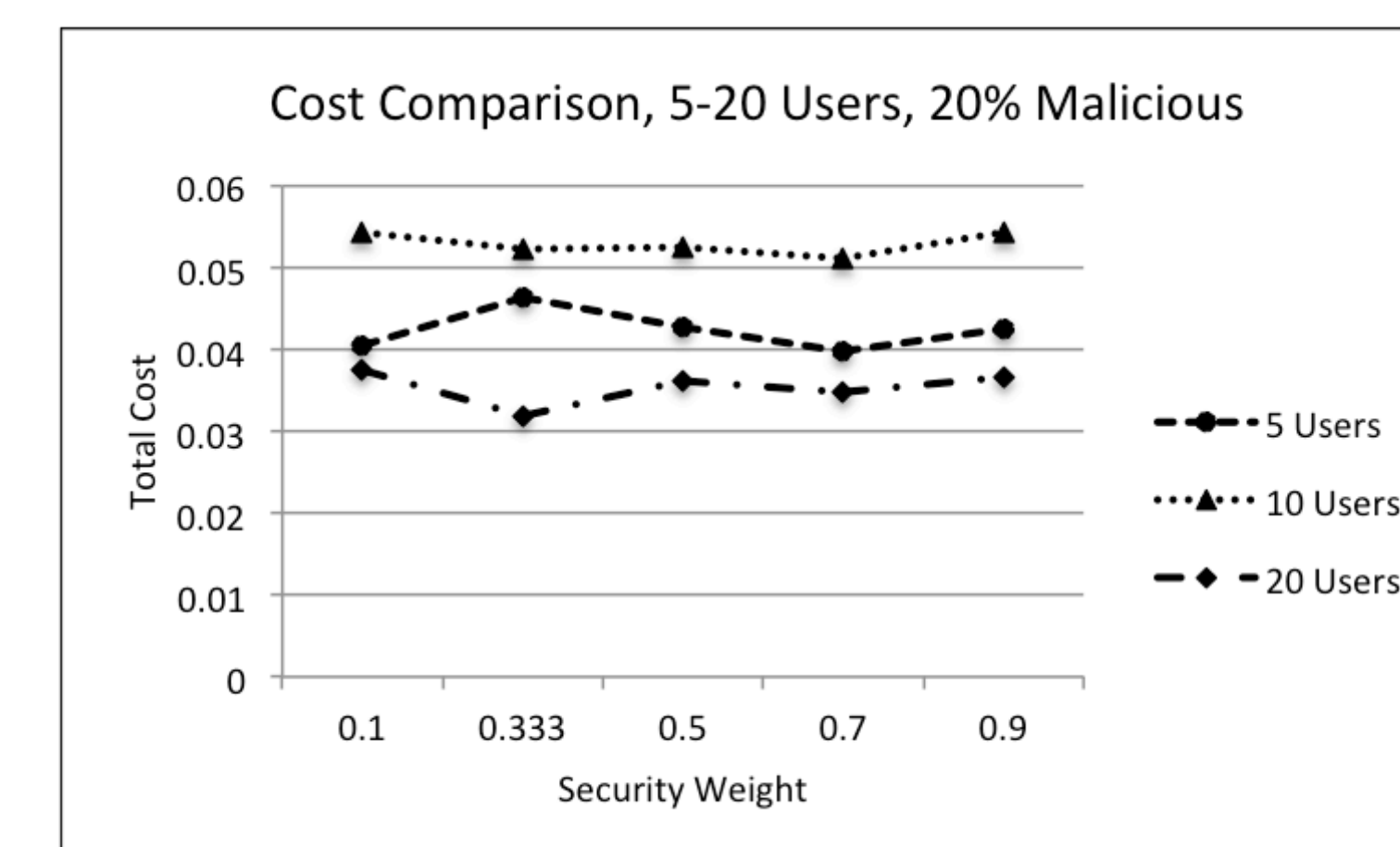
Two connections between ACO and VM allocation:

1. The pheromone that the ants leave on the trail are the cost of an assignment of a VM to a server. The cost is calculated from an integration of its security level, power consumption, and workload balance. The pheromone is inversely proportional to the cost.
2. The paths ants take and the different assignments of VMs to servers. At first, all the assignments of a list of VMs are performed randomly. As we run the assigning process for a number of iterations, the most optimized allocation path will stand out, since at each iteration, the VMs are likely to be assigned to a server with minimum cost depending on the pheromone.

We also introduced the sliding time window to handle the scalability of VM arrivals. The VM utilization and number of VM per user are randomized so that the program's behavior is more similar to real-world scenarios.

## Results

We showed that applying Ant Colony Optimization to VM allocation is effective and efficient. We evaluated our schema under different number of users and weight of security. The results indicated that a security weight of 0.7 results in the minimum amount of the overall cost.



We then used the security weight of 0.7 to evaluate our solution under different number of time windows. The result shows that regardless the number of users, increasing the number of time windows under certain amount of VMs would reduce the overall cost.

## Conclusion

Co-residence attack has raised significant concerns with the increasing popularity of cloud computing. We proposed to defend against such co-residence attacks through a secure, workload-balanced, and energy-efficient VM allocation strategy, and modeled the VM allocation problem as an optimization problem. We applied the Ant Colony Optimization (ACO) algorithm, an evolutionary algorithm inspired by natural ant activities, to identify the optimal allocation strategy. We further integrated real-world factors by splitting virtual machine arrivals into multiple time window, and also randomized the number of VMs per user. Experiment results demonstrated that the proposed scheme can make the multi-tenant cloud secure and power efficient.

## Future Plan

In the next few months, our main task is to expand the experiments to compare our solution with other proposed schemas, and finalize the journal paper. After that, we will also integrate our program with CloudSim to mimic our program's behavior in a real-world scenario.

## Contact Information

Advisors:

Yuhong Liu  
Xiaojun Ruan

yhliu@scu.edu  
xiaojun.ruan@gmail.com

Students:

Lu Cao  
Ruiwen Li  
Hanxiao He  
Songjie Cai

caoolu@gmail.com  
rli@scu.edu  
hhe1@scu.edu  
scai@scu.edu



# Multilingual News Search User Behaviors

## Exploring Multilingual Consumption Behaviors, Querying and Result Selection Through Crowdsourcing

Chenjun Ling, Silvia Figueira, Ben Steichen

Mobile Computing for Social Benefit Lab, Computer Science and Engineering, Department of Computer Engineering



Santa Clara University

School of Engineering

### Abstract

With the global expansion of the Internet, users have become increasingly diverse, particularly in terms of their languages. In fact, there are now many users who are polyglots, i.e. proficient in more than one language. However, such polyglot users often continue to suffer from unbalanced and fragmented information, as traditional news access systems seldom allow users to simultaneously search and/or compare news in different languages, even though existing research results showed that multilingual users make significant use of each of their languages when searching for information online.

In addition, with the rapid development of the Internet, the World Wide Web, and Mobile Computing, there are now a plethora of new ways to access news content. For example, searching and browsing news content on mobile devices has become an increasingly popular alternative to using desktop devices or traditional non-digital media. Likewise, social media has become a key platform for discovering and consuming news, challenging traditional outlets.

The research presented in this proposal aims to provide the first human-centered studies in multilingual news access. In particular, through a set of 2 phases of user studies, this research will study multilingual news search interface preferences and behaviors, including access modality (e.g. desktop, mobile) as well as news outlet diversity (e.g. traditional news media, social media).

### User Study Design /Research Questions/Platform

#### 2 Phases and Research Questions

##### Phase 1 - Consumption Survey

- (RQ1.1) Which platforms do multilingual users typically choose to search/browse news?
- (RQ1.2) Which topics do multilingual users typically choose to search/browse news?
- (RQ1.3) Which languages do multilingual users prefer with different news platforms and different news topics?
- (RQ1.4) How easy is it currently to receive news from a platform in different languages? What are current barriers to multilingual information access? And the suggestions for improving current multilingual access?



##### Phase 2 - Task-based Study

- (RQ2.1) Which of their language(s) do multilingual users generally use and why when querying and choosing search results?
- (RQ2.2) What is the effect of language proficiency on multilingual user query constructing/selection or result selection behavior?
- (RQ2.3) What are the effects of news domain/topic on multilingual user query constructing/selection or result selection behavior?

#### Platform

- Figure-eight crowdsourcing platform
  - With customized JavaScript.
- Interactive High Fidelity Demo
  - JavaScript, PHP, SQL.



### User Study Details

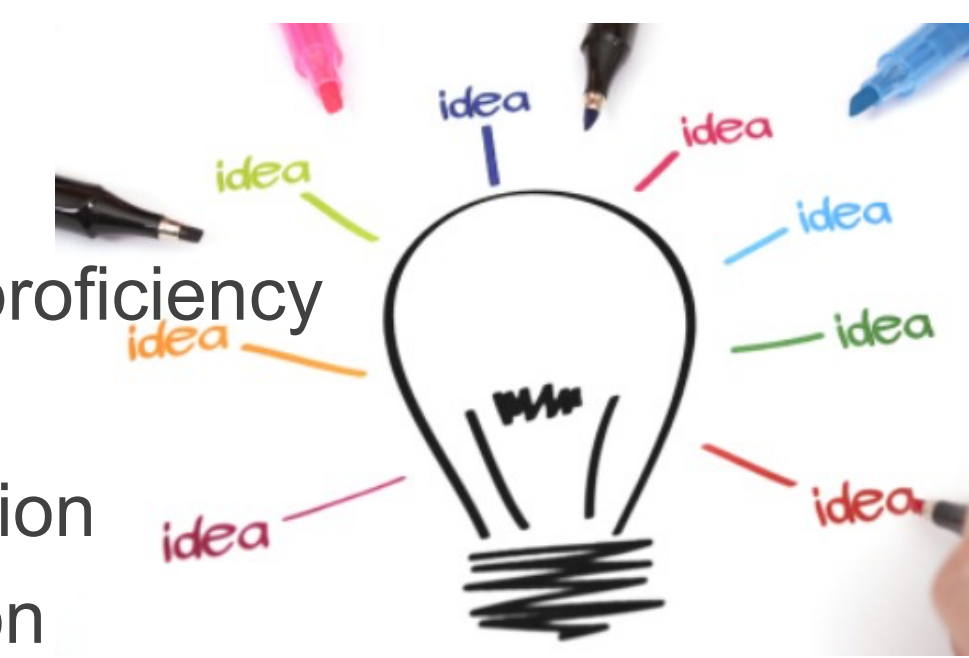
#### Phase 1 – Consumption Survey

- Procedure:** 2 steps; 30 minutes;
  - demographic and language proficiency, and
  - news consumption behavior, specifically platform usage frequency, access modality, news type, shortcomings of current news access systems, and suggestions (open-ended question)
- Participants:** 1200
- System Languages:** 6: English, Chinese (Simplified), Chinese (Traditional), French, German, and Spanish



#### Phase 2 – Task-based Study

- Procedure:** 2 steps; 40 minutes;
  - 1) demographic and language proficiency
  - 2) news tasks: 4 tasks
    - Task1- Query construction
    - Task 2 – Query selection
    - Task 3 – L1 and L2 result selection
    - Task 4 – L1 and Mix-L1&L2 result selection
- Participants:** 1600
- System Languages:** 4: English, Spanish, Chinese Simplified, Chinese Traditional
- Task topics/news titles:**
  - a total of 48 (12 topics per language \* 4 languages) topics were selected from Google Trends and Baidu Index based on the majority population geolocation of language



### Conclusions

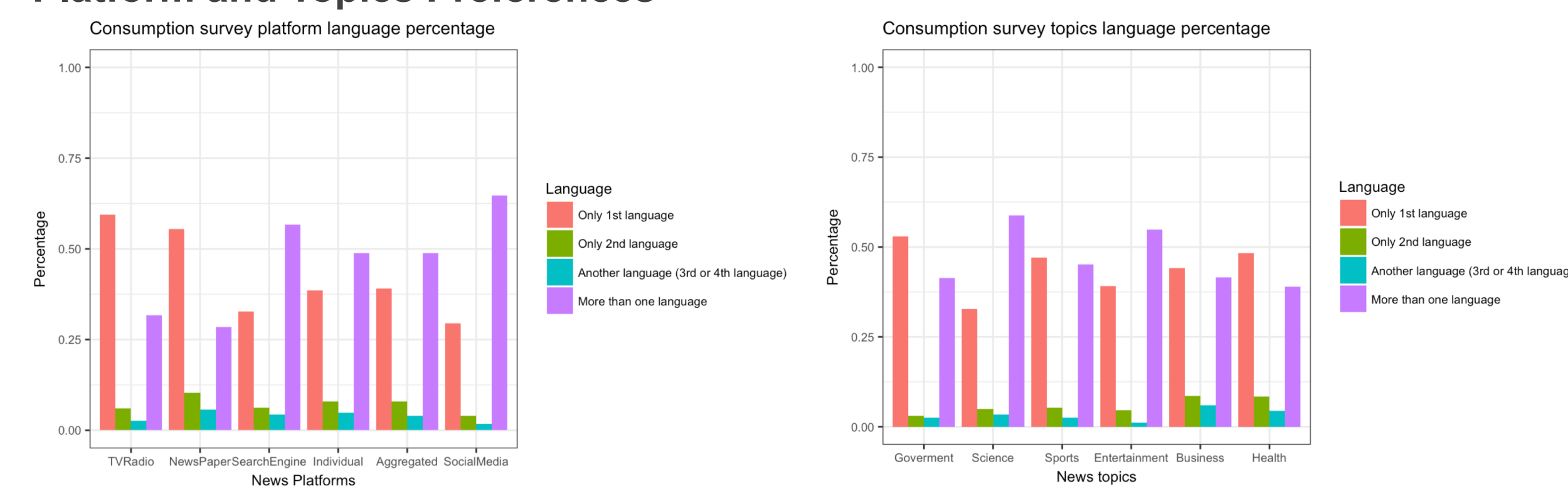
With the increasing polyglot population, more and more multilingual news exists, but polyglots are still facing information unbalancing and fragmentation due to language proficiency and ability, multilingual news quality, news availability, news system defects, and policy constraints. This paper is the first large-scale user study regarding multilingual news access, which includes two phases, phase 1 consumption user study and phase 2 task-based study.

To address these challenges, in next steps we aim to explore novel multilingual news search systems and interfaces that can support the discovery and browsing of multilingual news content 1) in multiple languages, 2) from multiple platforms (e.g. social media and traditional outlets), 3) across multiple device modalities (e.g. desktop and mobile), and 4) according to each individual user's personal abilities (e.g. language proficiencies) and preferences (e.g. interface preferences), and context (e.g. news topic).

### Results

#### Phase 1 – Consumption Survey

##### Platform and Topics Preferences

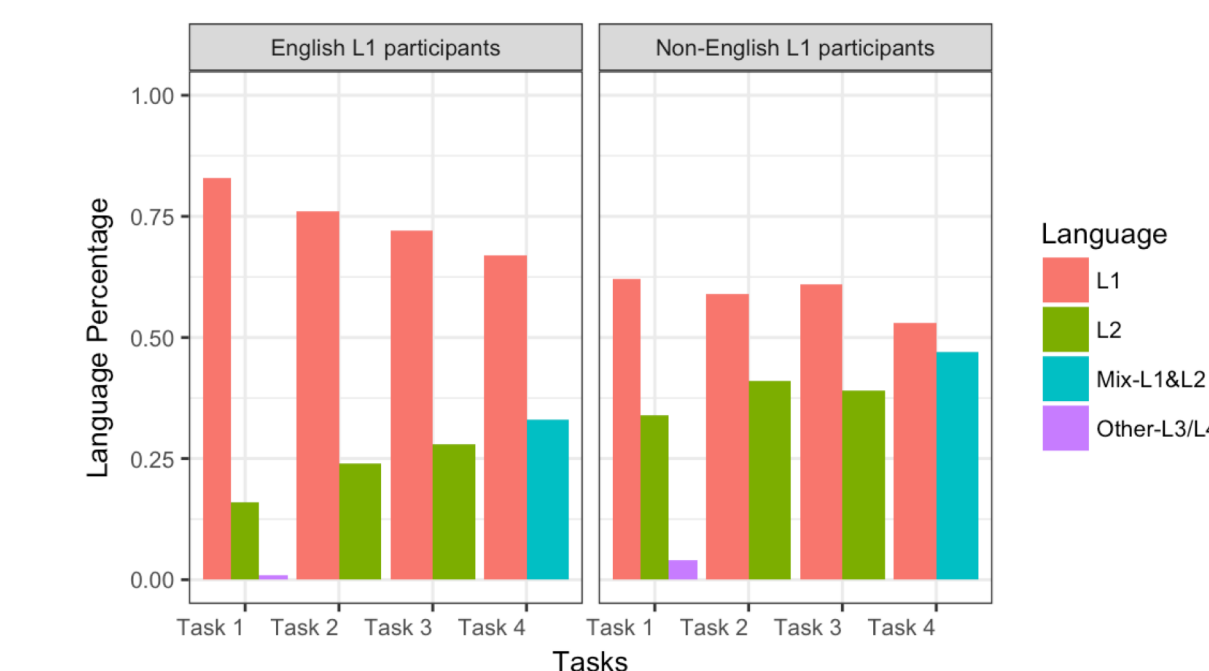


##### Open-ended questions

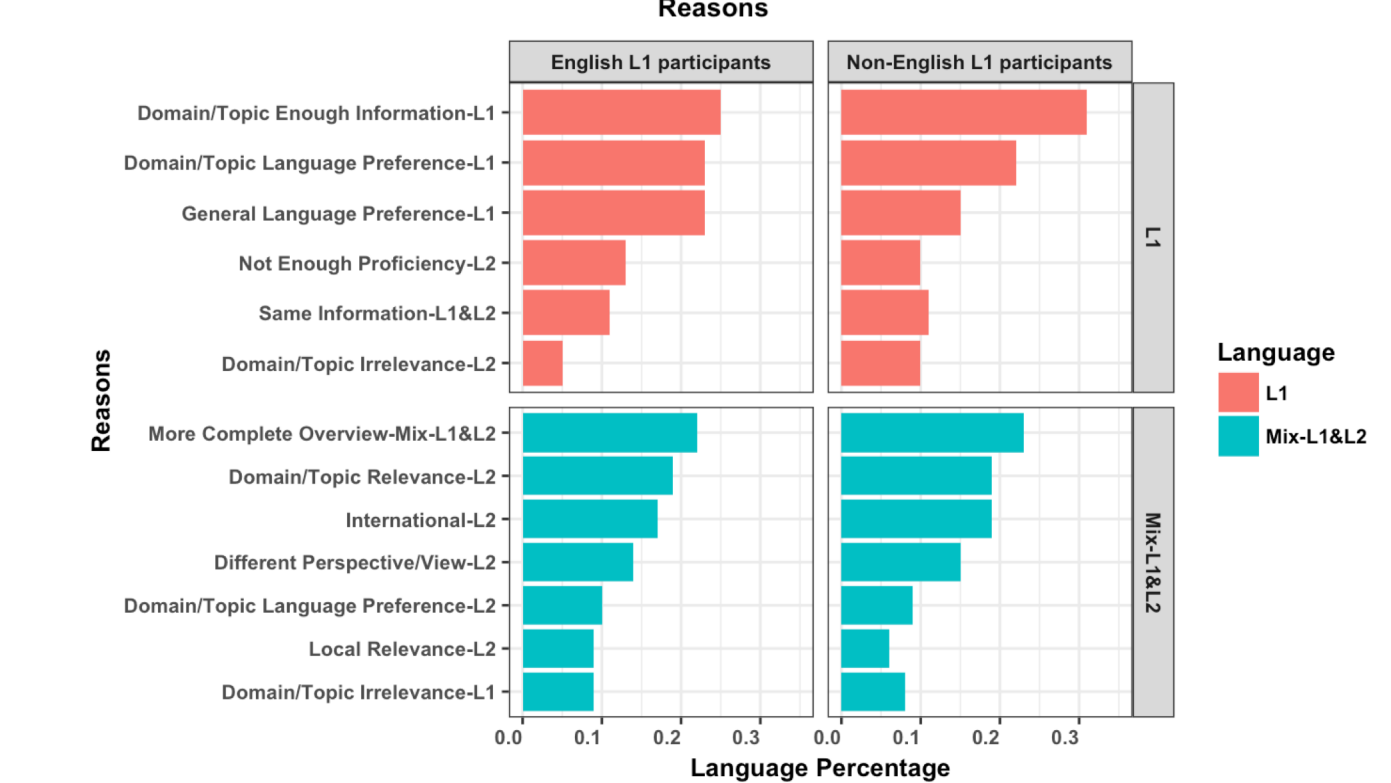
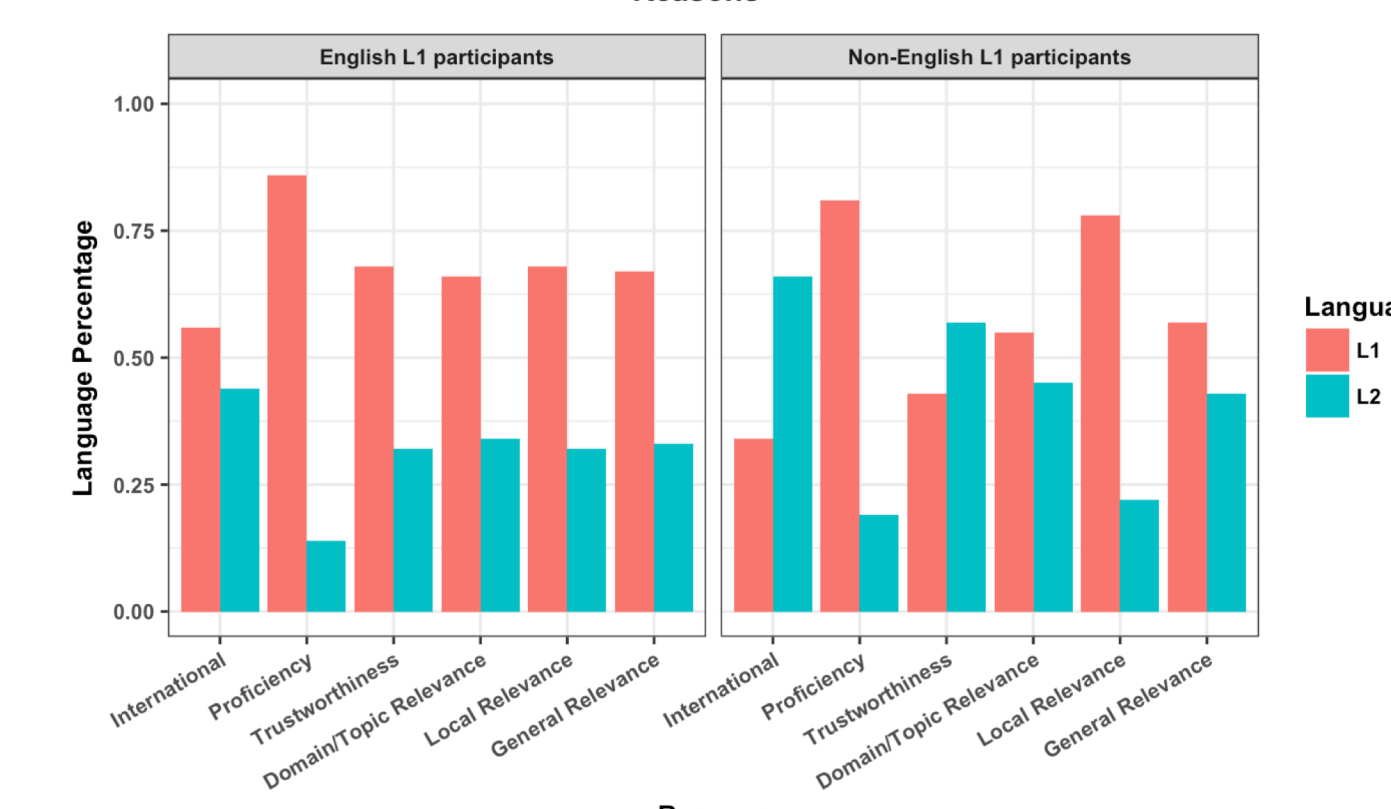
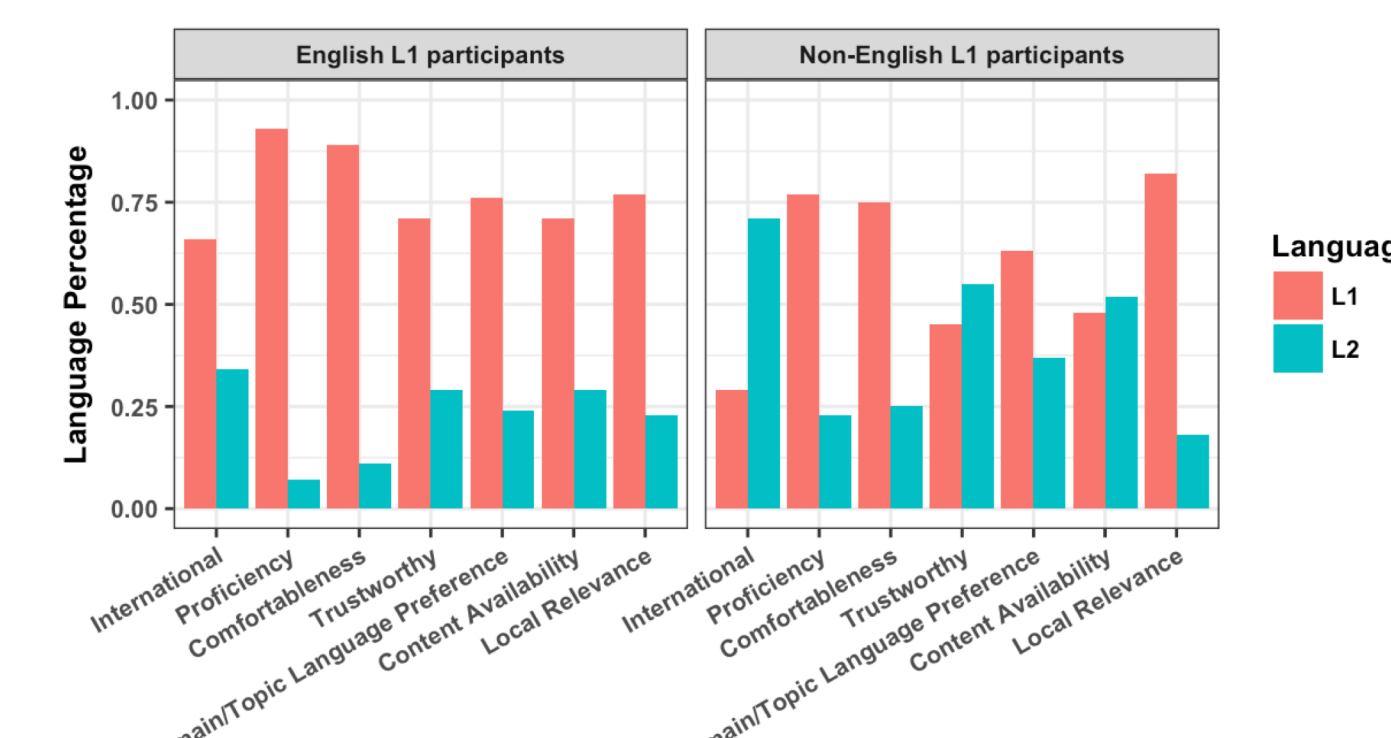
- Q1: Have you experienced any issues when consuming news in different languages?
  - Language understanding:
    - language proficiency and ability (e.g. words/terms, grammar, orthography)
    - other reasons (e.g. different expressions/language circumstance/culture)
  - News content itself: fake news, biased news
  - News availability: little or no information available in one of the languages, not knowing where to find news, censorship, or slow news updates
  - News systems: bad recommendations
  - News format: text vs. video
  - The requirement of extra effort: having to use translators, having to actively/manually switch between languages
- Q2: Do you feel there is a lack in news availability in your first language?
  - Non-English L1 participants
    - language understanding
    - news content/availability
  - English L1 participants
    - a lack of depth of the available information
    - slow information
    - too much choice to ensure the quality
  - In addition, participants specifically mentioned that they needed an aggregated multilingual news platform "to find high quality" (important and trustworthy) news "without wasting time".
- Q3: Do you have any other suggestion on how to improve the consumption of news in multiple languages?
  - The development of platforms/search engines that
    - retrieves multilingual news (based on the user's language preferences), in order to compare and/or switch easily between languages
    - has more "powerful" (e.g. accurate and easy to use) translation functions
    - has multilingual comment sections
    - provides targeted and in time multilingual recommendations
  - Multilingual news content:
    - has the "depiction of multiple viewpoints"
    - has "comment sentiment summarization from different regions"
  - In particular, for videos, participants mentioned that automatic subtitles in their first language (or another chosen language) would be extremely valuable.

#### Phase 2 – Task-based Study

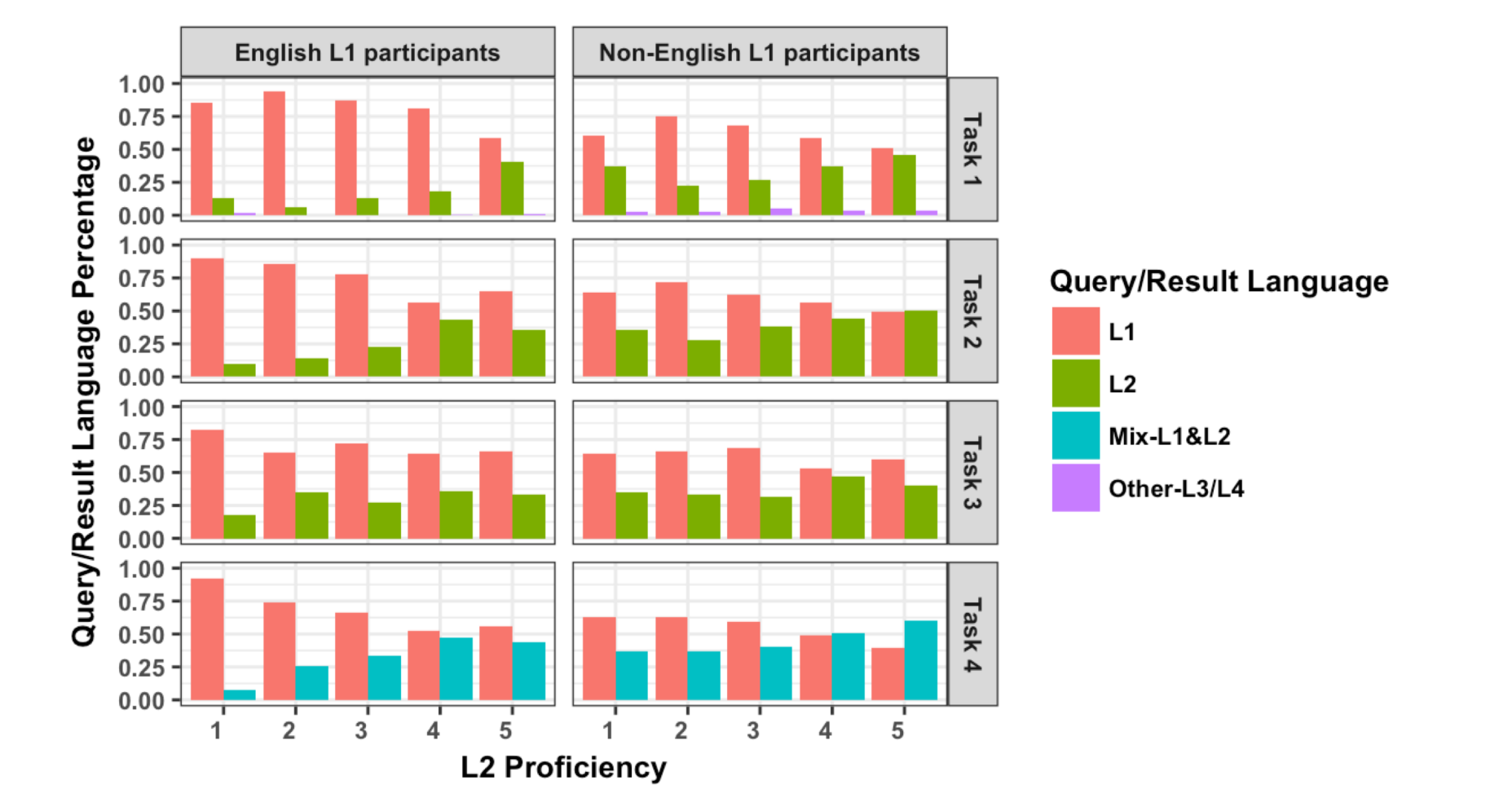
##### Language Choices per Task



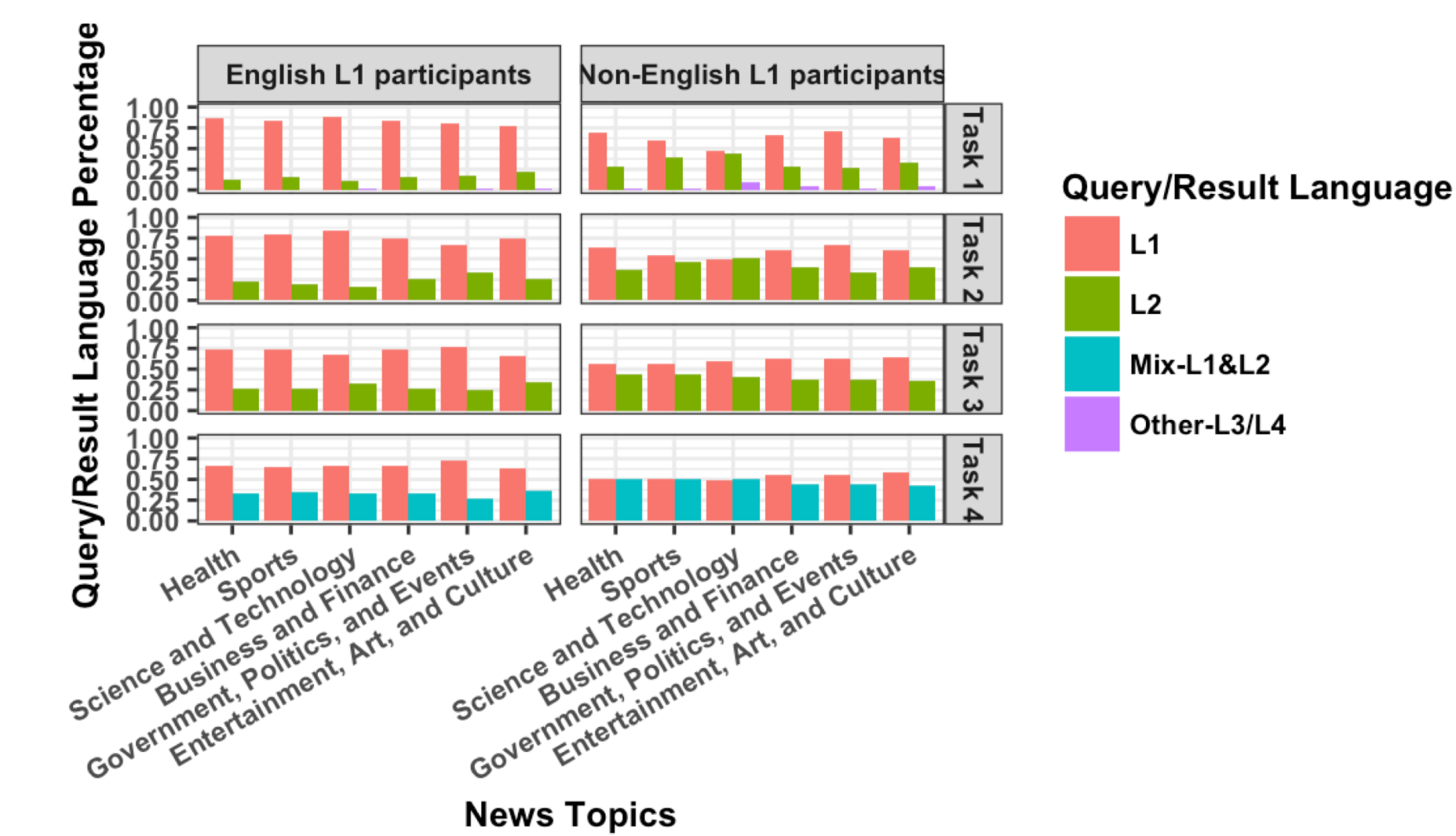
##### Language Choice Reasons per Task



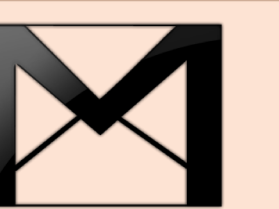
##### L2 proficiency and Query/Result Language Choice



##### News categories & Query/Result Language



Contact: Email: [cling@scu.edu](mailto:cling@scu.edu)



# An Efficient Co-design Partitioning for WLANs on Zynq SoC

{ RAMI AKEELA AND BEHNAM DEZFOULI } INTERNET OF THINGS RESEARCH LAB

## OBJECTIVES

Developing an SDR platform capable of implementing various wireless communication protocols efficiently for IoT and Vehicle-to-Vehicle (V2V).

1. A HW/SW Co-design based SDR platform using Zynq Soc
2. A domain-specific partitioning algorithm of WLAN
3. A set of design guidelines that aim at optimizing area, timing, and power
4. A formal partition evaluation method to determine the total cost
5. Optimization techniques to improve partition's efficiency

## EQUIPMENT & TOOLS

The following equipment was required to complete the research:

- Mathworks MATLAB & Simulink
- Xilinx ZC706 Zynq SoC
- Analog Devices AD-FMCOMMS2-EBZ
- Blade antennas
- Xilinx SDSoC
- Xilinx Vivado Design
- Xilinx HLS

The SDR is intended to be implemented on the Zynq SoC, which is composed of Dual-core ARM Cortex-A9 MPCore and FPGA fabric. The programmability of both enables the development of a highly programmable SDR, with hardware acceleration and power efficiency optimizations.

## REFERENCES

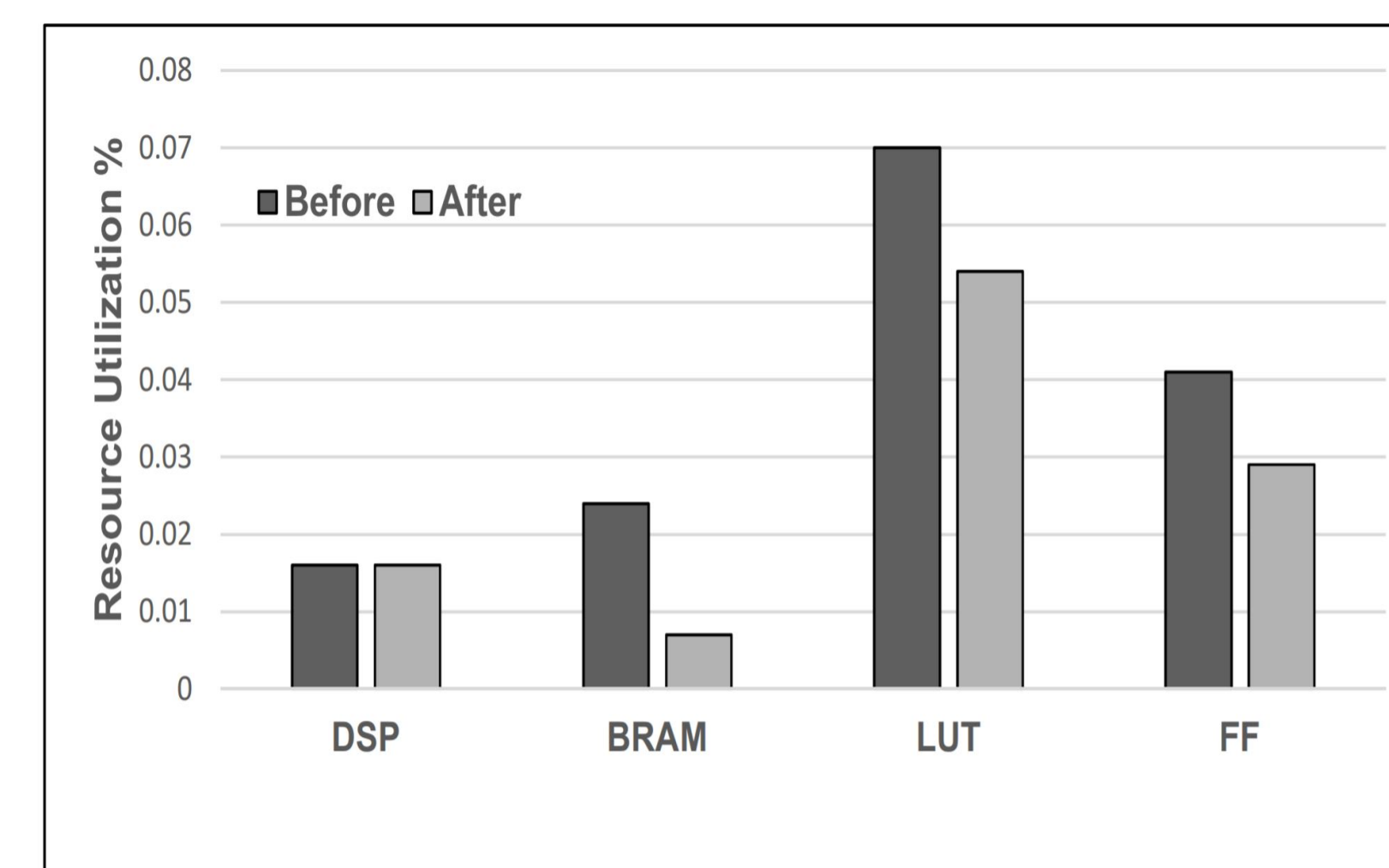
- [1] R. Akeela and B. Dezfouli, "Efficient Co-design Partitioning of IEEE 802.11a Using the Zynq SoC," 2018.
- [2] —, "Software-defined Radio: Architecture, State-of-the-art, and Challenges," *Elsevier Computer Communications*, pp. 106–125, 2018.
- [3] R. Akeela and Y. El Ziq, "Design and Verification of IEEE 802.11ah for IoT and M2M Applications," *2017 IEEE International Conference on Pervasive Computing and Communications Workshops (PerCom Workshops)*, pp. 491–496, Mar 2017.

## INTRODUCTION

WLAN networks like IEEE 802.11n offer faster connections and more simultaneous users. Highly dynamic workloads can be handled under tight, real-time constraints and thus increase reliability. However, baseband algorithms must be massively parallelized and optimized for heterogeneous platforms in order to fulfill all timing and power requirements. Due to the high processing power and high-bandwidth connectivity between the processor and the FPGA, the latency between the processor and the front end can be extremely reduced. Design using both HW and SW-based techniques is commonly referred to as the co-design approach. However, finding the optimal design partition is not trivial proven to be NP-hard.

## RESULTS 2

An FPGA-based SoC implementation of FFT block of the PHY layer of IEEE 802.11a WiFi protocol was demonstrated on ZC706 board.

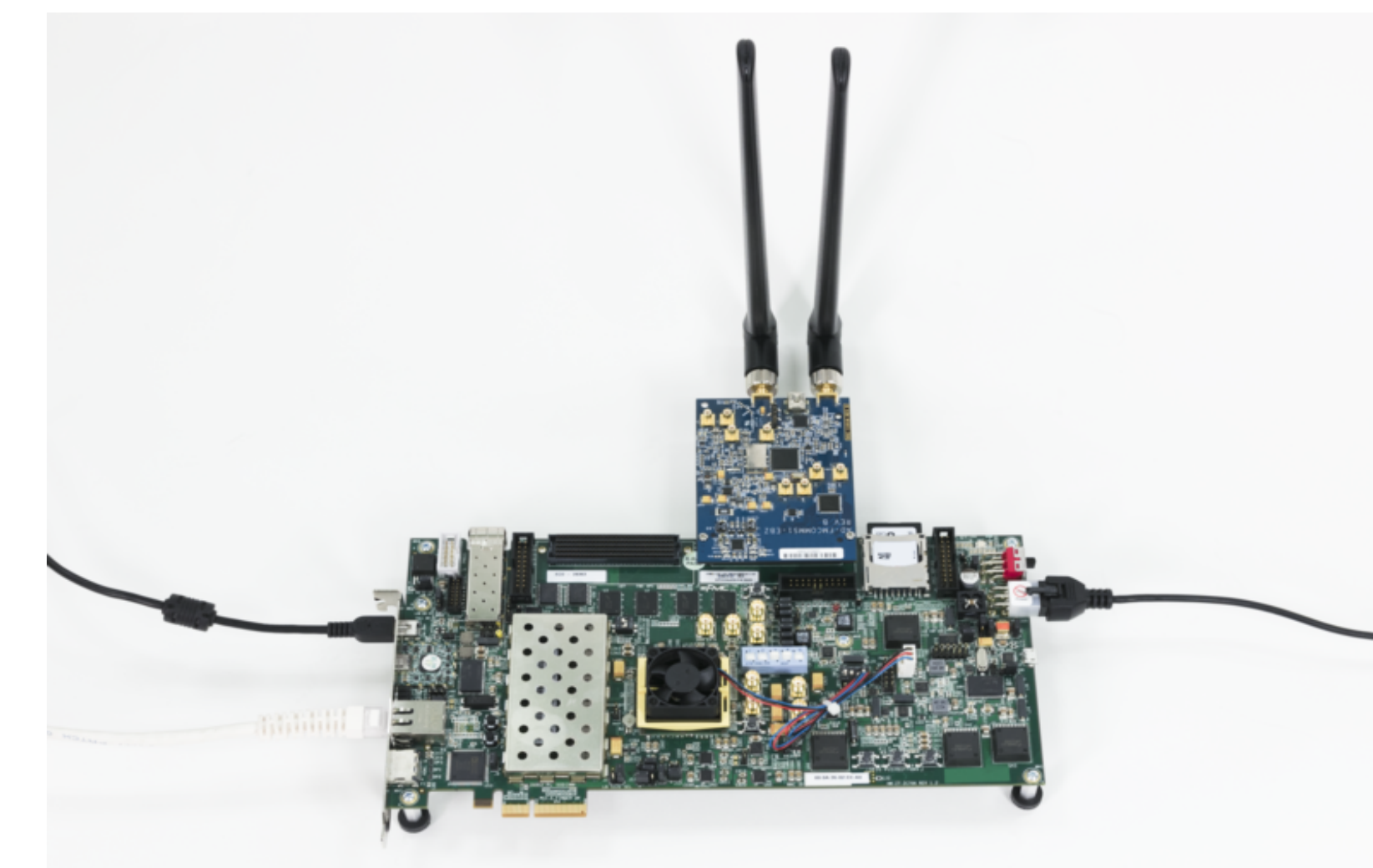


Results show FFT resource utilization estimates for HW functions before and after optimizations. Optimizations aim at increasing parallelism and throughput.

## FUTURE RESEARCH

For future work, memory access overhead will be studied and included in the cost function to fairly assess the partition. A communication cost is the cost of the interface between the hardware and software implementations. This includes the hardware interface area and delay, software driver delay, and

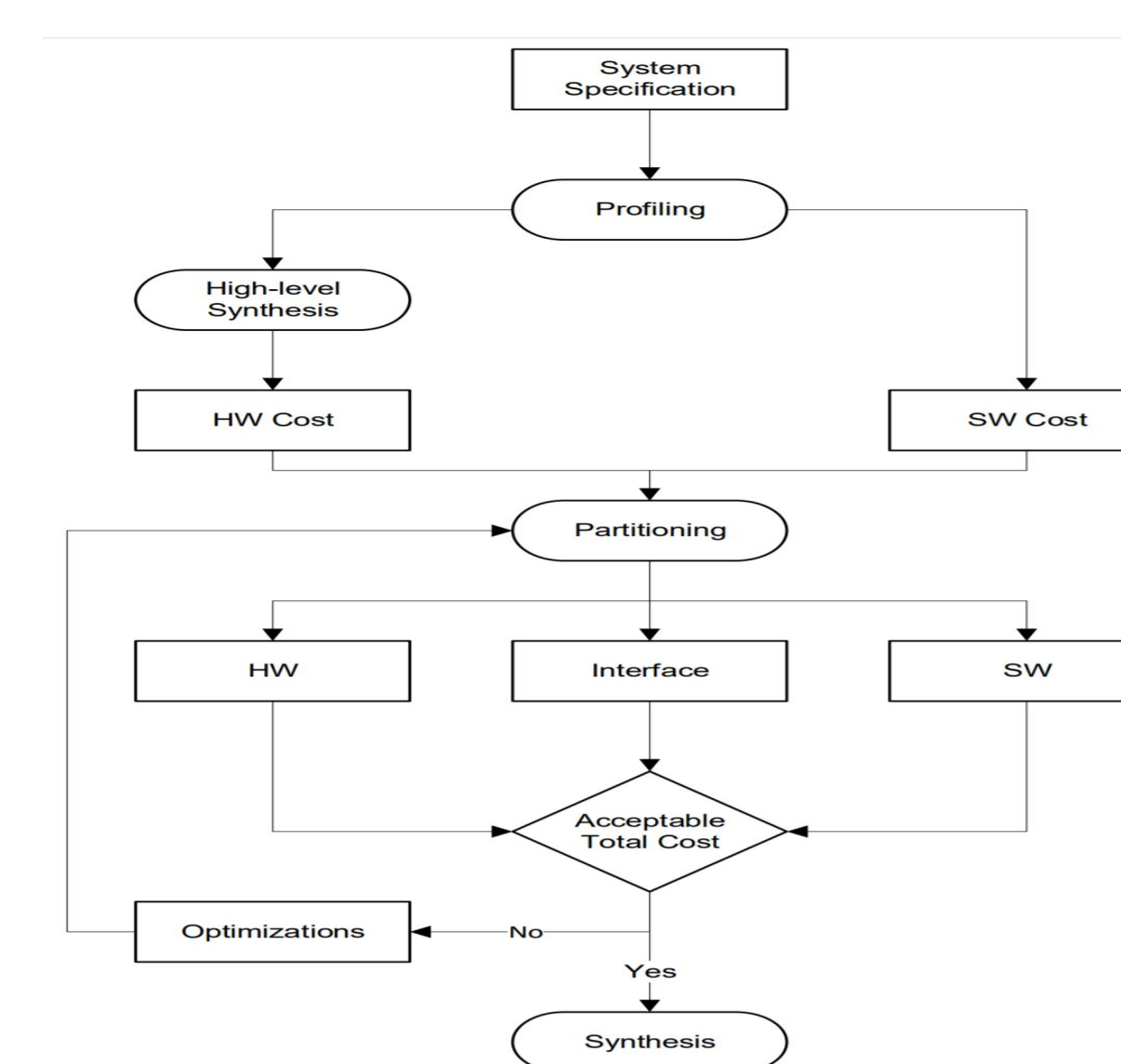
## RESULTS 1



$$Cost = 100 \times \left( \frac{T_{total}}{T_{max}} \times \beta_T + \frac{C_{total}^{SW}}{C_{max}^{SW}} \times \beta_{SW} + \frac{C_{total}^{HW}}{C_{max}^{HW}} \times \beta_{HW} + \frac{P_{total}}{P_{max}} \times \beta_P \right)$$

Component	Hardware Cost $C_{total}^{HW} (10^{-3})$	Software Cost $C_{total}^{SW} (10^{-3})$	Power Consumption $P_{total}^{HW} (mW)$	SW Execution Time $T_{total}^{SW} (ns)$	HW Execution Time $T_{total}^{HW} (ns)$
Scrambler	7.53	2.76	0.3	300.9	18.53
Encoder	8.24	2.77	0.32	600.78	24.31
Decoder	297.3	15.4	5.67	2900.7	91.32
Interleaver	265	16.3	4.21	4200.1	85.56
OFDM(FFT)	282.5	13.2	5.14	4900.8	93.21

## METHODOLOGY & CONCLUSION



- The functions accelerated in the HW/SW Co-Design achieved a speedup of up to 7x in comparison to the original SW-only implementation
- Evidenced by Ettus Research, the trend now is to develop hybrid platforms
- SoC-based SDRs have a better price to performance/Watt over GPP, GPU, and DSP-based
- This work can significantly contribute to the current efforts to develop EDA tools to automatically partition a system efficiently and customize it for a domain-specific application like SDRs

## CONTACT INFORMATION

**Web** [www.cse.scu.edu/~bdezfouli/bd-research.html](http://www.cse.scu.edu/~bdezfouli/bd-research.html)

**Author 1 E-mail** rakeela@scu.edu

**Author 2 E-mail** bdezfouli@scu.edu

shared memory size used to store the data and control. New findings can be compared to the results reported, where the authors showed that their partitioning algorithms are capable of minimizing the latency, area, and execution time without taking into account the communication cost.



# Cost Effective Camera-LIDAR Sensor Object Detection for Autonomous Vehicle Applications

Robert H. Christiansen  
rhchristiansen@scu.edu

Sally L. Wood  
swood@scu.edu

Department of Electrical Engineering

## Objective

- Develop state-of-the-art computer vision algorithms for a cost-effective Camera-LIDAR sensor pair to detect, classify, locate and track dynamic road scene objects for autonomous vehicle applications

## Camera-LIDAR Sensor Pair

- The field test platform fig 1 consists of a Logitech C615 webcam and a LedderTech 16 segment LIDAR module mounted to the roof of the host vehicle.
- The camera provides high density image sensing which the CNN Tensor Flow object detector (fig 2) processes and outputs a frame by frame list of the objects (cars) annotated by bounding boxes, present in the image.  $bb_i = [x_1^i \ y_1^i \ x_2^i \ y_2^i]^T$
- The 2D color camera resolution is set to 1280 x 720, 16:9 FOV
- The LIDAR (Light Detection and Ranging) sparsely covers the area indicated by the white rectangle and subrectangles (segments) shown in figure 4.
- This is the LIDAR FoD (Field of Detection) and the calibrated FoD infers that only objects (bounding boxes) that intersect with this area can be detected. [TOP: 384, BOTTOM: 517, LEFT: 200, RIGHT: 1067, Segment\_Width: 54.17]

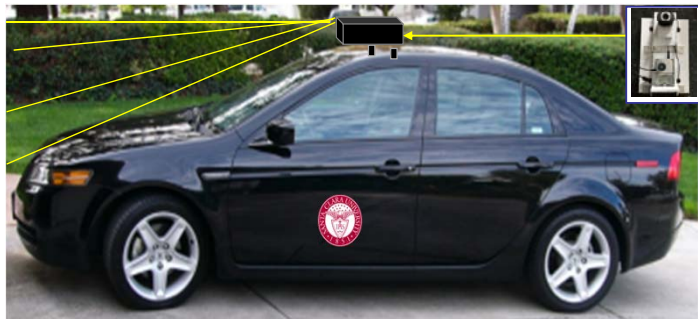


figure 1

## System Block Diagram

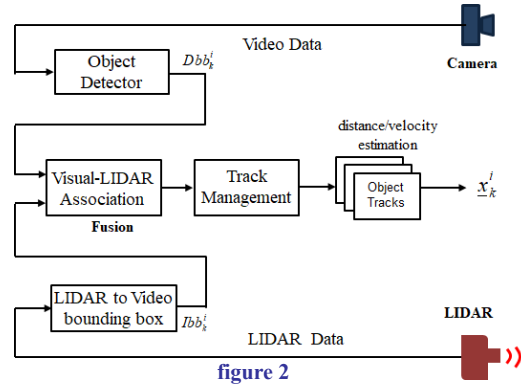


figure 2

## Ideal Bounding Box LIDAR Representation

- The 2D-LIDAR readings,  $L_j(d, s)$ , in polar coordinates :

$$L_j = [d_j \ s_j]^T$$

$d$  : distance (ft)  
 $s$  : segment number

- To associate LIDAR readings with corresponding detections requires projecting LIDAR readings onto the image plane. This is accomplished by converting LIDAR detections to “Ideal (Car)” bounding boxes – an ideal projection based on assuming a target car (mean) width of 5.8 feet, figure 3.

$$(x_2 - x_1) = f \cdot \frac{W_c}{Z} \text{ pxls} \quad f = 900 \text{ pixel} \quad H_c = 6.7 \text{ ft}$$

$$Z = d \cdot \sin \beta$$

$f$  : camera focal length (pxls)

$W_c$  : assumed width car object

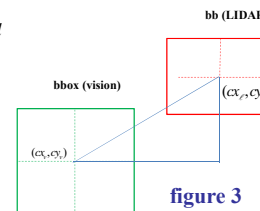


figure 3

## Hungarian Association Algorithm

Association Cost Function

$$c_{ij} = (w^1 \cdot c_{ij}^1) + (w^2 \cdot c_{ij}^2) + (w^3 \cdot c_{ij}^3)$$

$L_2$  NORM : Ideal  $L\_bb$  to car detection  $C\_bb$

$$c_{ij}^1 = \text{cost}[i, j] = \sqrt{(cx_e - cx_v)^2 + (cy_e - cy_v)^2}$$

$y_2$  distance cue: distance estimation based on  $bb_c y_2$

$$Z_{est} = \frac{f}{(y_2 - 240)} H_c \text{ ft.}$$

$$c_{ij}^2 = \text{cost}[i, j] = (d_e - z_v)$$

IOU: Intersection Over Union

$$IOU = \frac{bb_{union}}{bb_{overlapping}}$$

Solve Assignment Matrix

$$\begin{bmatrix} c_{11} & c_{12} & \dots & c_{1j} \\ \vdots & \vdots & \dots & \vdots \\ c_{i1} & c_{i2} & \dots & c_{ij} \end{bmatrix}$$

## Multi-Object Tracking (MOT)

- Kalman filter for tracking objects
  - Prediction of object's future location
  - Correction of the prediction based on new measurements
  - Reduction of noise introduced by inaccurate detections
  - Facilitating the processes of association of multiple objects to their tracks



figure 4

## MOTIVATING APPLICATION

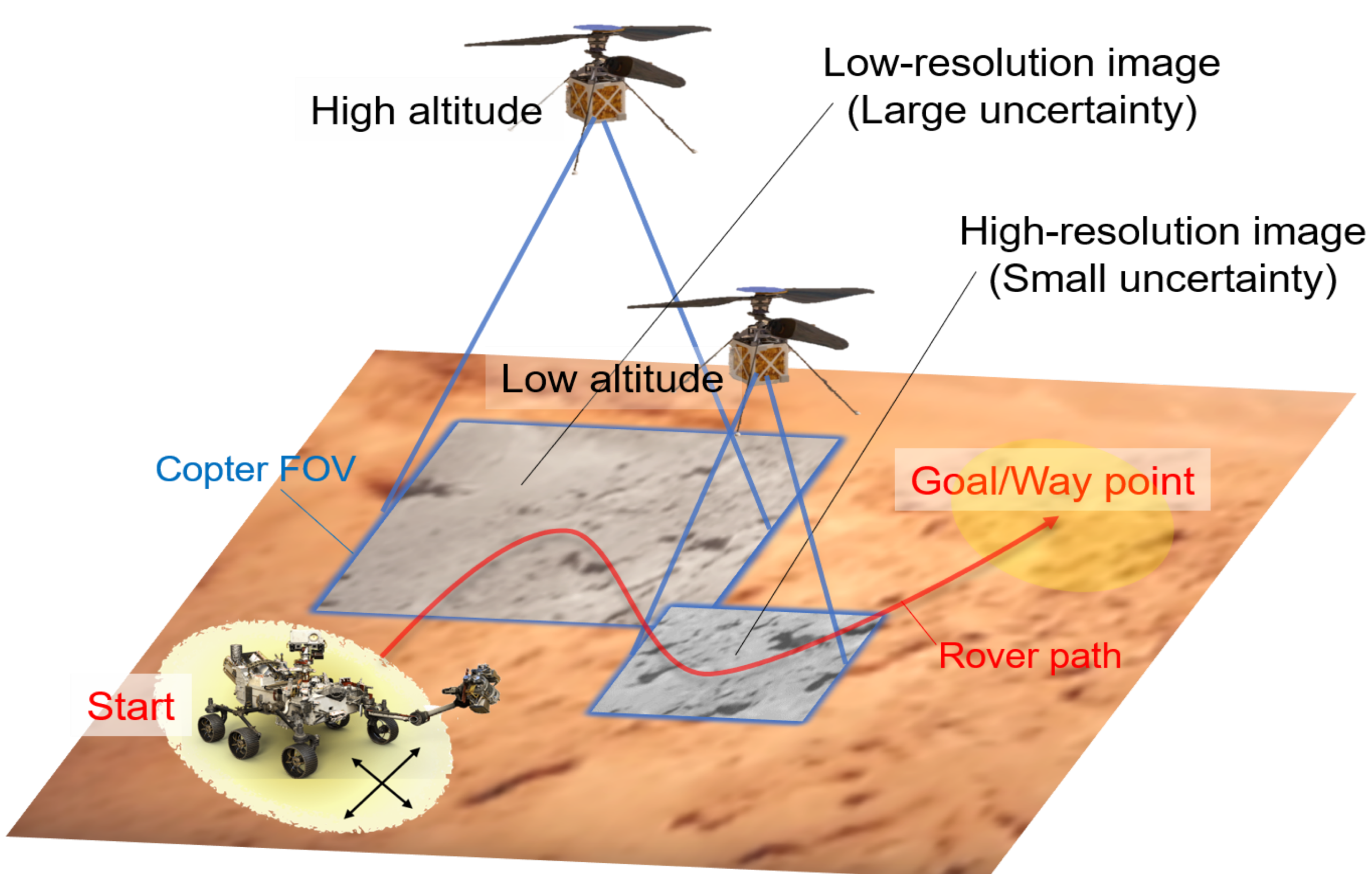


In 2020, NASA will send a rotary-powered aircraft to Mars to

- ✓ Scout the local terrain
- ✓ Create high resolution maps
- ✓ Identify interesting science targets

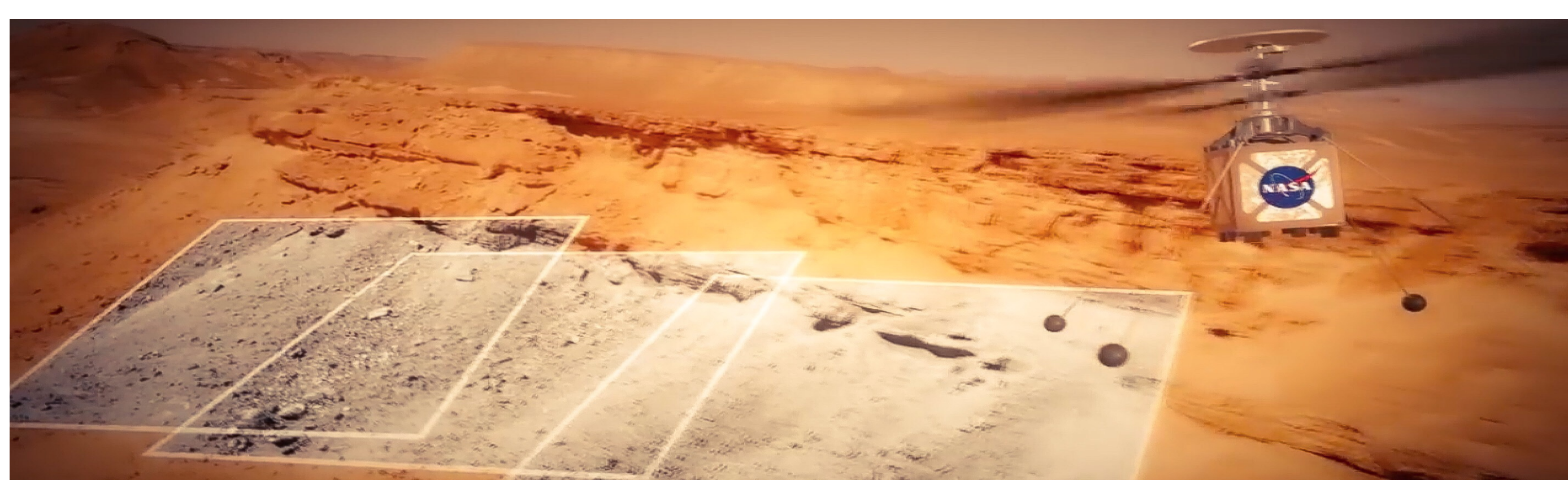
## THE CHALLENGE

- Collaborative localization and mapping for a rover/helicopter team
- Perceptual aliasing and ambiguity in data association
- Perceptually degraded environment

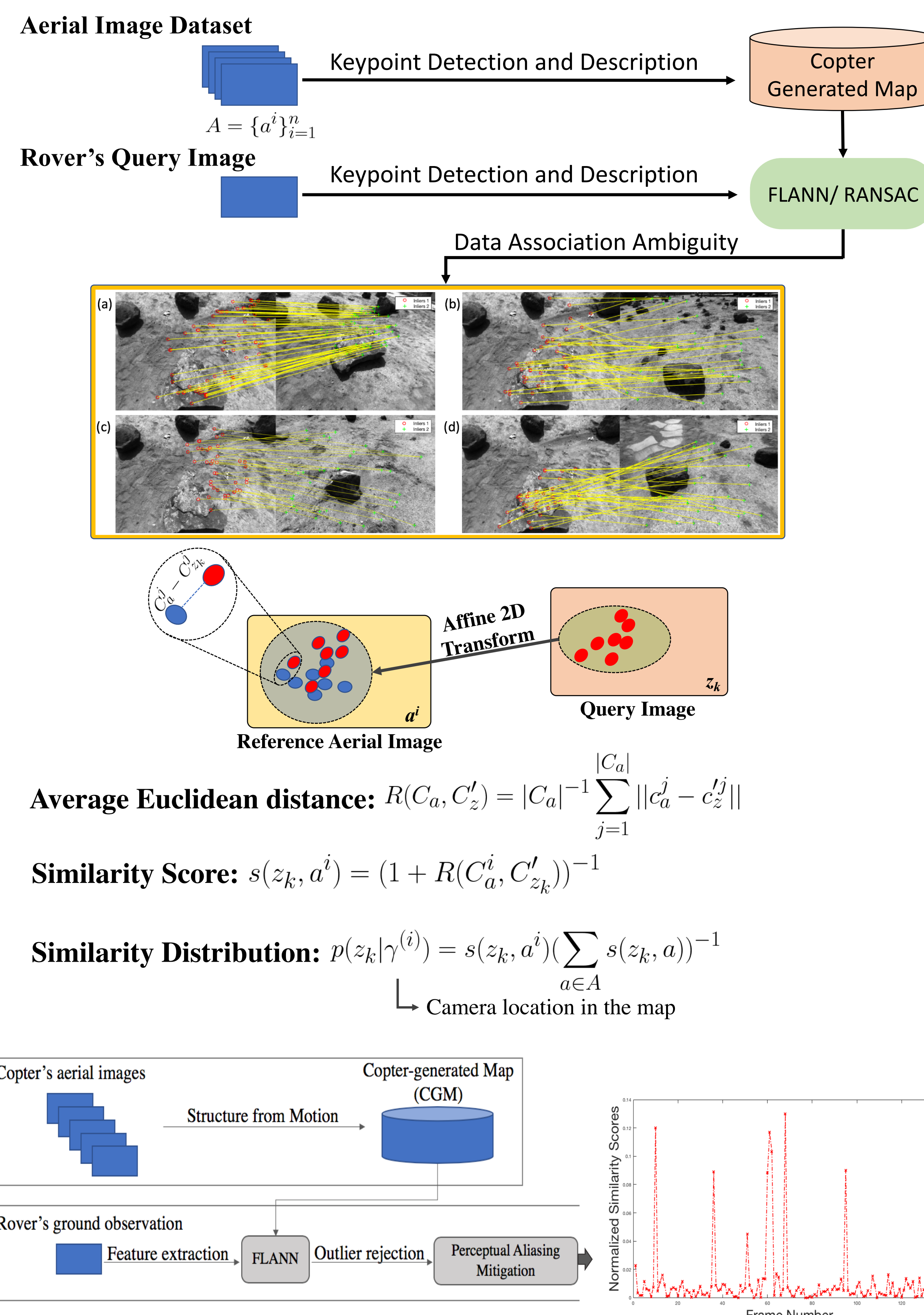


## PROBLEM FORMULATION

- Rover's system dynamics:  $x_{k+1} = f(x_k, u_k, q_k) = x_k + u_k + q_k$
- Rover's 2D location in the map:  $x_k$
- Rover's action at the  $k$ -th time step:  $u_k$
- State dependent process noise:  $q_k \sim \mathcal{N}(0, Q \| u_k \|)$
- Rover's estimated 2D location in the map:  $\hat{x}_k$



## PROPOSED METHOD



## Monte Carlo (Particle Filter) Localization:

### 1- Approximate the belief with a finite set of particles

$$b_k = p(x_k | z_{0:k}) \rightarrow \text{Probability distribution over all possible states of the rover at time } k$$

$$b_k(x) = \sum_{i=1}^n w_k^{(i)} \delta(x - p_k^{(i)}) \cdot s_k = (p_k^{(i)}, w_k^{(i)})_{(i=1:n)}$$

### 2- Prediction Step

$$w_{k+1}^{(i)-} = w_k^{(i)}, p_{k+1}^{(i)-} = f(p_k^{(i)-}, u_k, q_k^{(i)})_{(i=1:n)}, q_k^{(i)} \sim \mathcal{N}(0, Q \| u_k \|)$$

### 3- Importance Weight Update

$$\gamma^{(i)} = \arg \min_{\Gamma} \|p^{(i)} - \gamma\|, i = 1 \dots n \text{ The closest camera location to a particle}$$

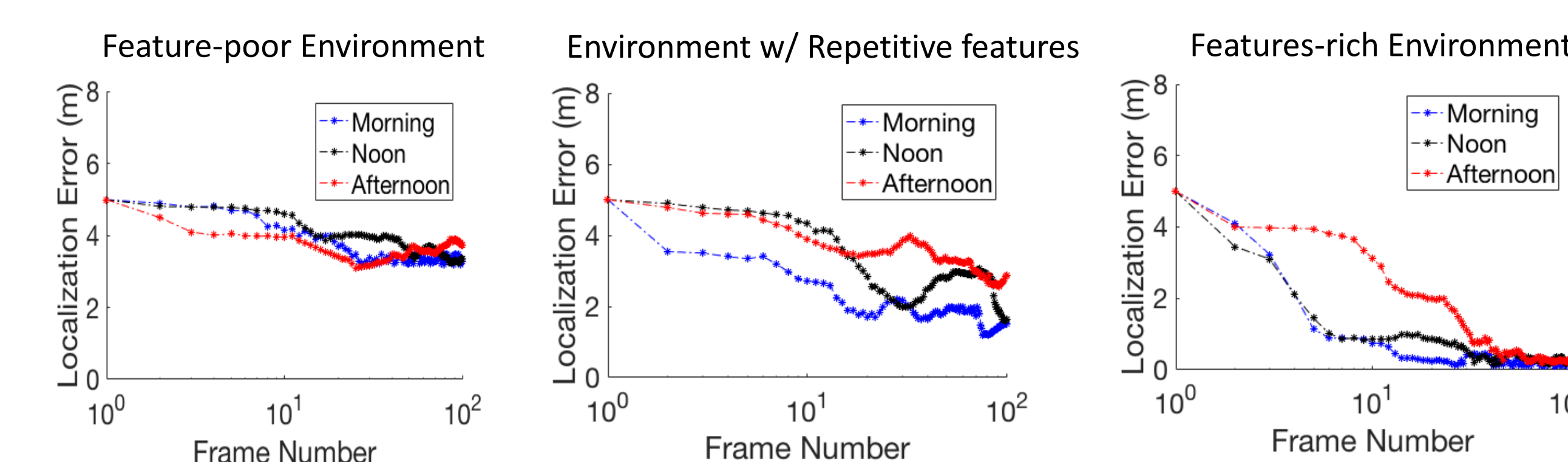
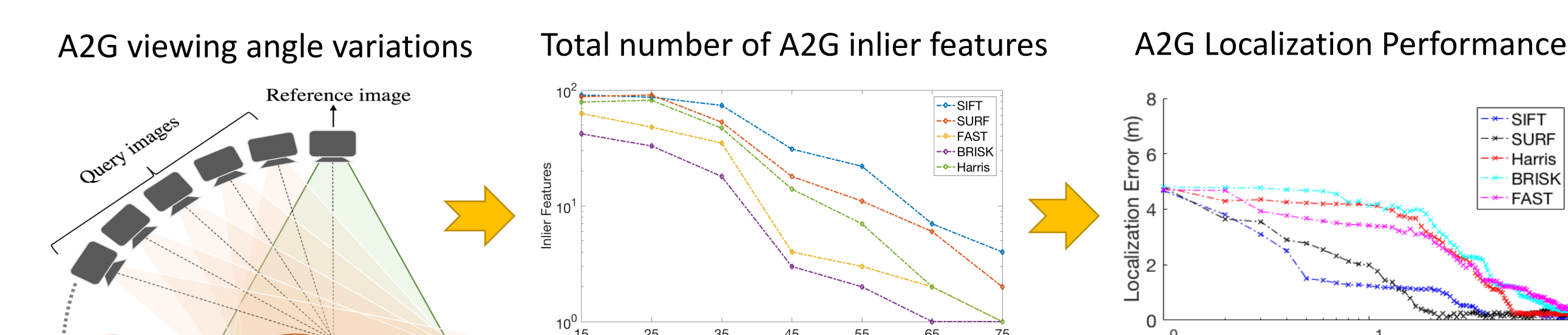
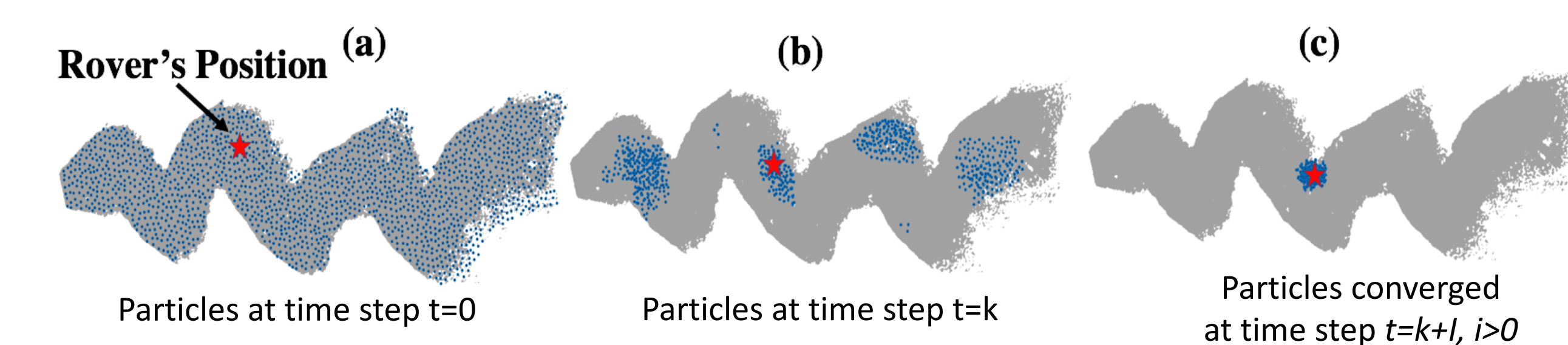
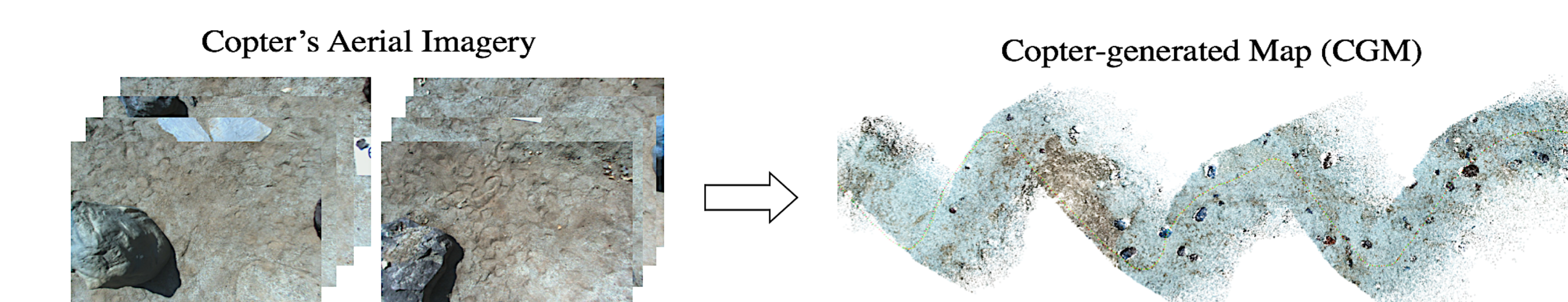
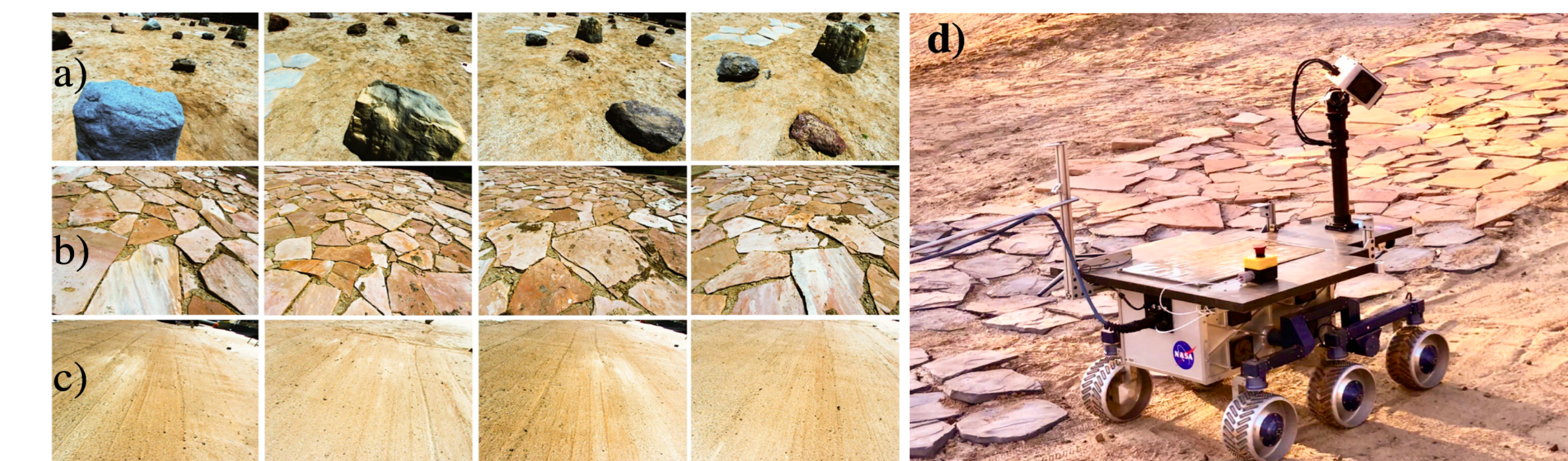
$$\hat{w}_{k+1}^{(i)} = p(z_k | \gamma^{(i)}), \hat{p}_{k+1}^{(i)} = p_{k+1}^{(i)-}, i = 1 \dots n$$

### 4- Importance Resampling

$$w_{k+1}^{(i)} = \hat{w}_{k+1}^{(i)} \left( \sum_{i=1:n} \hat{w}_{k+1}^{(i)} \right)^{-1}, p_{k+1}^{(i)} \sim b_{k+1}(x), i = 1 \dots n$$

## EXPERIMENTAL RESULTS

Athena rover at the Mars Yard at NASA's Jet Propulsion Laboratory:



## CONCLUSION

- We proposed a method based on A2G image similarity evaluation and Bayesian filtering for localization of a Mars rover in the aerial maps generated by a Mars helicopter.
- Various challenges including viewpoint, scale, and illumination variations as well as variations in the sparsity of perceptual features were studied in different terrain types.
- For future work, we are investigating the multi-agent graph-based methods for collaborative mapping in unstructured and Mars-like environments with a team of rover and helicopter.

## ACKNOWLEDGEMENT

This research has been carried out at NASA Jet Propulsion Laboratory, California Institute of Technology, under a contract with the National Aeronautics and Space Administration.

# Image Content Identification from CNNs with Sparse Sampling

Allen Rush, Sally Wood

Dept. of Electrical Engineering



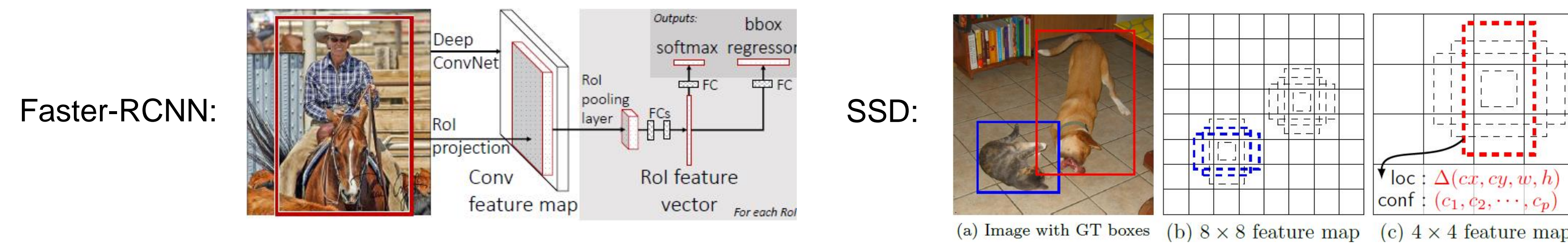
**Motivation:** Object detection in complex images can take either complex models or many passes of a regions-based FOV approach. We aim to find regions of interest whose location and size correspond to high probability object detection.

**Problem statement:** Need to find the top  $n$  objects in an image corresponding to their prior probabilities that they would be detected as an image in a dedicated FOV. Moreover, we want to determine a minimum number of regions or ROIs that are accurate for location and size for each object. In addition, we want to use a relatively simple CNN pre-trained network

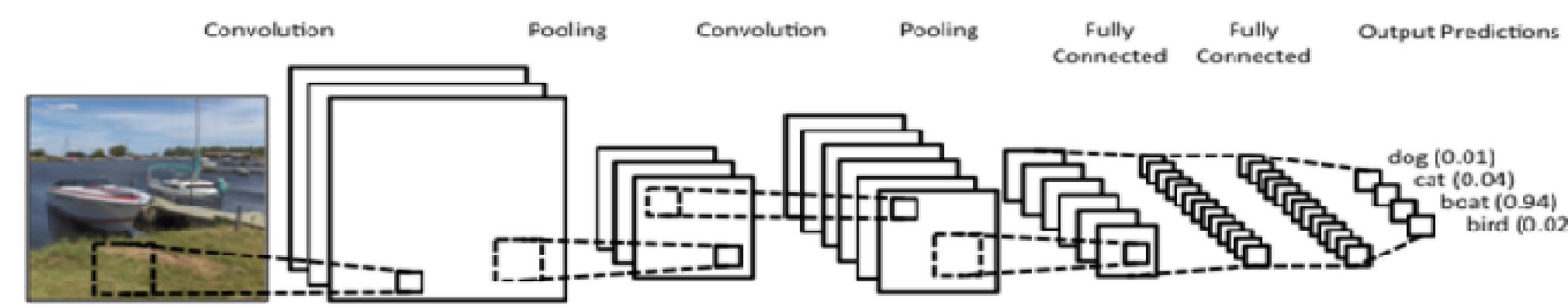
**Approach:** Since random images have no prior information regarding objects, we search for guiding information in the trained network. By examining the output of the first layer of the network, we can estimate the strength and location of the top  $n$  objects in the image.

**Prior work:**

- Fast/Faster-RCNN (Girshick): Finds candidate regions of interest by examining last layer of feature map
- SSD: Single-Shot Multi-Box Detector (Liu et al): uses additional scaled feature maps and multi-box training



Typical CNN Structure: VGG16/19



In this work, we generate region proposals by examining the output of the first convolutional layer of a CNN. It has substantially less structural information about the final object, but concentrations of feature map energy are indicators of possible object detections that get further enhanced with the downstream convolutions and feature maps.

Proposals are generated by one of two approaches:

- Initial candidate locations are determined by sorting the first layer outputs and selecting the top  $n$  and defining a dilation constant for growing the local mask for the ROI. The proposal ROI is applied as a mask to the original image, and the resulting test image is processed to determine the classification output. When the classification is a) correct and b) high enough confidence (e.g. > 50%), then the dilation stops.
- Initial candidate locations are determined by identifying a cluster of feature map locations that exceed a certain threshold. Small masks are defined with these locations as the center of the mask. The test image is sampled by the collection of these "mini-samples" to build a sparse representation of the entire FOV. The resulting sparse sampled image is evaluated as the entire FOV. The process is iterated by lowering the threshold and increasing the number of non-zero sample blobs that define the sparse sampled image. The iteration stops when the confidence of the detected object reaches an arbitrary level (>50% to have high confidence).

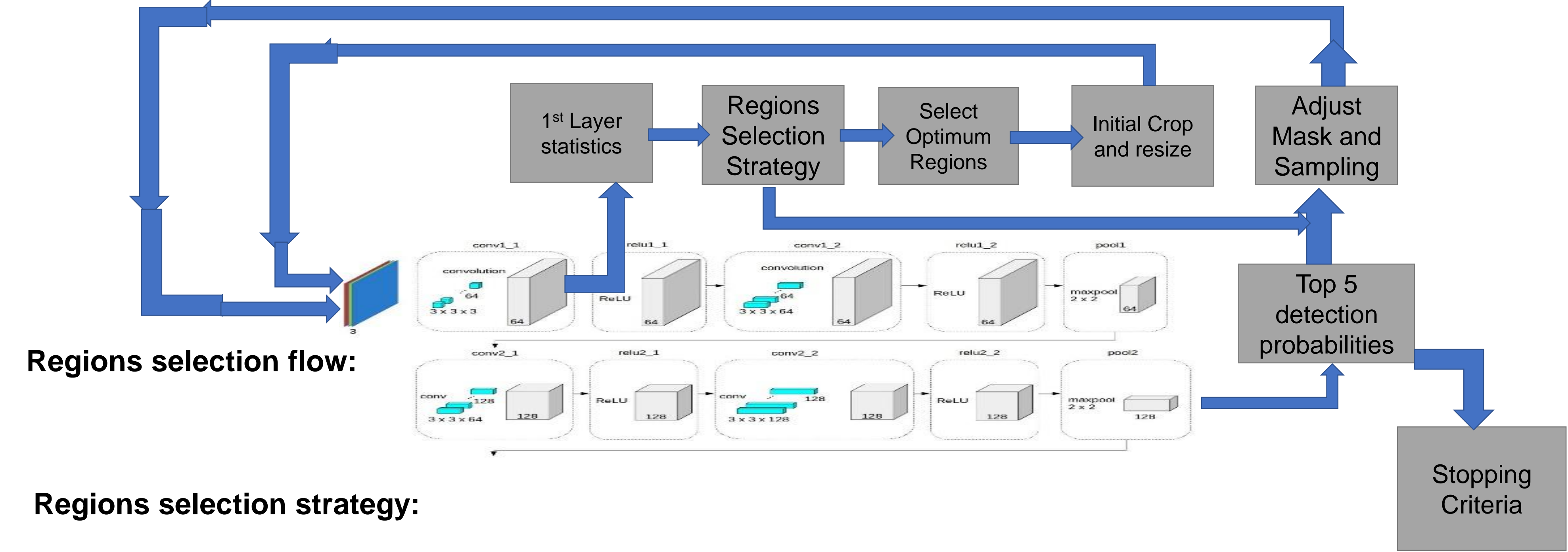
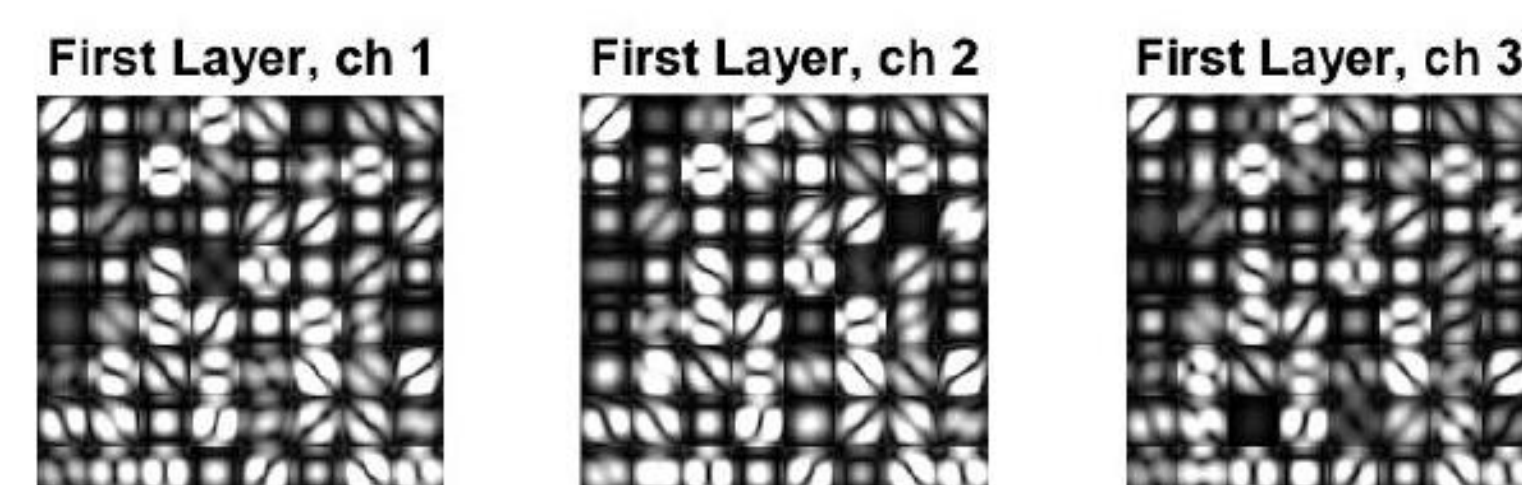
This approach can minimize the number of region proposals in several aspects:

- The number of proposals or the sizes can be limited to some arbitrary threshold based on the statistics of the first level output feature map energy
- The rate of mask generation or size (2<sup>nd</sup> approach) can be controlled by a parameter: a low number will take longer to converge, but the resulting size will be close to optimal;

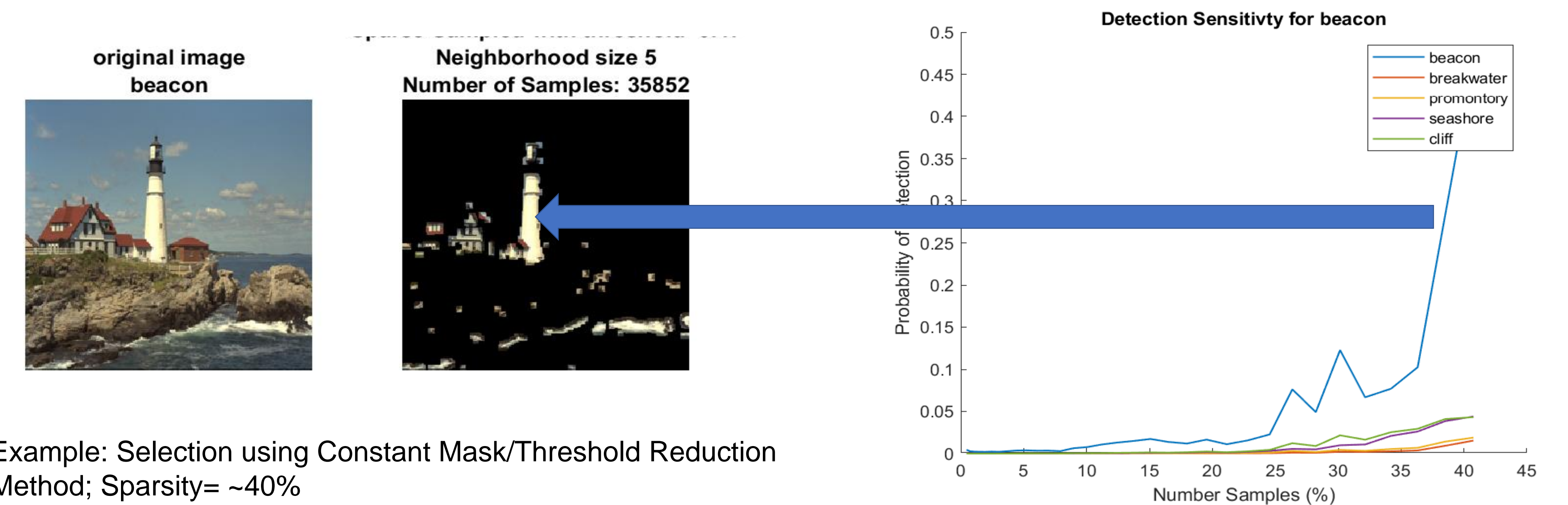
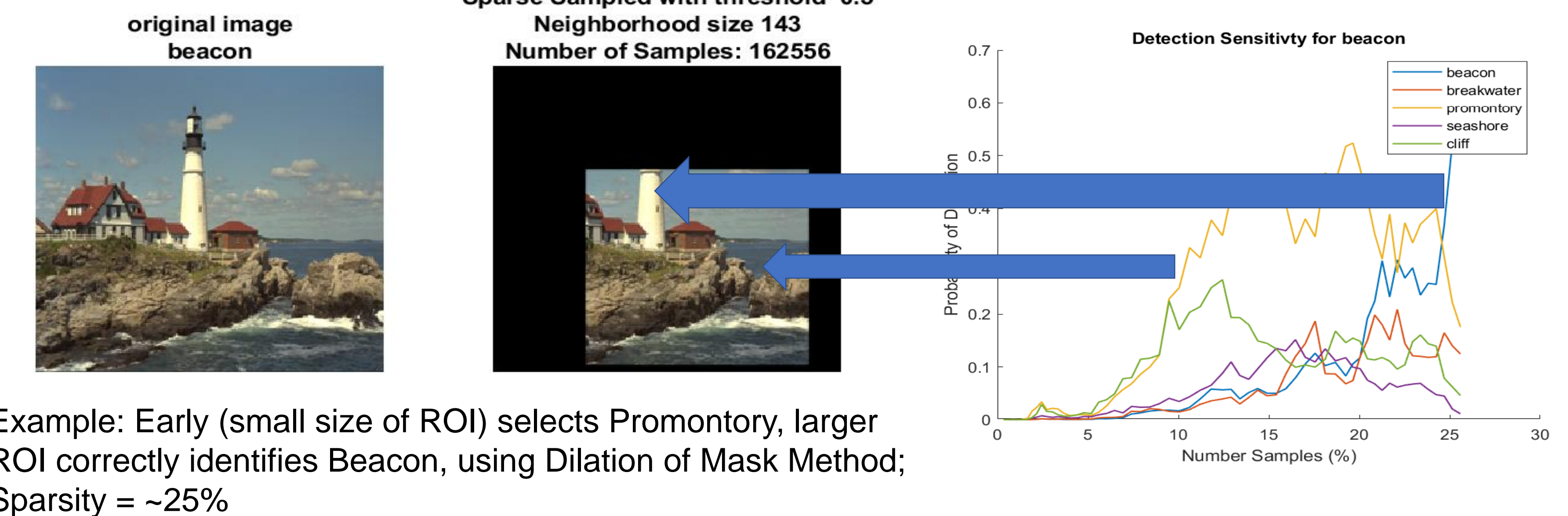
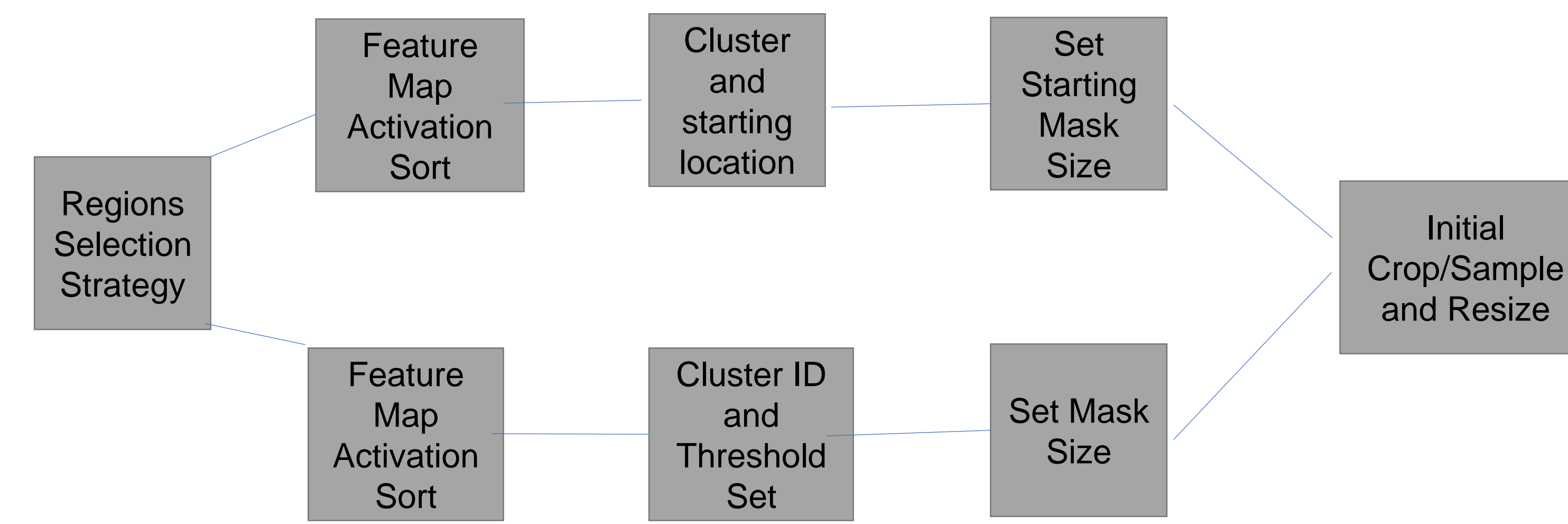
For Convolution (2-D):  

$$I_c(x, y) = \sum_{k=-n}^n \sum_{l=-m}^m I(x-k, y-l) h(k, l)$$

First layer convolutions: spectral response:



Regions selection strategy:



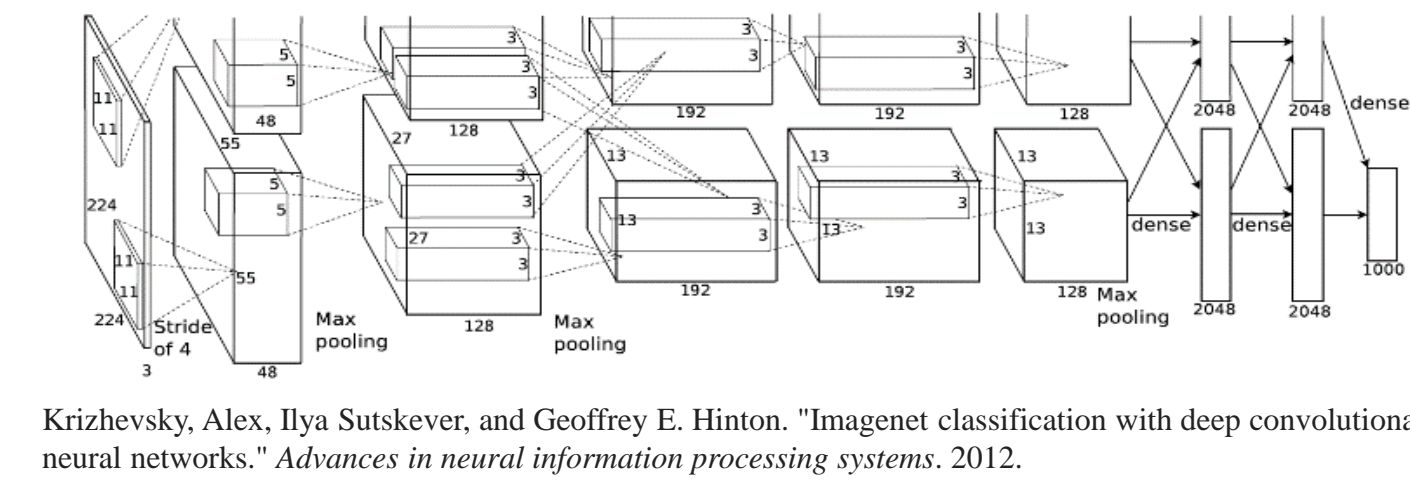
## Implications

For the single mask dilation strategy, need to find the most likely starting location in order to minimize the number and size of dilation steps	For small ROIs, need to find most likely center of object to cluster collection of ROIs to grow a sparse sample space for the object
For the constant mask size/threshold reduction strategy, need to find mask size that minimizes the number of threshold reduction steps	For compound objects, need to sort high confidence detections with clusters of ROIs
For large ROIs, on the order of 8-16 non-overlapping crops of the original image, need to make sure the size is sufficient to overcome secondary objects	

## ABSTRACT

Convolutional Neural Networks (CNN) have changed the direction of image and speech signal processing. They have become prolific in applications such as self driving cars and voice assistants like Siri and Alexa. Since the success of AlexNet, many deep learning networks like GoogleNet, ResidualNet, etc., have been introduced. These networks are highly competent in image classification however, they are very large in size and have a lot of parameters, for example, AlexNet has 60M parameters. On-Chip data transfer is a great engineering challenge that needs to be addressed while implementing CNN in hardware. Hardware Acceleration and parallelization are constrained by energy cost of reading and writing data from memory. For one forward pass during inference, one image needs to go through to all the CNN layers and be classified into a softmax determined category. During this process, the memory bandwidth is used by three types of payloads that need to be moved on and off-chip - input image, intermediate feature maps, and filter weights. This research is focused on reducing weight-related memory traffic that occurs between off-chip memory and on-chip buffers. In this paper, we propose a technique named 'weight sharing selective transfer' (WS-ST) that uses processing-in-memory architecture to selectively transfer weights from the DRAM memory structure to the computation unit. We observe a 30% decrease in memory transfer traffic compared to a non-selective approach for AlexNet. We achieve this by implementing a selector logic in the DRAM itself. This logic helps us select the weights that need to be updated and avoid the transfer if the weight value is the same.

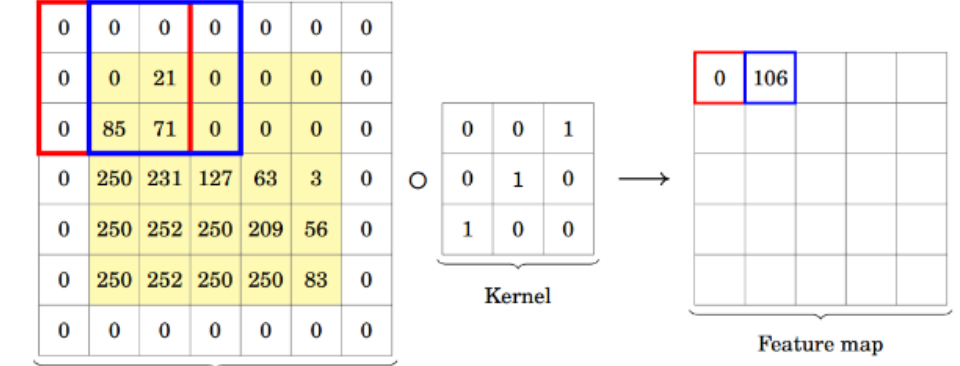
## INTRODUCTION



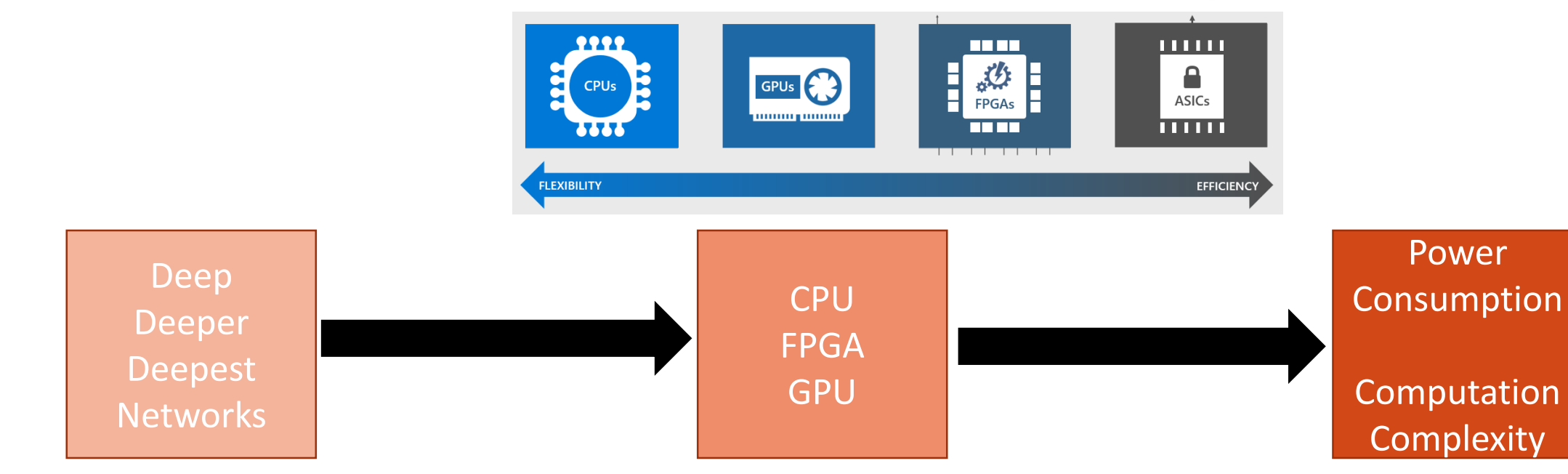
ENERGY COST OF DRAM ACCESS COMPARED TO OTHER OPERATIONS

Operation	Energy (pJ)	Relative Cost
32 bit int ADD	0.1	1
32 bit float ADD	0.9	9
32 bit int MULT	3.1	31
32 bit float MULT	3.7	37
128 bit SRAM	5	50
32 bit DRAM	640	6400

Han, Song, et al. "EIE: efficient inference engine on compressed deep neural network." *Computer Architecture (ISCA), 2016 ACM/IEEE 43rd Annual International Symposium on*. IEEE, 2016.



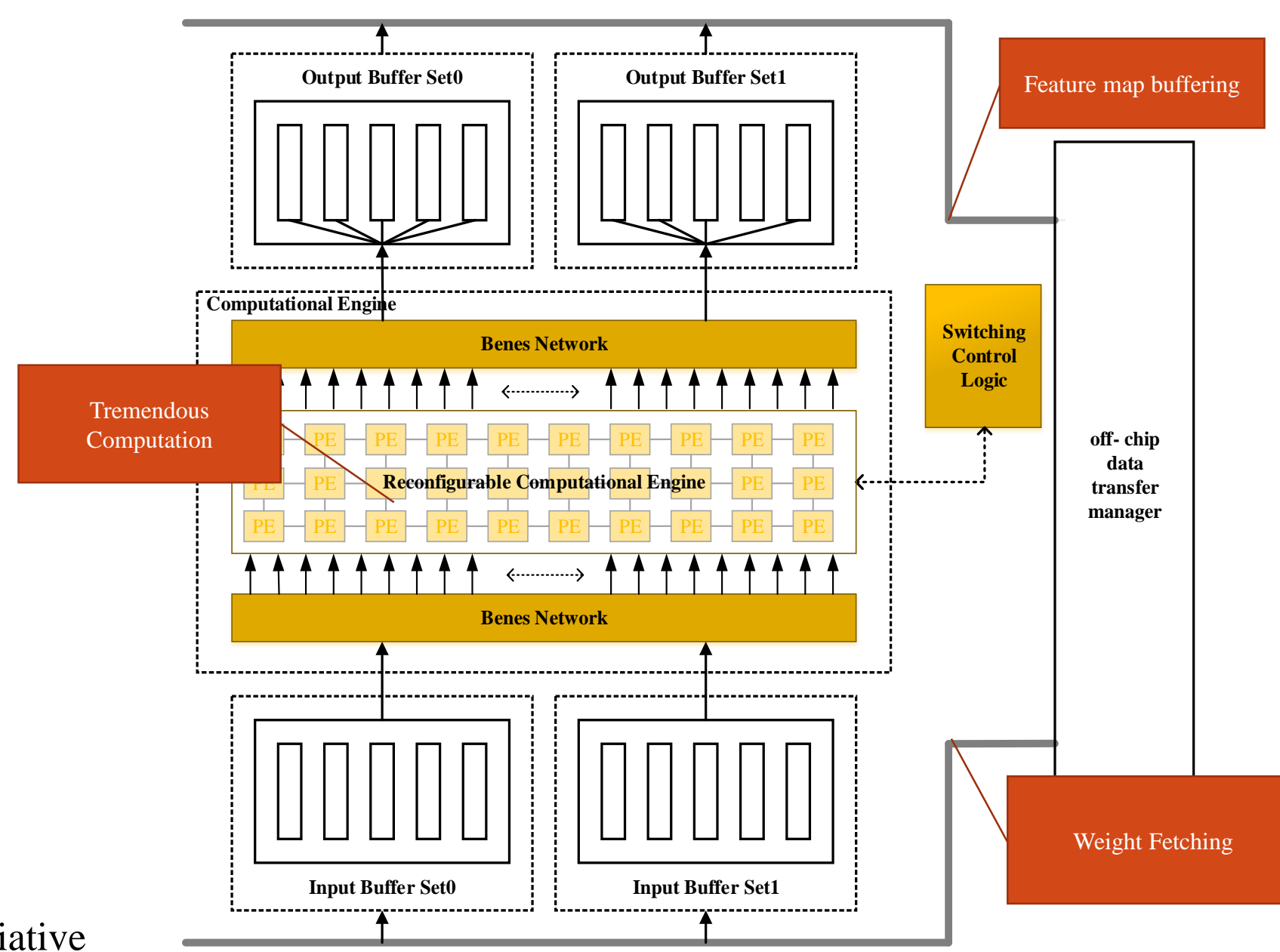
Segedy, Christian, et al. "Going deeper with convolutions." *Proceedings of the IEEE conference on computer vision and pattern recognition*, 2015.



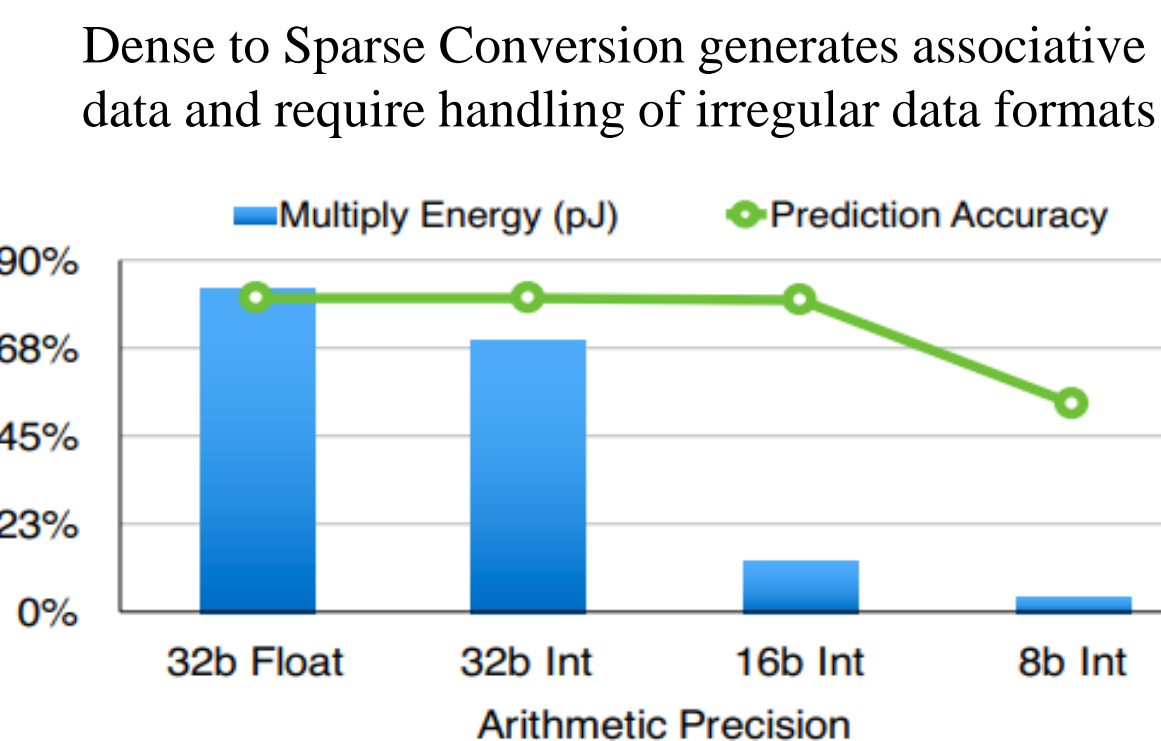
Networks get deeper → Hardware plays catchup → Power and computation challenges get renewed

## CHALLENGES AND MOTIVATION

- Weight Fetching/ Feature Map buffering from off-chip memory.
- Large scale calculation required
- Latency issues
- Power consumptions constraints while performing inference on embedded solutions



Dense to Sparse Conversion  
 val = [ 8 7 3 2 ]  
 col\_ind = [ 3 3 1 2 ]  
 row\_ptr = [ 1 2 3 ]



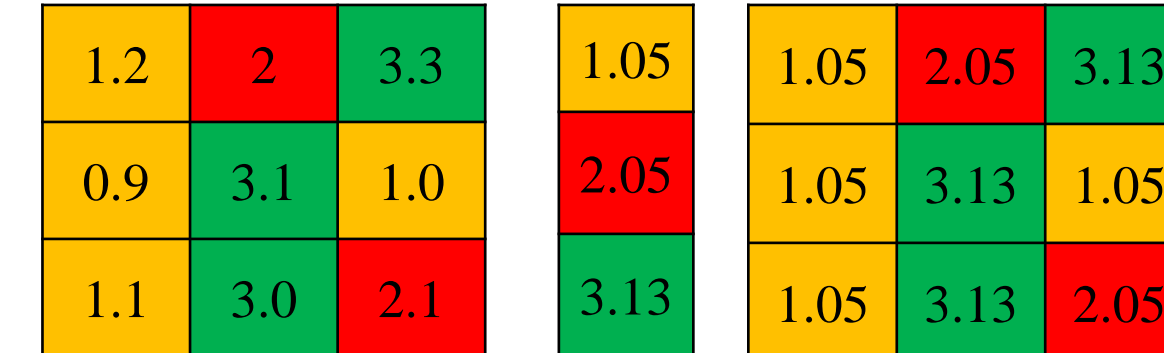
Challenges to implement Deep Learning inference

Quantization – decreases the accuracy if exploited without checks

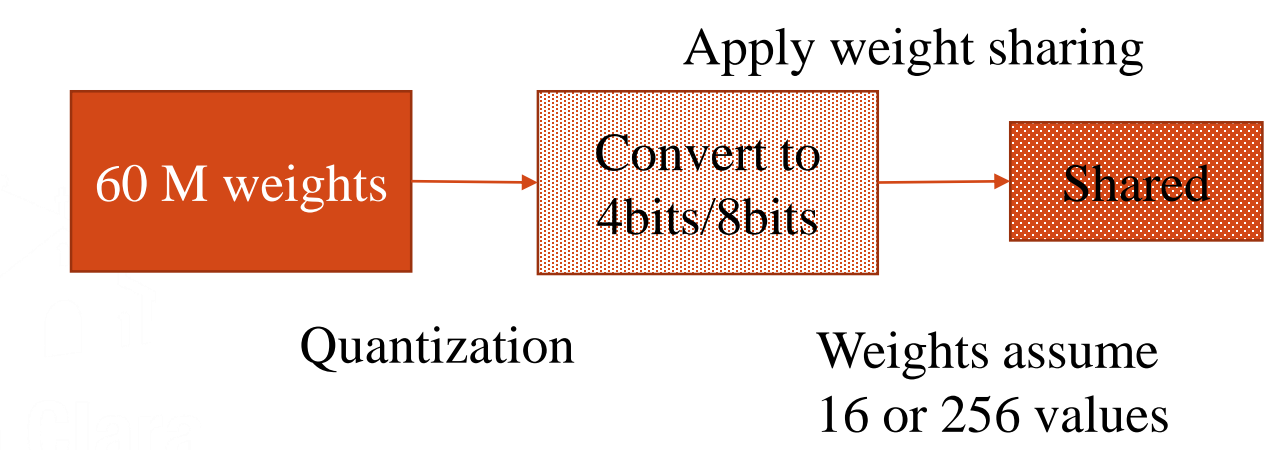
Han, Song, et al. "EIE: efficient inference engine on compressed deep neural network." *Computer Architecture (ISCA), 2016 ACM/IEEE 43rd Annual International Symposium on*. IEEE, 2016.

## WEIGHT SHARING

- Weight sharing is a pruning technique to combat overfitting
- Reduces the number of weights
- Strategic value from an algorithmic and engineering point of view

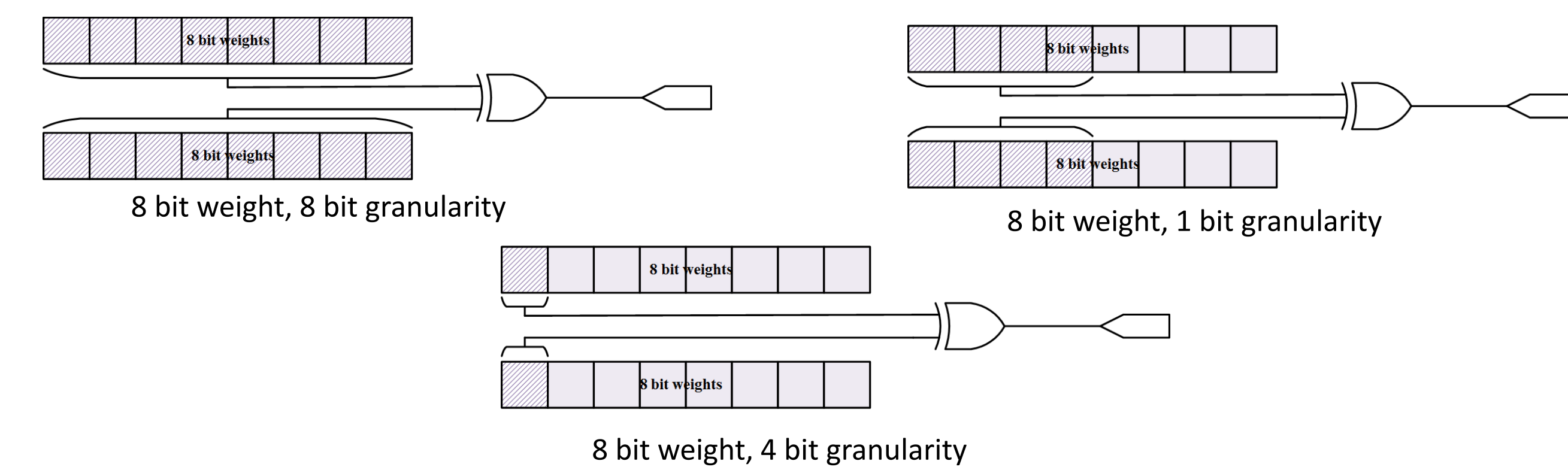
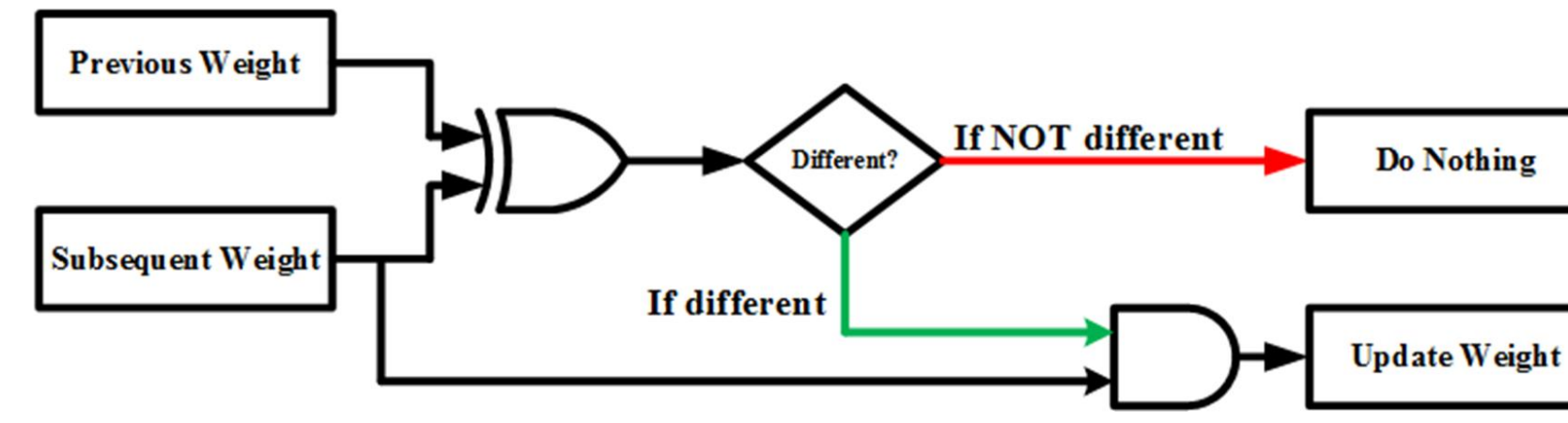


- We convert the weights to a 4 bit precision and 8 bit precision
- This gives us 16 and 256 weight values respectively
- Once the 16 and 256 weights are shared among all the layers (Convolutional and Fully connected layers) we implement the selection process



## SELECTIVE PASS-THROUGH

- Redundancy analysis is performed on different levels of granularity.
- Granularity is defined as the group of bits we consider for comparing in a N bit weight.



## REDUNDANCY ANALYSIS

### Matlab Analysis

The analysis process is as follows

- Comparing 4 bit weights for 16 shared weights at the granularity level of 4 bits
- Comparing 4 bit weights for 16 shared weights at the granularity level of 1 bit
- Comparing 8 bit weights for 256 shared weights at the granularity level of 8 bits
- Comparing 8 bit weights for 256 shared weights at the granularity level of 1 bit

REDUNDANCY ANALYSIS FOR 4 BIT WEIGHTS WITH 4 BIT GRANULARITY

Layer	height	width	c	kernels	total weights	selective weights	difference	% Improvement
conv1	11	11	3	96	34848	23092	11756	33.74
conv2	5	5	48	256	307200	97045	210155	68.41
conv3	3	3	256	384	884736	446751	437985	49.50
conv4	3	3	192	384	663552	312345	351207	52.93
conv5	3	3	192	256	442368	239363	203005	45.89
fc1	4096	9216	1	1	37748736	25618179	12130557	32.14
fc2	4096	4096	1	1	16777216	11661838	5115378	30.49
fc3	1000	4096	1	1	4096000	4096000	0	0
total					60954656	42494613	18460043	30.28

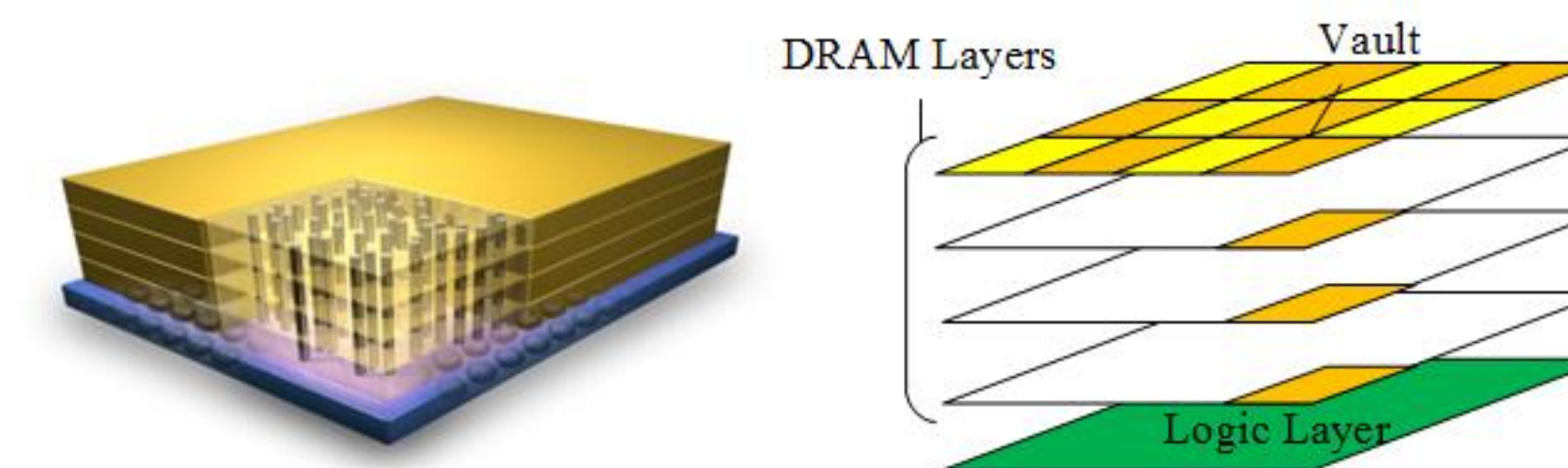
$$\text{difference} = \text{total weights} - \text{selective weights}$$

$$\% \text{ improvement} = \frac{\text{difference} \times 100}{\text{total weights}}$$

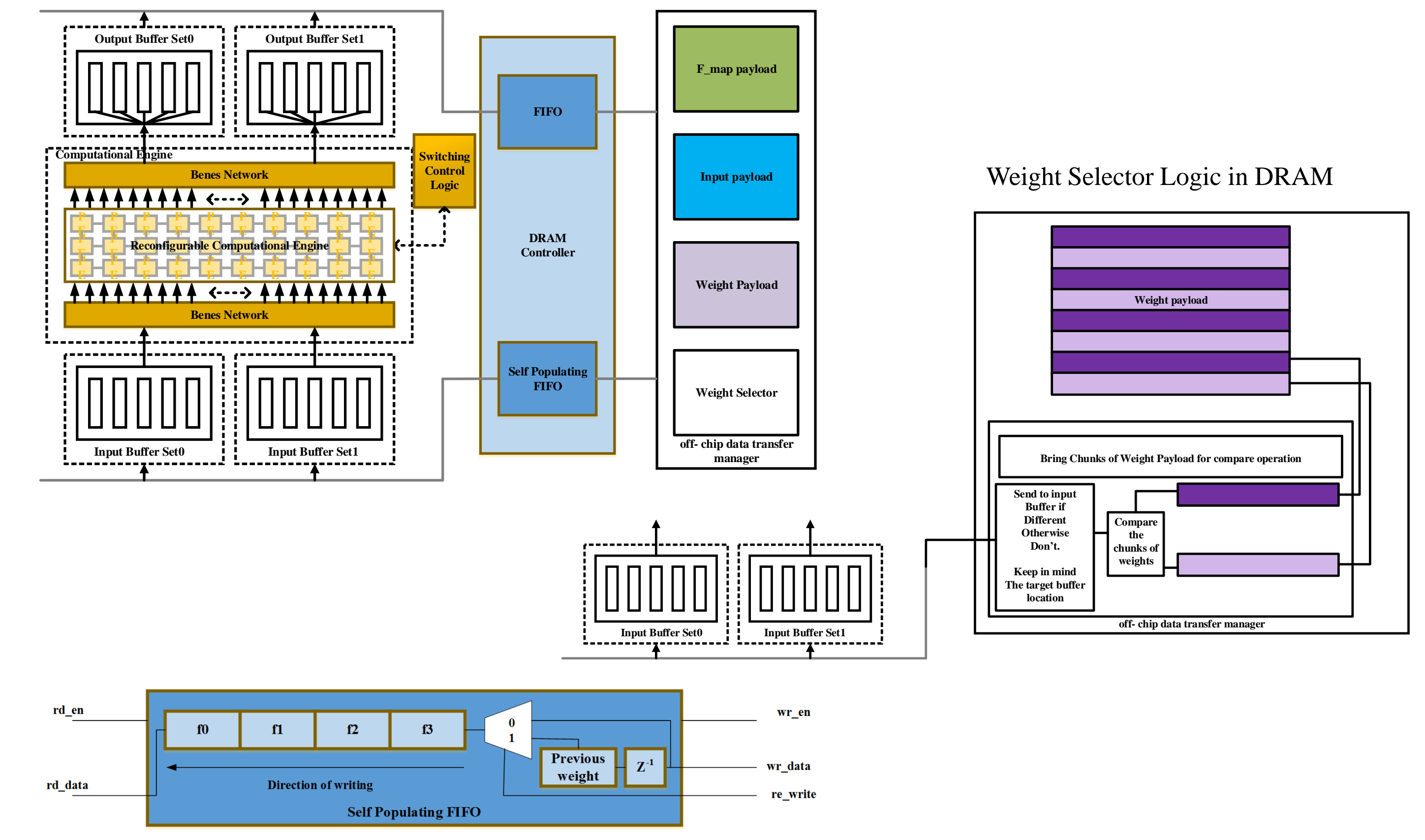
## PROCESSING IN MEMORY

- Processing in memory or near data processing is done in a stacked DRAM
- Each slice of DRAM is connected to each other with through silicon vias (TSVs).
- The DRAM is divided into smaller subsections called vaults.
- Each vertical vault is connected through and through, all the way to the logic layer. We implement the weight selector in the logic layer of the stacked DRAM.

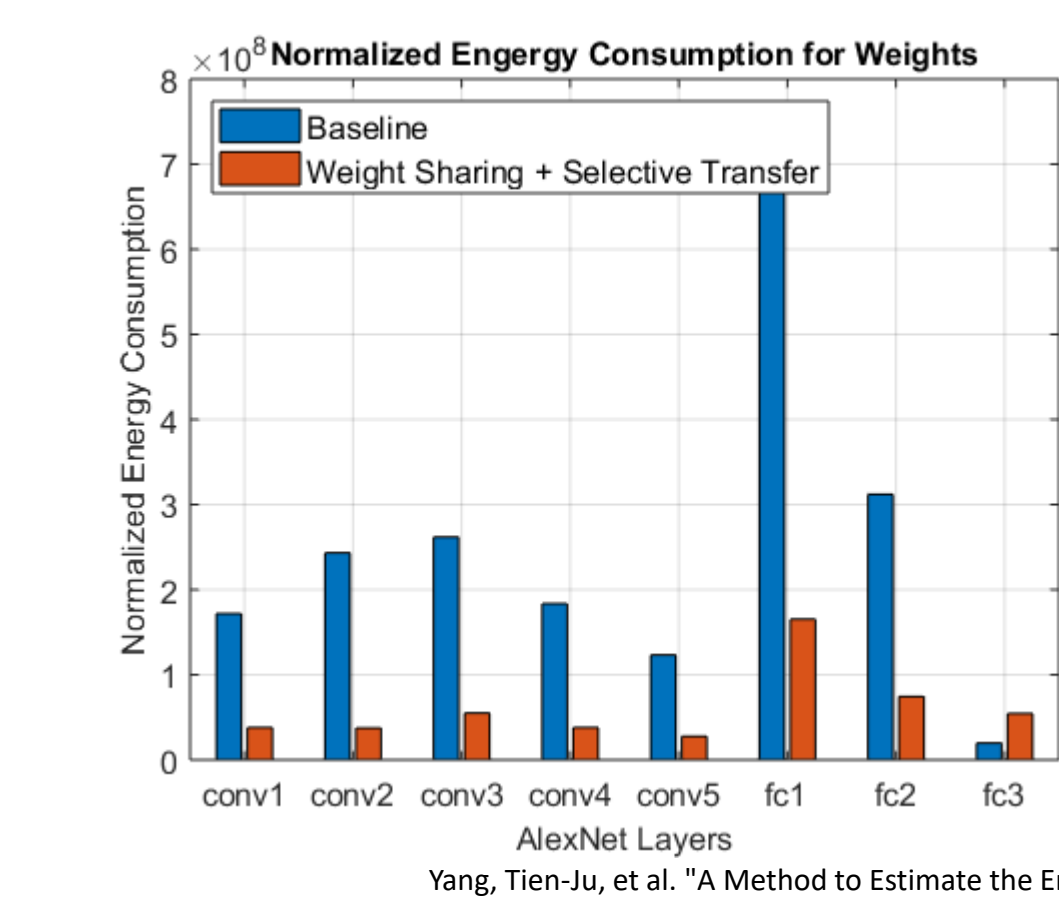
### HMC model



## WEIGHT SELECTOR & SELF POPULATING FIFO



## POWER ESTIMATION



- online tool by [Yang, Tien-Ju, et al.] to estimate the energy consumption of DNN implementations using both computation and memory transfer cost
- The values are normalized with respect to the energy cost of performing a MAC operation.
- We used the tool to estimate the energy consumption of the baseline AlexNet and the weight-sharing selective transfer AlexNet (WS-ST AlexNet).

## RESULTS

DYNAMIC POWER (DP) AND STATIC POWER (SP) FOR BASELINE ALEXNET AND WS-ST ALEXNET IN WATTS

Layer	Baseline		Selective		% Improvements	
	DP (W)	SP (W)	DP (W)	SP (W)	DP	SP
conv1	2.40	0.26	2.33	0.26	2.75	0.00
conv2	2.40	0.26	2.33	0.26	2.75	0.00
conv3	3.51	0.28	3.43	0.28	2.17	0.36
conv4	4.62	0.30	4.55	0.29	1.45	0.34
conv5	3.56	0.28	3.59	0.28	-0.87	-0.36

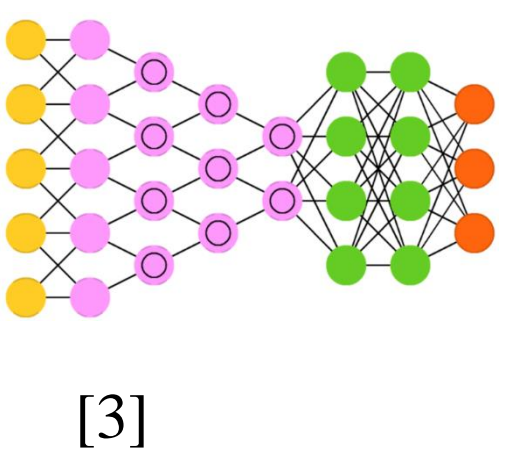
LOGIC AND IO POWER FOR BASELINE ALEXNET AND WS-ST ALEXNET IN WATTS

Layer	Baseline		Selective		% Improvements	
	IO (W)	Logic (W)	IO (W)	Logic (W)	IO	Logic
conv1	1.788	0.016	1.684	0.031	5.82	0
conv2	1.788	0.016	1.684	0.031	5.82	0
conv3	1.844	0.164	1.749	0.163	5.15	0
conv4	1.844	0.178	1.749	0.193	5.15	0
conv5	1.69	0.104	1.602	0.128	5.21	0

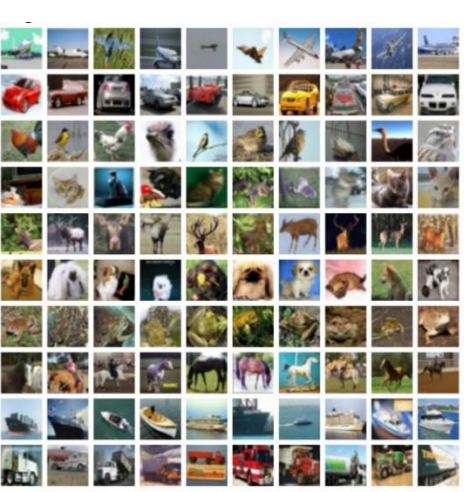
## CONCLUSIONS AND FUTURE WORK

- We achieve a 30% reduction in the memory transfer of weights and 2% saving in dynamic power due to weights for AlexNet
- Similar reduction could be observed in other popular networks
- The fully connected layers really raise the energy consumption of the device, thus we will be required to formulate a new technique to store the fully connected layer parameters
- In order to have a symmetry in architecture, we will also need to implement a selection scheme on the output of the CNN layers
- This will help us improve the offload data write and read to the main memory
- Thus contributing to the overall of reduction in memory transfer traffic and, consequently, a reduction in energy consumption

## Introduction



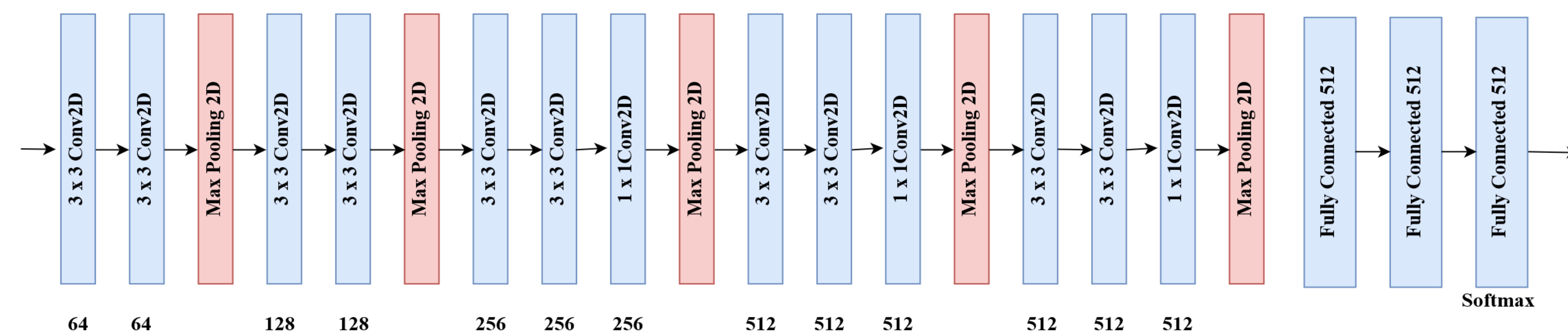
- Agriculture has been identified as one of the pathways to achieve the Zero hunger goal of the United Nation's Sustainable Development Goal. [1].
- Pests are one of the most significant factors affecting agricultural yield.
- Ineffective pest management leads to losses.
- Deep learning is a subset of AI which has become popular in recent years to perform tasks like image classification and speech recognition.
- Convolutional Neural Networks (CNNs) are the most widely used architectures for image classification and can be used to identify pests in images.
- We analyzed the effects of dataset size on CNN accuracy for image classification tasks.**
- We trained VGG16, ResNet and Inception CNNs with CIFAR10, CIFAR100 and a small custom image dataset. These datasets consist of 32x32 color images [4].
- Our results show that larger training data leads to higher classification accuracy. We plan to test this technology using a large agricultural pests dataset and deploy it for farmers in rural communities in India.**



Dataset	No. of Training images	No. of classes	No. of Images per class
Custom dataset	1,000	10	100
CIFAR10	50,000	10	5,000
CIFAR100	50,000	100	500

## CNN Architectures

- VGG16 consists of a number of convolution layers and Max Pooling layers followed by 3 fully connected layers. We reduced the size of the last 3 fully connected layers in VGG16 from 4096 to 512 [5].
- We used the ResNet18 configuration in our study. ResNet 18 stacks 6 blocks of 3 Convolution layers, the first and third layer in each block are connected by a "Shortcut" connection [6].
- The Inception architecture used in our study has 6 Inception modules. An Inception module performs 1x1, 3x3 and 5x5 convolution in parallel and concatenates the results [7].

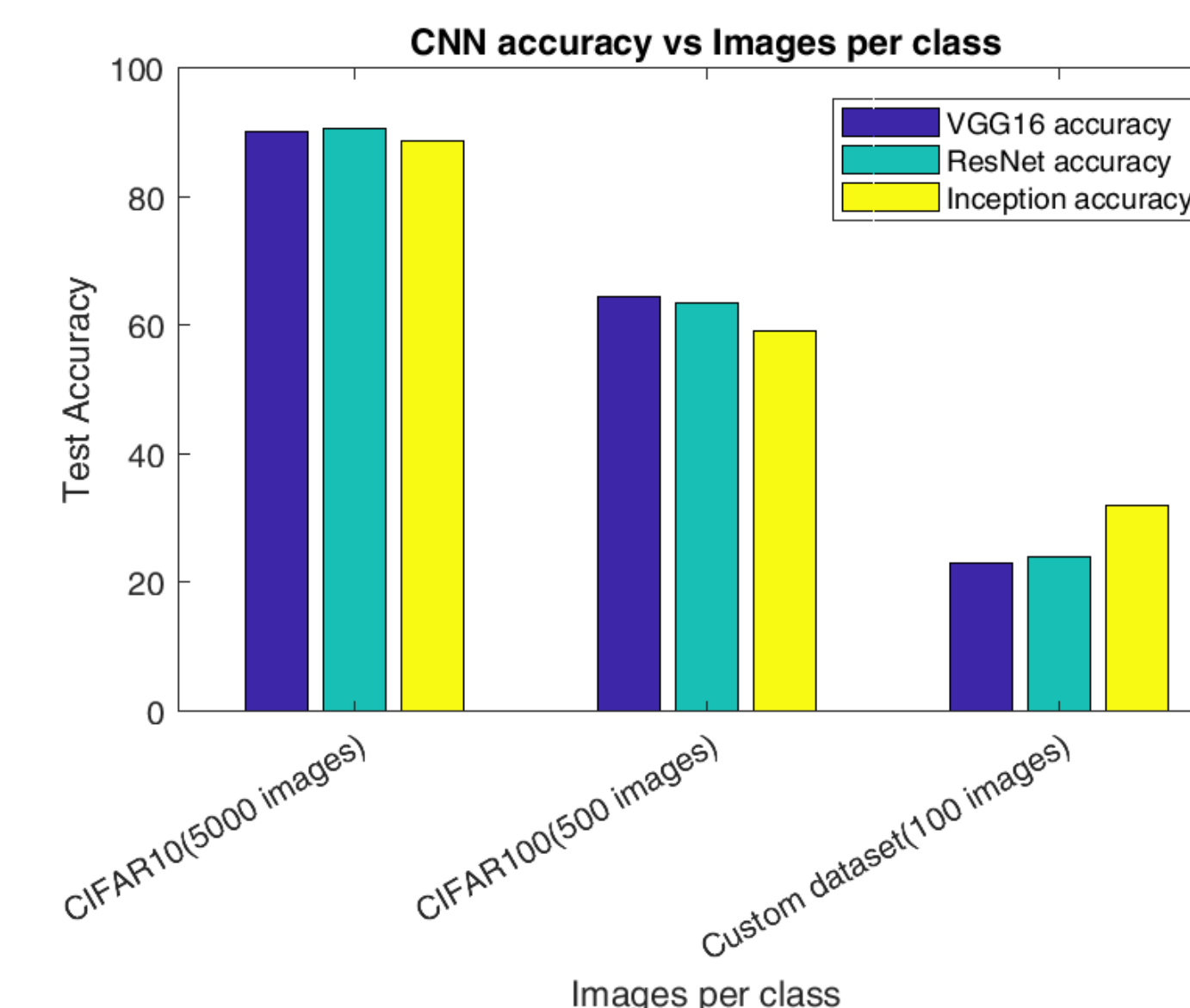


VGG16 Architecture used in the study

## Implementation & Results

- We implemented our CNNs using Keras with Tensorflow backend. The training was carried out on 8 core Intel Xeon CPU and Nvidia Tesla K80 GPU platforms.

CNN Architecture	Custom dataset accuracy	CIFAR100 accuracy	CIFAR10 accuracy
VGG16	23.00%	64.49%	90.17%
ResNet	24.00%	63.36%	90.64%
Inception	32.00%	58.99%	88.70%

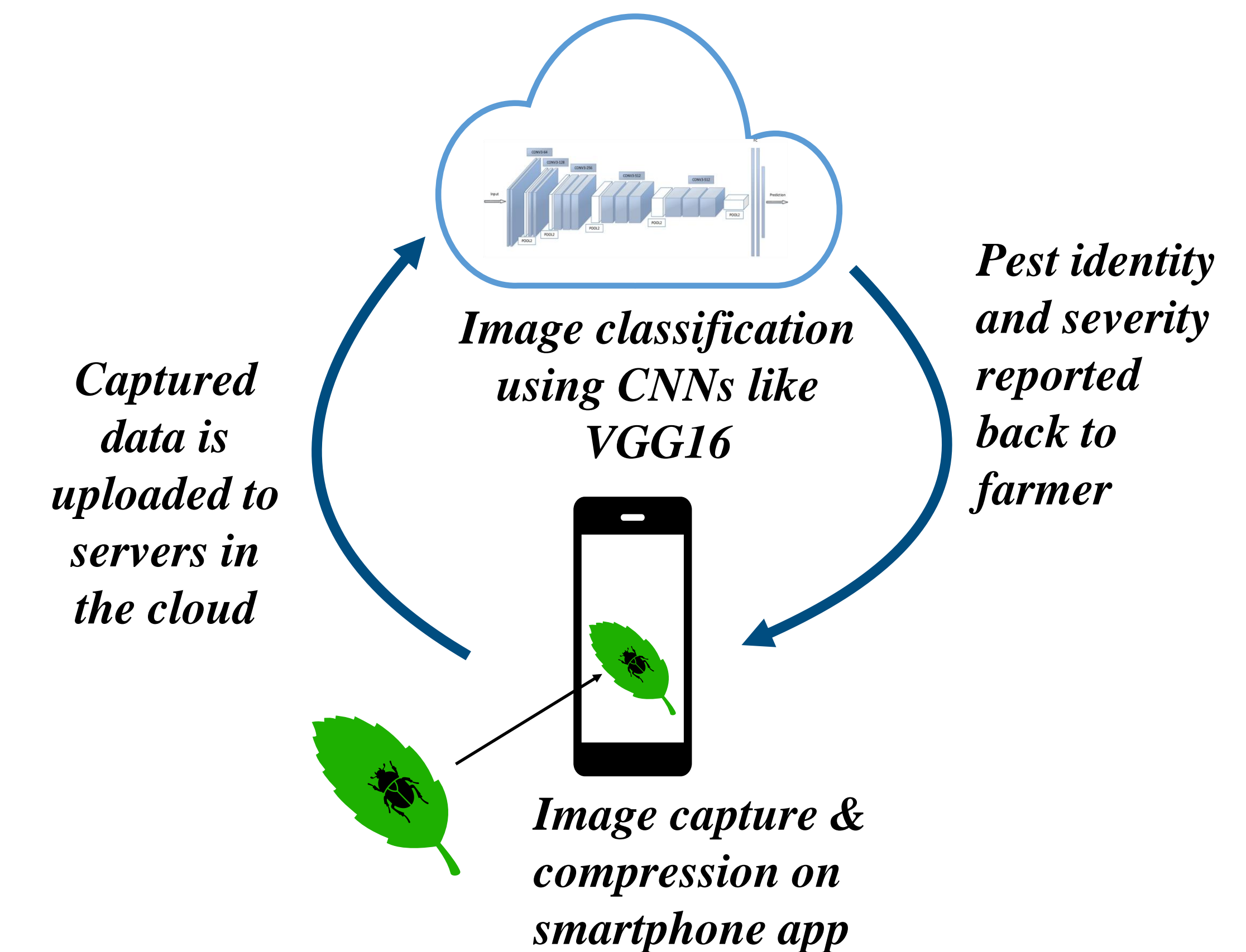


- Transfer learning is an effective method to train Deep Neural Networks to overcome the deficit of training data by adapting pre-trained classifiers. We carried out transfer learning on VGG16 trained on ImageNet datasets to build a pest image classifier.
- We collated a dataset with images belonging to four pest classes – Caterpillar (285 images), Japanese Beetle (341 images), Locust (220 images) and Weevil (415 images).
- We retrained the last fully connected layer of VGG16 on this pest image dataset and achieved an accuracy of 79.70%.**

## Conclusion & Future Work

- Larger the dataset, more accurate the identification.** We plan to collaborate with farmers and agricultural research institutes in India to create a large dataset of pest images. With more data, the classification model will achieve higher accuracy.

- We aim to develop a mobile application to identify pests, their severity and prescribe remedies.



Mobile application workflow

- When a crop is infected, the farmer would click a picture of the pest and pest infected crop using the app.
- The app would then compress and upload the images to the cloud servers. The cloud servers equipped with powerful GPUs would classify the images using CNN retrained using pest images.
- Following which, depending on the pest type and severity, the app would suggest the prescribed pesticides to the farmer by text messages.

## References & attributions

- United Nation's Sustainable Development Goals. <https://www.un.org/sustainabledevelopment/sustainable-development-goals/>
- roach by Ben Davis from the Noun Project
- <http://www.asimovinstitute.org/neural-network-zoo/>
- CIFAR10 & CIFAR100 datasets <https://www.cs.toronto.edu/~kriz/cifar.html>
- Very Deep Convolutional Networks for Large-Scale Image Recognition, Karen Simonyan, Andrew Zisserman
- Deep Residual Learning for Image Recognition, Kaiming He et al.
- Going deeper with convolutions, Christian Szegedy et al.



# Model Predictive Control of a Nanogrid

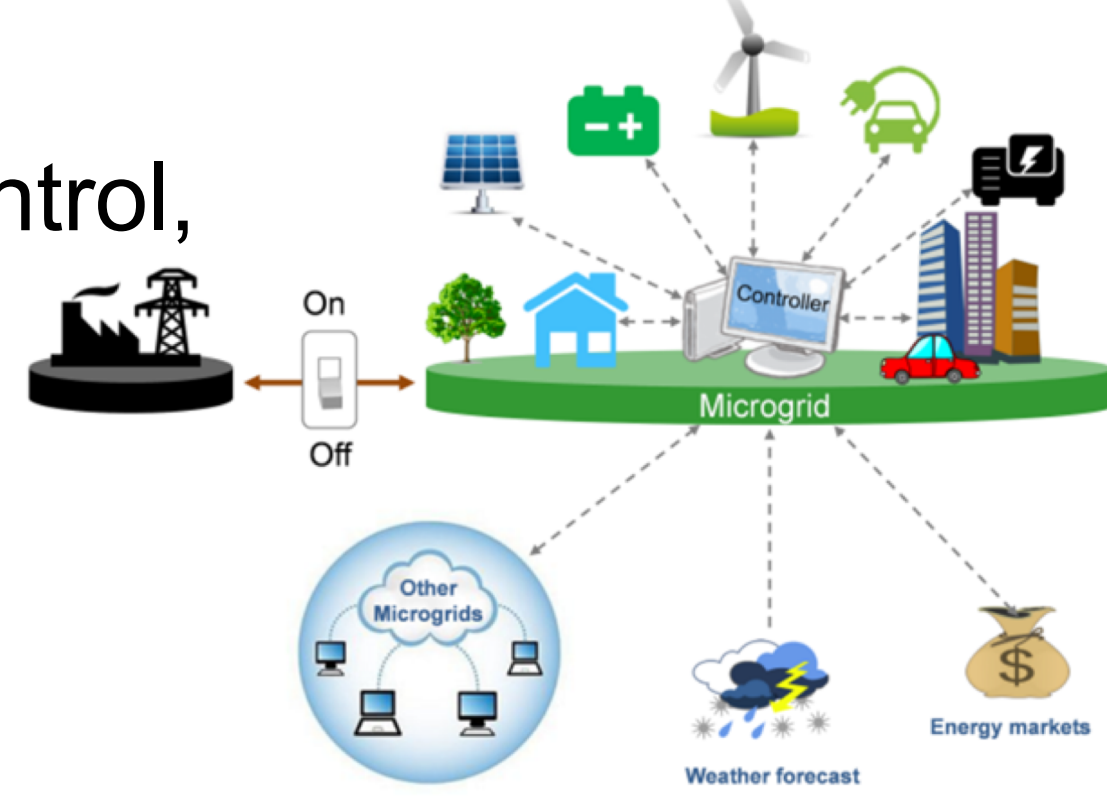
Frank Cannizzaro and Ramin Vafadary  
 Advisor: Dr. Maryam Khanbaghi  
 Department of Electrical Engineering

## BACKGROUND

### Microgrid

A localized group of electricity sources and loads that normally operates connected to and synchronous with macrogrid, but can also disconnect to “islanded mode”

- **Self-healing** and **adaptive**
- **Interactive** with consumers and markets
- **Optimized** to make best use of resources and equipment
- **Predictive** rather than reactive
- **Distributed**
- **Integrated**, merging monitoring, control, protection and maintenance
- **More secure** from attacks



### Microgrid Engineering Challenges

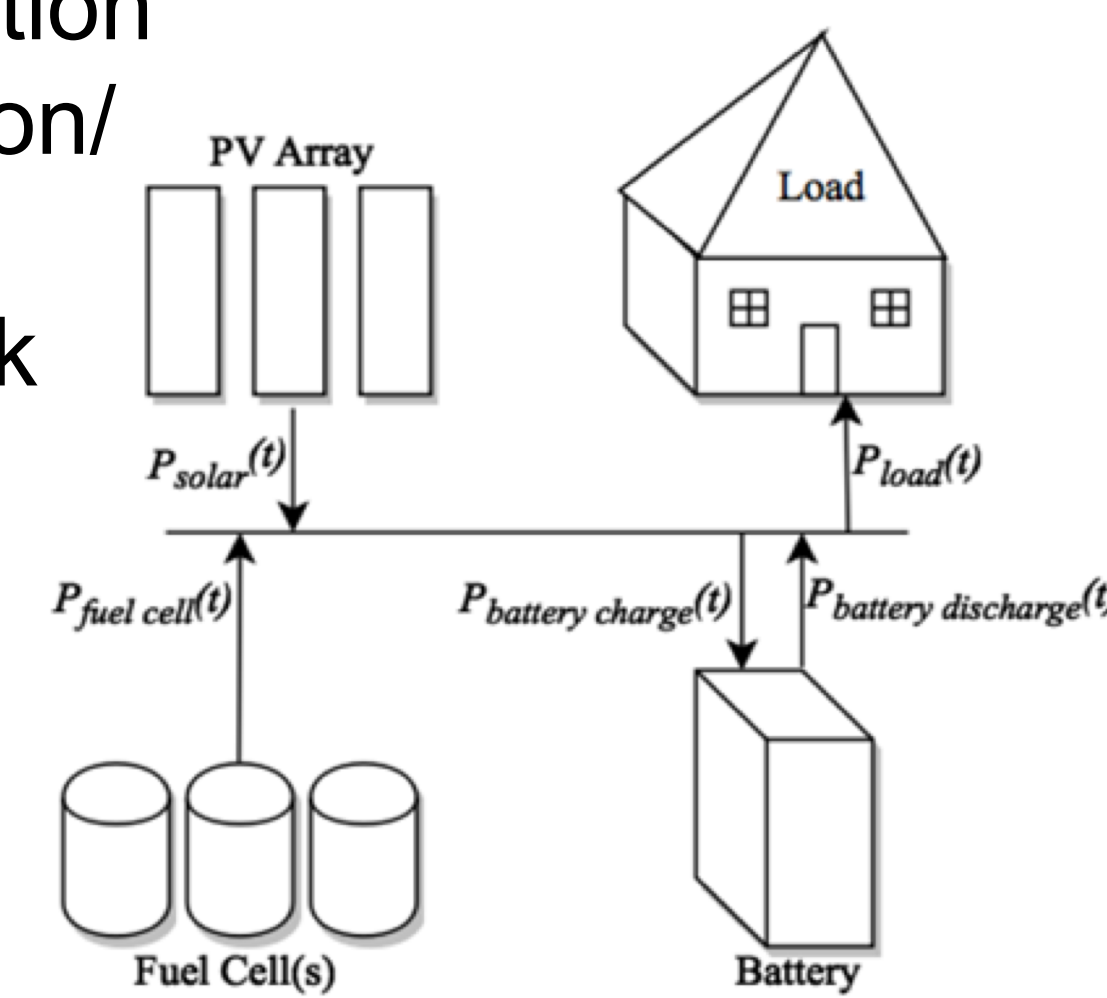
- **Bidirectional power flows**: can cause reverse power flows that may lead to complication in protection coordination and undesirable power flow patterns
- **Stability issue**: interaction of units may create local oscillations
- **Uncertainty**: load profile and weather forecast are two uncertainties

### Nanogrid

- Completely disconnected from the grid
- Integrated renewable energy with energy storage
- Increases customers’ control of their own energy generation
- Can store excess energy and use the stored energy optimally

### Nanogrid Model

- A photovoltaic array for generation during daytime
- A hydrogen fuel cell for using instead of the main grid
- A battery storage system acting as a buffer to smooth intermittent generation and to optimize the energy generation/usage balance
- A single house as the load with duck curve load profile

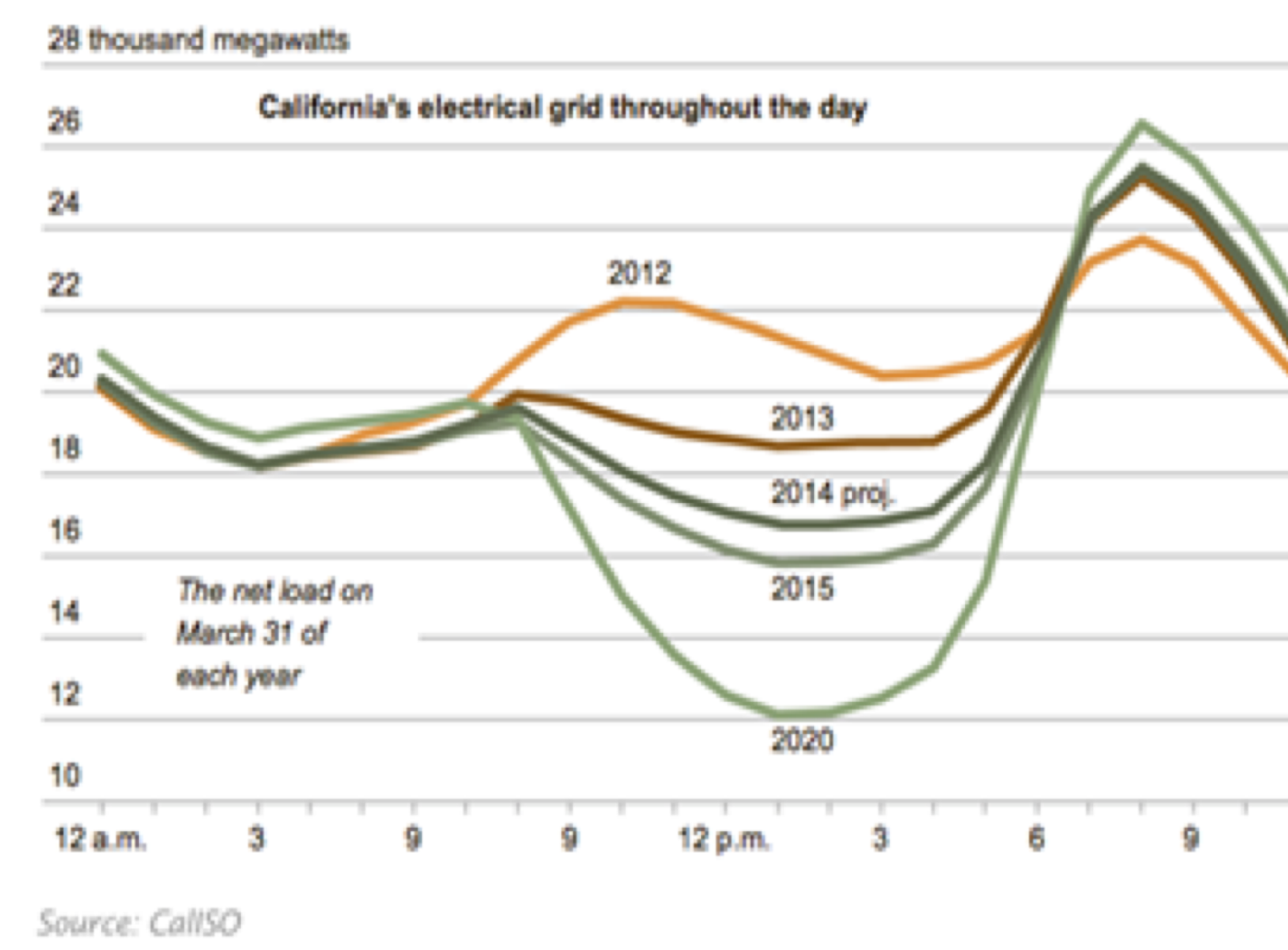


### Load Data

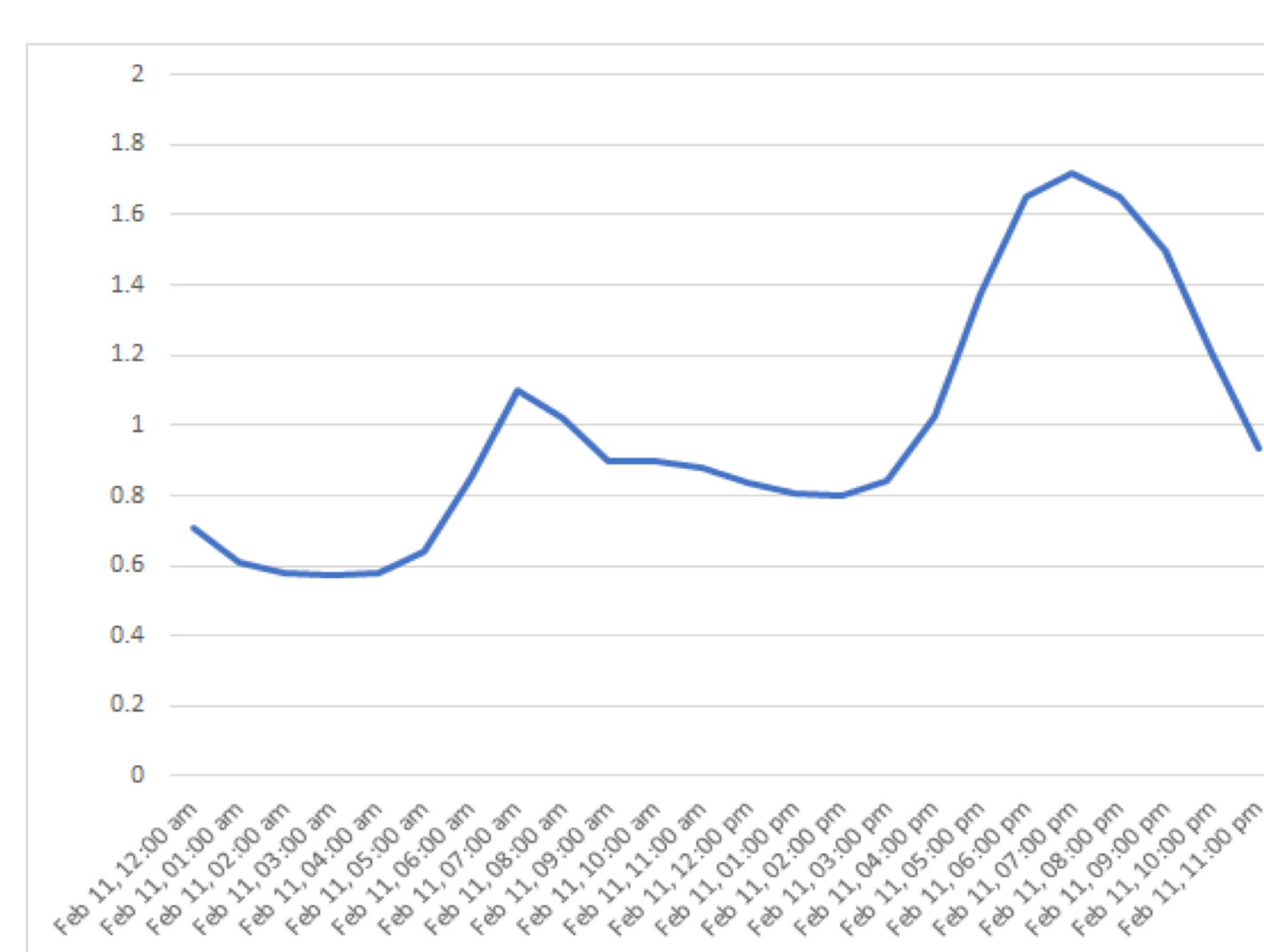
- National Renewable Energy Laboratory System Advisor Model Dataset
- Average United States household

## SYSTEM MODEL

### Duck Curve



### Residential Load Data



### Transition probability between states calculated for daylight hours

- Spring-Summer (6AM-8PM)
- Fall-Winter (7AM-5PM)

### Modeling Solar Energy as Disturbance to the System

#### Monte Carlo Simulation

- Utilizes probability transition matrix
- Generates sequence of random hourly steps
- Models weather over a specified period

#### Solar Disturbance

Solar panels power output are state dependent

- Clear: 0.6 kWh
- Partially Cloudy: 0.4 kWh
- Overcast: 0.3 kWh

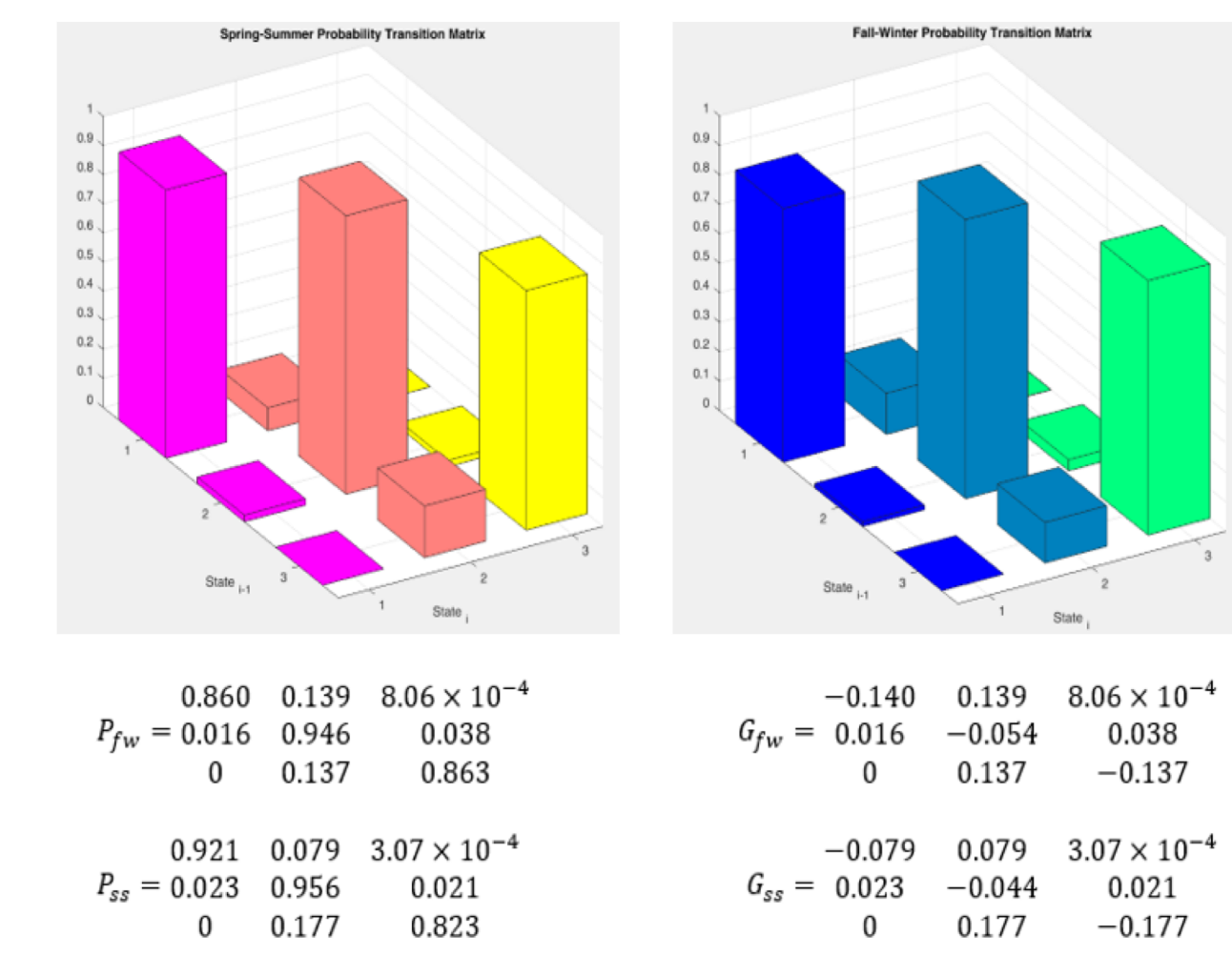
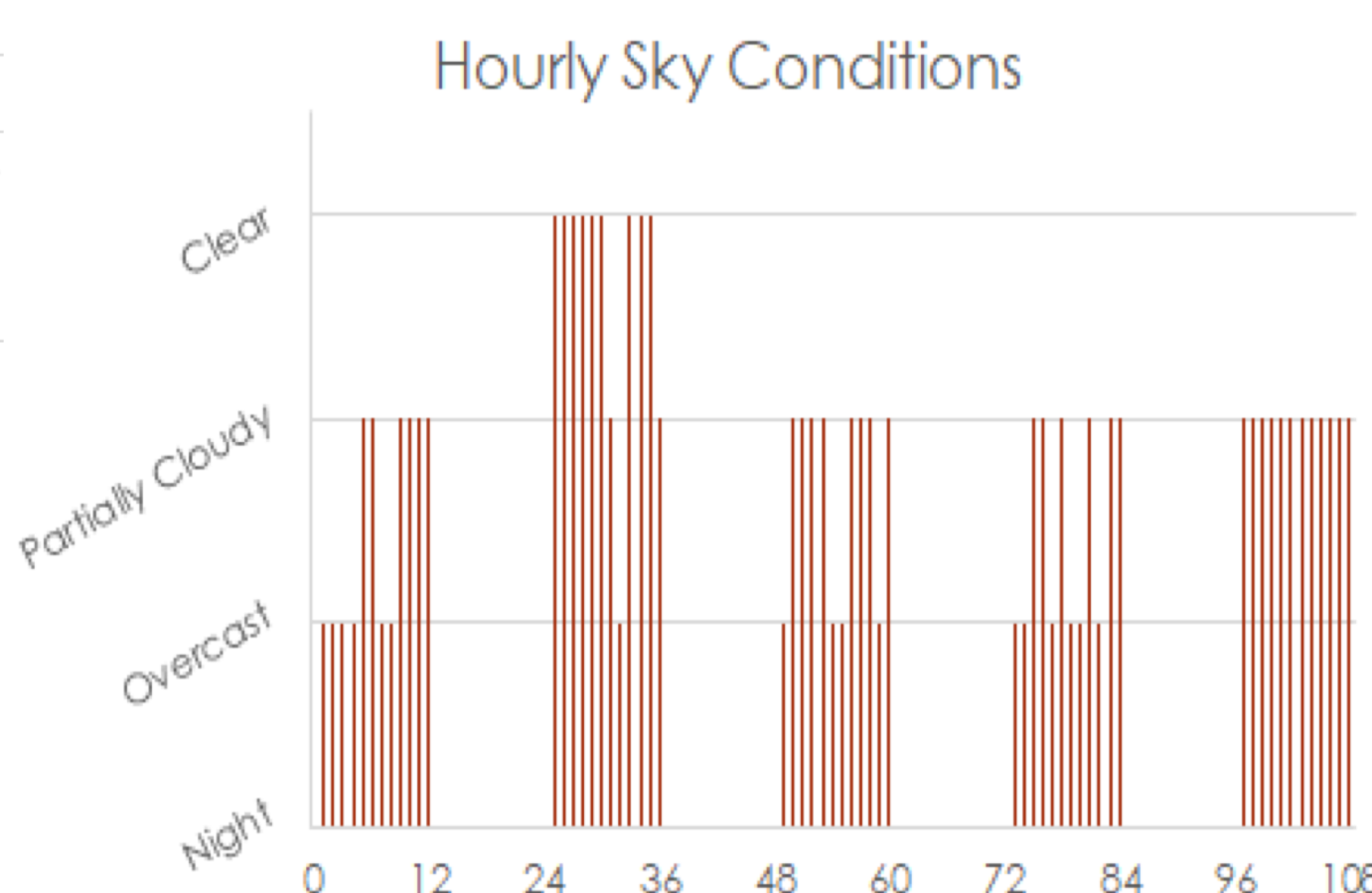
### Modeling Solar Energy Input as a Markov Chain Data

#### Weather Data

- NOAA NCEI local climatological data for San Jose, CA
- Hourly readings spanning 2008-2017
- Contains sky cloud coverage classifications

#### Three Weather States

- Clear
- Partially Cloudy
- Overcast

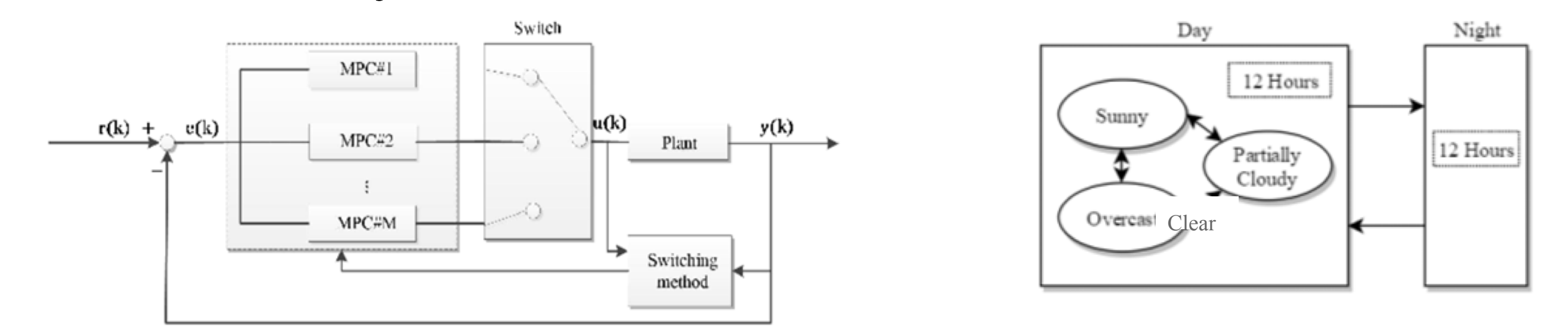


$F_{ww}$	0.860	0.139	$8.06 \times 10^{-4}$
	0.016	0.946	0.038
	0	0.137	0.863
$F_{ww}$	0.921	0.079	$3.07 \times 10^{-4}$
	0.023	0.956	0.021
	0	0.177	0.823

## RESULTS & RESEARCH

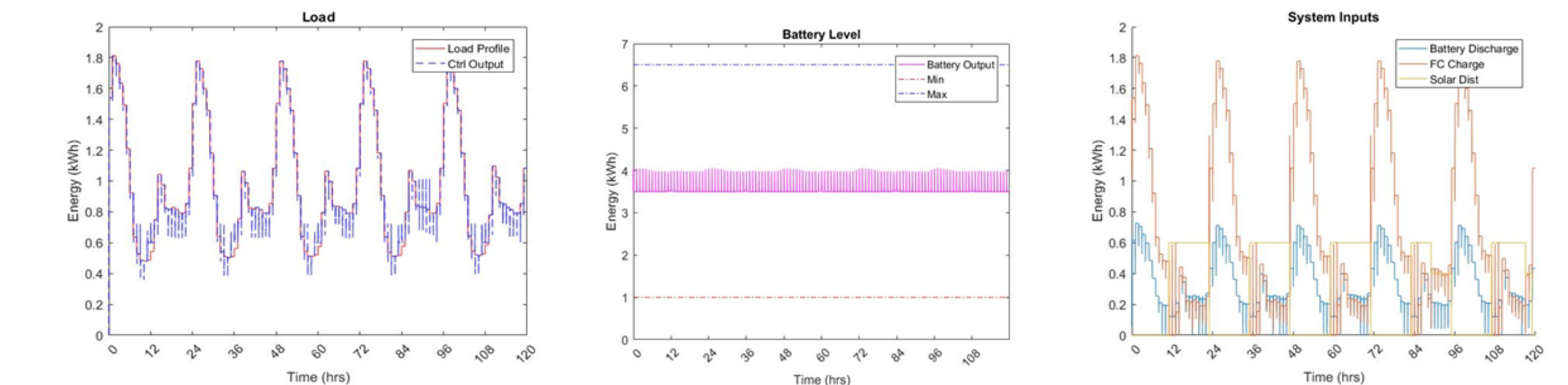
### Switched Model Predictive Control

- Designing a control strategy for energy management of the NanoGrid,
- Using a switched MPC based on the weather condition,
- Advantages of MPC: can handle constraints and is suitable for MIMO systems.



### Preliminary Simulation Results

The results for 5 days of simulation are shown below:



### Conclusions & Future Directions

- The proposed control method is able to track the load profile of the house.
- The control method was able to accommodate constraints on the battery level and fuel cell energy production.
- It is suggested to use a larger fuel cell in case of longer periods of intemperate weather during winter.
- Future work could include more cloud coverage states in the Markov process.
- The model of the system can be improved for future work.

### References

- “Jump Linear Quadratic Control for Energy Management of a Nanogrid”, N. Tucker and M. Khanbaghi, *American Control Conference*, p 3171 – 3177, June 2018, Minneapolis.
- “Mathematical model for a microgrid consisting of wind turbine, PV panels, and energy storage unit”, E. Ufluoglu and G. Kayakutlu, *J. Renewable & Sustainable Energy*, p 1-14, Sept. 2016.

### Acknowledgment

Authors would like to thank School of Engineering and Latimer Energy lab. for their support.

# Design and Measurement of a Miniaturized Beam-Forming Network for a 4-Element Patch Antenna Array at 5.8GHz

Brian Tjahjadi, Undergraduate Alumni; Dr. Ramesh Abhari, Advisor  
Department of Electrical Engineering

## Motivation:

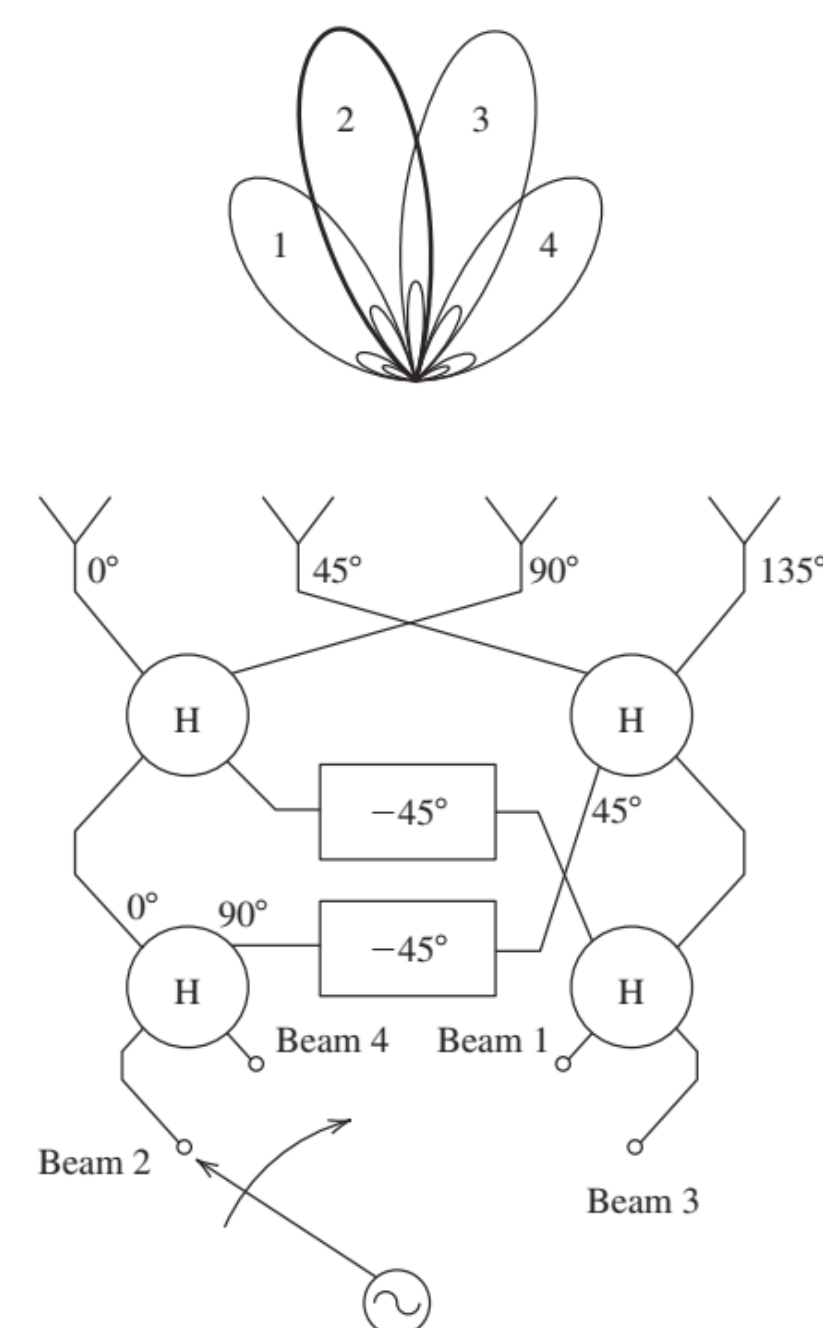
- Compact antenna array front-ends are needed in emerging wireless systems
- Often it is desired to steer the radiation beam of the antenna to scan an area or to establish communication for multiple users in different directions without physically moving the antenna

## Objectives:

1. Design a passive beamforming network to create the needed input phases and magnitudes for switching the beam in 4 directions at 5.8GHz
  - Use Butler Matrix design for beam forming
2. Significantly reduce the footprint of a 1x4 patch antenna array and its feed network
  - Use Metamaterial design concept to reduce the footprint of components of Butler Matrix

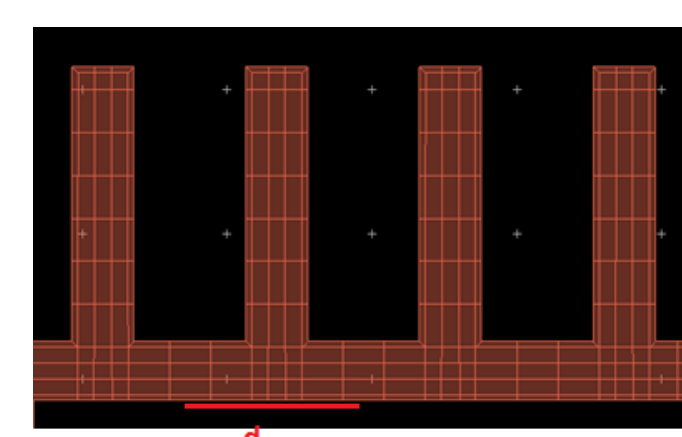
## Butler Matrix:

- Splits the power from one of the input ports equally to all 4 output ports
- Creates the desired phase differences at the output ports



## Metamaterial-based Design:

- Controlling the phase delay, i.e. propagation constant, by periodic loading
- When employed in transmission lines also referred to as Artificial Transmission Line (ATL)
- Slows down traveling waves to get the same phase shift with a shorter length compared to regular transmission line

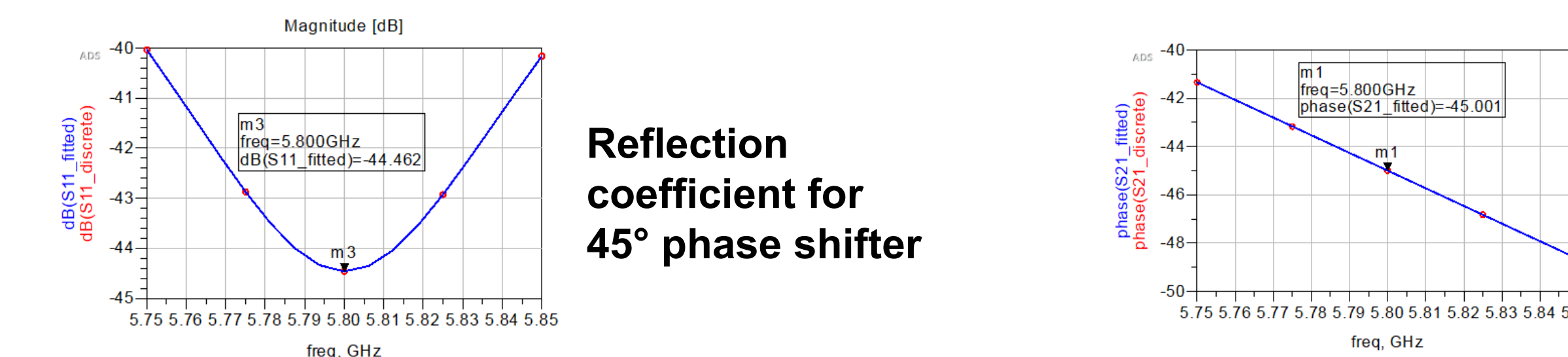


## Butler Matrix Design:

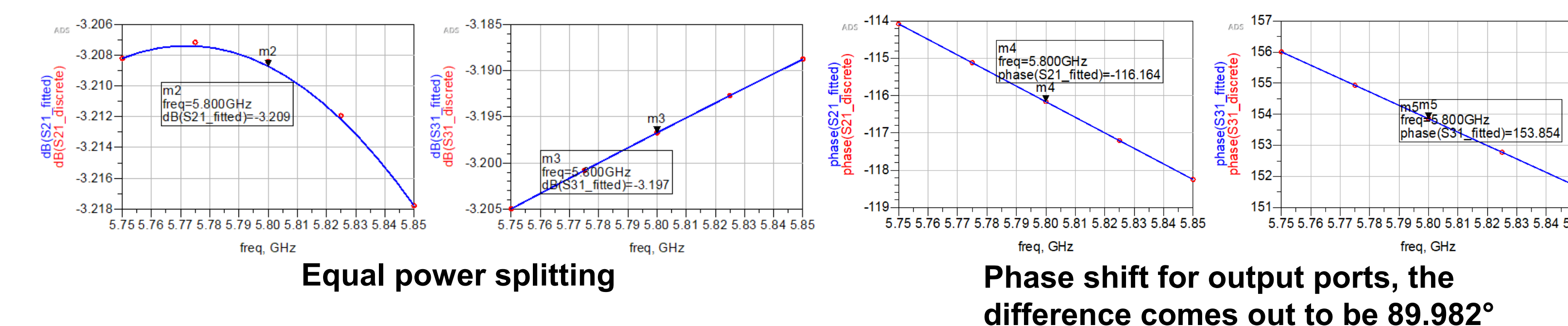
Substrate: Rogers 4350B with 10 mil thickness

Main Components: Phase shifters, Crossover, Quadrature Hybrid

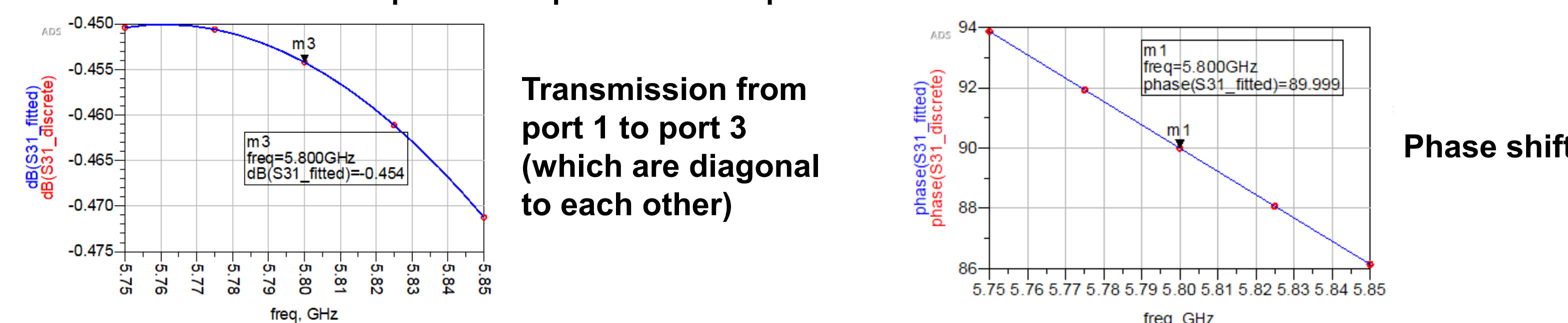
Phase Shifters: A transmission line used to introduce relative phase shift in signal at output compared to input



Quadrature Hybrid: A structure that divides power equally to 2 outputs but with relative phase shift of 90° between the outputs

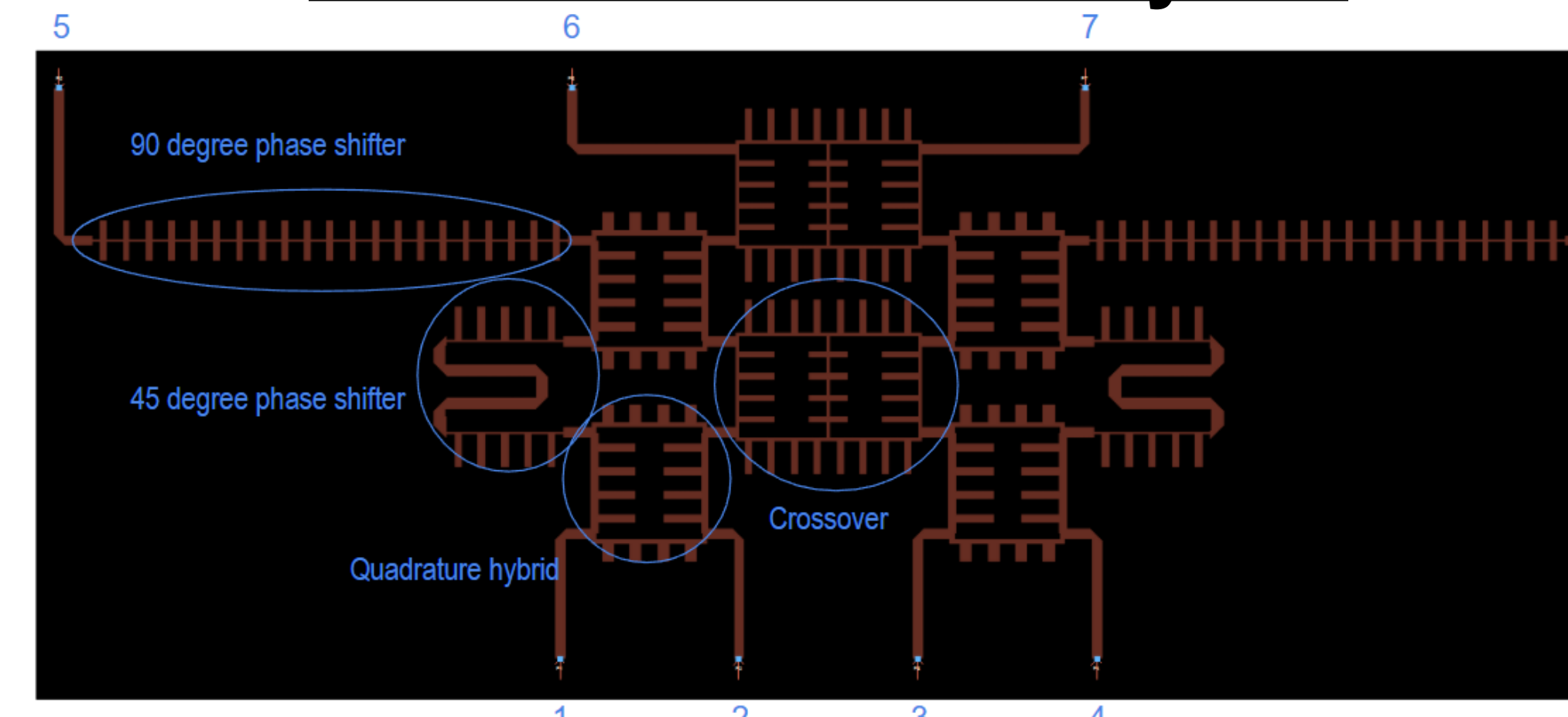


Crossover: A structure that passes signals diagonally only with a relative phase shift of 270° at output compared to input



All plots are simulation results using ADS

## Final Butler Matrix Layout:



## Measurement Result Using VNA:

	Power (dB)	Phase difference(°)
S51	-7.969	-
S61	-7.022	-144.7
S71	-8.562	-147.1
S81	-7.943	-114.9

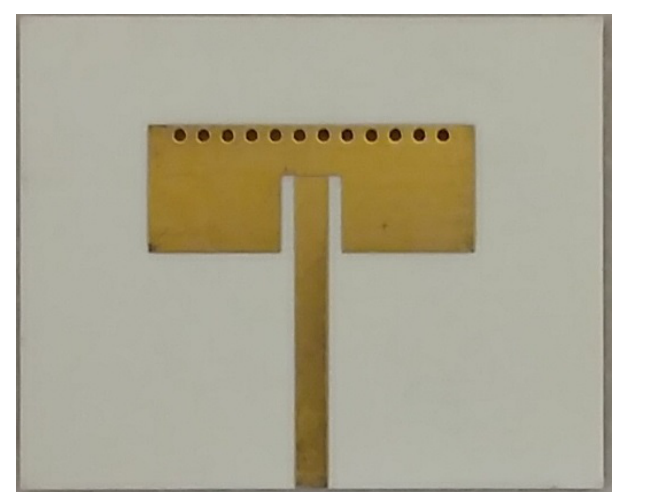
Port 1 Excitation; ideal phase difference is -135°

	Power (dB)	Phase difference(°)
S52	-9.085	-
S62	-9.515	46.25
S72	-7.277	49.11
S82	-8.997	45.81

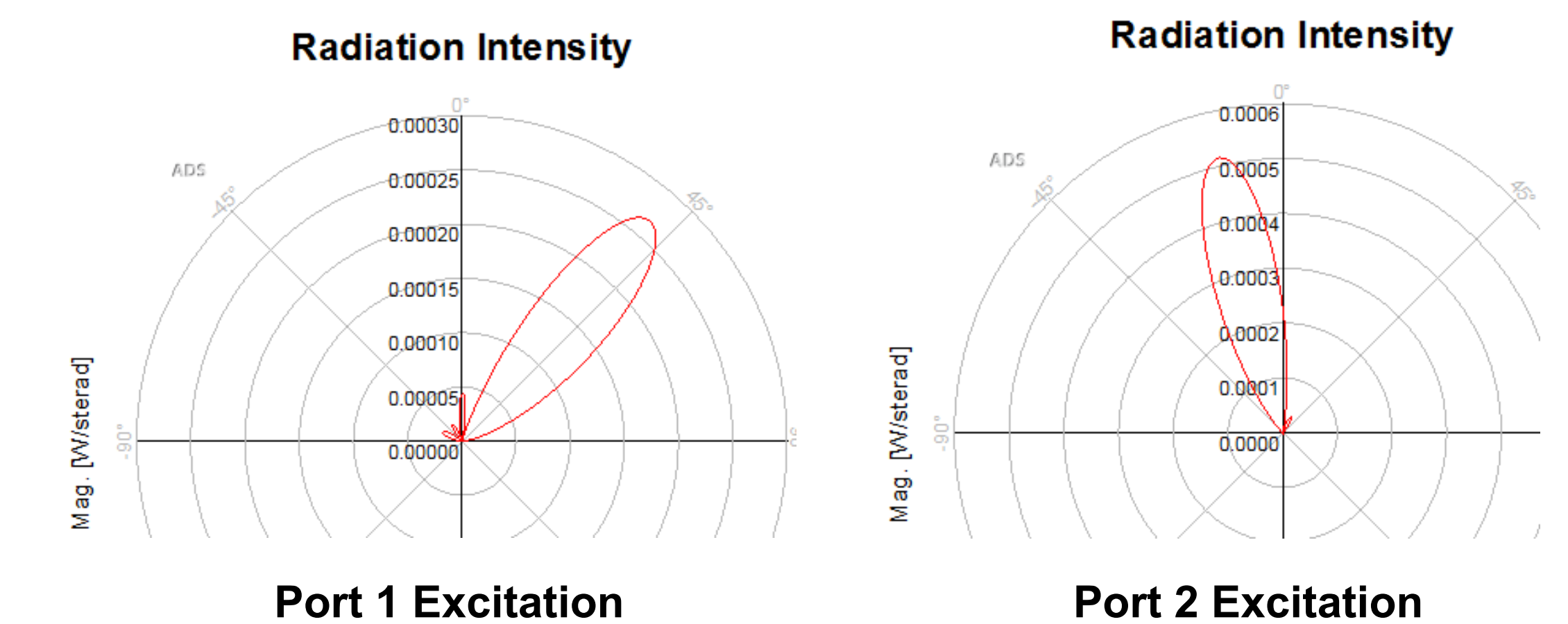
Port 2 Excitation; ideal phase difference is 45°

## Single Antenna Design:

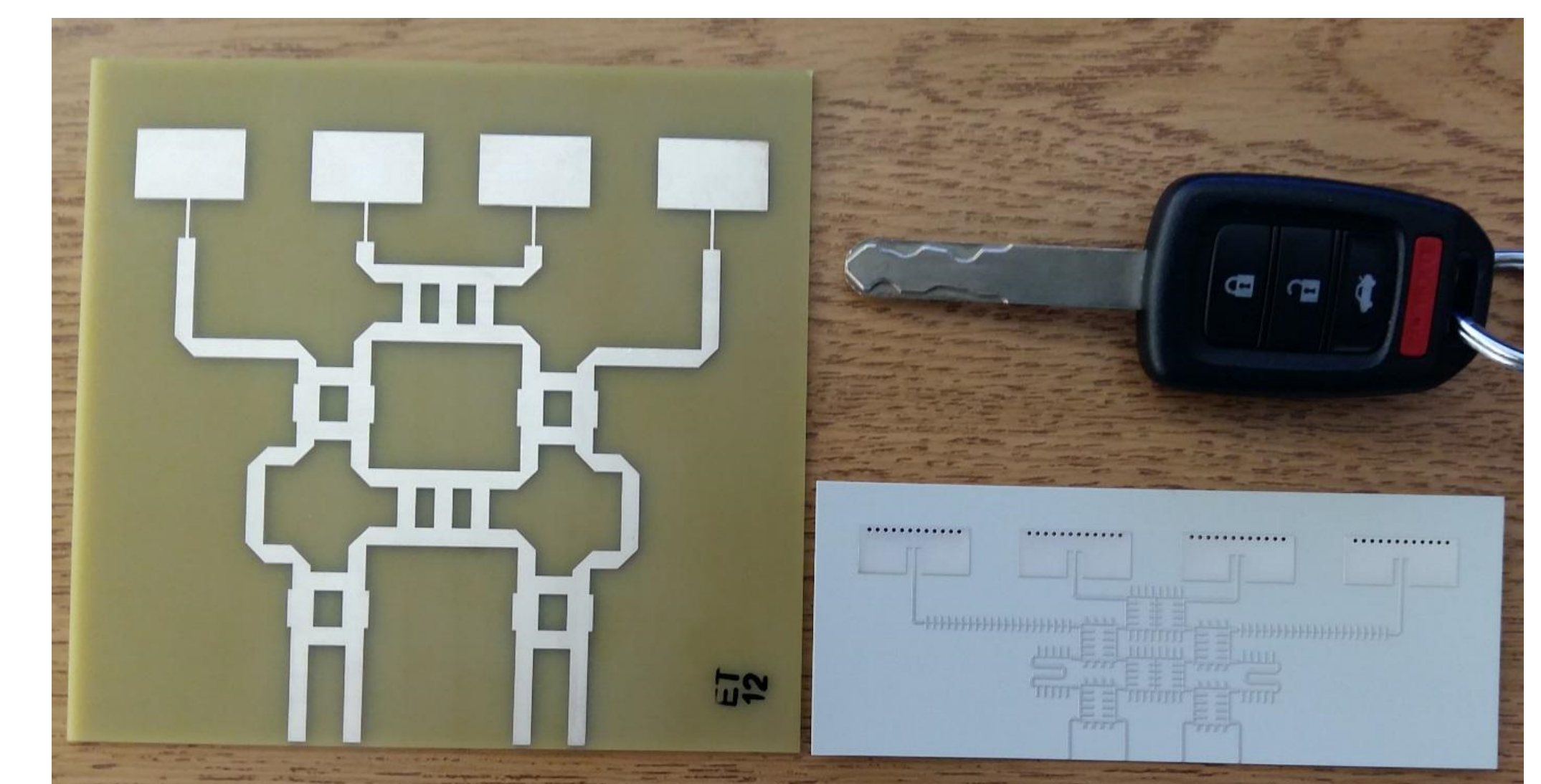
- Microstrip quarter wave patch antenna
- Half the size of a regular patch antenna
- Shorted at the end with vias to GND



## Beamforming Feature:



## Miniaturized Footprint:



## Key Findings of this Project:

1. The ATL structure with open-circuit stubs is effective at slowing down waves and reducing size.
2. The ATL structure has bandpass characteristics which is a boon since design frequency in simulation and real life can differ slightly.
3. Gain of antennas is impacted negatively for very thin boards.
4. The butler matrix is able to change the direction of the main lobe but performance is sensitive to design and physical imperfections.

## References:

1. W. L. Stutzman, and G. A. Thiele, *Antenna Theory and Design*, Hoboken, NJ: J. Wiley & Sons, 2013.
2. K. W. Eccleston and S. H. M. Ong, "Compact planar microstripline branch-line and rat-race couplers," *IEEE Transactions on Microwave Theory and Techniques*, vol. 51, no. 10, pp. 2119-2125, Oct 2003.
3. J. Butler & R. Lowe, "Beam-Forming Matrix Simplifies Design of Electronically Scanned Antennas", *Electronic Design*, volume 9, pp. 170-173, April 12, 1961

# A Highly Isolated 2x2 Printed Yagi-Uda Antenna Array for Small Form Factor Devices at 5.8 GHz

Nivedita Parthasarathy, PhD Student; Dr. Ramesh Abhari, Advisor  
Department of Electrical Engineering

School of Engineering

## Full-wave Electromagnetic Simulation in CST

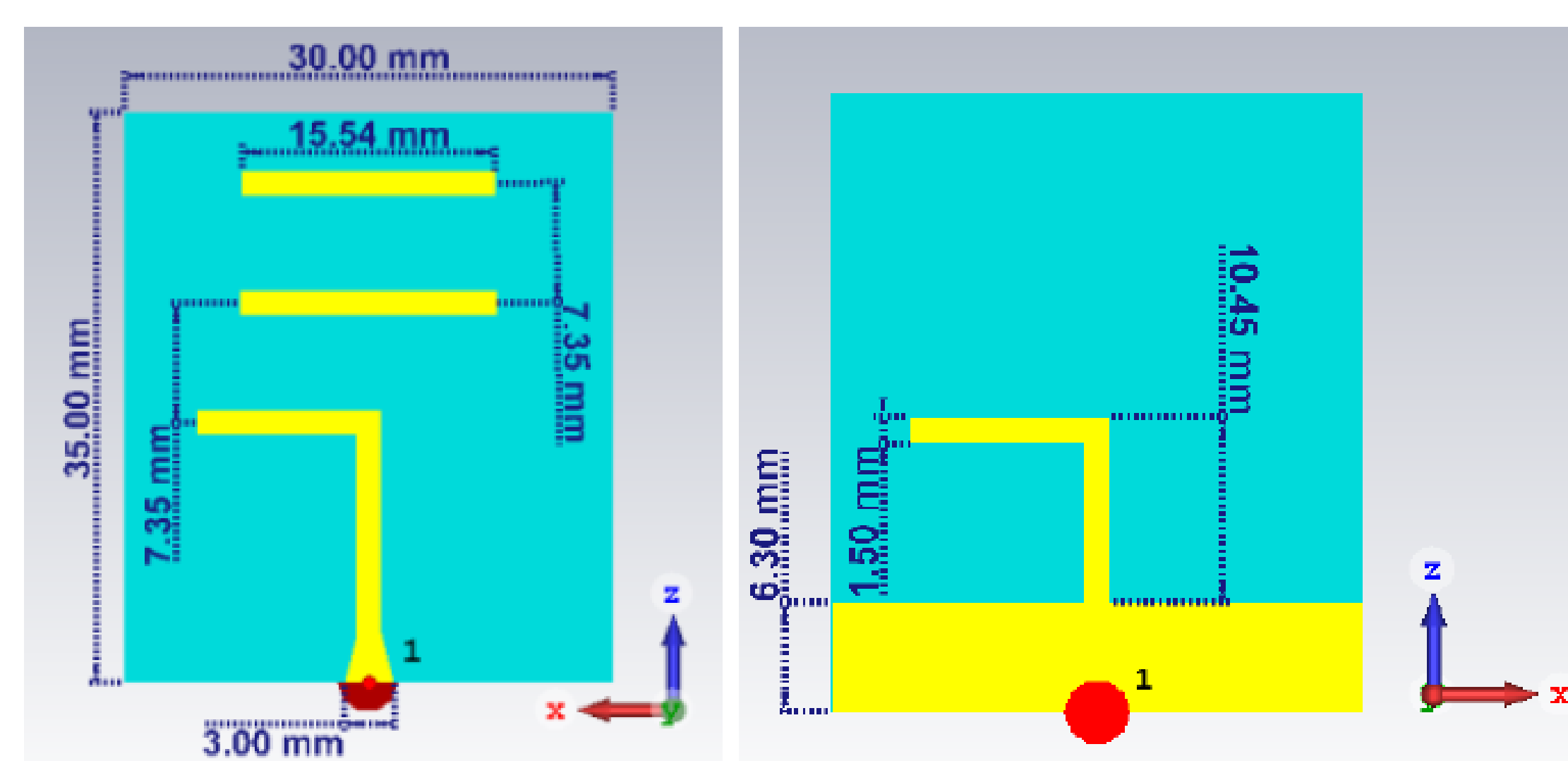
### Motivation:

- Many emerging applications from 5G FR1 band (<6GHz) to Microwave Hyperthermia and ablation require high gain and focused radiation patterns at 5.8 GHz.
- Studies of Specific Absorption Rate (SAR) patterns in human tissues have shown optimum radiation absorption at the skin/fat interface occurs at 5.8 GHz.
- Antenna arrays provide the high gain and narrow beam features needed at these applications but occupy a large foot print.
- A low-cost compact planar antenna array is desired but the designers need to deal with the challenge of mutual coupling in closely spaced array elements.

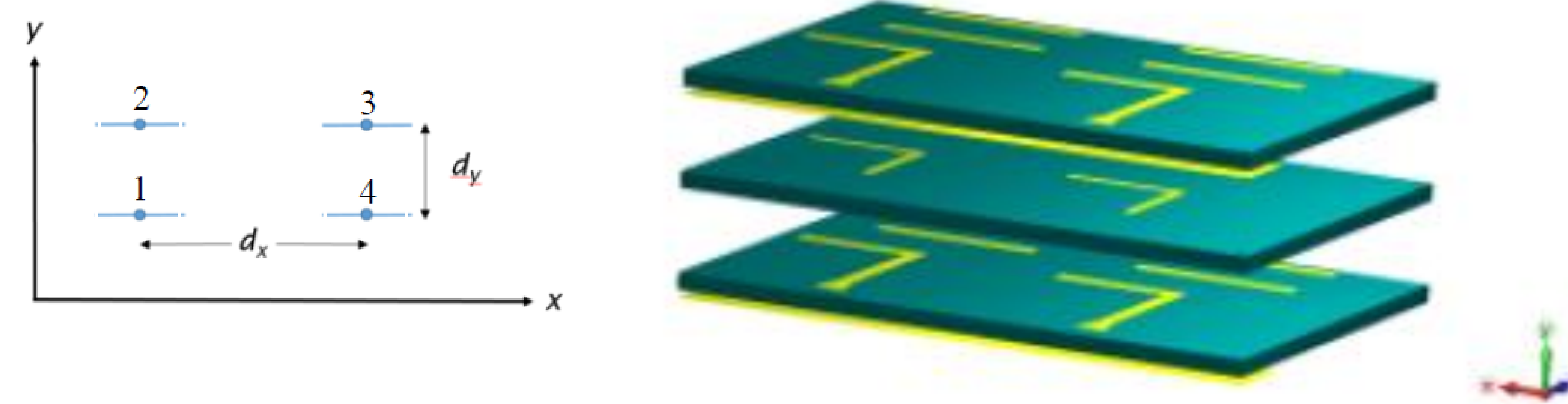
### Objectives:

1. Design and fabricate a 2x2 microstrip Yagi-Uda antenna array in a stacked arrangement with small planar footprint to maximize peak gain.
2. Enhance isolation in the array by introducing dual-plane parasitic dipoles to reduce mutual coupling between the stacked active elements.
3. Simulation of various Yagi array arrangement to study the performance of collinear and parallel design.

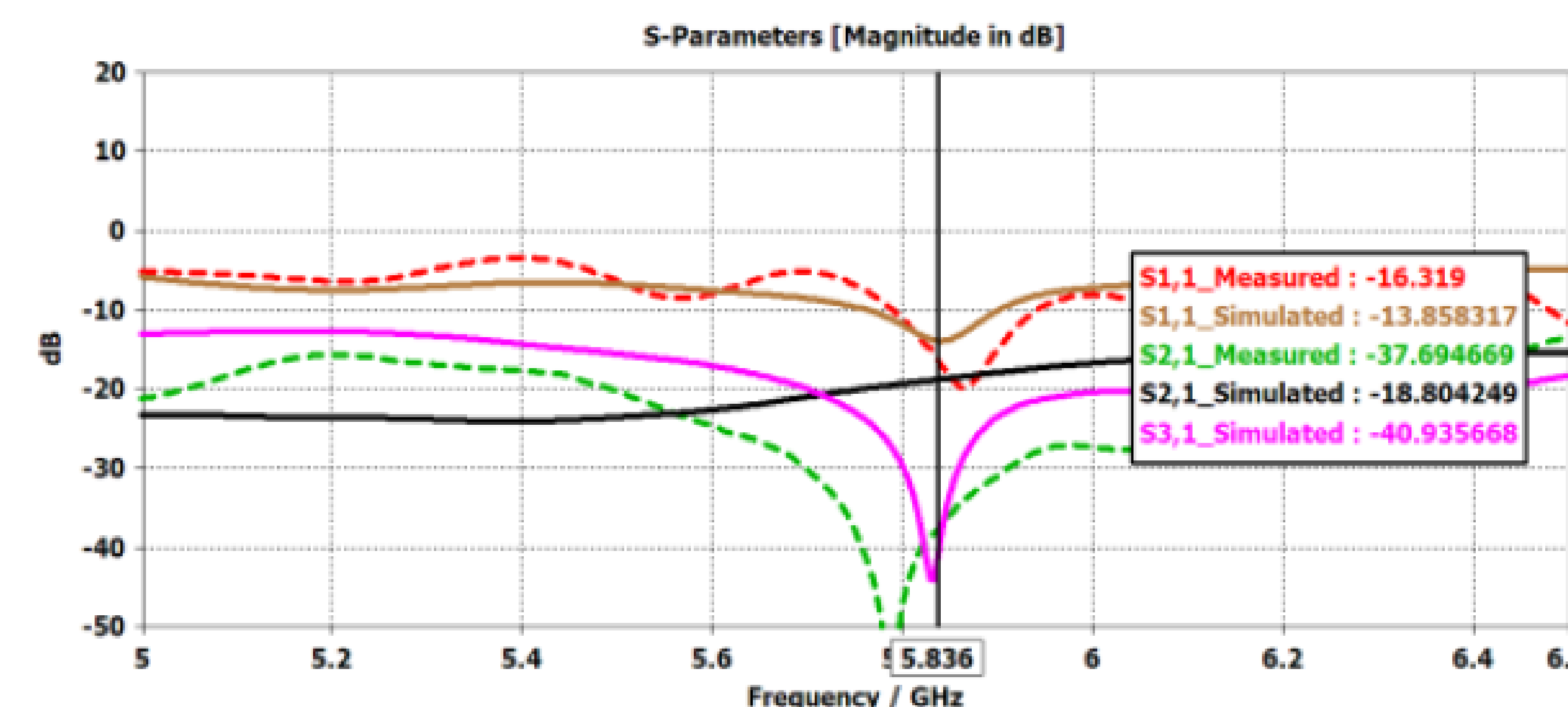
### Design of Free-standing Yagi Antenna:



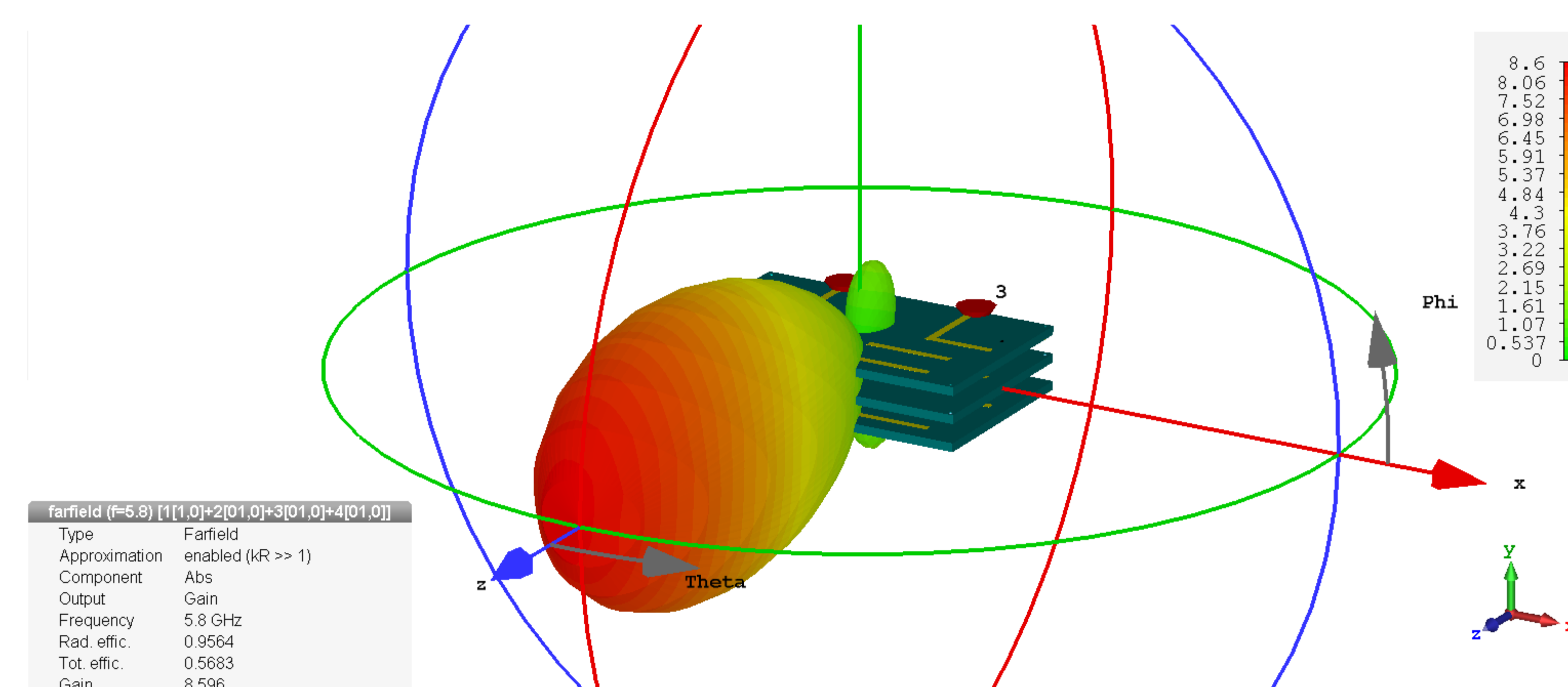
### 3D View of Stacked Array with Dual-Plane Parasitic Dipole



### S-Parameter Results of 2x2 Antenna Array with Reduced Coupling



### Array Radiation Pattern with Peak Gain

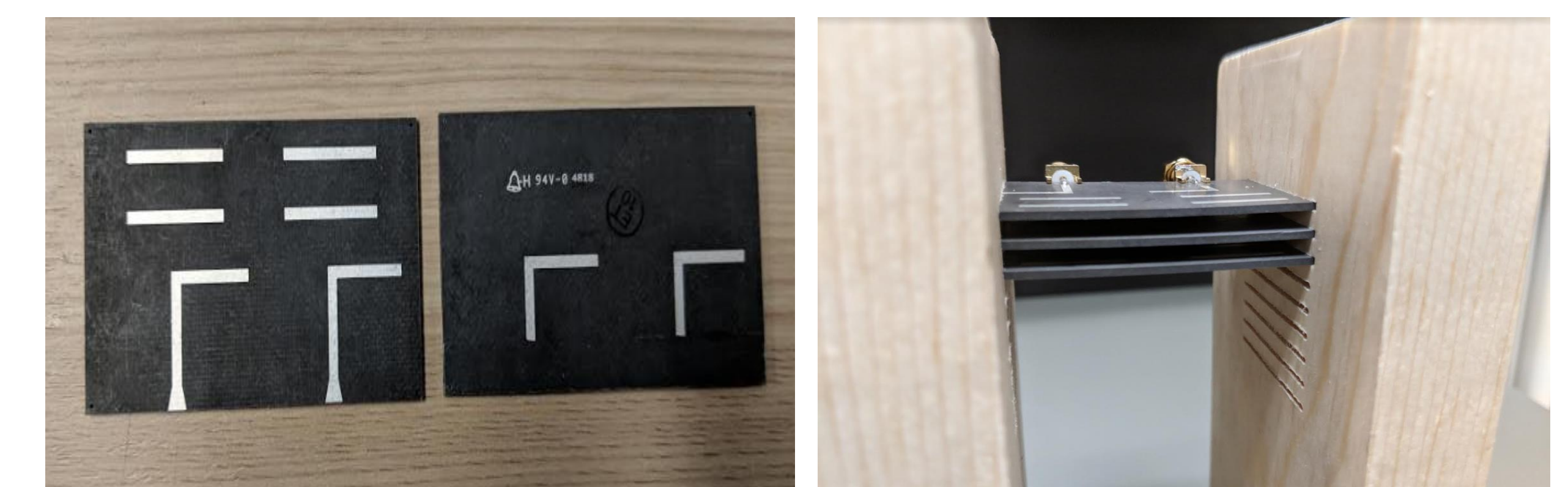


### Comparative Analysis of Printed Arrays:

Yagi Antenna Arrangement	Antenna Performance	
	Isolation ( $S_{21}$ )	Peak Gain
Single dual-plane Yagi	N/A	7.20 dB
2 Element Collinear Yagi Array	17.13 dB	9.028 dB
2 Element Stacked Parallel Yagi Array ( $0.5\lambda$ spacing)	17.328 dB	10.05 dB
2x2 Stacked Yagi Array ( $0.2\lambda$ spacing)	5.48 dB	7.760 dB
2x2 Stacked Yagi Array with Parasitic Coupling ( $0.2\lambda$ spacing)	18.8 dB	9.343 dB

### Prototype Fabrication:

- The antennas were fabricated on Rogers RT/Duroid 5880 substrate with 1.575 mm thickness.
- A birch wood test fixture was designed and fabricated in the Maker Lab for stacking the antenna boards at the needed spacing.



### Result Findings and Future Work:

- A novel design is proposed that showcases a new strategy for isolation enhancement in 2D printed Yagi arrays for the first time.
- Measured and simulated results demonstrate successful coupling reduction in closely spaced ( $0.2\lambda$ ) parallel Yagi arrays, while delivering high-gain and improved RF integrity.
- Next steps:
  - Measurement of radiation pattern
  - Increasing the number of array
  - Implementing beam steering strategies
  - Employing the proposed design in microwave hyperthermia applications



# Mitigation and Identification of the Cause of Radiated Emissions in an 8 Gbps High-Speed System

Ali Khoshniat and Ramesh Abhari  
 Department of Electrical Engineering, Santa Clara University  
 akhoshniat@scu.edu, rabhari@scu.edu



## Background

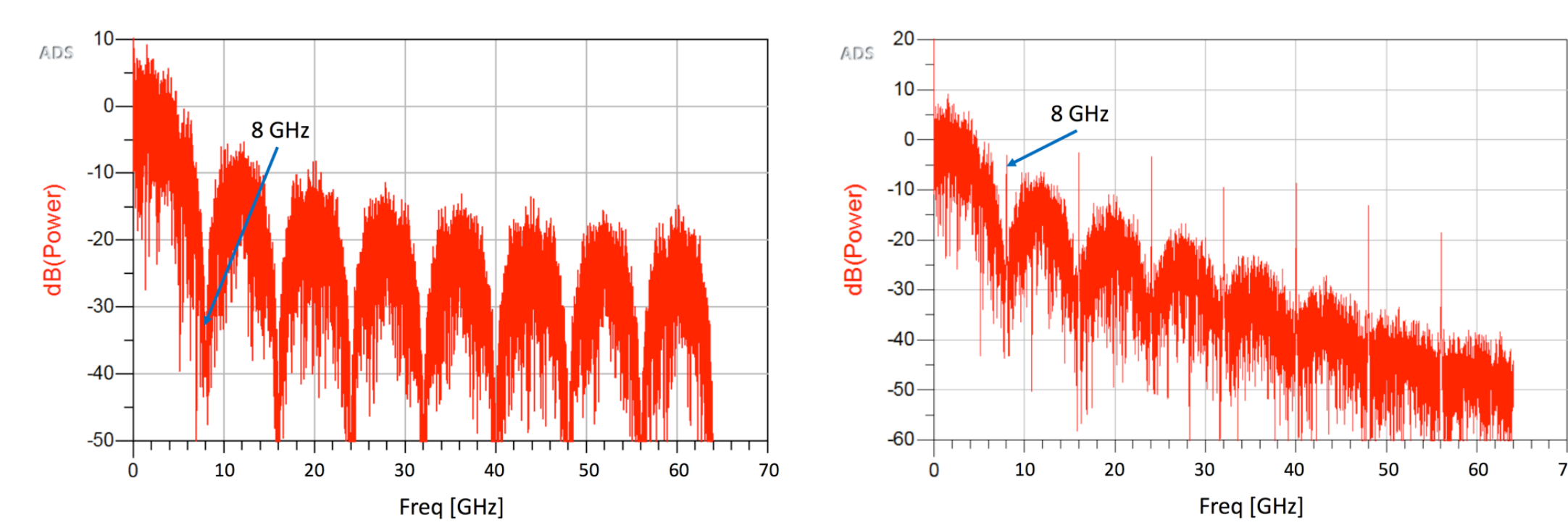
- Market demand is pushing computer and networking systems to operate at continually increasing data rates
- The byproduct of these advances is the generation of unintentional radiated emissions at the higher frequencies
- For systems with differential interfaces, emission is mostly from the common mode signals
- Common EMC solutions may not be enough and sometimes a custom design solution is needed to solve the EMI failures

## Objective

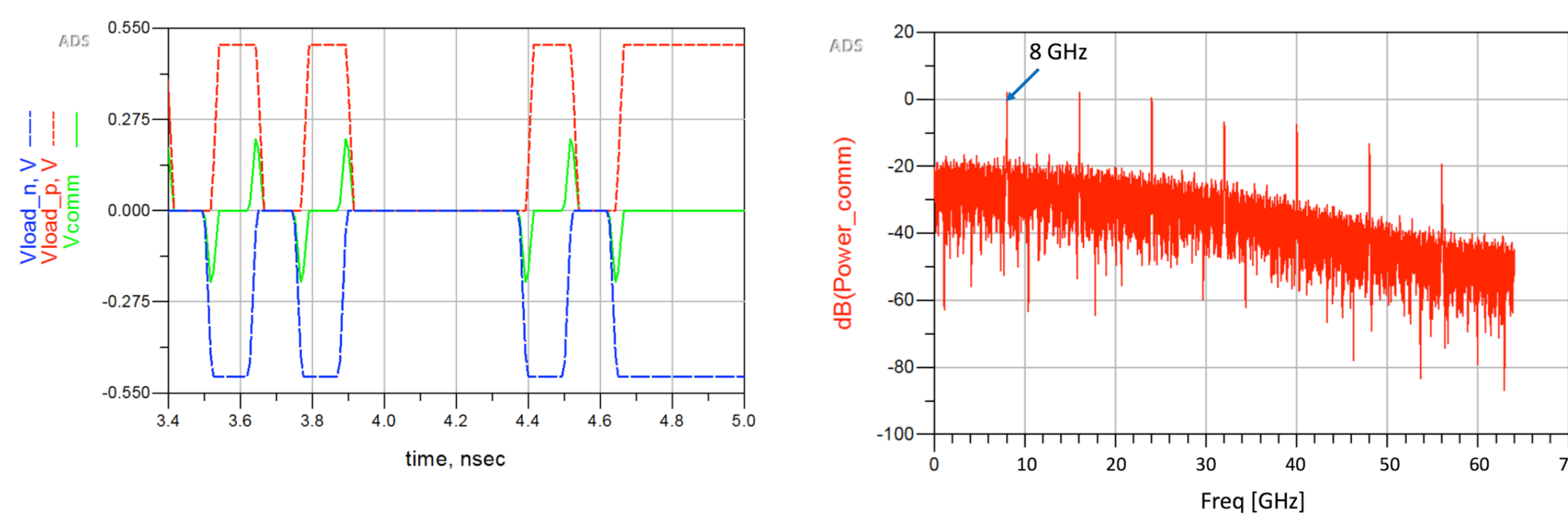
- To understand effect of signal waveform (rise time and phase mismatch) on common mode signals and their power spectrum
- To design a custom solution that works at the frequency of failure
- To simulate, fabricate, and measure the effectiveness of the EMC solution and compare with a commercially available microwave absorber solution

## Signals in Time Domain and Power Spectrum

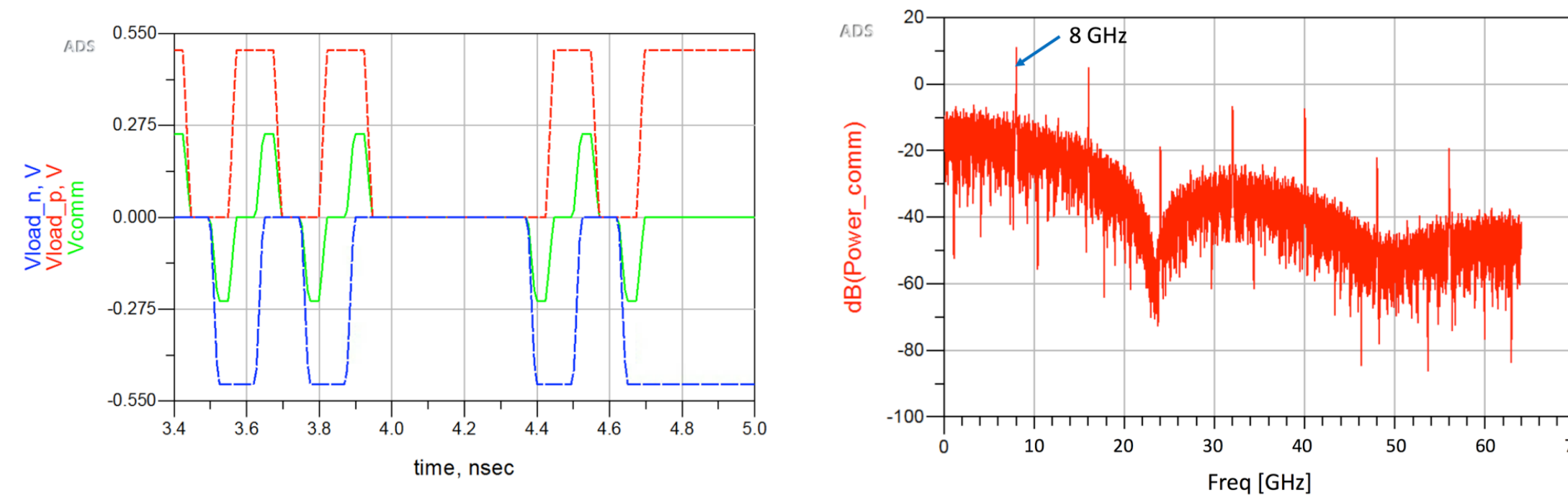
- Spectrum of an ideal 8 Gbps single ended signal with 0 ps rise/fall time (left plot) and 20 ps rise/fall time (right plot)
- Ideal signal has no spike at 8 GHz



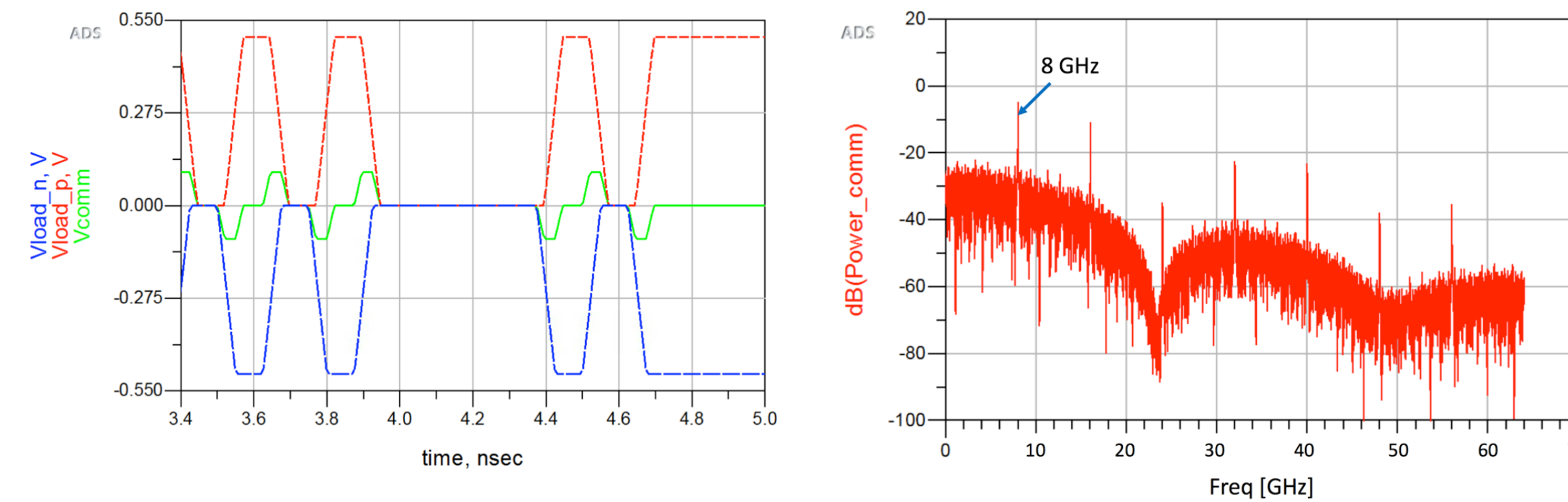
- Waveform of an 8 Gbps differential signal and its common mode with rise/fall time of 20 ps and delay mismatch of 20 ps (left plot) and power spectrum of the common mode signal (right plot)



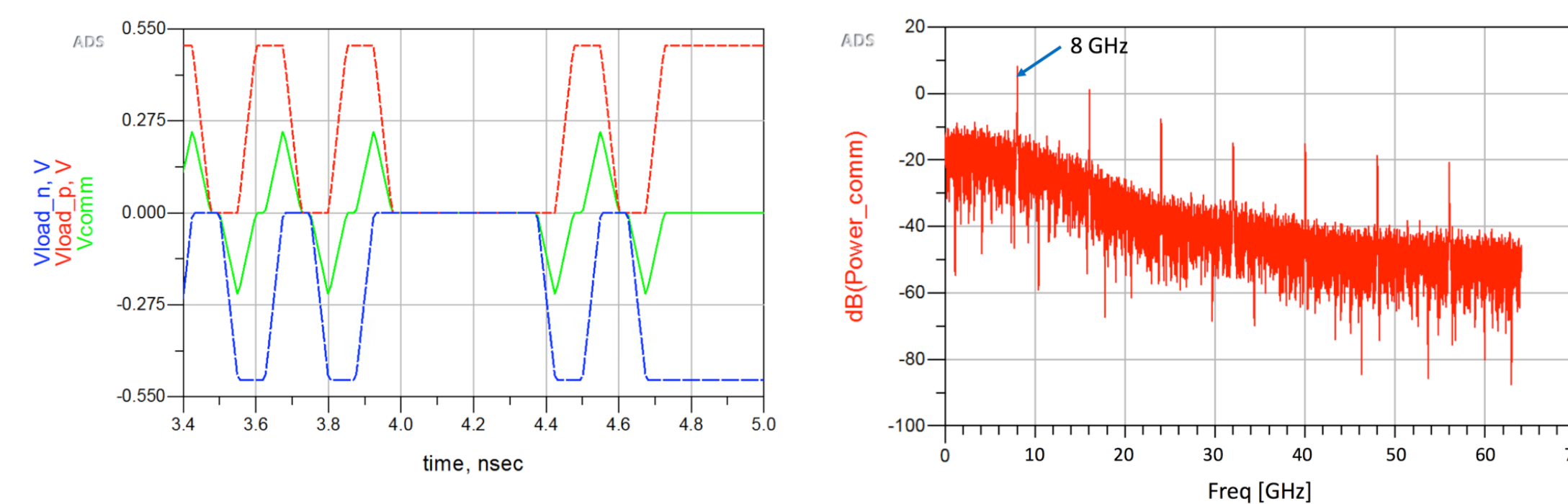
- Waveform of an 8 Gbps differential signal and its common mode with rise/fall time of 20 ps and delay mismatch of 50 ps (left plot) and power spectrum of the common mode signal (right plot)



- Waveform of an 8 Gbps differential signal and its common mode with rise/fall time of 50 ps and delay mismatch of 20 ps (left plot) and power spectrum of the common mode signal (right plot)

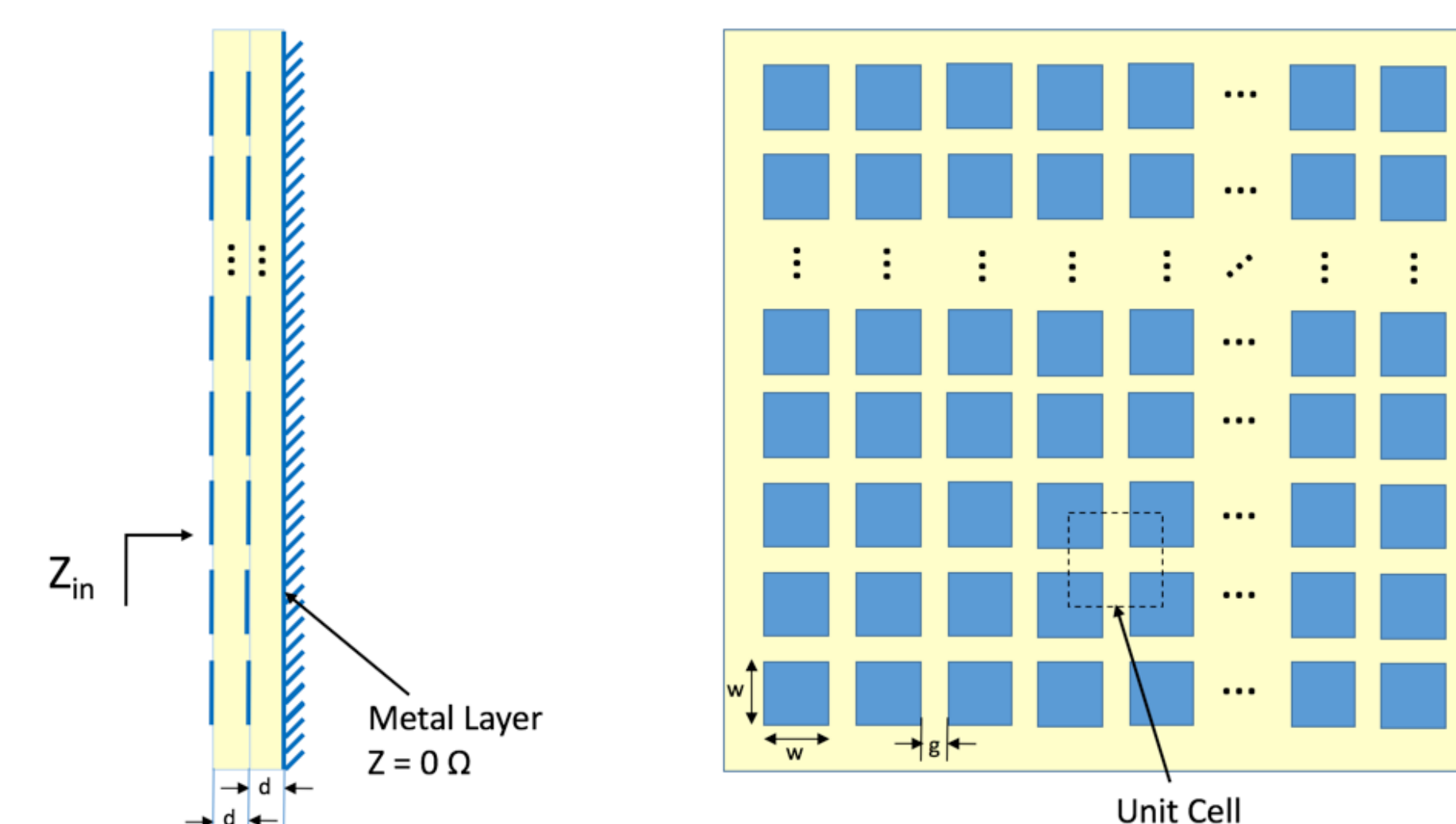


- Waveform of an 8 Gbps differential signal and its common mode with rise/fall time of 50 ps and delay mismatch of 50 ps (left plot) and power spectrum of the common mode signal (right plot)



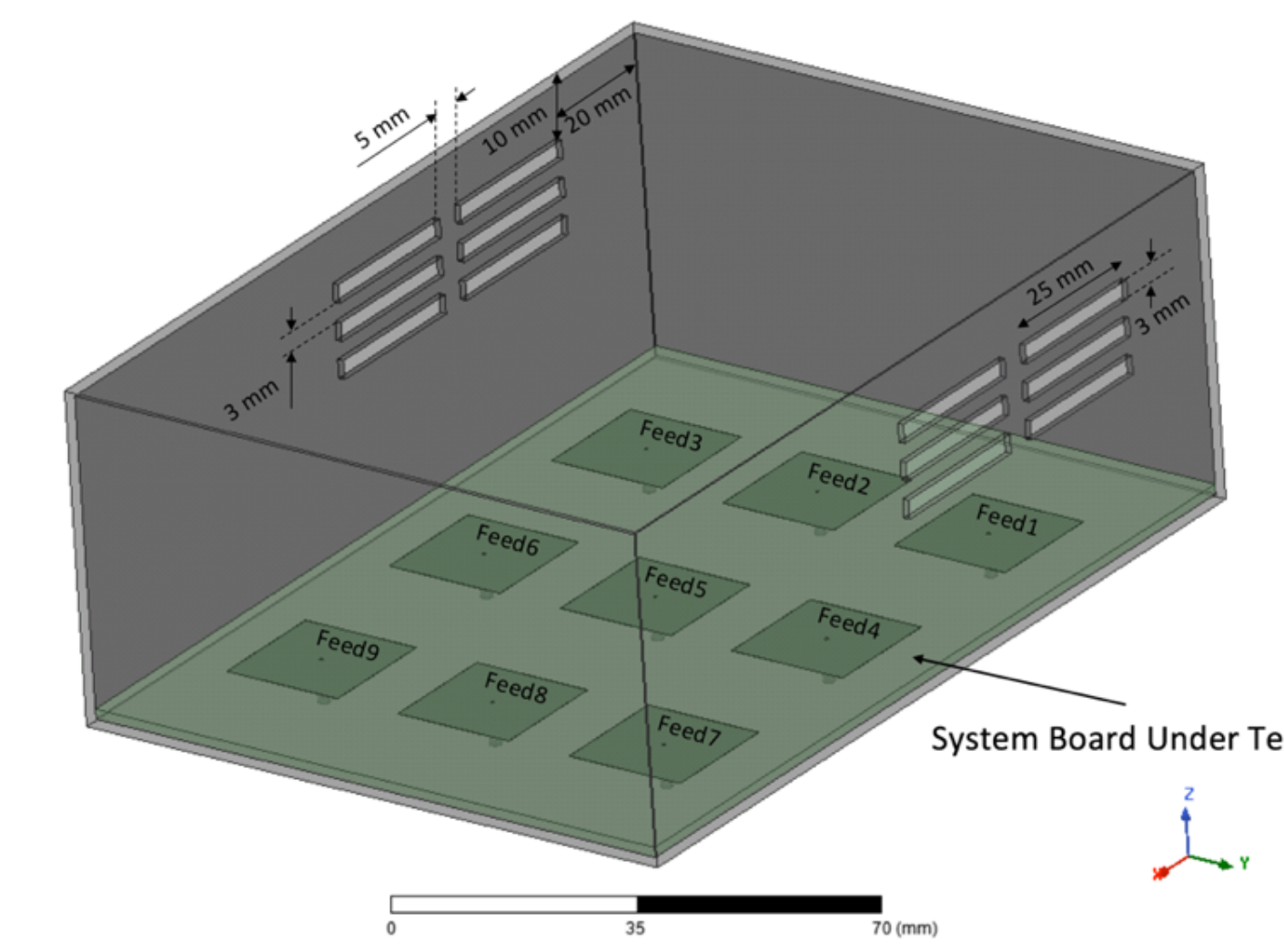
## FSS Absorber Design

- 2-layer periodic arrangement of resistive square patches with the thickness of  $0.1 \mu\text{m}$  printed on an FR406 substrate with the thickness of  $d = 1.5748 \text{ mm}$ ,  $\epsilon_r = 3.93$ , and  $\tan \delta = 0.0167$
- Match  $0 \Omega$  impedance of the metallic wall of the system case box to wave impedance of  $377 \Omega$  at 8 GHz
- Unit cell layout dimensions:  $w = 3.525 \text{ mm}$  and  $g = 1.075 \text{ mm}$

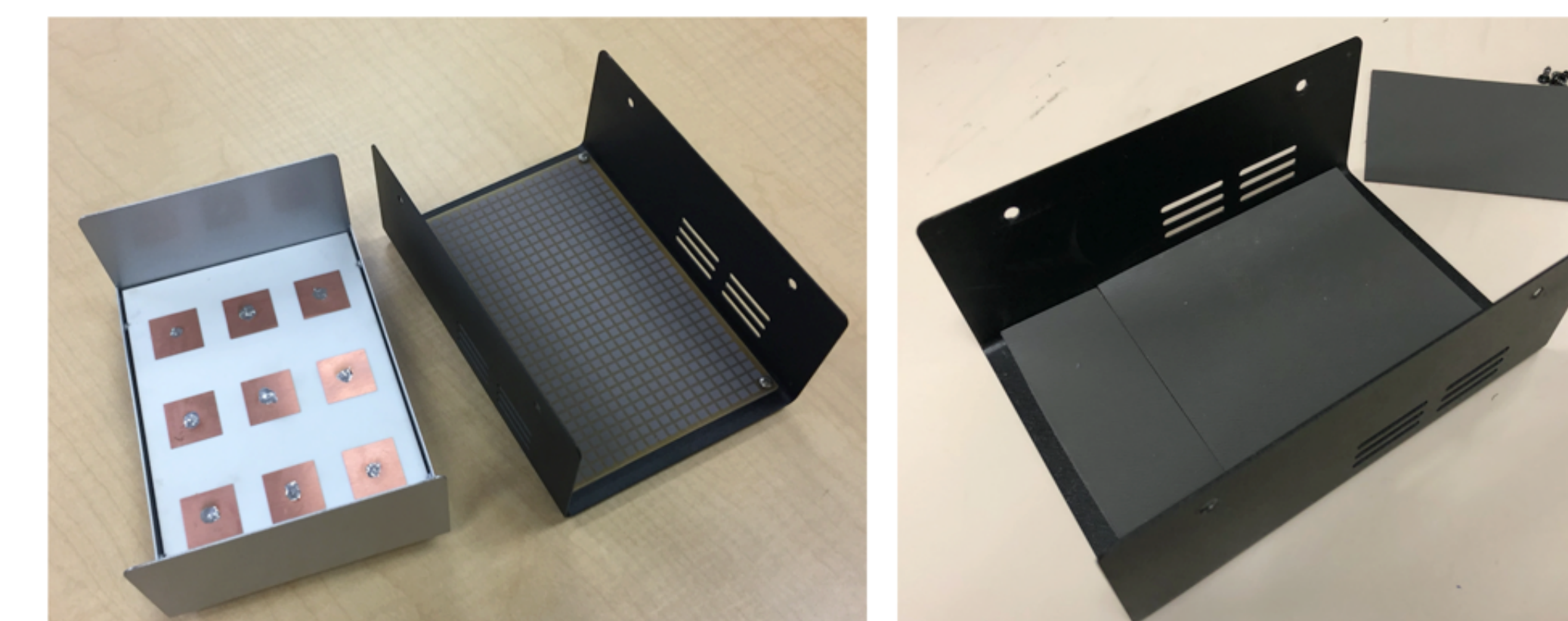


## Test System with Enclosure Box

- Radiated emissions at 8 GHz made by a 3x3 array of center fed  $19.4 \times 19.4 \text{ mm}^2$  patch antennas
- Substrate RO4003C,  $\epsilon_r = 3.55$  and the thickness of 1.524 mm



- Fabricated system prototype and its metal enclosure box (left) when the designed FSS absorber covers the top inside wall, and (right) when the commercial microwave absorber covers the top inside wall



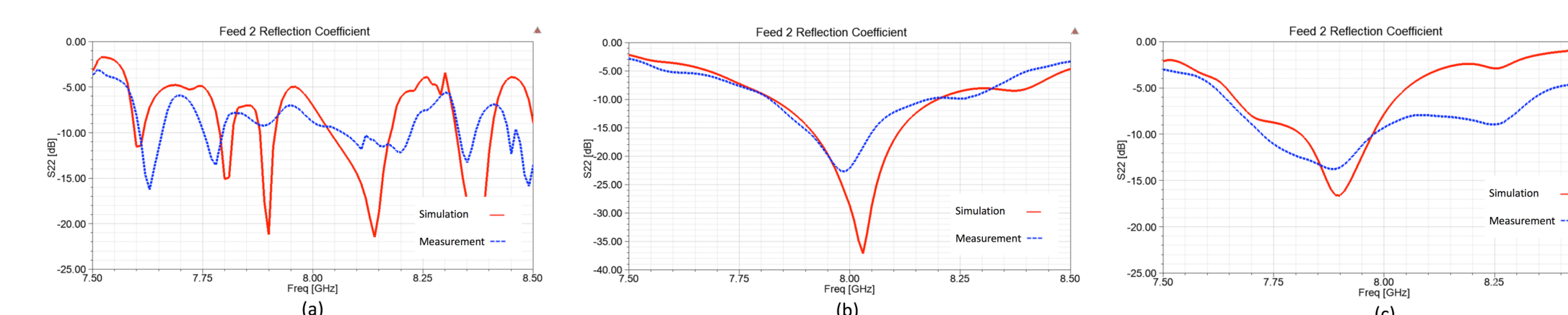
## Measurement Results

- VNA is used to measure return loss, coupling, and radiated emission from the test box
- Effect of return loss and coupling is calculated in coefficient K (dB)

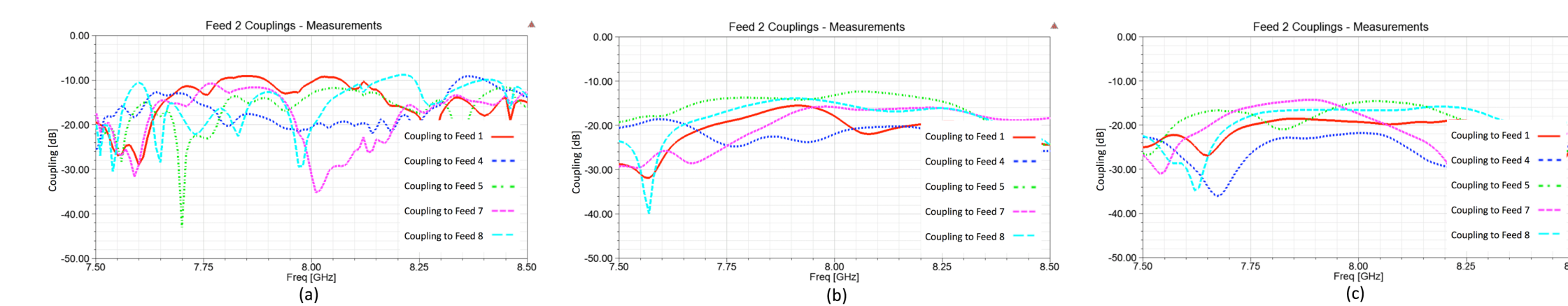
$$K = 10 \times \text{Log}_{10} \left( 1 - \sum_{j=1}^9 |S_{2j}|^2 \right)$$

Test Case	Coefficient K (dB)	
	Simulation	Measurement
No Absorber	-2.51	-2.20
Absorbing FSS	-1.07	-1.06
Microwave Absorber	-1.37	-1.36

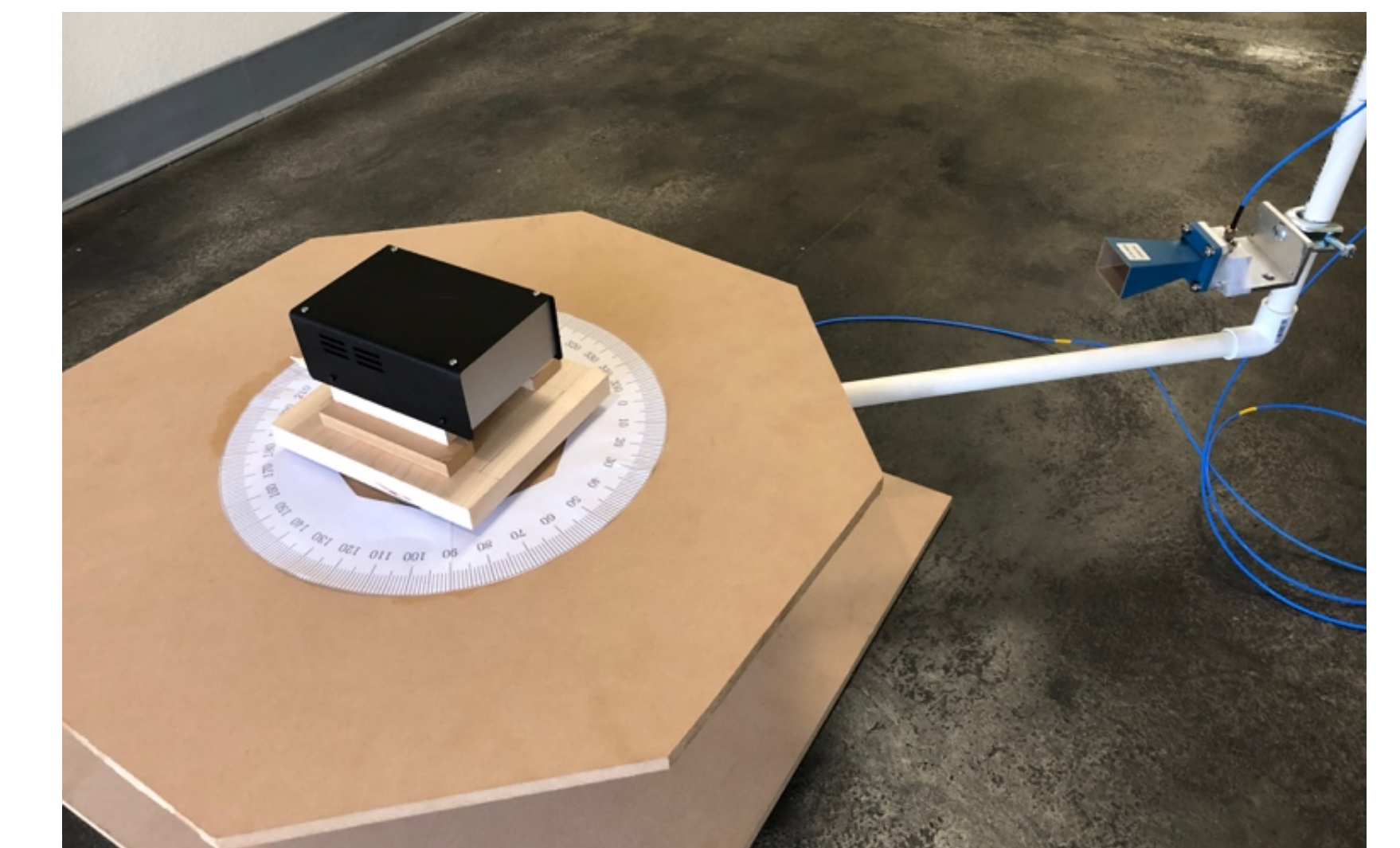
- Simulated and measured reflection coefficient of Feed 2 (for worst case emission) when there is no absorber (a), with absorbing FSS (b), and with microwave absorber (c)



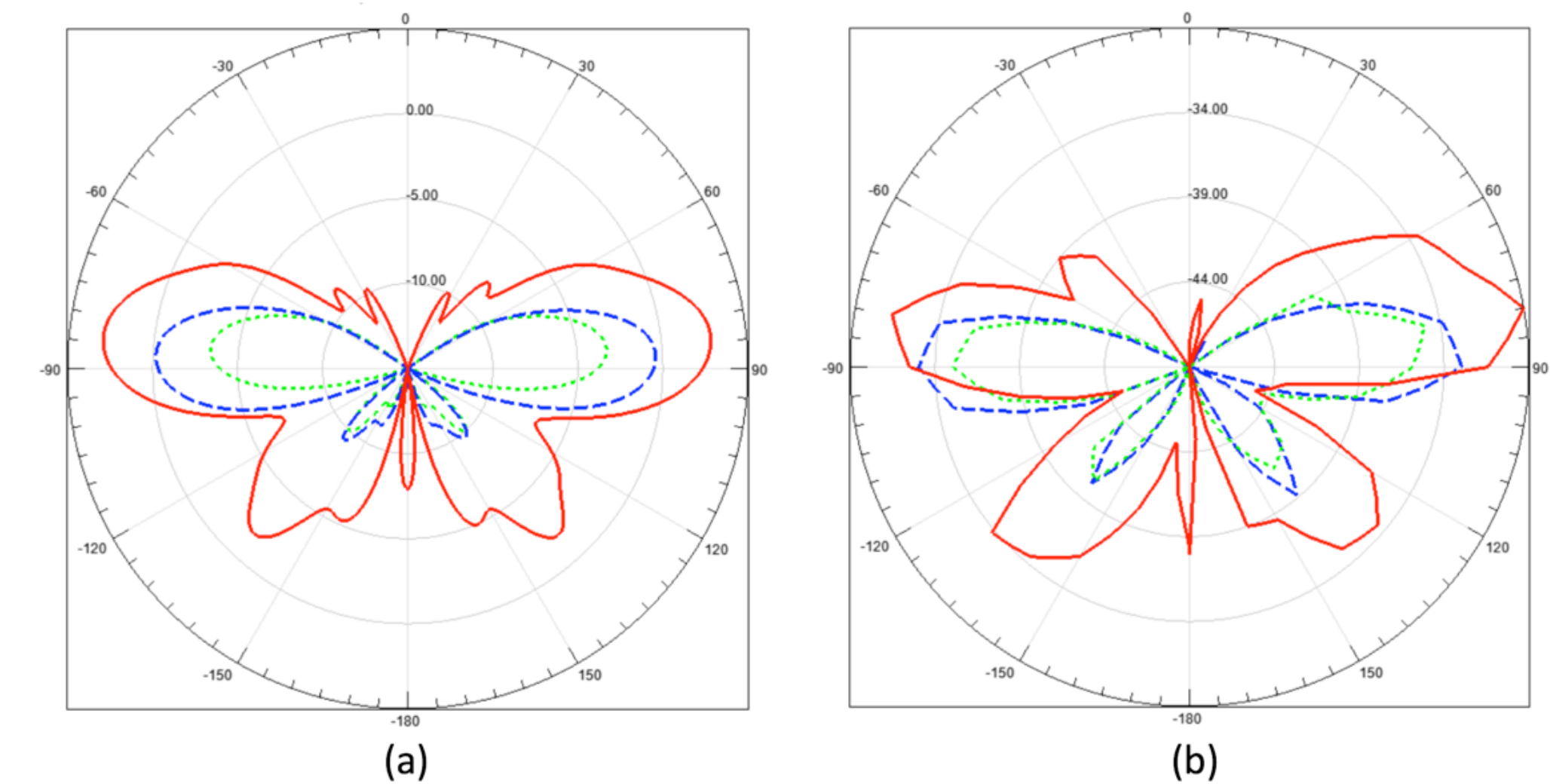
- Measured coupling from Feed 2 to other Feeds (worst case emission) when there is no absorber (a), with absorbing FSS (b), and with microwave absorber (c)



- Low-cost in-house set-up developed for over-the-air emission tests
- Cylindrical pattern measurement done by using a table that turns to freely rotate the probe antenna around the prototype box
- Probe: a horn antenna with 10 dB gain at 8 GHz at the distance of 53 cm from the center



- (a) Simulated, and (b) measured radiation patterns of emissions outside the prototype box



## Conclusions and Future Work

- Effect of rise time and delay mismatch is studied to show why there is emission at 8 GHz
- Effect of FSS and absorber on return loss and coupling is studied and considered in absorber effectiveness
- FSS shows 6 dB and microwave absorber shows 3-4 dB of emission reduction compared to box without absorber
- Future work is to study the FSS design and its effectiveness when placed closer to the radiation sources



Santa Clara University

School of Engineering

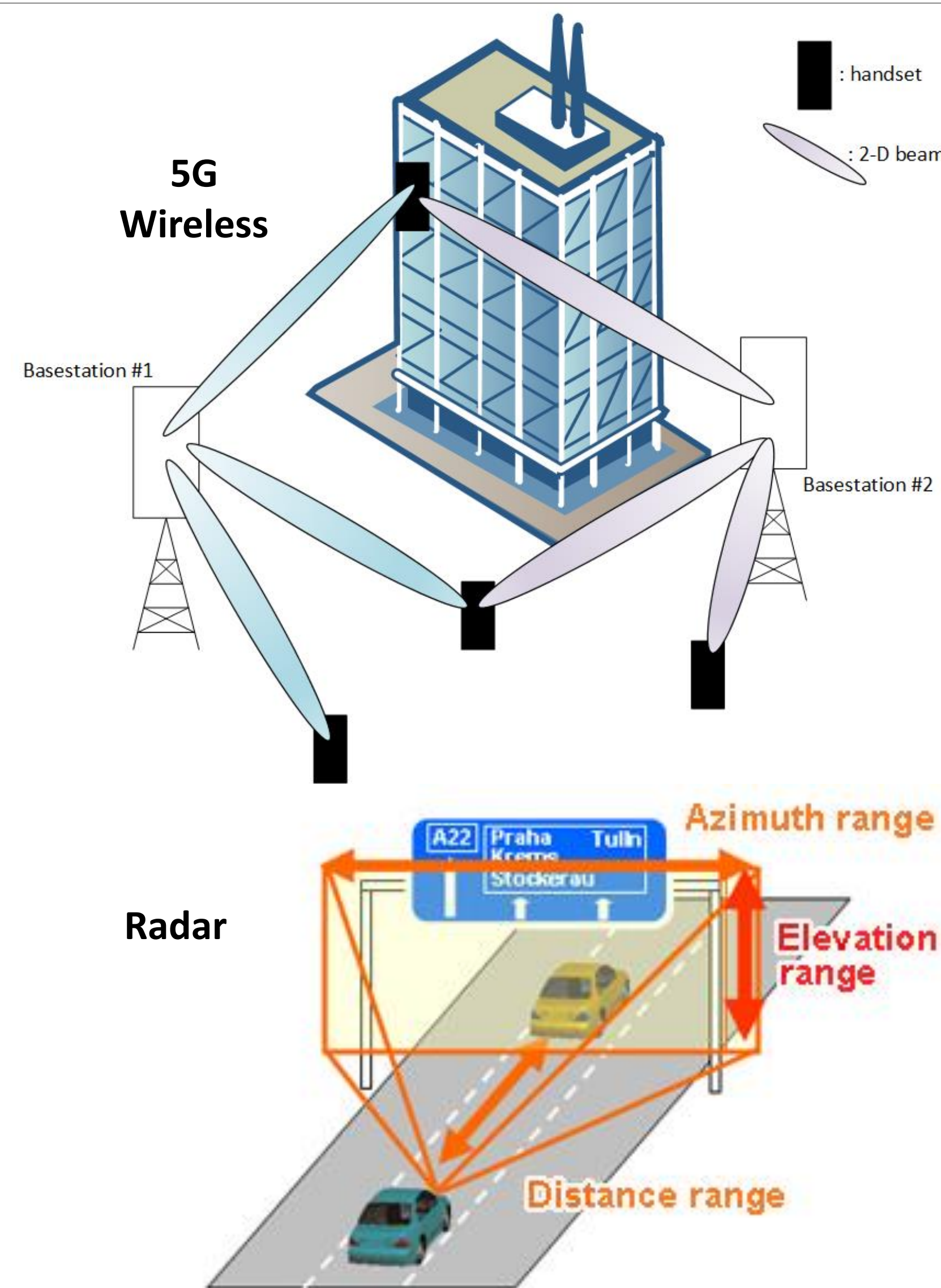
# Millimeter-wave 2-D Beam Steering Planar Array

Benjamin Horwath, PhD Student; Dr. Ramesh Abhari, Advisor  
Department of Electrical Engineering



**Motivation:** Many emerging radar and 5G applications use mm-wave spectrum

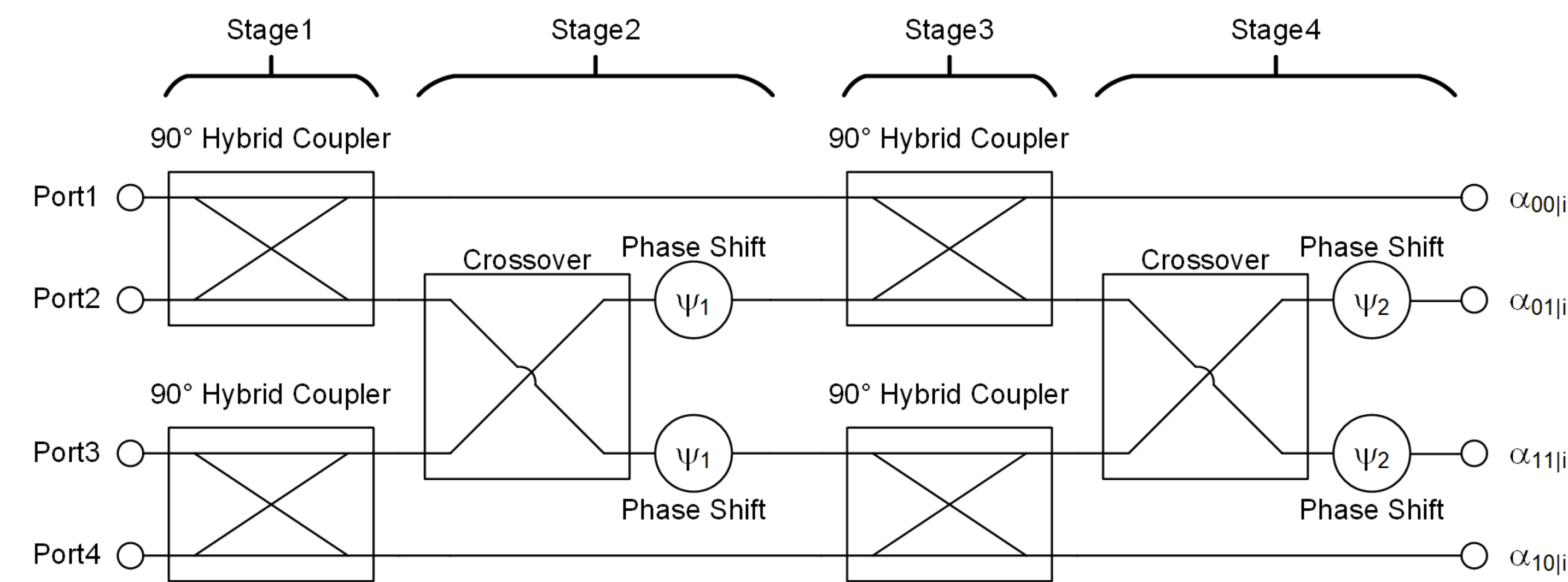
- **Benefits:**
  - Available bandwidth in 57-81GHz range, meaning higher data rates and better quality of service
  - Feature sizes are smaller ( $\sim \lambda_0/2$ ), enabling smaller antennas and easier mobile integration
- **Drawbacks:**
  - Higher losses, sensitivity to parasitics, discontinuities, and fabrication tolerances
  - Industry addresses with arrays, but this can be cost prohibitive for mobile devices
  - Need scanning beyond 1-D to bring more spatial resolution between users and cells



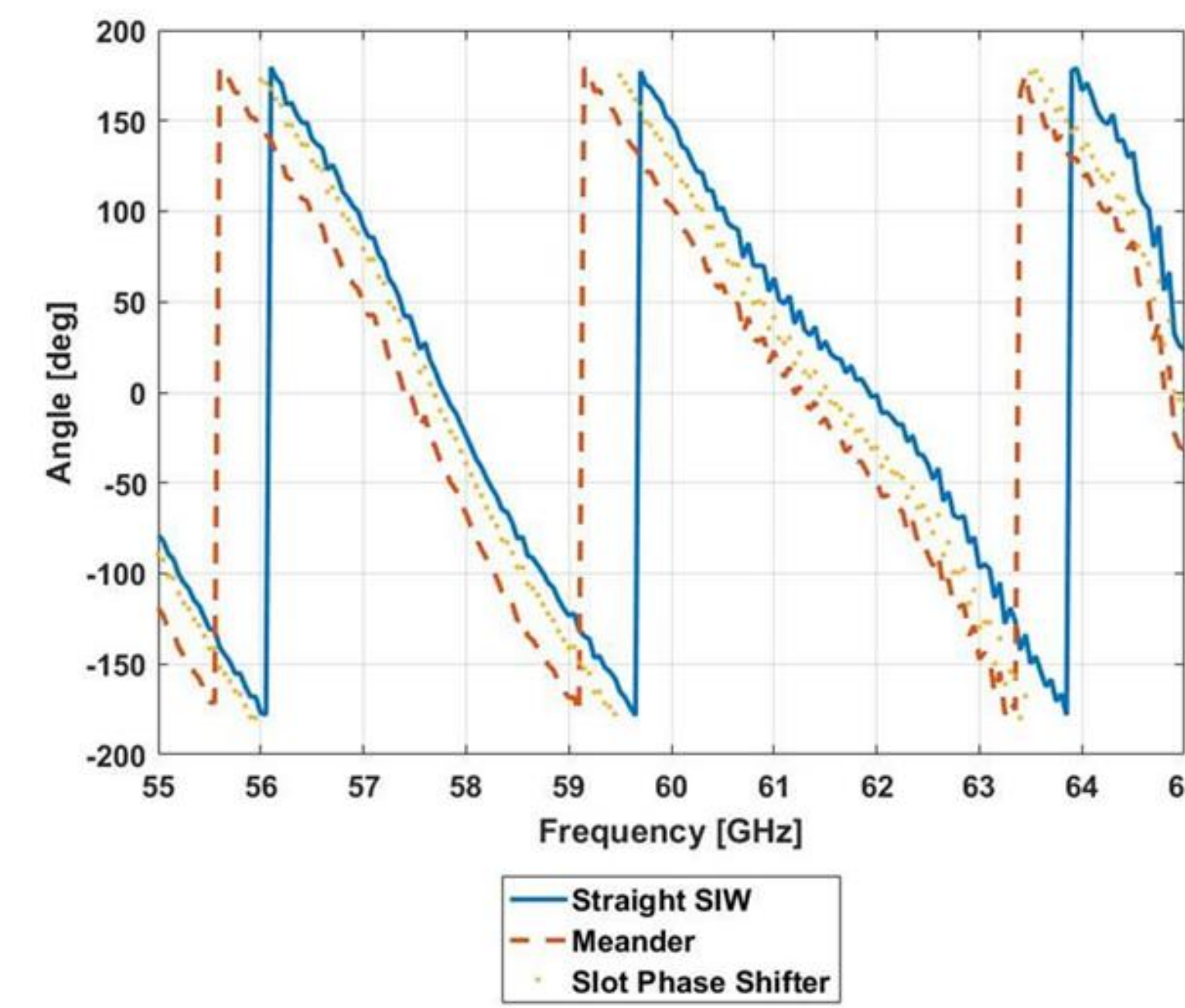
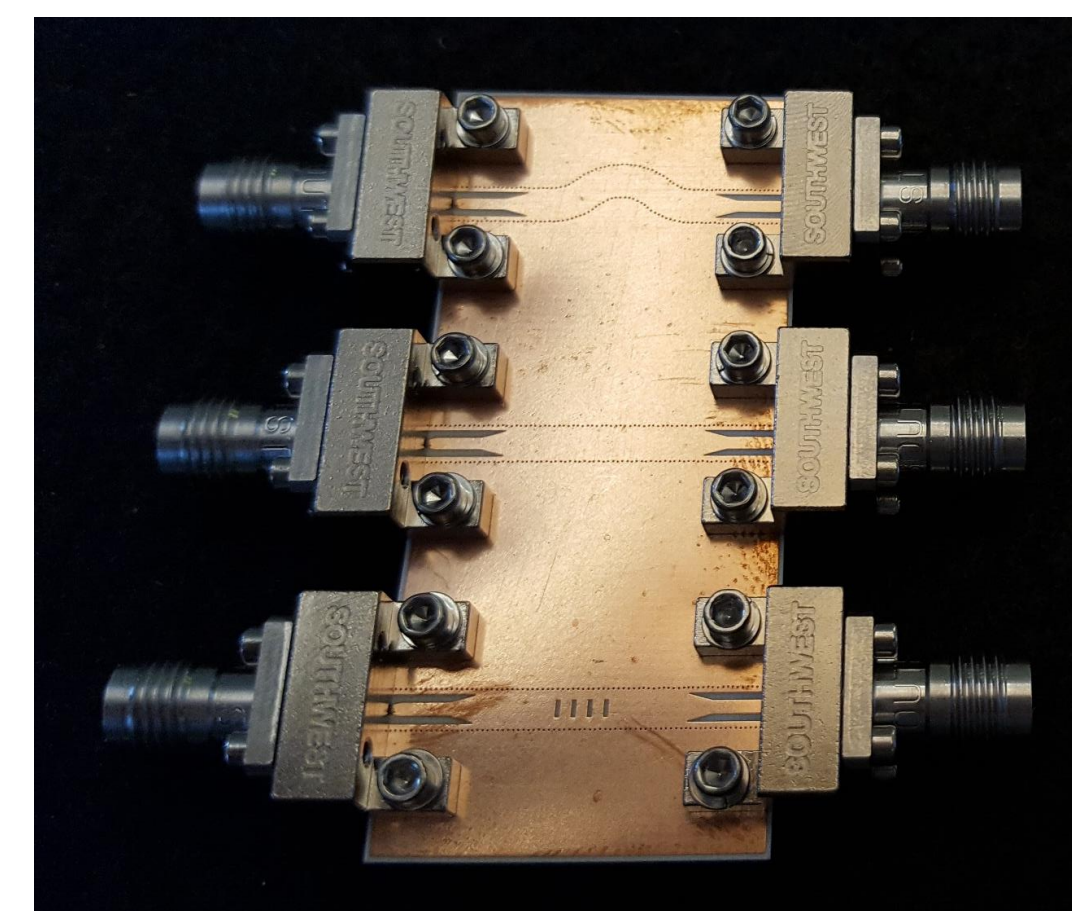
**Objective:** Passive 2-D beam steering!

- Using a passive beam-steering front-end leads to an array system with lower cost and power consumption
- Introduce a fully-integrated passive 2-D beam-steering to mitigate losses, discontinuity effects, interference in a low-cost package
- Develop a test system for experimental evaluations

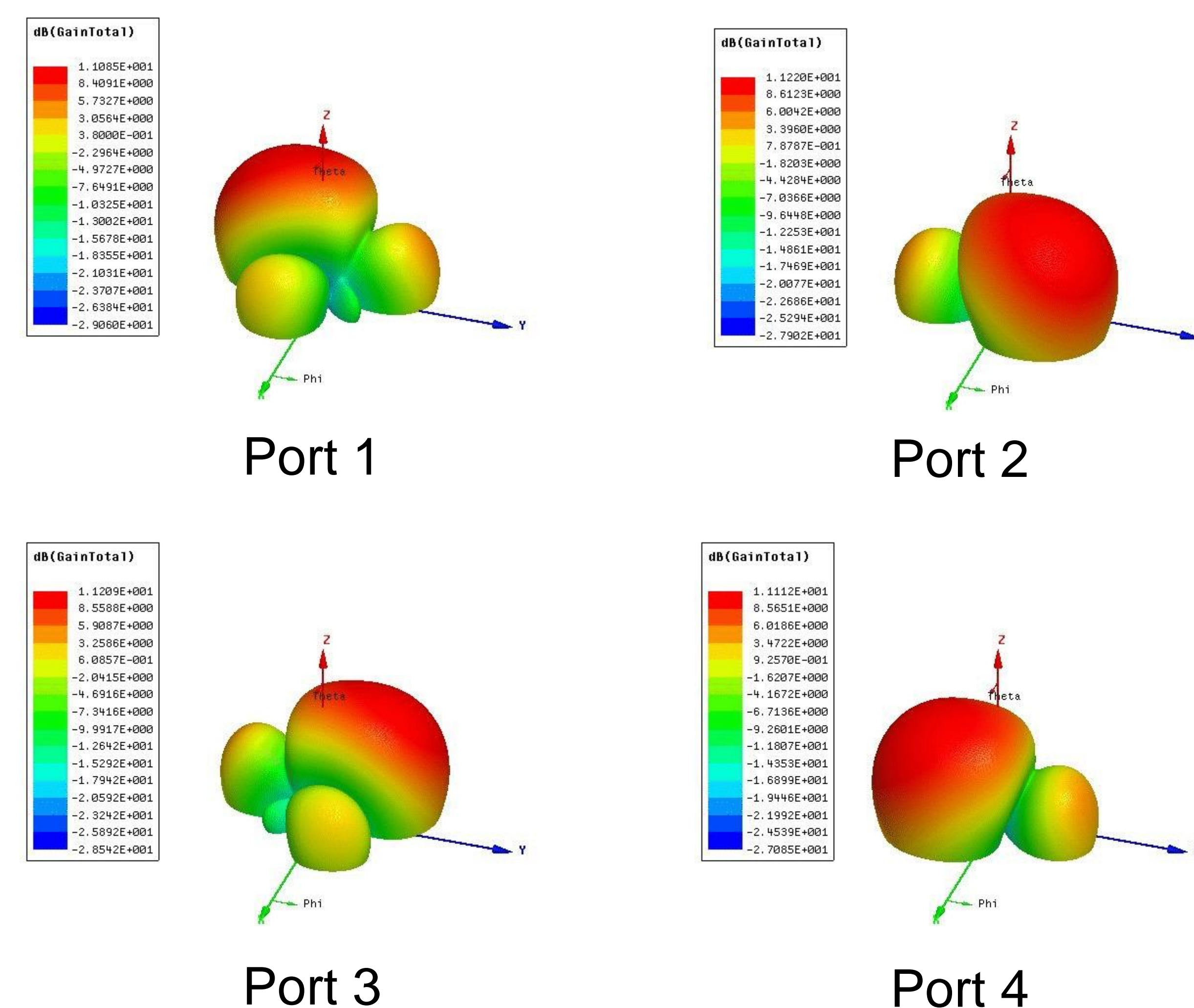
## Passive Beam Steering with the Butler Matrix:



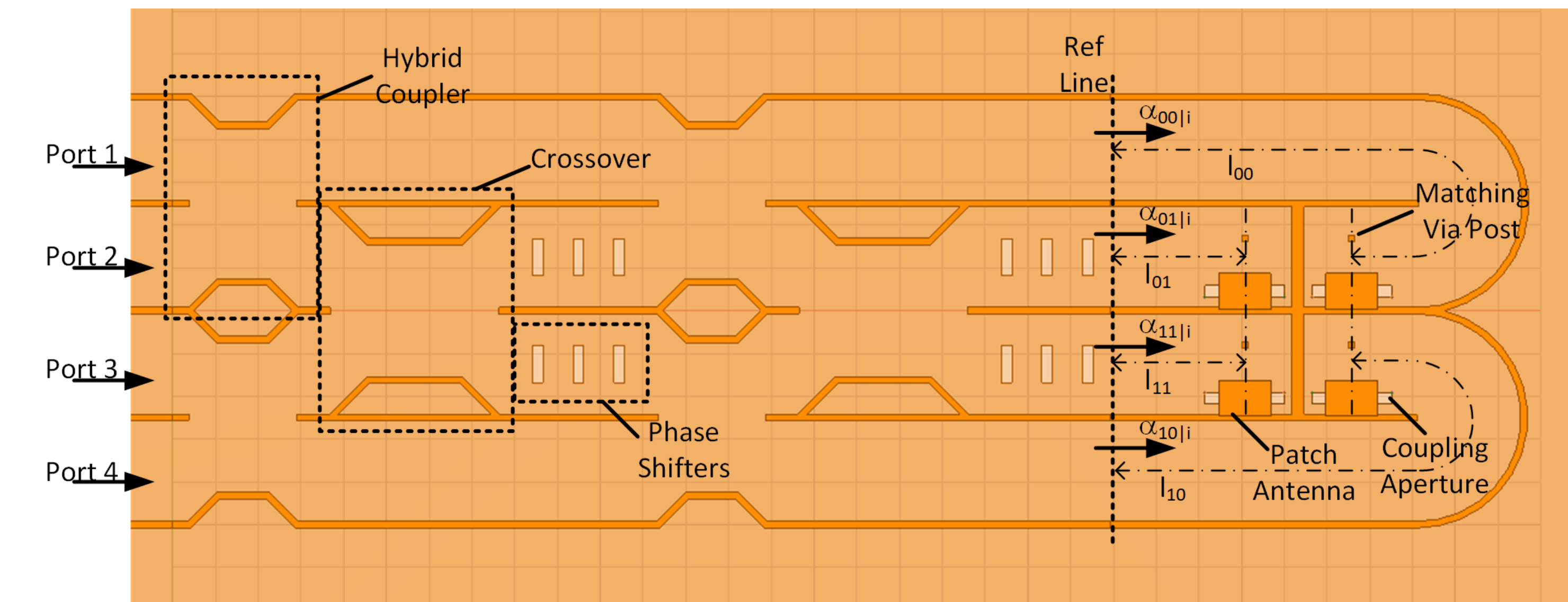
## Substrate Integrated Waveguide (SIW) Phase Shifter:



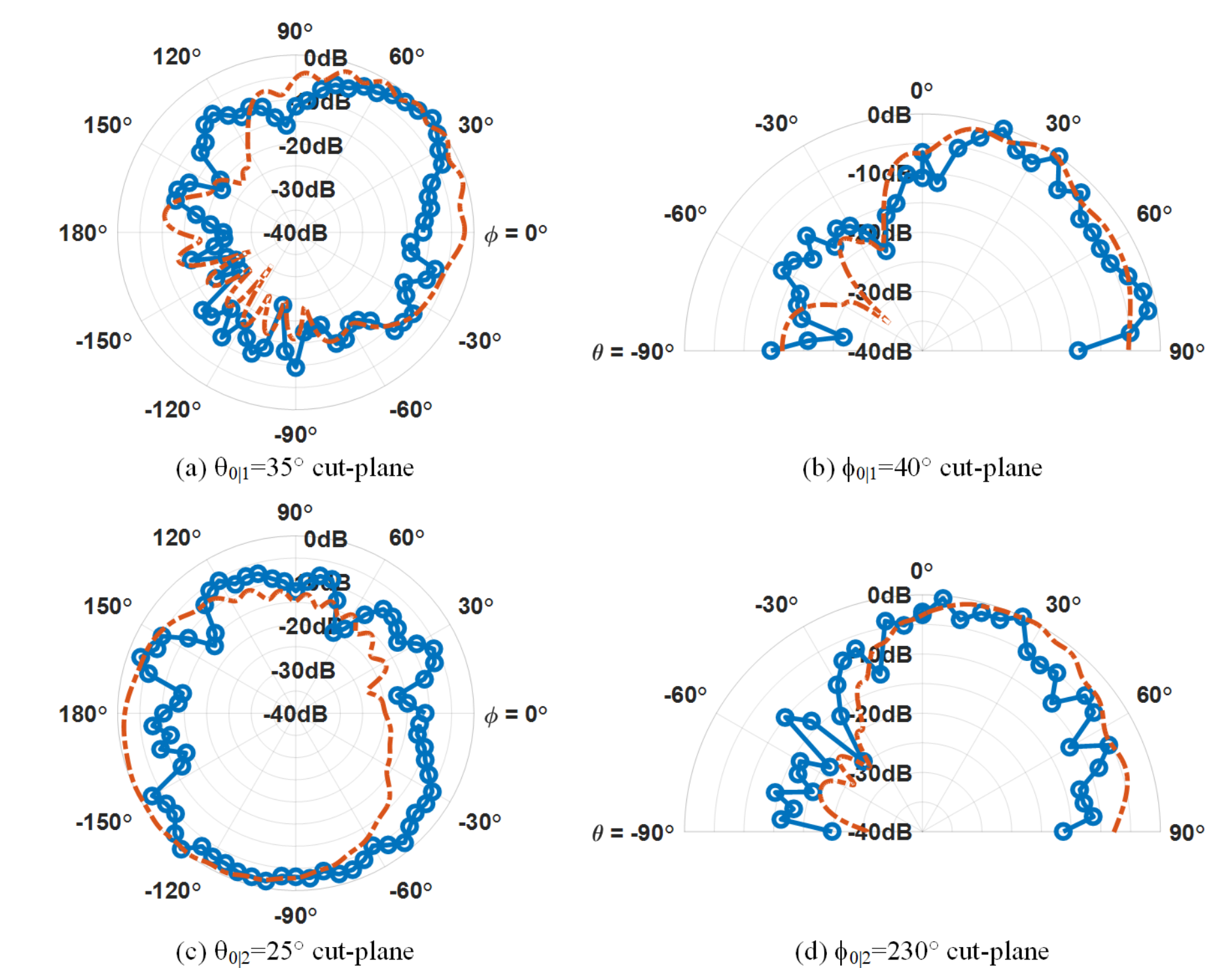
## 2-D Beam Steering Achieved:



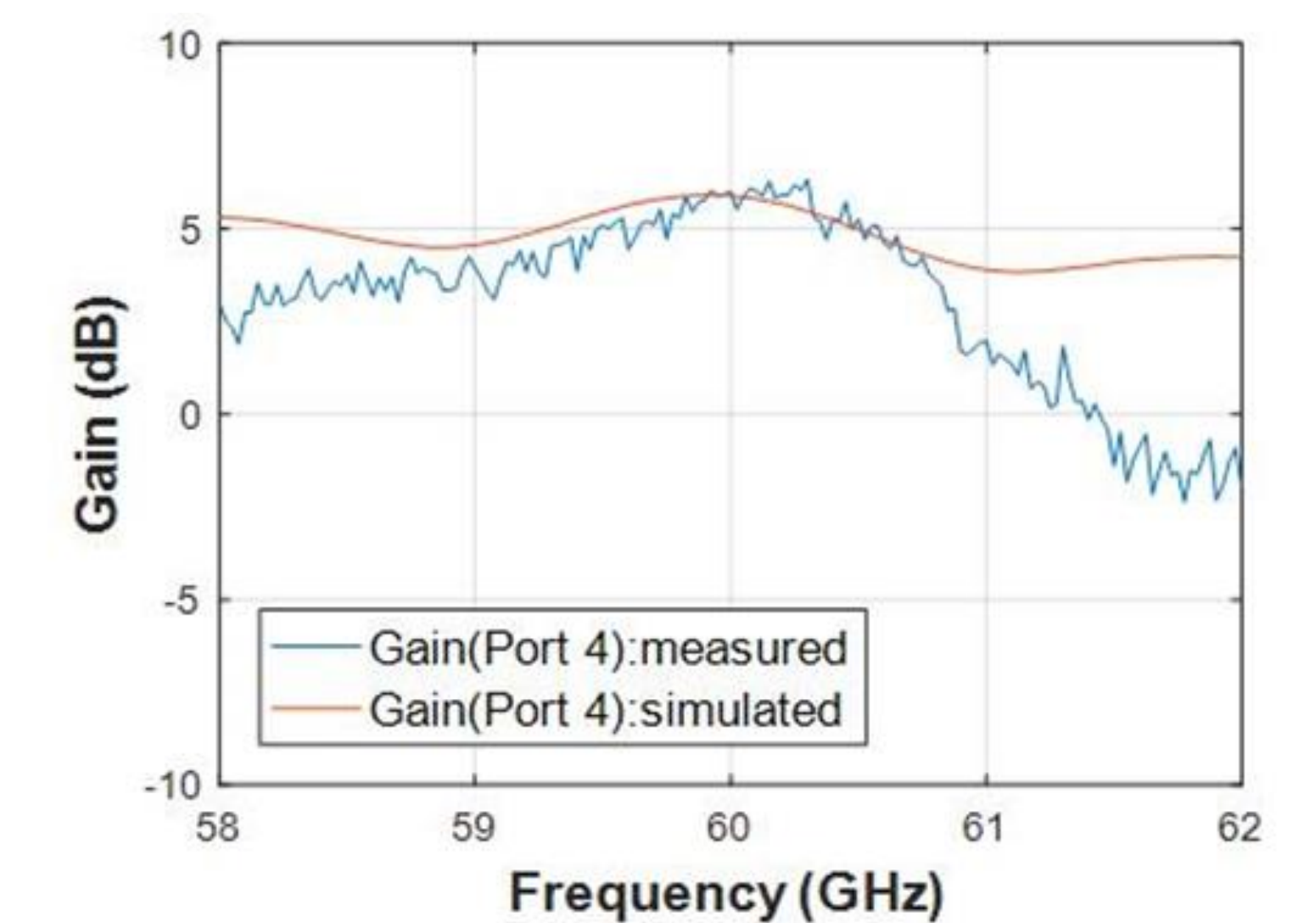
## Fully-integrated SIW Butler Matrix with planar patch array:



Measured field patterns:



Measured gain over frequency:



## Conclusions: Design feasibility confirmed

- First ever 4x4 Butler Matrix modified to achieve 2-D beam steering with an integrated 2x2 planar patch antenna array in SIW technology
- Field patterns and gain measured at SCU to achieve beam switching at  $\theta_0=30\pm 5^\circ$  and  $\phi_{0i}=40^\circ, 120^\circ, 230^\circ,$  and  $320^\circ$  with a gain of 5dB at 60 GHz

# A Discontinuous Charging Technique with Programmable Duty-Cycle for Switched-Capacitor Based Energy Harvesting Circuits in IoT Applications

PhD Student: Sanad Kawar. Advisors: Shoba Krishnan and Khaldoon Abugharbieh  
Department of Electrical Engineering

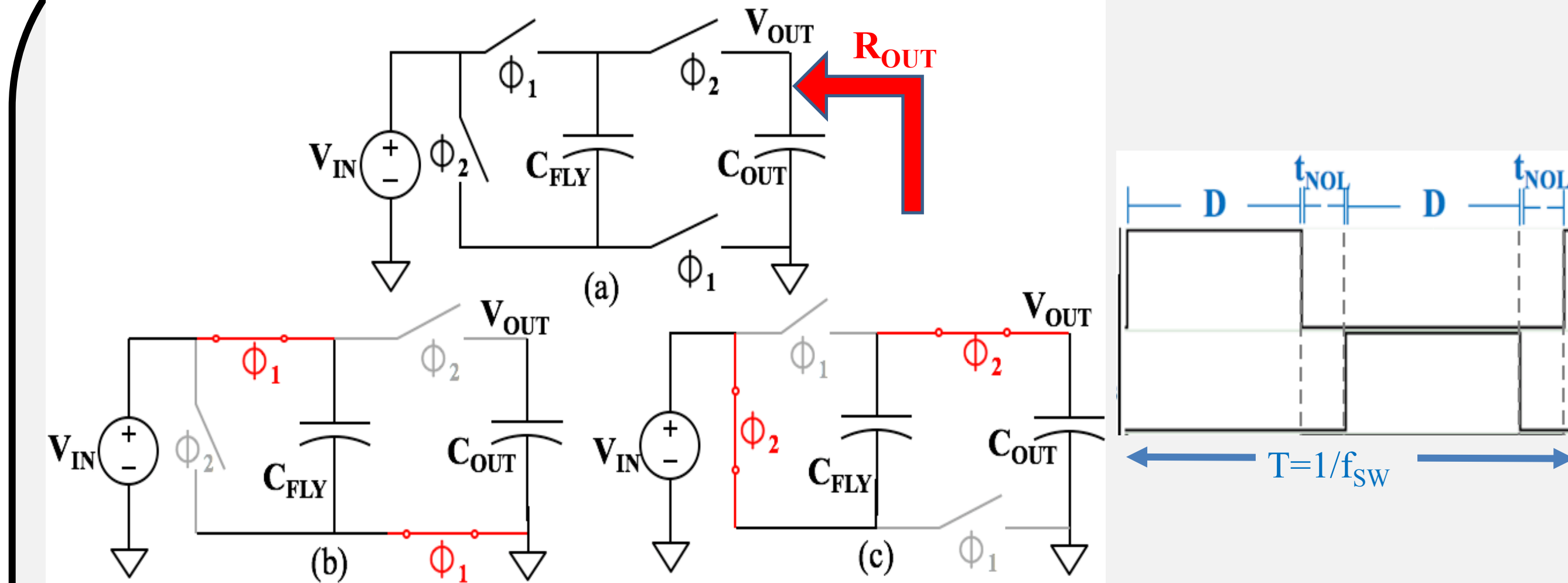
## Introduction

- The Internet of Things (IoT):**
  - Enables intelligent monitoring and management
  - Small Wireless Sensor nodes (WSN) → battery powered
  - Limited battery capacity → periodic replacement costly/hard
- Solution: Energy harvesting (EH)**
  - Recharge batteries or storage capacitors
  - Energy-autonomous. Minimizes maintenance costs
  - Harvest from DC sources (light and thermal), AC (vibration) or RF

## Challenges

- Harvested voltage too low → Need to boost voltage
  - Solar cell typical output ~0.3-0.6V
  - Too low to charge batteries or power CMOS
- Environment-dependent energy
  - mm-scale solar cell: 20nW-200uW depending on illuminance
- Low ambient power levels → Difficult to achieve high efficiency
  - Quiet, cold and/or dark environment : pW-nW in some applications

## Ideal Voltage Doubler



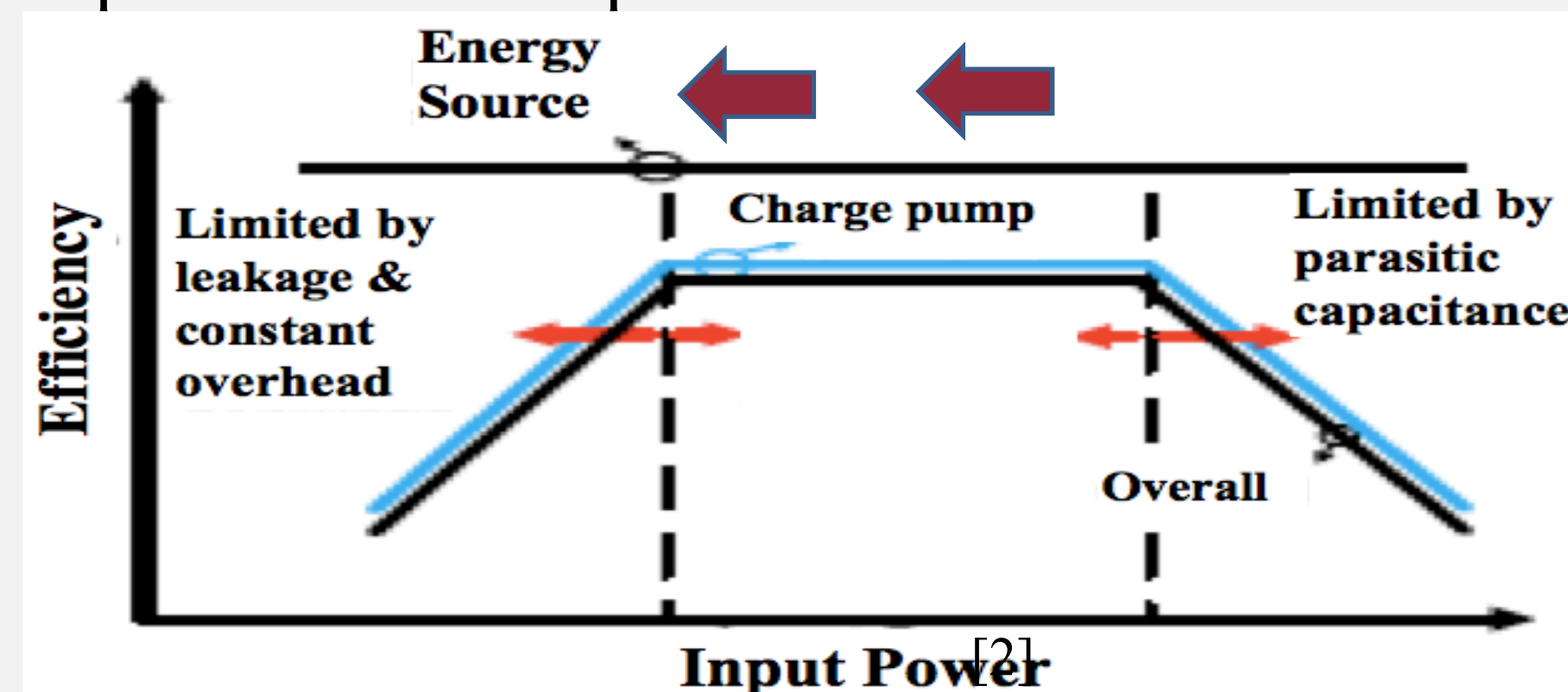
- Phase 1 :  $C_{FLY} \parallel V_{IN} \rightarrow$  Charge  $C_{FLY}$  to  $V_{IN}$ .
- Phase 2 :  $V_{IN}$  at bottom plate of  $C_{FLY} \rightarrow V_{OUT} = 2V_{IN}$
- $\phi_1$  and  $\phi_2$  non-overlapping

$R_{OUT}$  models two losses due to:

- Capacitors Charge Redistribution →  $R_{SSL} = \frac{1}{f_{SW} C_{FLY}}$
- Switch Conduction →  $R_{FSL} = \sum_i \frac{R_{SWi}}{D}$

## Objective

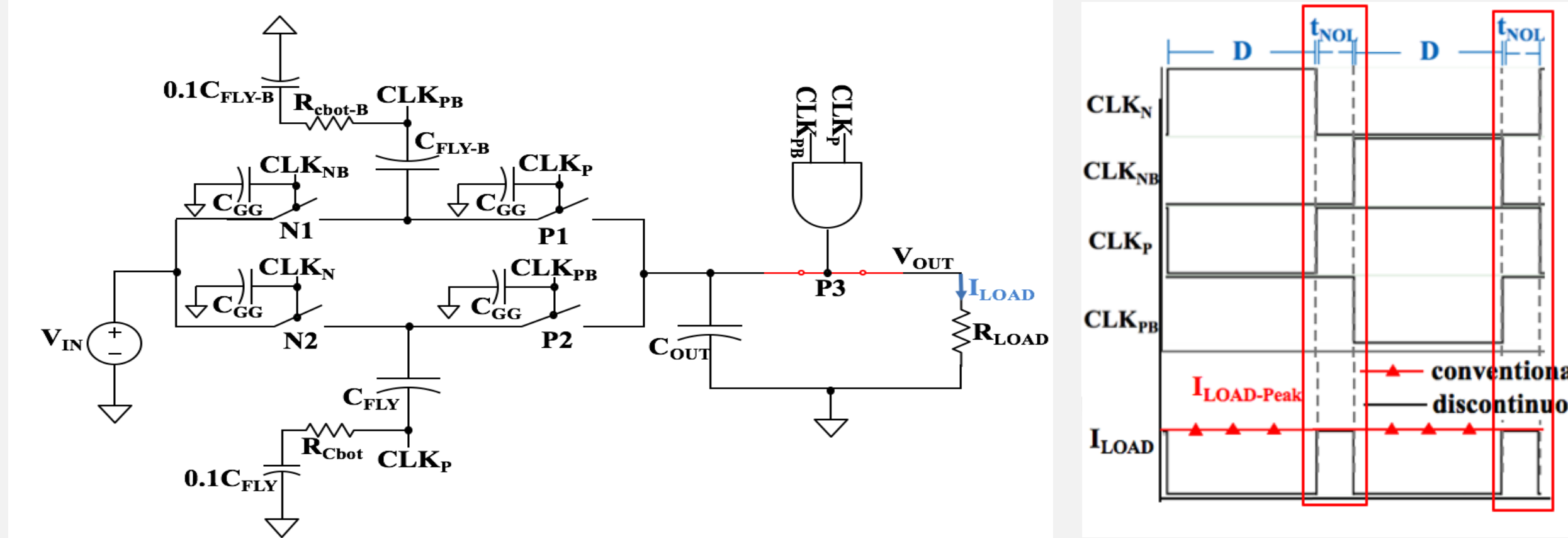
Adjust average power delivered to the load → tune the max. efficiency based on expected ambient power levels



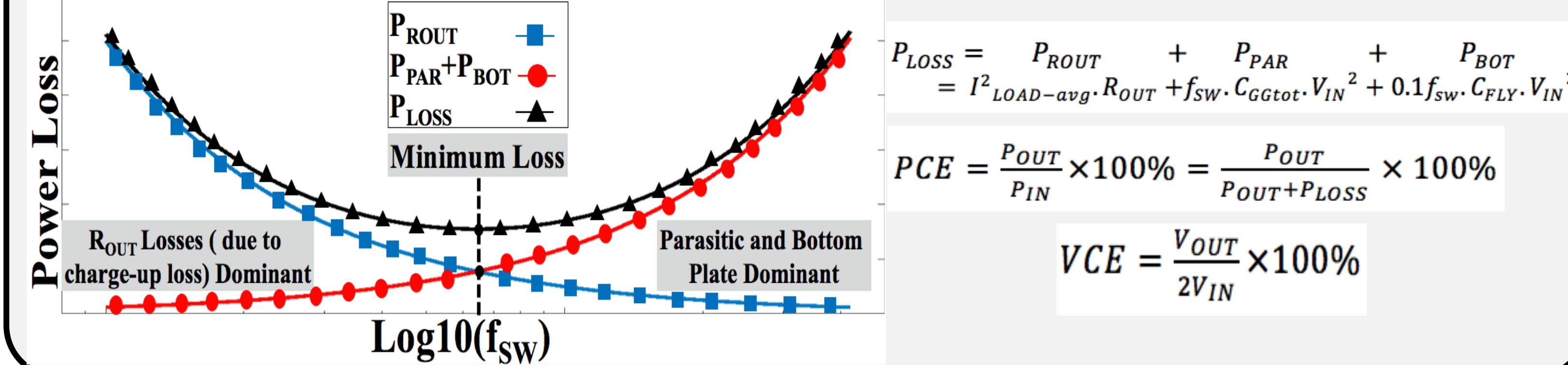
## Proposed Design Features

- Key Feature: Deliver current only during clock non overlap → Control average current delivered to the load**
- Done by gating clocks to control switch P3

Conventional ( Continuous)	Proposed ( Discontinuous)
$t_{NOL}$ minimum for Duty cycle ~50%	Up to 20% of period
Continuously provides current to load	Provides current to the load only during $t_{NOL}$
$I_{LOAD-AVG} = I_{LOAD-PEAK} = V_{OUT}/R_{LOAD}$	$I_{LOAD-AVG} = 2 \cdot t_{NOL} \cdot I_{LOAD-PEAK} = (1-2D) \cdot V_{OUT}/R_{LOAD}$



## Power Losses and Efficiency



## Achieving Max. Efficiency at Anticipated $P_{IN}$

- Supply current only during clock non-overlap.
- $I_{LOAD-AVG}$  in discontinuous mode smaller than in conventional

Converter obtains same  $P_{ROUT}$  and  $V_{OUT}$  at higher  $R_{OUT}$

$$V_{OUT} = 2V_{IN} - I_{LOAD-avg} \cdot R_{OUT} \quad P_{ROUT} = I_{LOAD-avg}^2 \cdot R_{OUT}$$

$R_{OUT} \propto (1/f_{SW}) \rightarrow$  converter obtains same  $P_{ROUT}$  and  $V_{OUT}$  at lower  $f_{SW}$

$$R_{SSL} = \frac{1}{f_{SW} C_{FLY}}$$

Lower parasitic bottom plate and switching losses

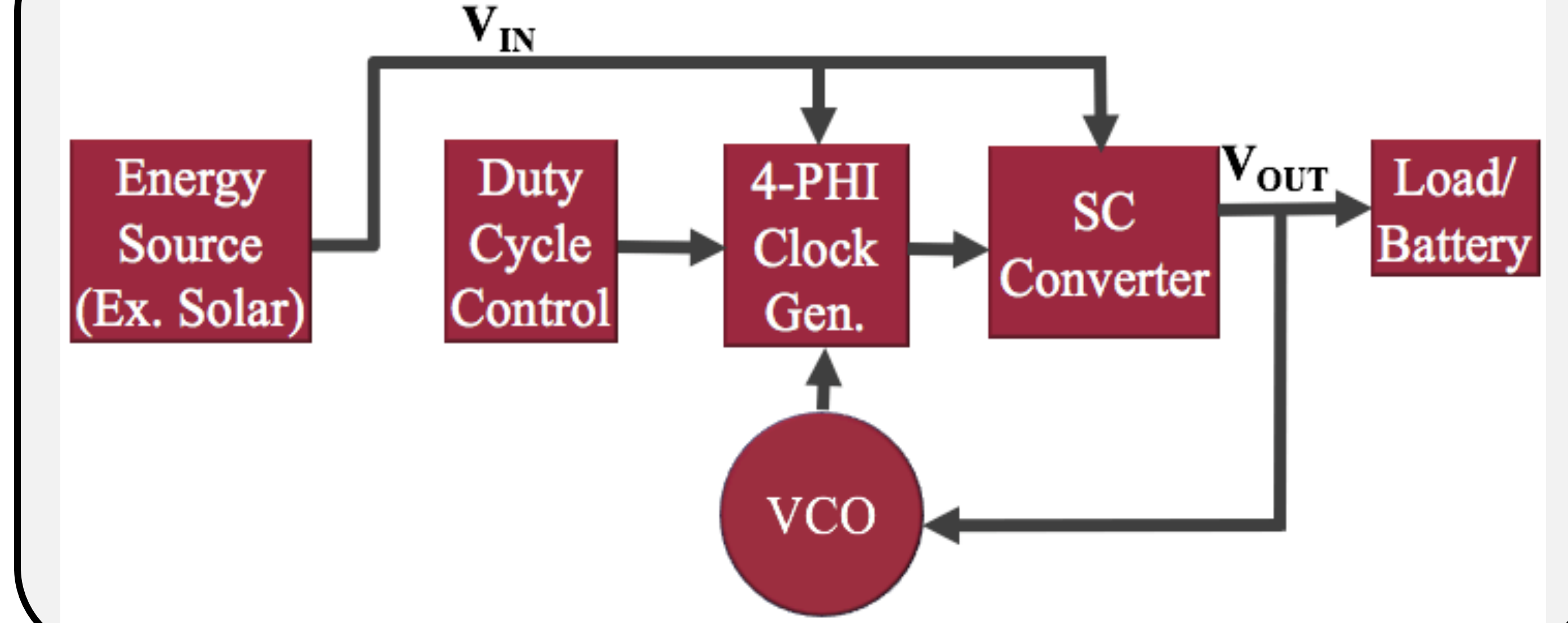
$$P_{PAR} + P_{BOT} = f_{SW} \cdot C_{GGtot} \cdot V_{IN}^2 + 0.1 f_{SW} \cdot C_{FLY} \cdot V_{IN}^2$$

Converter achieves same power and voltage conversion efficiencies with less input power due to minimized losses.

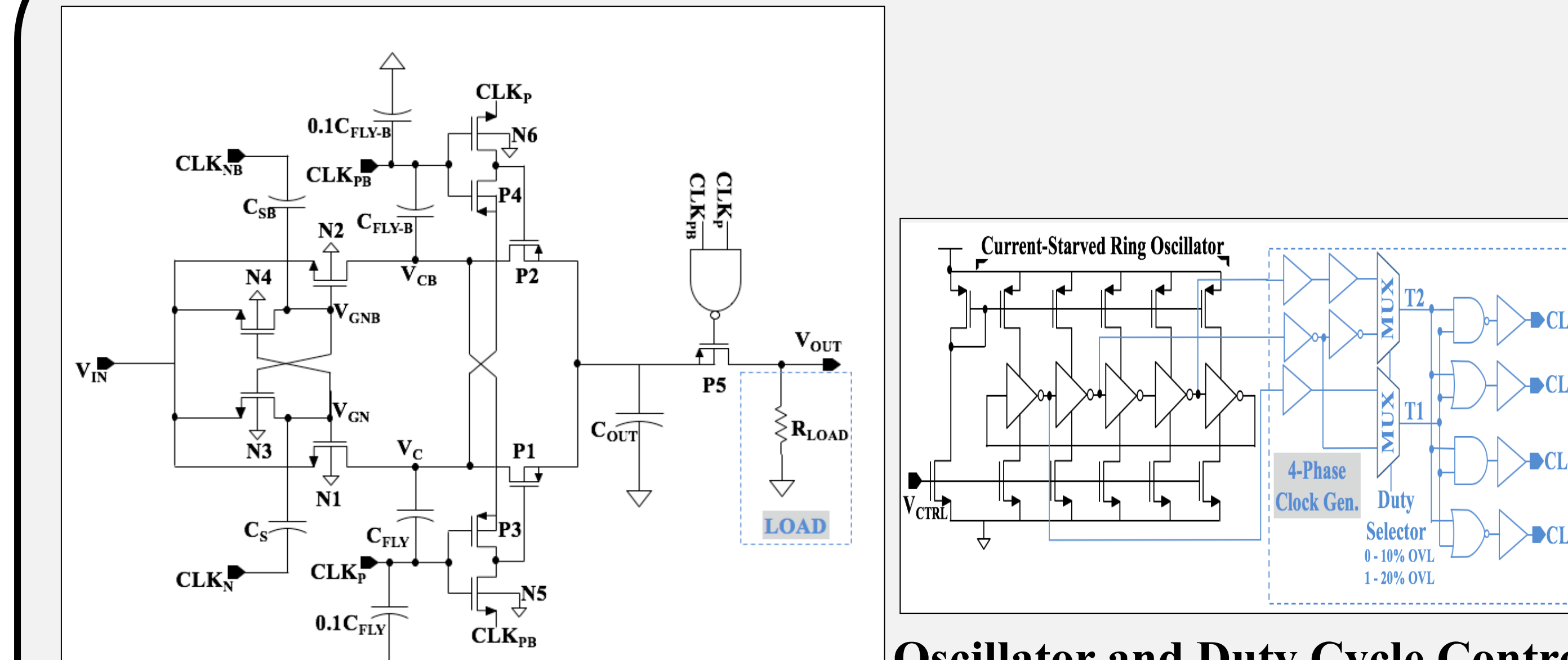
## References

[1] International Electrotechnical Commission, "Internet of Things: Wireless Sensor Networks," 2014. [Online]. Available: <http://www.iec.ch/whitepaper/pdf/iec-WP-internetofthings-LR-en.pdf>.  
 [2] X. Liu, L. Huang, K. Ravichandran, and E. Sanchez-Sinencio, "A Highly Efficient Reconfigurable Charge Pump Energy Harvester With Wide Harvesting Range and Two-Dimensional MPPT for Internet of Things," *IEEE J. Solid-State Circuits*, vol. 51, no. 5, pp. 1302–1312, May 2016.  
 [3] G. Chowdhary and S. Chatterjee, "A 300-nW Sensitive, 50-nA DC-DC Converter for Energy Harvesting Applications," *IEEE Trans. Circuits Syst. Regul. Pap.*, vol. 62, no. 11, pp. 2674–2684, Nov. 2015.  
 [4] M. R. Elhebeary, M. A. A. Ibrahim, M. M. Aboudina, and A. N. Mohiieldin, "Dual-Source Self-Start High-Efficiency Microscale Smart Energy Harvesting System for IoT," *IEEE Trans. Ind. Electron.*, vol. 65, no. 1, pp. 342–351, Jan. 2018.  
 [5] W. Jung et al., "An Ultra-Low Power Fully Integrated Energy Harvester Based on Self-Oscillating Switched-Capacitor Voltage Doubler," *IEEE J. Solid-State Circuits*, vol. 49, no. 12, pp. 2800–2811, Dec. 2014.  
 [6] D. Maksimovic and S. Dhar, "Switched-capacitor DC-DC converters for low-power on-chip applications," in *IEEE Power Electronics Specialists Conf.*, 1999, vol. 1, pp. 54–59.  
 [7] M. D. Seeman, "A Design Methodology for Switched-Capacitor DC-DC Converters," University of California, Berkeley, CA, UCB/ECS-2009-78, May 2009.  
 [8] T. Ozaki, T. Hirose, H. Asano, N. Kuroki, and M. Numa, "Fully-Integrated High-Conversion-Ratio Dual-Output Voltage Boost Converter With MPPT for Low-Voltage Energy Harvesting," *IEEE J. Solid-State Circuits*, vol. 51, no. 10, pp. 2398–2407, Oct. 2016.

## System Block Diagram



## Circuits

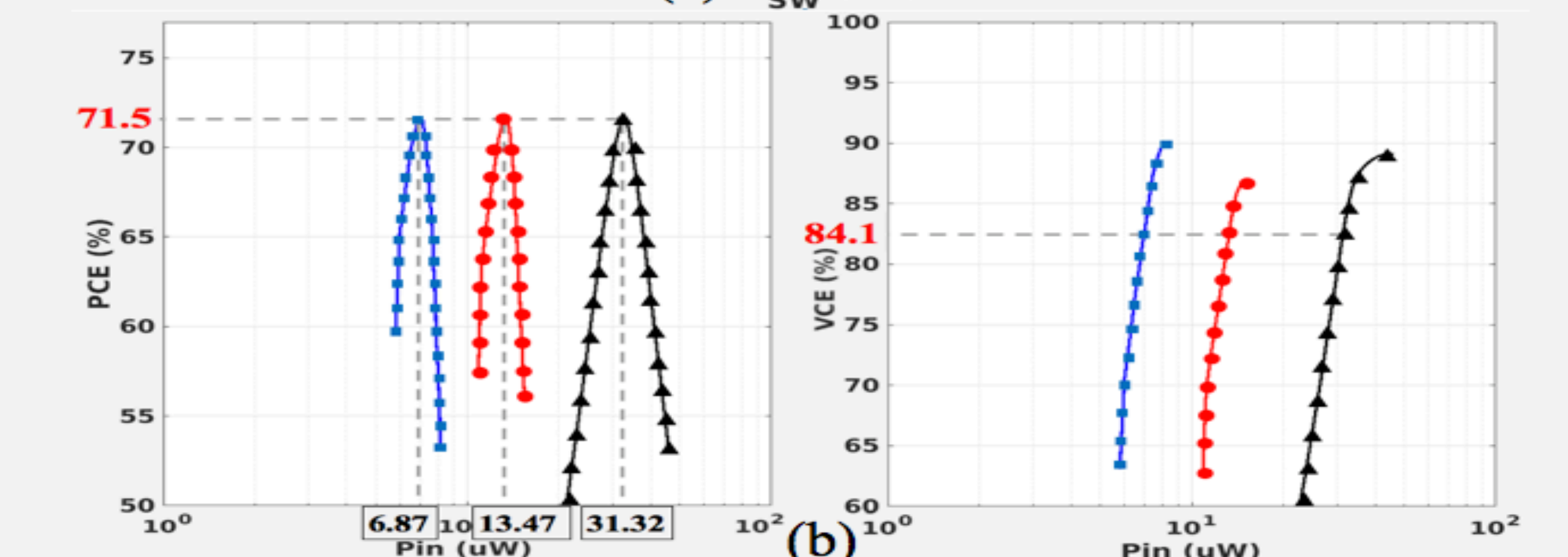
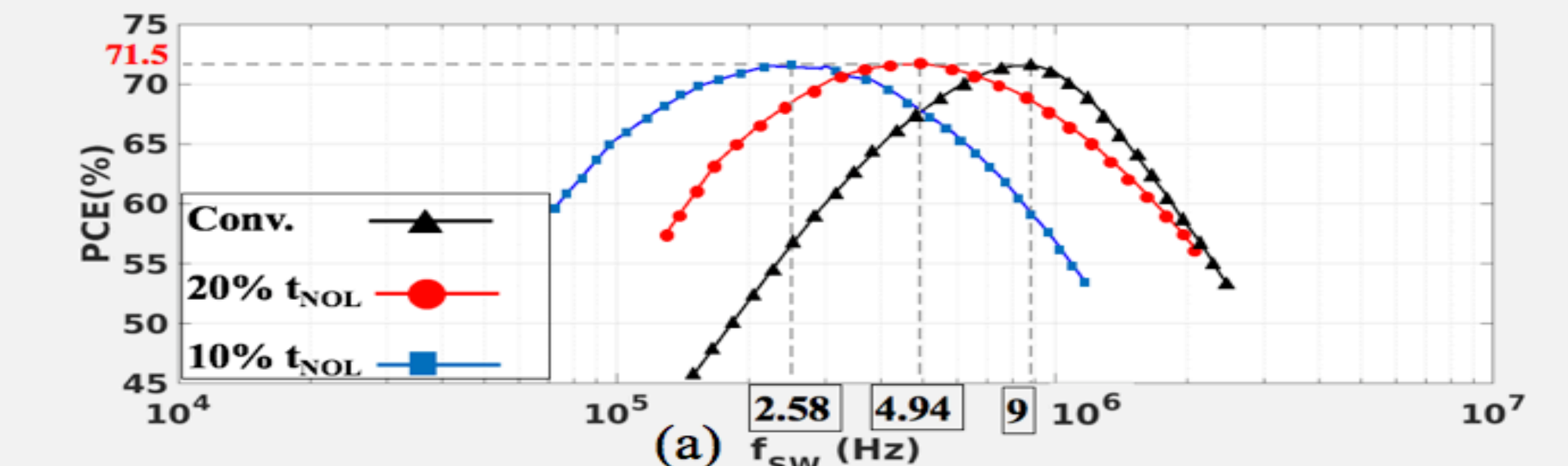


**Cross-Coupled SC Voltage doubler**  
Incorporates discontinuous charging

**Oscillator and Duty Cycle Control**  
Selects non-overlap by selecting which phases pass through logic

## Transistor-Level Simulations Results

- Proposed system tunes peak PCE to desired input power
- For given load, peak efficiency occurs at up to 78% lower  $P_{IN}$



Values at Peak PCE	Conventional	Discontinuous 20% $t_{NOL}$	Discontinuous 10% $t_{NOL}$
fsw(KHz)	900	494	258
Input Power (uW)	31.32	13.47	6.87
Peak PCE		71.5%	

## Future Plans

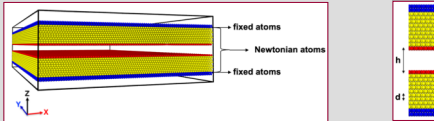
Currently working on incorporating clock duty cycle/non-overlap along with switching frequency to design a two-dimensional maximum power point tracking scheme.

## Abstract

With the use of molecular dynamics simulations, the contact between two substrates, made of the same material, is studied for three FCC metals (Cu, Ag, and Al). The effect of material properties, temperature, misorientation, and initial gap between substrates on the JC behavior and defect generation following contact is investigated.

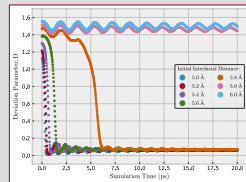
## Background

Nanoscale contact between two substrates [1]:

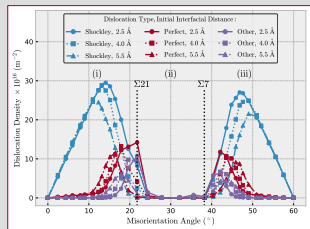
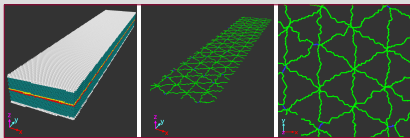


1. Jump-to-Contact (JC) behavior:

$$D(t) = \frac{|h(t)-d|}{d}$$



2. Dislocation generation at the interface:



## Objectives

The main purpose of this study was to advance our previous study [1] by comparing three metals (Copper, Silver, and Aluminum) with each other, in terms of the following:

1. JC behavior:

The JC phenomenon is a competition between the short-range attractive forces between two surfaces and the stiffness of substrates. So, the JC behavior is expected to be different in different materials.

2. Evolution of interfacial dislocations:

After occurrence of JC, dislocations are generated at the interface to accommodate the misorientation between substrates. These dislocations are expected to multiply, especially since some level of strain is always present in our system due to existence of initial gap. Dislocation multiplication is of great scientific importance since it affects the distribution/density of dislocations, resulting in change in many properties of materials.

## Methods

- Method: Molecular Dynamics
- Simulation package:
- Visualization and defect analysis: Open Visualization Tool
- Data analysis:
- Normalized initial gap size:
- Elastic Strain:

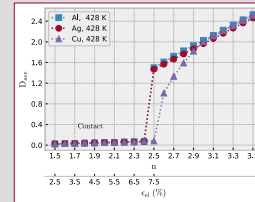
$$n = \frac{h_{initial}}{d}$$

$$\epsilon_{el} (\%) = \frac{0.5 \times (h_{initial} - h_{final})}{10 \times d} \times 100$$

$$h_{final} \approx d \rightarrow \epsilon_{el} (\%) \approx 5 \times (n - 1)$$

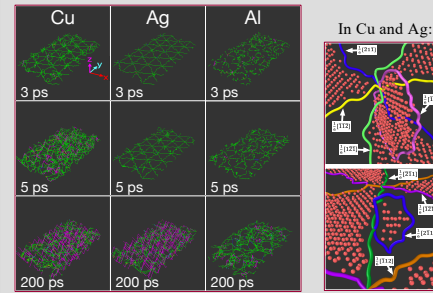
## Results

1. JC behavior: Cu presents a smooth behavior for separations right above the critical distance for JC.

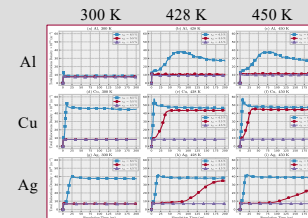


2. Dislocation multiplication:

Mechanisms: dislocation nucleation from the interface (in Cu or Ag) or cross-slip (in Al)



Effect of material type, temperature, strain, and misorientation on the possibility of occurrence:



Strain	Dislocation multiplication occurs for:
5.00 %	$0 < \theta \leq 2.45^\circ$
5.75 %	$0 < \theta \leq 10.99^\circ$
6.50 %	$0 < \theta \leq 21.79^\circ$

## Discussion

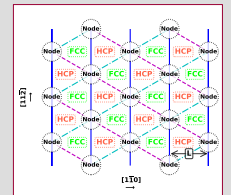
- Smooth JC behavior of Cu is due to its high surface energy and Young's modulus.
- Cross-slip occurs more predominantly in Al because of its high stacking fault energy.
- Compared to Ag, Cu is more prone to dislocation multiplication, because of its lower Peierls stress.
- Higher misorientation results in higher fraction of dislocation nodes, which decreases the strain value and possibility of multiplication.

	Al	Cu	Ag
$\gamma_{(111)} \left(\frac{mJ}{m^2}\right)$ [2]	634	1387	977
$E$ (GPa) [2]	69	125	78
$\gamma_{ISF} \left(\frac{mJ}{m^2}\right)$ [2]	117	53	26
$\tau_P$ (MPa) [3]	1.4	0.28	0.9

$$L = \frac{3 b_P}{4 \sin(\frac{\theta}{2})}$$

$b_P$ : Burgers vector of partial dislocations

$\theta$ : Misorientation angle



## Conclusions

- Cu exhibits a smooth JC behavior, as opposed to Ag and Al.
- Interfacial dislocations may multiply after contact, resulting in change in their density and distribution. Predominant mechanism for multiplication in Al is cross-slip, whereas in Cu and Ag it is the nucleation of new dislocations.
- Dislocation multiplication is more probable to occur at high temperatures, high strain values, and low misorientation angles close to zero.

## References

- Khajehvand, M., & Sepehrband, P. (2018). The effect of crystallographic misorientation and interfacial separation on jump-to-contact behavior and defect generation in aluminum. *Modelling and Simulation in Materials Science and Engineering*, 26(5), 055007.
- Sheng, H. W., Kramer, M. J., Cadore, A., Fujita, T., & Chen, M. W. (2011). Highly optimized embedded-atom-method potentials for fourteen fcc metals. *Physical Review B*, 83(13), 134118.
- Kamimura, Y., Edgawa, K., & Takeuchi, S. (2013). Experimental evaluation of the Peierls stresses in a variety of crystals and their relation to the crystal structure. *Acta Materialia*, 61(1), 294-309.
- De Hosson, J. T. M., & Vitek, V. (1990). Atomic structure of (111) twist grain boundaries in fcc metals. *Philosophical Magazine A*, 61(2), 305-327.

## Contact Information

mkhajehvand@scu.edu  
psepehrband@scu.edu

## Acknowledgment

This study was supported by the National Science Foundation and the School of Engineering at Santa Clara University.



# Multi-robot Transport and Manipulation of Objects

Fritz Huizenga

Advisor: Professor Christopher Kitts



## Abstract

This research focuses on the continued development of the multi-robot hybrid force/position control for simultaneous transport and manipulation of objects. A hybrid-based object controller for a two-robot system is tested to demonstrate the system's ability to push a bar along specified paths with a specified amount of force. An adaptive positioning technique is used to allow for more aggressive turning of an object by the cluster. Gazebo, a powerful simulation environment, new to the RSL, is being utilized to understand the behavior of the robots in a physics-based realm.

## Multi-Robot Applications

**Collaborative construction** – assembling flexible objects to form large structures (space telescopes, colonies on other worlds)

**Manufacturing** – perform multiple tasks in parallel which increases throughput (welding)

**Redundancy** – overcome single robot failures

## Virtual Reality

Gazebo supports a VR environment which helps developers and operators visualize system operation and enhances telerobotic control.

## Conclusion

A Cluster Space hybrid-based object controller can command a system of robots to transport an object along desired paths with a desired force. Torque applied to the object by the cluster can be varied with an adaptive positioning technique (sharp turns).

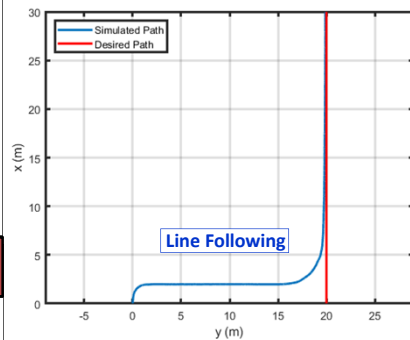
## Future Work

Design a 3-robot hybrid controller capable of simultaneous transport / reconfiguration for a jointed two link object.

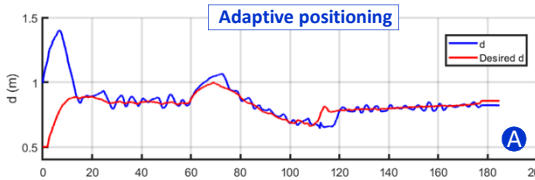
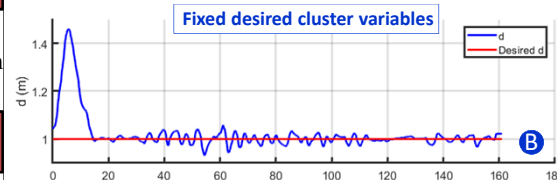
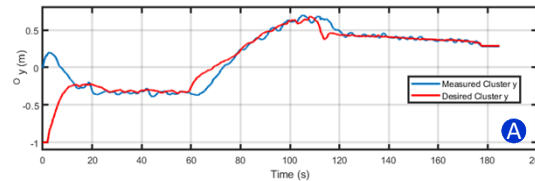
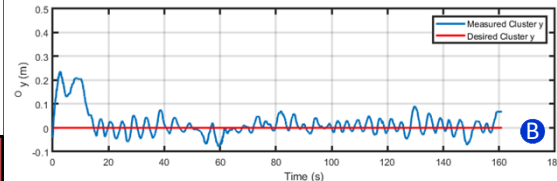
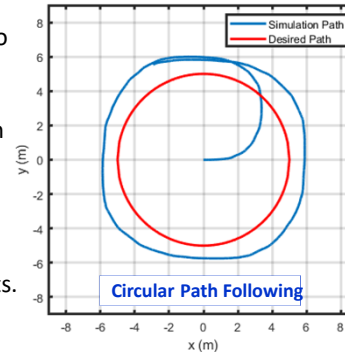
## Background

**The Robotic Systems Laboratory has developed the first hybrid force/position control architecture used with mobile robot formations. An object controller wrapped around the hybrid-controller allows the robots to be commanded as a virtual actuator. This allows for position control of the object during transportation and allows for force regulation between the cluster and object.**

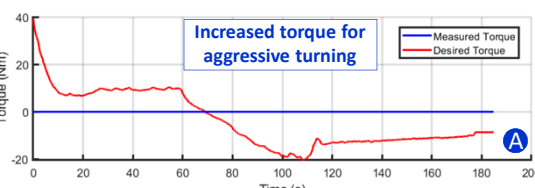
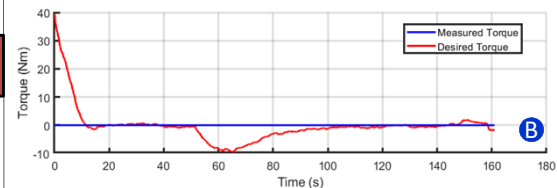
## Hybrid-based object controller in action



A two-robot system was used to transport a 13.5kg, .2m x .2m x 4m bar along a line of  $y = 20\text{m}$  (left) and around a circular path of 5m radius (right). The object controller calculates force and torque to be applied to the object. Force was regulated to 30N (6.7lbs) for the experiments.

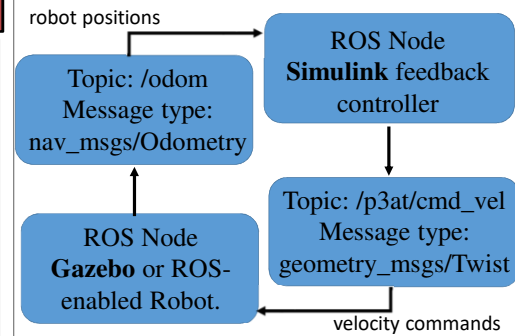


The Cluster Space control system commands object referenced cluster position variables  $y$  and  $d$  (above). Variable  $d$  controls robot spacing about the cluster center. Variable  $y$  controls the cluster's midpoint relative to the object's midpoint. An adaptive positioning technique varies  $y$  and  $d$  to allow the cluster to apply greater torque to the object, which results in more aggressive turning of the object towards the desired path. The plots labeled "A" show a line following test with adaptive positioning on (plots "B" off).



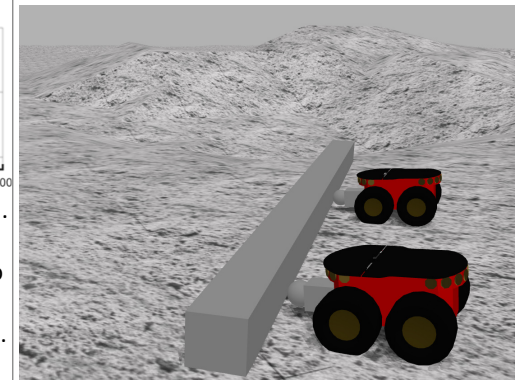
## Simulation Architecture

Matlab's Robotic System Toolbox provides connectivity between Simulink and a ROS-enabled robot or a ROS-based simulator (Gazebo). Gazebo 7 and ROS Kinetic run on an Ubuntu 16.04 machine. (TCP/IP comm)



## Gazebo

Gazebo offers 4 high-performance physics engines including Open Dynamics Engine (ODE), Bullet, Simbody, and DART. A variety of environments can be simulated including the moon (below).



## Acknowledgements

Robotic Systems Laboratory  
Dr. Michael Neumann  
School of Engineering





# Adaptive Navigation in 3-Dimensions with a Multirobot Virtual Structure



Robert K. Lee  
Advisor: Dr. Christopher Kitts

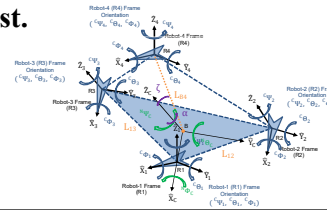
## Abstract

Adaptive navigation techniques, based on robot mounted sensor measurements, form a powerful class of controllers that can enable more time- and energy-efficient exploration of the scalar characteristics of an unknown and possibly dynamic region of interest (e.g., temperature, magnetic field, concentration level, etc.).

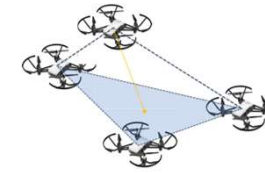
This presentation reports on the on-going research in autonomous adaptive navigation control methods using a multirobot test platform behaving as a virtual structure to perform real world applications.

## Background

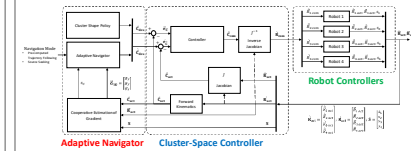
We have developed new distributed adaptive navigation control techniques using a fully controllable, 3-dimensional virtual structure composed of multiple robots to enable autonomous exploration and mapping of critical parameters, such as radiation or pollution, within a 3-D field of interest.



- 4-robot tetrahedral acts as virtual structure
- Robot cluster spans three-dimensions
- Controllable in all twenty four (24) degrees-of-freedom



## Control Architecture



- **Adaptive Navigator:** Steers the cluster based on characteristics like the field gradient, which are determined by processing robot-based sensor measurements
- **Cluster-Space Controller:** Maintains virtual structure attitude and geometry
- **Robot Controllers:** Ensure platform stability and execute velocity commands

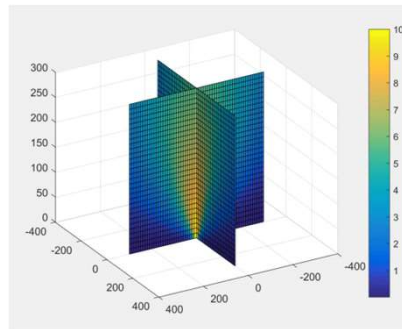
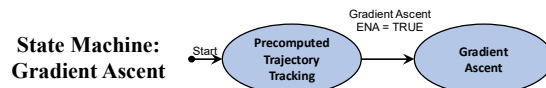
## Applications

- **Environmental Sensing** – Locating points of scientific interest, pollution sources, etc.
- **Exploration** – Characterizing hazardous or human inaccessible environments
- **Disaster Response** – Finding dangerous sources, establishing safety perimeters, identifying low exposure paths for travel

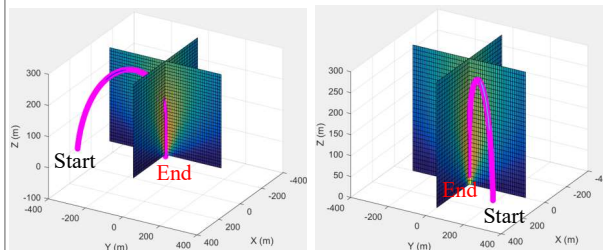
## Acknowledgements

Dr. Christopher Kitts  
Dr. Michael Neumann  
Robert McDonald  
SCU School of Engineering  
SCU Robotic Systems Laboratory

**Autonomously Seek Out Unknown Source**  
Actively estimate gradient to adaptively navigate robot cluster to maximum (i.e.: source) while controlling virtual structure attitude and geometry



Visualization of Plume of Interest



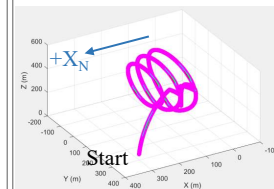
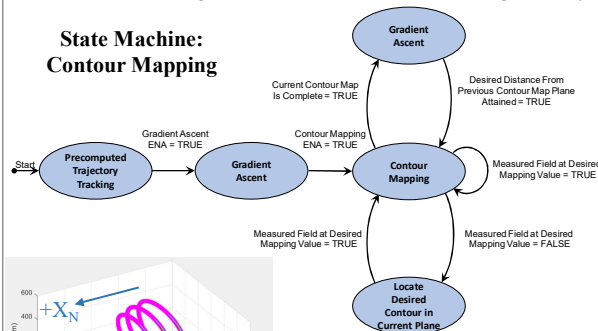
Flight Path from Initial Position I

Flight Path from Initial Position II

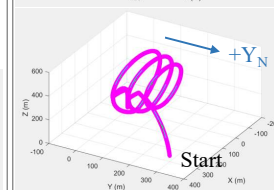
**Autonomously Map Regions of Interest**

Fly robot cluster along isoclines (i.e.: contours) in 3D space while maintaining virtual structure attitude and geometry

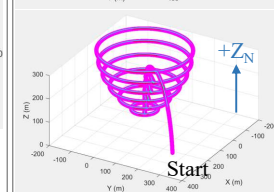
State Machine:  
Contour Mapping



Flight Path: Contour Map of X-Axis Slices with respect to Inertial (Newtonian) Frame



Flight Path: Contour Map of Y-Axis Slices with respect to Inertial (Newtonian) Frame



Flight Path: Contour Map of Z-Axis Slices with respect to Inertial (Newtonian) Frame

## Conclusion

A new 3-D adaptive navigation capability has been developed and verified in simulation for simple cases, laying the groundwork for continued development, field testing and application.

## Future Work

- Incorporate realistic robot dynamics, noise and disturbances
- Perform simulations with more complex scalar fields
- Develop additional navigation capabilities to perform functions such as following plumes, finding low exposure routes, etc.



# Mobile Robotics Swarm Behavior Development Platform

Shae Hart, Nathan Metzger, Max Reese  
Advisor: Dr. Christopher Kitts



## Abstract

Swarm control strategies allow for decentralized control of many simple robots to perform collective behaviors based on local interactions. We have created a new platform for developing and exploring swarm behaviors, supporting both simulation and experimental verification. While most swarm research efforts focus on “emergent” group behaviors based on local rules, we are using this platform to explore novel “top down” approaches that can derive local rules based on desired group behavior. Our focus for this work is on group “adaptive navigation” capabilities for exploring and navigating through scalar fields.

## Behaviors

The Swarm simulator implements behavior-based control. Base behaviors can be selected independently, or combined for more sophisticated “emergent” behaviors. Current base behaviors include:

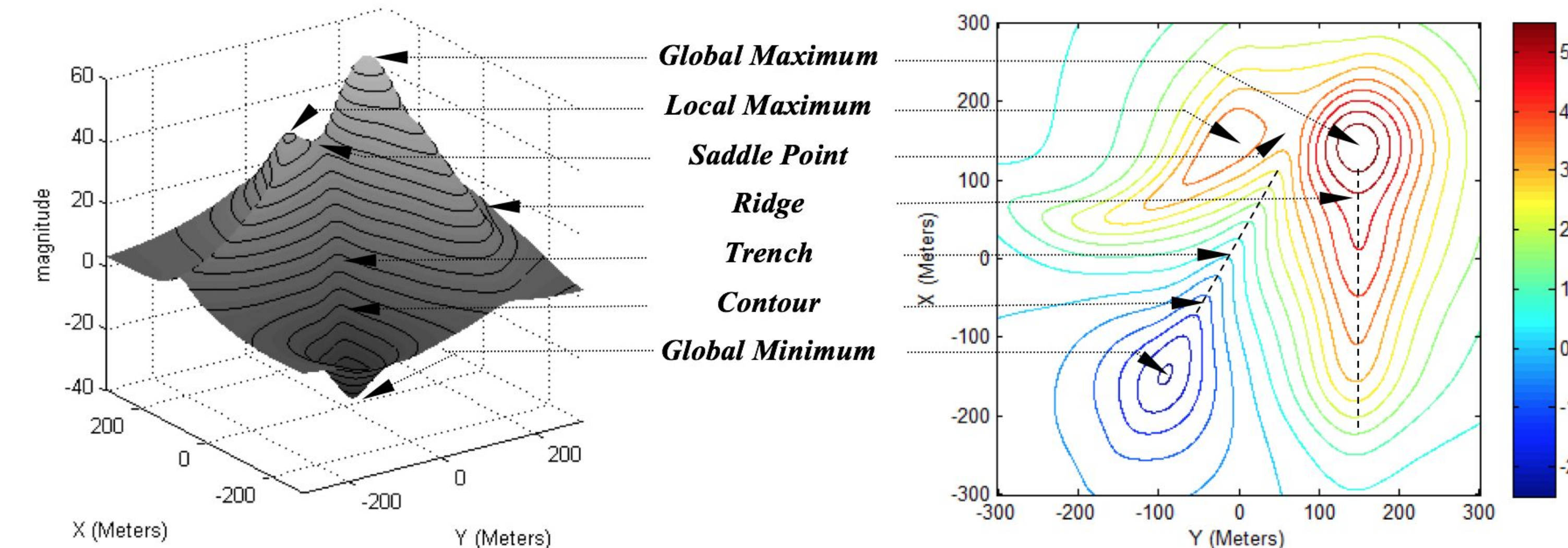
- *Attract*
- *Disperse*
- *Obstacle Avoidance*
- *Source Seeking (Minima & Maxima)*
- *Contour Following*

## Acknowledgements

Robotic Systems Laboratory  
Dr. Michael Neumann & Robert McDonald  
SCU School of Engineering

## Background

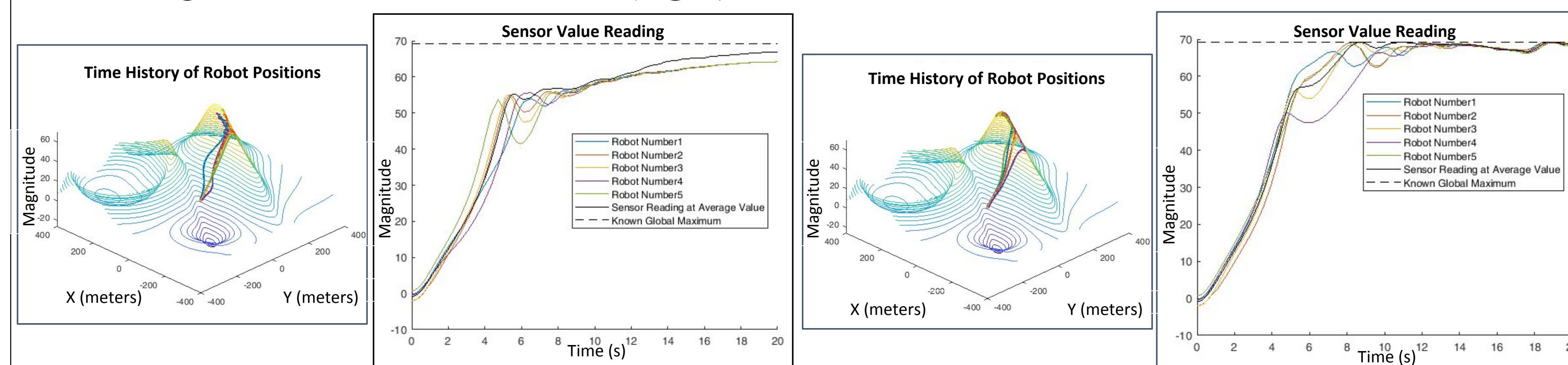
The Robotic Systems Laboratory researchers have developed a complete set of cluster-based adaptive navigation behaviors for locating or moving along all critical features of a scalar field. Our new work seeks to replicate this capabilities using a decentralized swarm control architecture that does not require full degree of freedom formation control.



## Simulation & Experimental Results

### Minima and Maxima Finding

Local Minima and Maxima in a scalar field can be found using “source seeking” behaviors. These behaviors are operable independently (*left*) but are improved with “stacking” of the attract function (*right*).

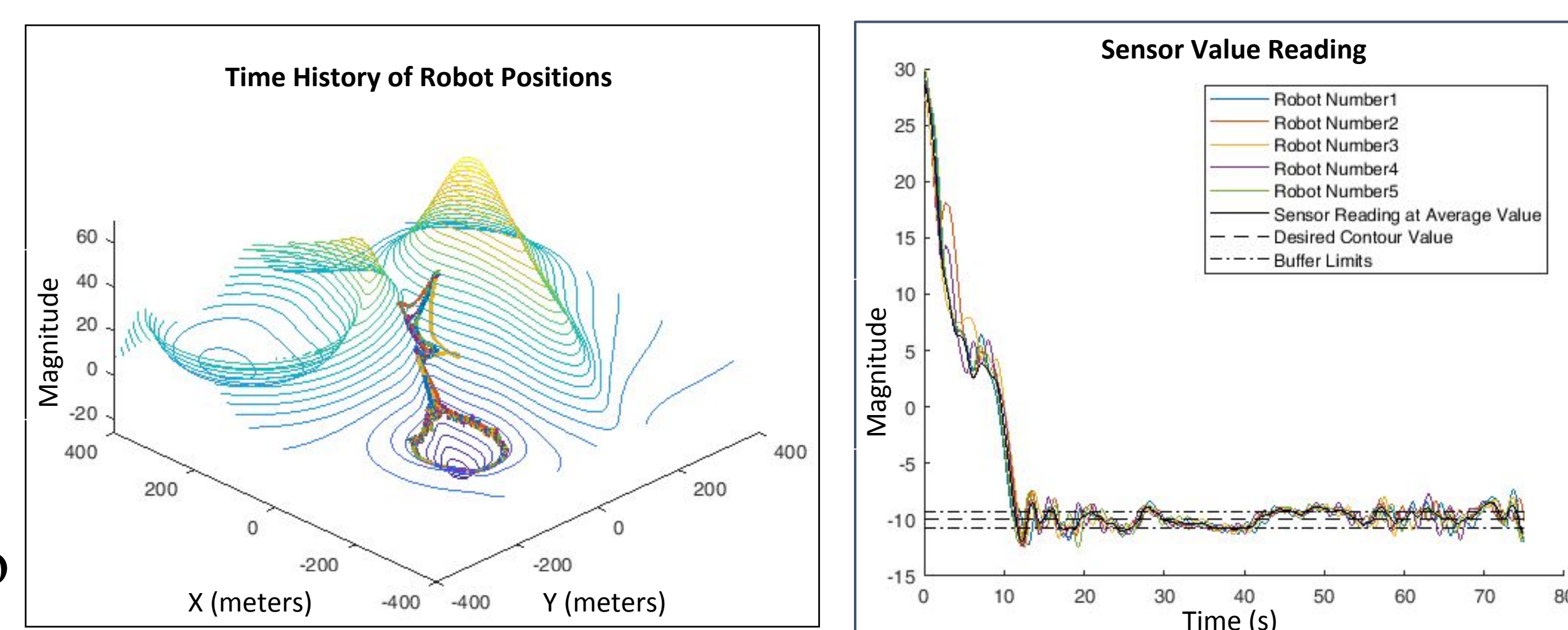


Position and Sensor Value Reading for Find Max Behavior

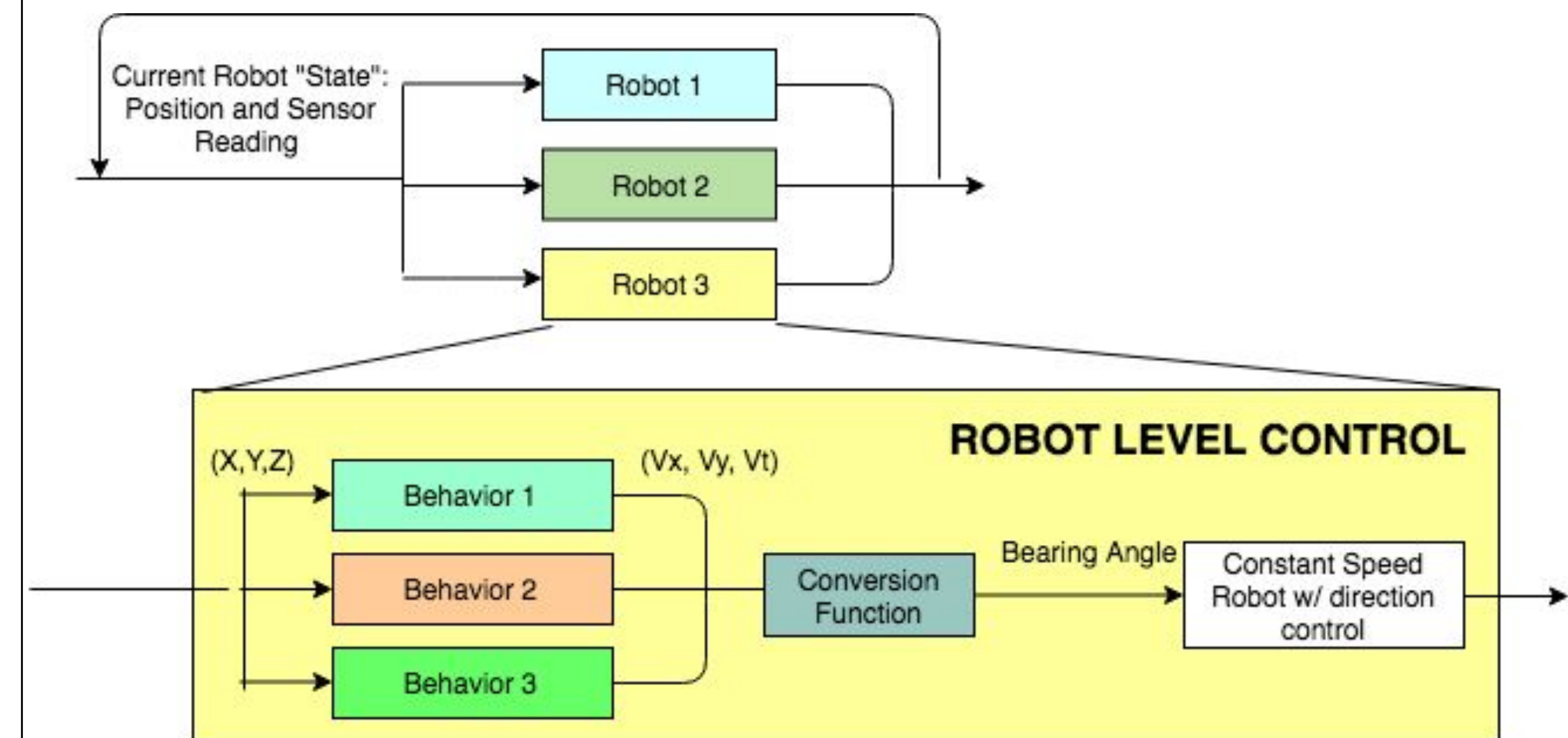
Position and Sensor Value Reading for Find Max and Attract Behavior

### Contour Finding and Following

For contour following, the robots first move along the scalar field to proper contour. Once found, the swarm follows the contour while remaining within a buffer of the desired contour. Position and sensor value readings for contour following with attract are shown to the right.



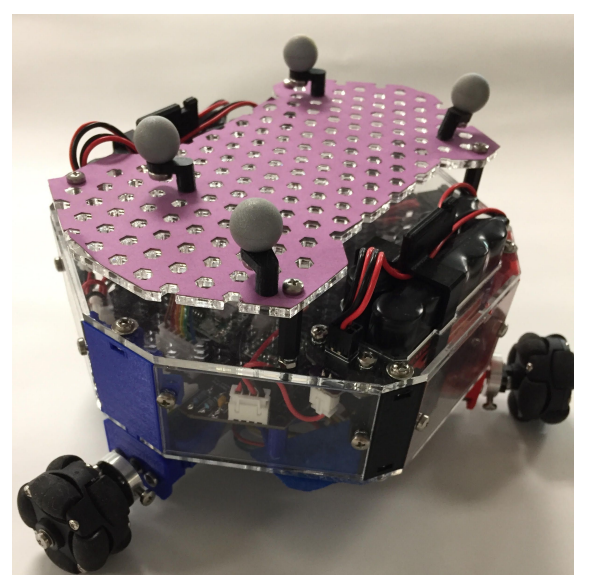
## Control Architecture



## Experimental Testbed

The RSL’s testbed uses up to 10 holonomic omnibots (shown below) equipped with sensors for reading grayscale scalar field printouts. Using this testbed, we have demonstrated the effectiveness of the following behaviors:

- *Attract*
- *Obstacle Avoidance*
- *Extrema Seeking*
- *Contour Following*



## Conclusion

Using swarm robotics for adaptive navigation provides a novel approach to adaptive navigation problems, while also evolving the swarm robotics field toward explicitly specified rather than “emergent” group behaviors.

## Future Work

- Continued development of adaptive navigation behaviors
- Monte Carlo analysis of behaviors
- Experimental testing on a variety of different scalar fields

# Stress reduction for crack-like geometries in auxetic metamaterials

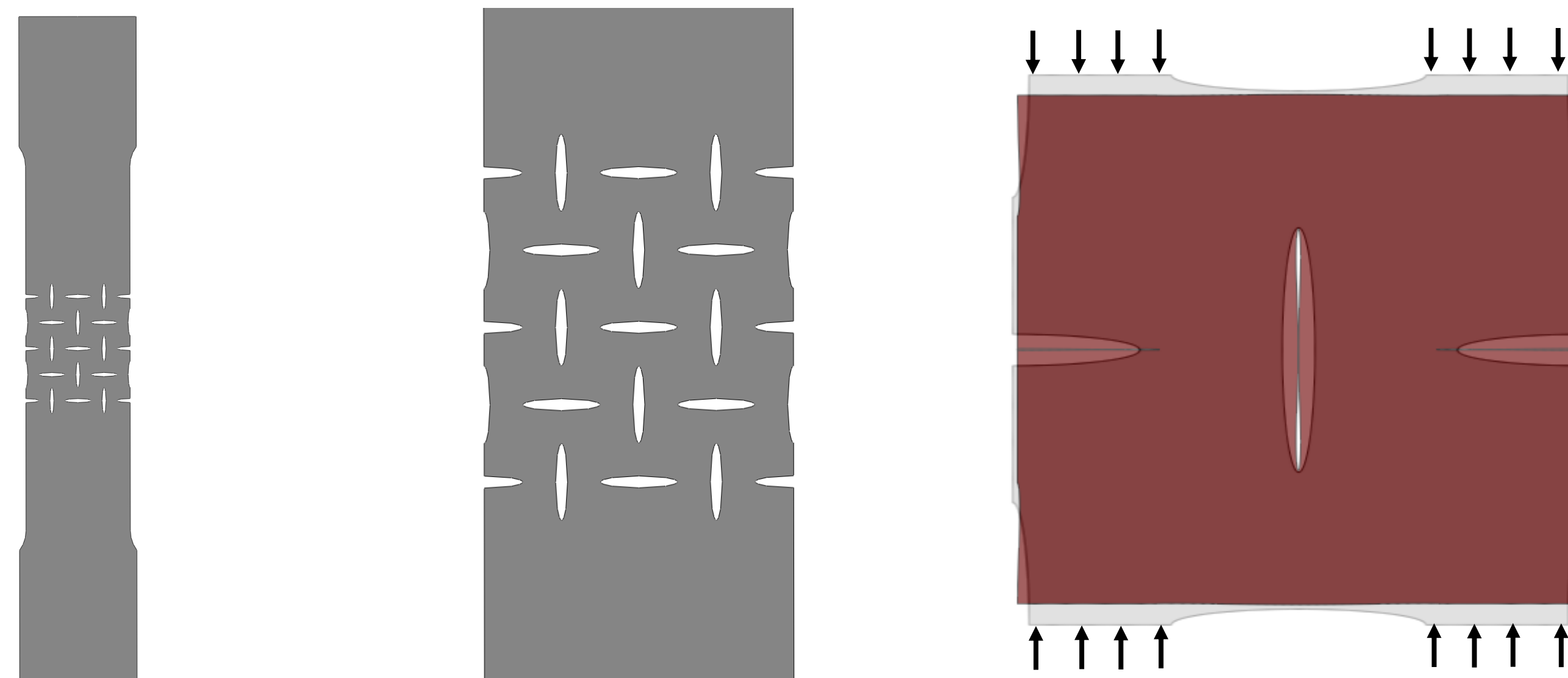
Max Barillas,<sup>1,2</sup> Luca Francesconi<sup>1</sup> and Michael Taylor<sup>1</sup>

<sup>1</sup>Department of Mechanical Engineering, Santa Clara University.

<sup>2</sup>Department of Structural Mechanics, University of Central America "José Simeón Cañas".

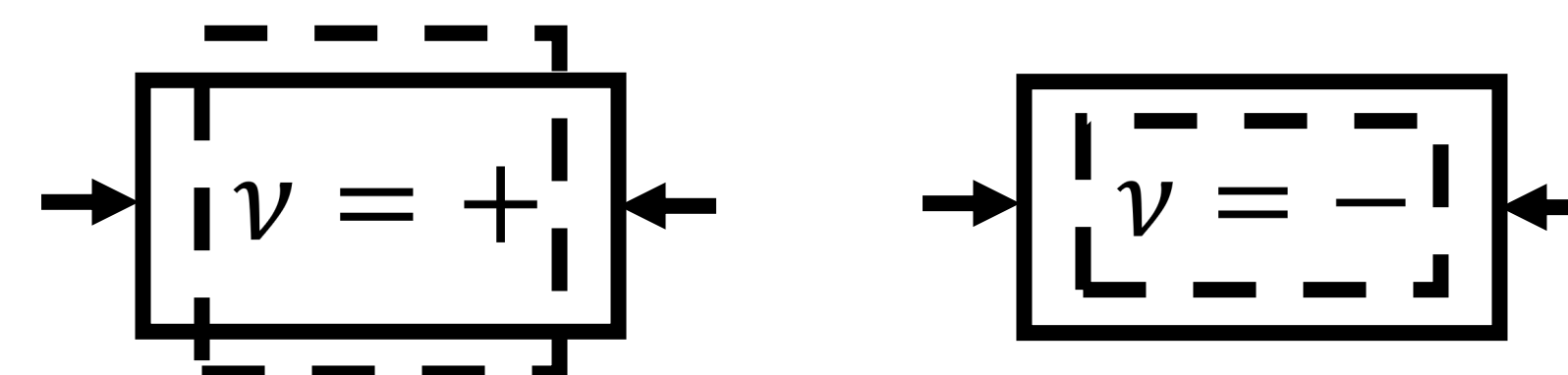
## Introduction

Recently, auxetic metamaterials have drawn increased attention due to their promise in applications ranging from impact absorption [1], improving fatigue life [2], and reducing thermal expansion [3]. Auxetics are those materials having a negative Poisson's ratio, while metamaterials are those which gain remarkable effective properties from deliberate design of their geometric micro-structure. In low-porosity materials, auxeticity can be obtained by utilizing a periodic array of alternating elongated voids (e.g. ellipses). Unfortunately, these shapes have high stress concentrations at their tips, which limits their utility.



## Poisson's Ratio

Poisson's ratio is defined as the negative ratio between the transverse and axial strain in a material under load, considering an extensional strain as positive and a compressive strain as negative.

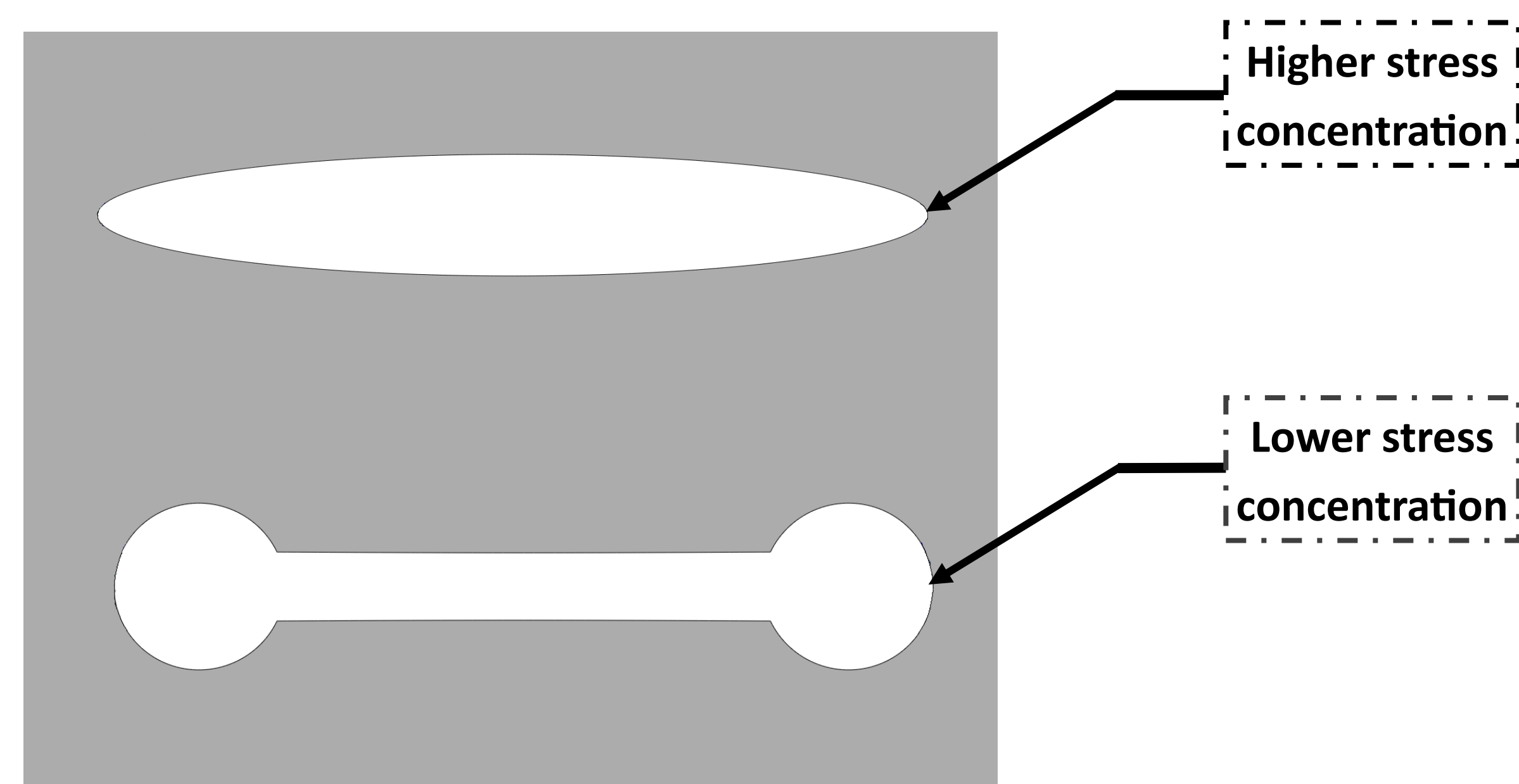


$$\nu = -\frac{\epsilon_{trans}}{\epsilon_{axial}}$$

## Objectives

The main interest of this investigation is to find, in a methodical manner, geometries that improve the stress condition of void patterns, while keeping or improving the auxetic behavior they induce in linear elastic engineering materials.

The method proposed to achieve this objective is the usage of rounded parametric geometries at the tips of the voids to reduce the stress concentration.

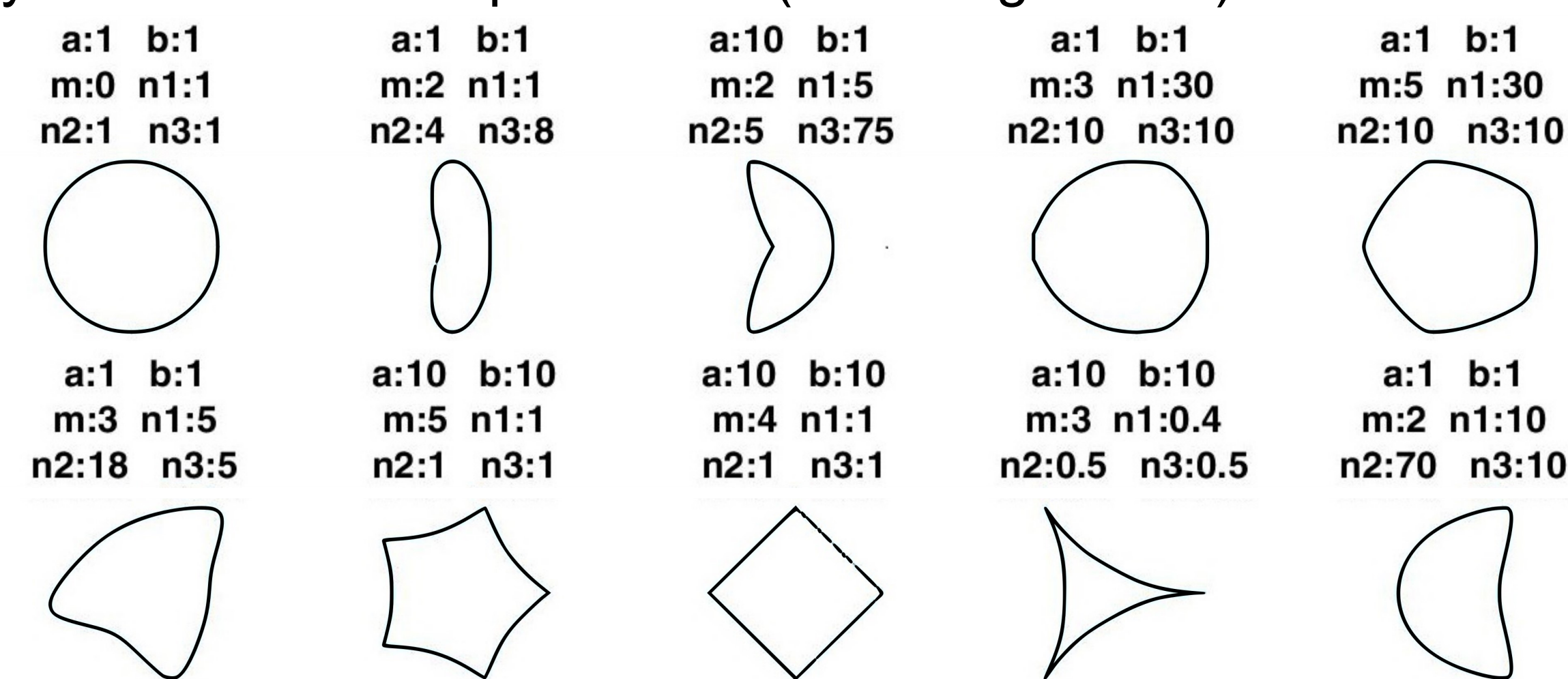


## Shape Selection

The superformula, first proposed by Gielis [4] as a generalized ellipse equation, was chosen as a way to parametrize the shape of the tips of the voids due to its versatility to represent rounded shapes. The superformula defines a shape in polar coordinates as the combination of powers of the harmonic functions, allowing 6 parameters to control the resulting shape.

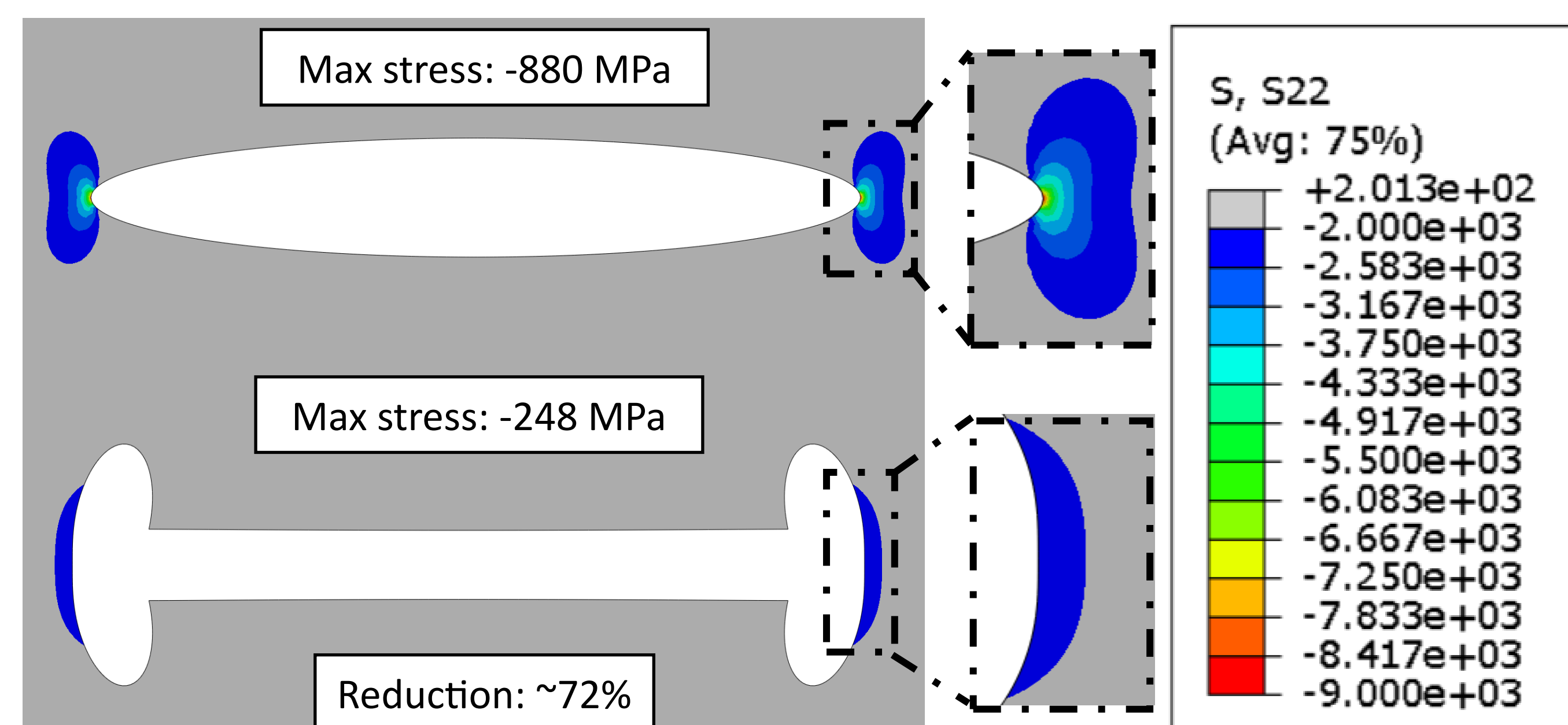
$$r(\theta) = \left( \left| \frac{\cos\left(\frac{m\theta}{4}\right)}{a} \right|^{n_2} + \left| \frac{\sin\left(\frac{m\theta}{4}\right)}{b} \right|^{n_3} \right)^{-\frac{1}{n_1}}$$

Choosing the right parameters for minimizing the stress represented a big challenge given the size of the design space for these 6 parameters. Therefore, reducing the design space of parameters is required to keep the study feasible and to ensure that the resulting geometries comply with minimum requirements (i.e. being closed).

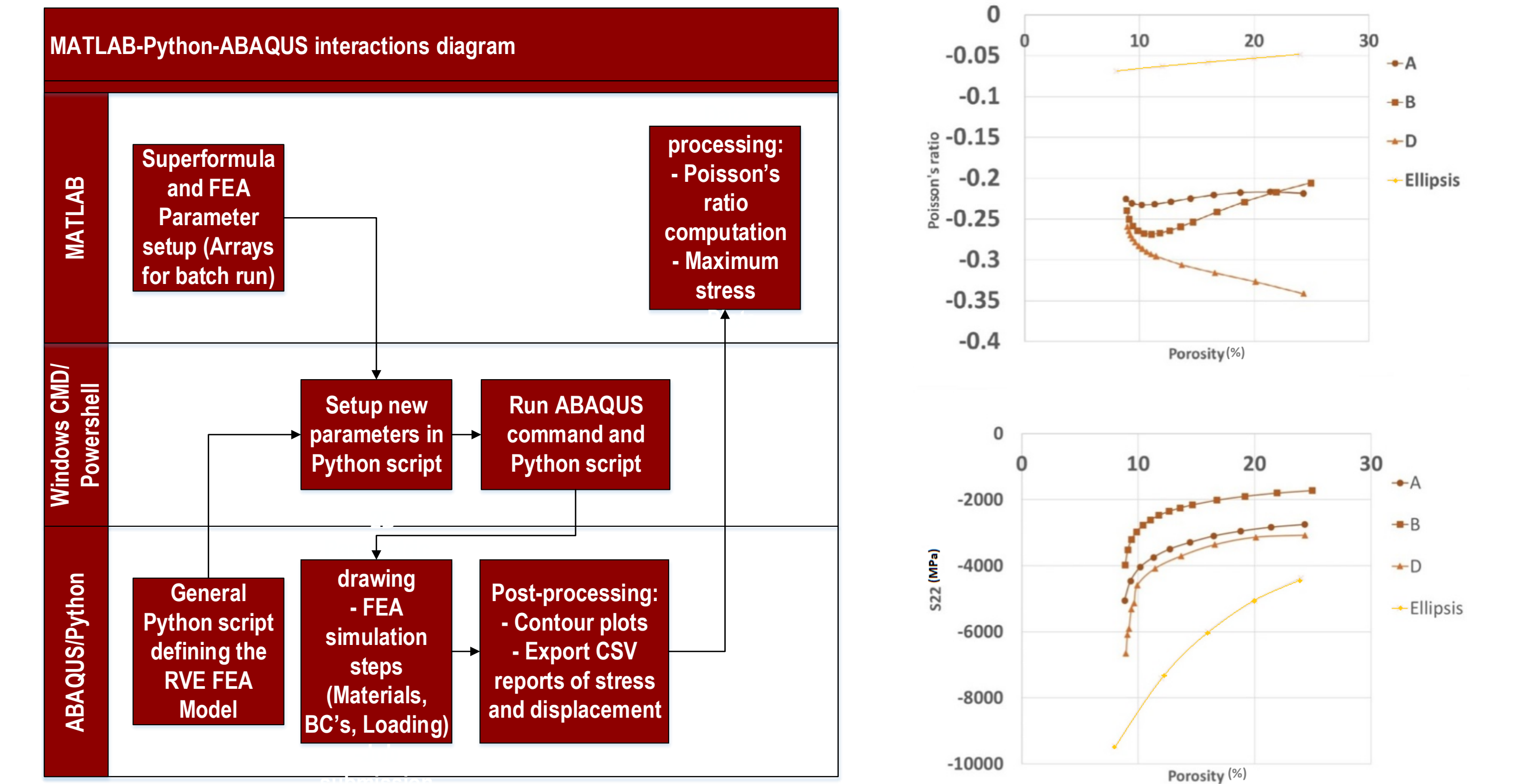


## FEA Simulation

To understand the behavior of these metamaterials, a representative volume element (RVE) FEA model was implemented using ABAQUS Standard. The models contained an alternating voids pattern where at the tip the superformula shapes were added. To compare the effectiveness of the geometry the overall length of the void and the width of the groove in between the shapes was kept constant in between comparisons, as it was the porosity that the voids represented (showing results at 12%). Finally, the models were compressed equally in the vertical direction for comparison purposes. The variables of interest were the displacements (U1,U2), to show their auxetic behavior, and the normal stress in the vertical direction, in order to spot which geometry offers the most promising stress concentration reduction.



## In-depth Comparison



Via automating the simulation process, it was possible to perform an in-depth comparison of the most promising shapes. The objective achieved this way is to show the dependence of the stress reduction on the porosity of the voids (i.e. increasing the size of the shapes at the tips).

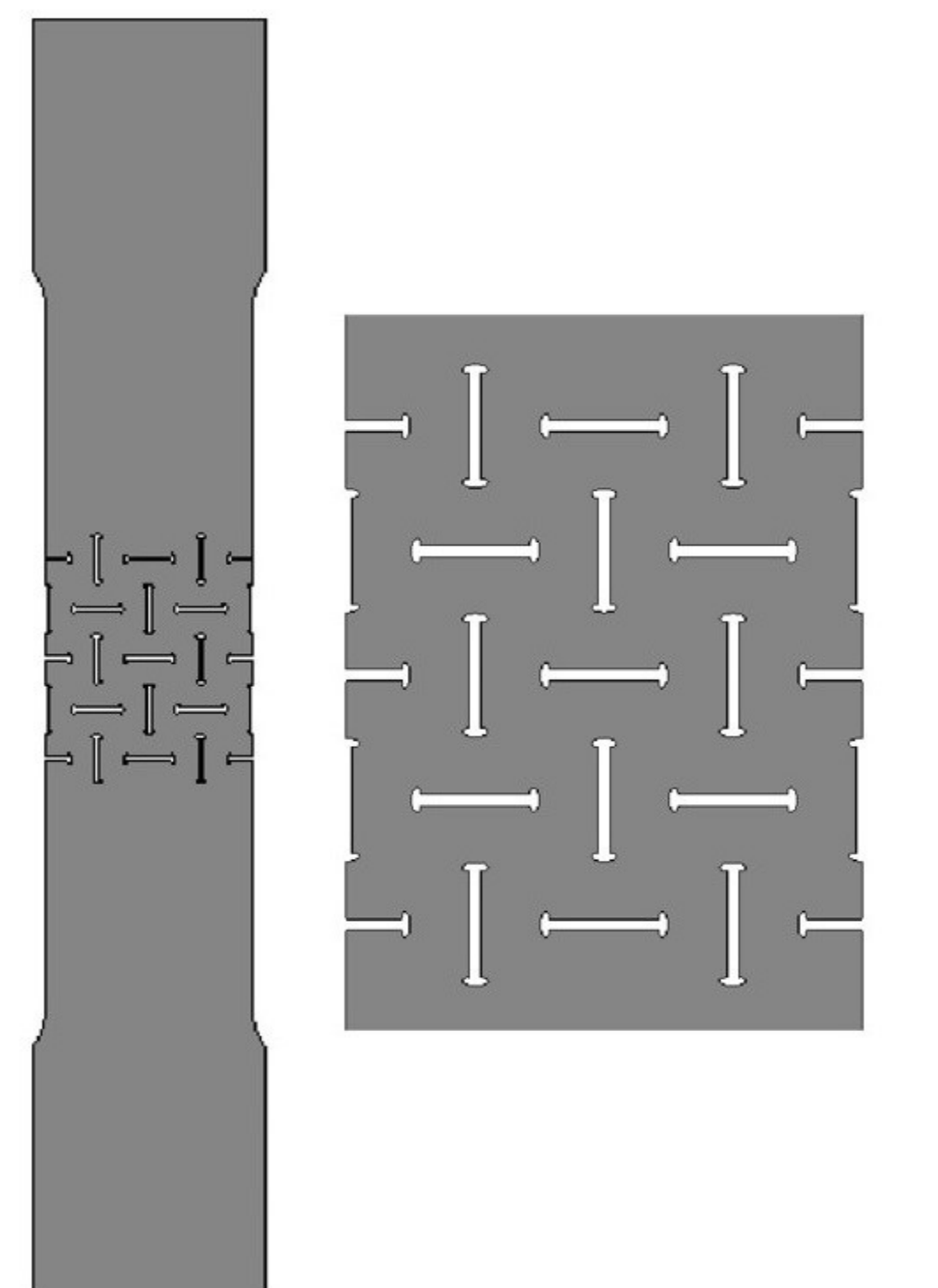
## Future Work

### Fatigue experiments in full size samples

One of main reasons for the interest of reducing the stress concentration in auxetic metamaterials is to improve their fatigue life, increasing the range of their possible applications. Therefore experimentally determining the fatigue behavior of the improved geometries is of future interest.

### Shape optimization

Even though the geometries evaluated until now present a significant improvement in stress reduction and auxetic behavior, there are chances of even bigger improvements. Numerical optimization algorithms can be applicable to this matter, particularly genetic algorithms present promising characteristics for increasing the improvement.



## References

- [1] L. Francesconi, A. Baldi, X. Liang, F. Aymerich, and M. Taylor, Variable Poisson's ratio materials for globally stable static and dynamic compression resistance, *Extreme Mech. Lett.*, 26, 1-7 (2019).
- [2] F. Javid, J. Liu, A. Rafsanjani, M. Schaezner, M. Q. Pham, D. Backman, S. Yandt, M. C. Innes, C. Booth-Morrison, M. Gerendas, T. Scarinci, A. Shanian and K. Bertoldi, "On the design of porous structures with enhanced fatigue life," *Extreme Mechanics Letters*, vol. 16, pp. 13-17, 2017
- [3] M. Taylor, L. Francesconi, M. Gerendas, A. Shanian, C. Carson and K. Bertoldi, "Low porosity metallic periodic structures with negative poisson's ratio," *Advanced Materials*, vol.26, no. 15, pp. 2365-23-70, 2014.
- [4] J. Gielis, "A generic geometric transformation that unifies a wide range of natural and abstract shapes," *American Journal of Botany*, vol. 90, no. 3, pp. 333-338, 2003.



# Self-learning How To Swim at Low Reynolds Numbers



Alan C. H. Tsang  
Bioengineering  
Stanford University

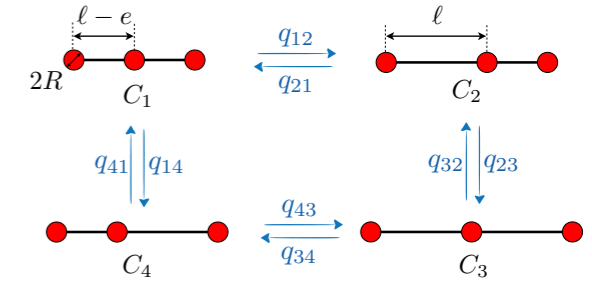
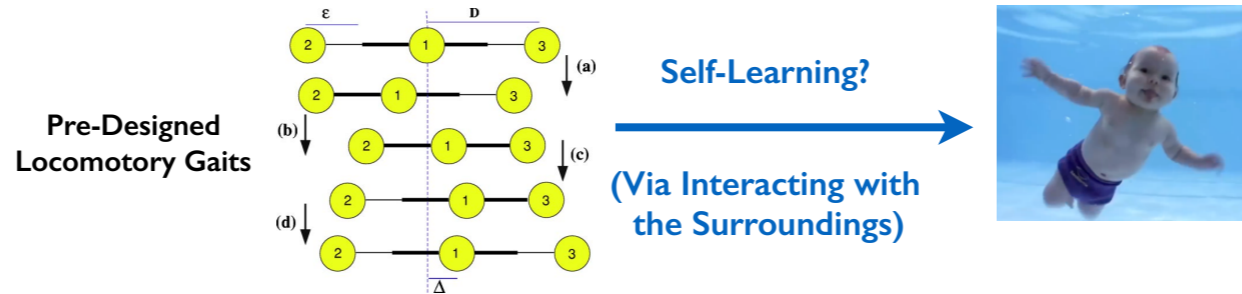
Pun Wai Tong  
Clinical Genomics Program  
Stanford Health Care

Shreyes Nallan  
Electrical Engineering  
Santa Clara University

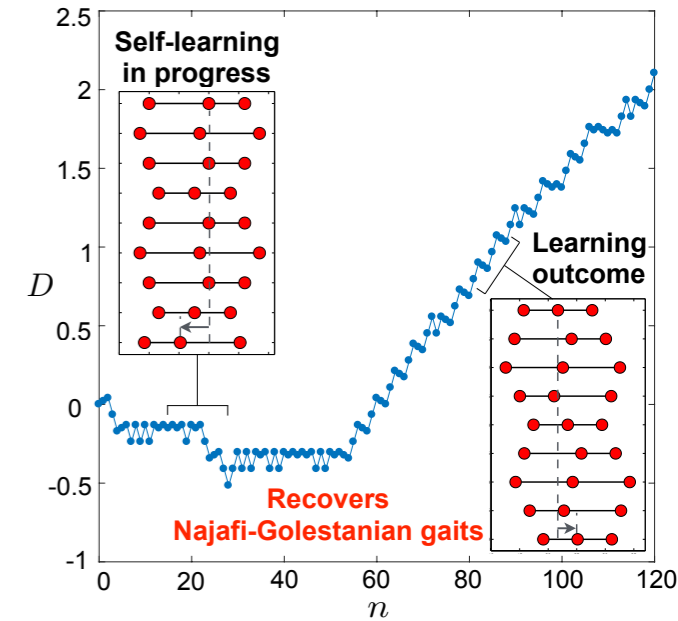
Grant Mishler and On Shun Pak  
Mechanical Engineering  
Santa Clara University

**Abstract:** Synthetic swimmers capable of moving at the microscopic scale offer exciting opportunities for biomedical applications (e.g., drug delivery and micro-surgeries). Their locomotion, however, is subject to stringent constraints due to the dominance of viscous over inertial forces at low Reynolds number (Re) in the microscopic world. Furthermore, locomotory gaits designed for one medium may become ineffective in a different medium. Successful biomedical applications of synthetic microswimmers rely on their ability to traverse biological environments with vastly different properties. To overcome these challenges, here we leverage the prowess of machine learning to present an alternative approach to designing low Re swimmers.

## Low Re Swimming: A Self-Learning Approach



### Part A: For N = 3



## Introduction: Swimming Under the Microscope

### Navier-Stokes Equation:

$$\text{Re} \left( \frac{\partial \mathbf{u}}{\partial t} + \mathbf{u} \cdot \nabla \mathbf{u} \right) = -\nabla p + \nabla^2 \mathbf{u}$$

$\text{Re} \gg 1$        $\text{Re} \ll 1$

$$\text{Re} = \frac{\rho U L}{\mu} = \frac{\text{Inertial force}}{\text{Viscous force}}$$



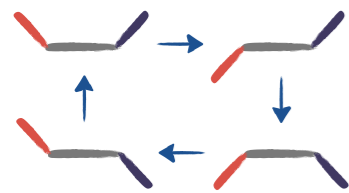
<http://media.washingtontimes.com/>

### Kinematic Reversibility and Scallop Theorem

- Reciprocal motion (e.g. flapping) cannot generate self-propulsion at small scales

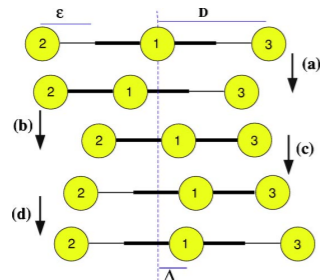
### Artificial Micro-swimmers

Purcell's swimmer



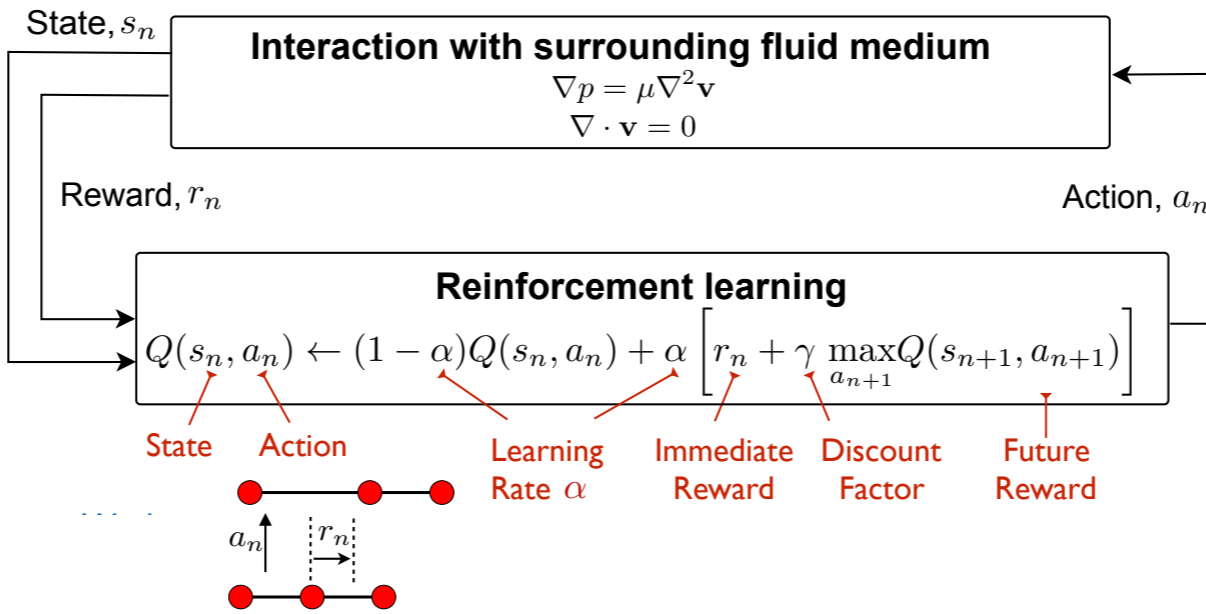
Purcell (1977)

Najafi-Golestanian swimmer

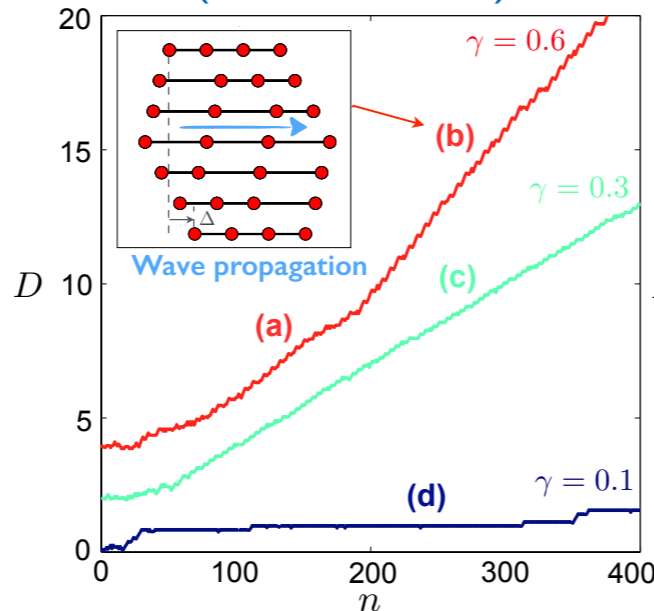


Najafi and Golestanian (2004)

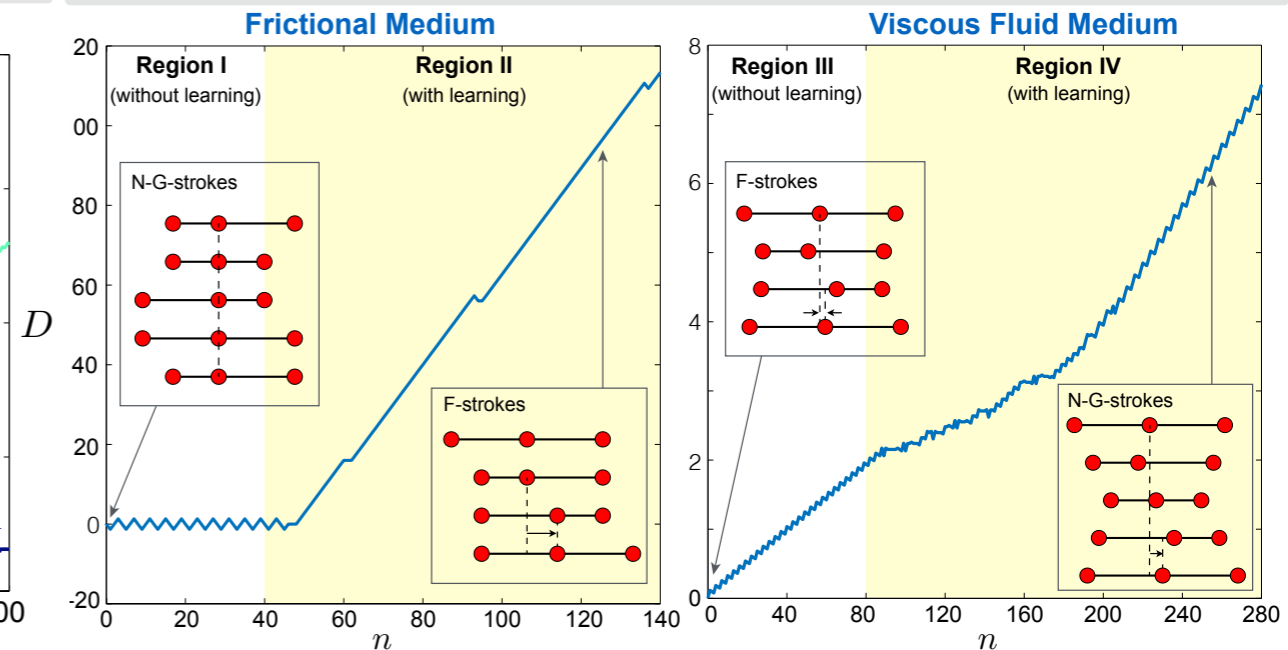
**Conclusion:** In this work we present the first example of integrating machine learning into the design of low Re swimmers. Without requiring prior knowledge on low Re hydrodynamics, a self-learning swimmer can recover classical swimming strategies, identify more effective locomotory gaits with increased degrees of freedom, and adapt locomotory gaits in different media.



### Part B: Increased Number of Spheres (From N = 3 to 10)



### Part C: Adaptive Locomotory Gaits Across Different Media



# Thermoelectric Generator Integration in Wearable Devices

Joshua Vincent, Department of Bioengineering, and Professor Hohyun Lee, Department of Mechanical Engineering

## Problem

Nearly two million United States citizens suffer from upper or lower limb amputation and the amputee population increases at a rate of approximately 185,000 amputations per year [1]. Amputation limits an individual's ability to perform basic tasks, such as tie his or her shoes. Electric prostheses restore an individual's ability to perform basic tasks, as in Image 1. However, the batteries that power these prostheses have a limited operation time. Upon battery discharge, the prosthesis loses all sensory and data storage capability.



Image 1: A prosthetic arm, the HACKberry, allows a man to tie his shoes [2].

## Solution

Electric prostheses must integrate a secondary power source to maintain sensory and computational functions after battery depletion. Thermoelectric generators (TEGs) may serve as such a power source.

## Challenges

1. Maintain user comfort
2. Maximize TEG power output
3. Maintain a large temperature gradient across all TEGs
4. Maintain a uniform temperature gradient across all TEGs

## Resources

- [1] Ziegler-Graham et al. Estimating the Prevalence of Limb Loss in the United States: 2005 to 2050. *Arch Phys Med Rehabil*, vol. 89, pp 422-429.
- [2] "HACKberry [3D-printable open-source bionic arm.]" <http://exiii-hackberry.com/>

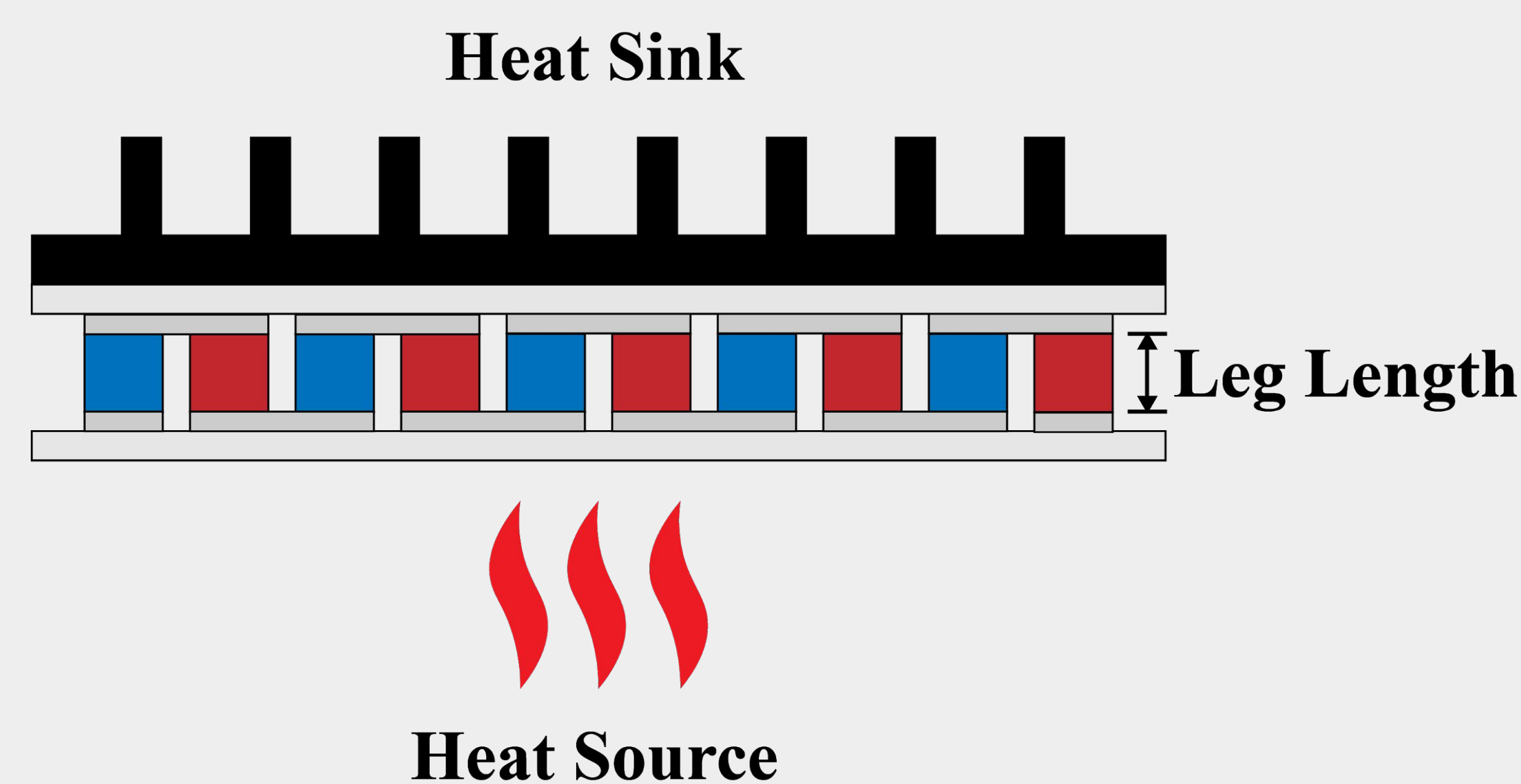


Image 2: The TEG side view reveals positively and negatively doped legs, red and blue, respectively, connected by solder, centered between two ceramic plates.

## Chassis Design

The wearable chassis functions as a large heatsink, as in Image 3. The chassis' large surface area allows for a large heat transfer rate. In addition, a copper heatpipe spreads heat evenly across the surface of the heatsinks to ensure that they dissipate heat through their full surface area.

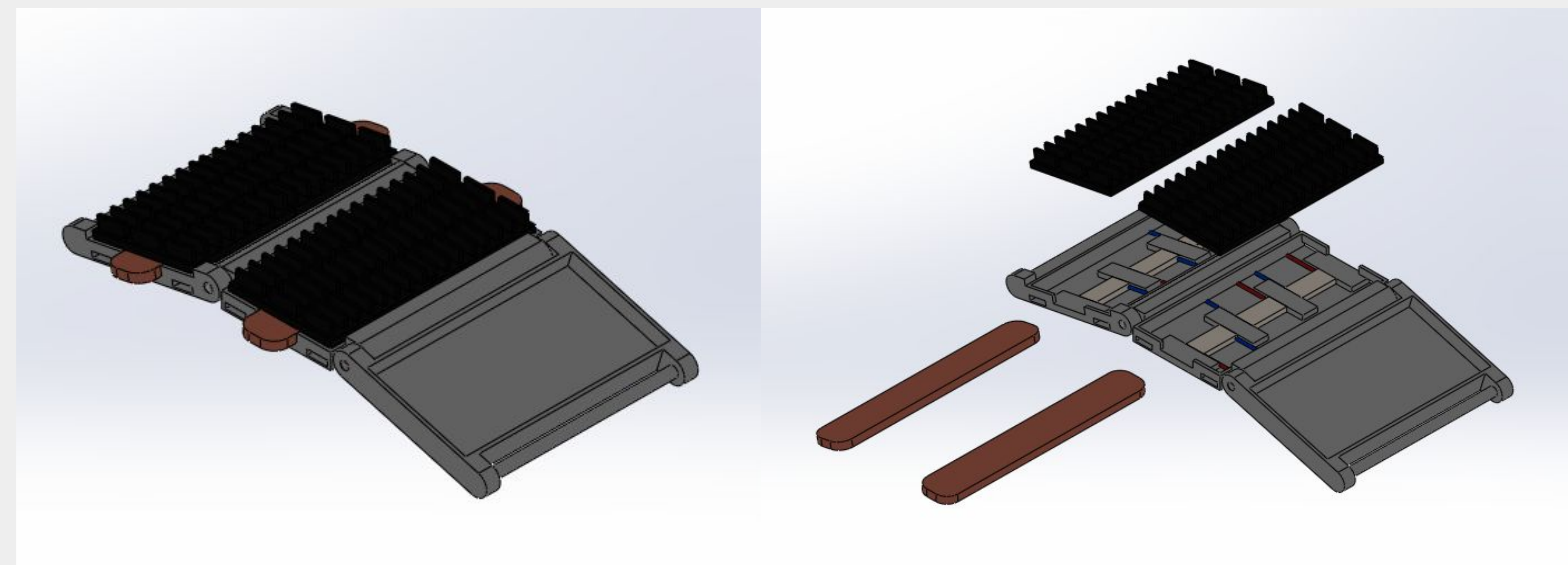


Image 3: An assembly (left) and explosion (right) of the TEG integrated wearable device.

## Principle

In the presence of a temperature gradient, a TEG generates a voltage, proportional to the temperature gradient across the TEG, as in equation 1.

$$(1) V = 2n\alpha\Delta T$$

In equation 1,  $V$  is the voltage generated across the TEGs terminals,  $n$  is the number of leg pairs,  $\alpha$  is the Seebeck coefficient of the legs, and  $\Delta T$  is the temperature difference across the TEG. In order to maintain a large temperature difference, it is necessary to minimize the thermal resistance, resistance to heat flow, in the system. Thermal resistance is inversely proportional to the surface area of heat dissipation. Therefore, a large surface area decreases thermal resistance and allows a large temperature gradient to exist.

## Circuit Design

In the presence of a temperature gradient between the human skin and air, about 10 C, the TEG array generates a voltage on the order of millivolts. A DC-DC step-up converter must be used to amplify the voltage to an order of volts without the additional power input of traditional amplifiers. At a higher voltage, the power generated by the TEG array may be distributed through a charge controller to applications, such as the battery and microcontroller in Image 4.

## Future Work

Presently, we power an exterior evaluation board, microcontroller, and sensor. We want to integrate these elements into our wearable device and, eventually, into a full scale upper limb prosthesis. In addition, TEG operation causes user discomfort due to the device's cooling effect.

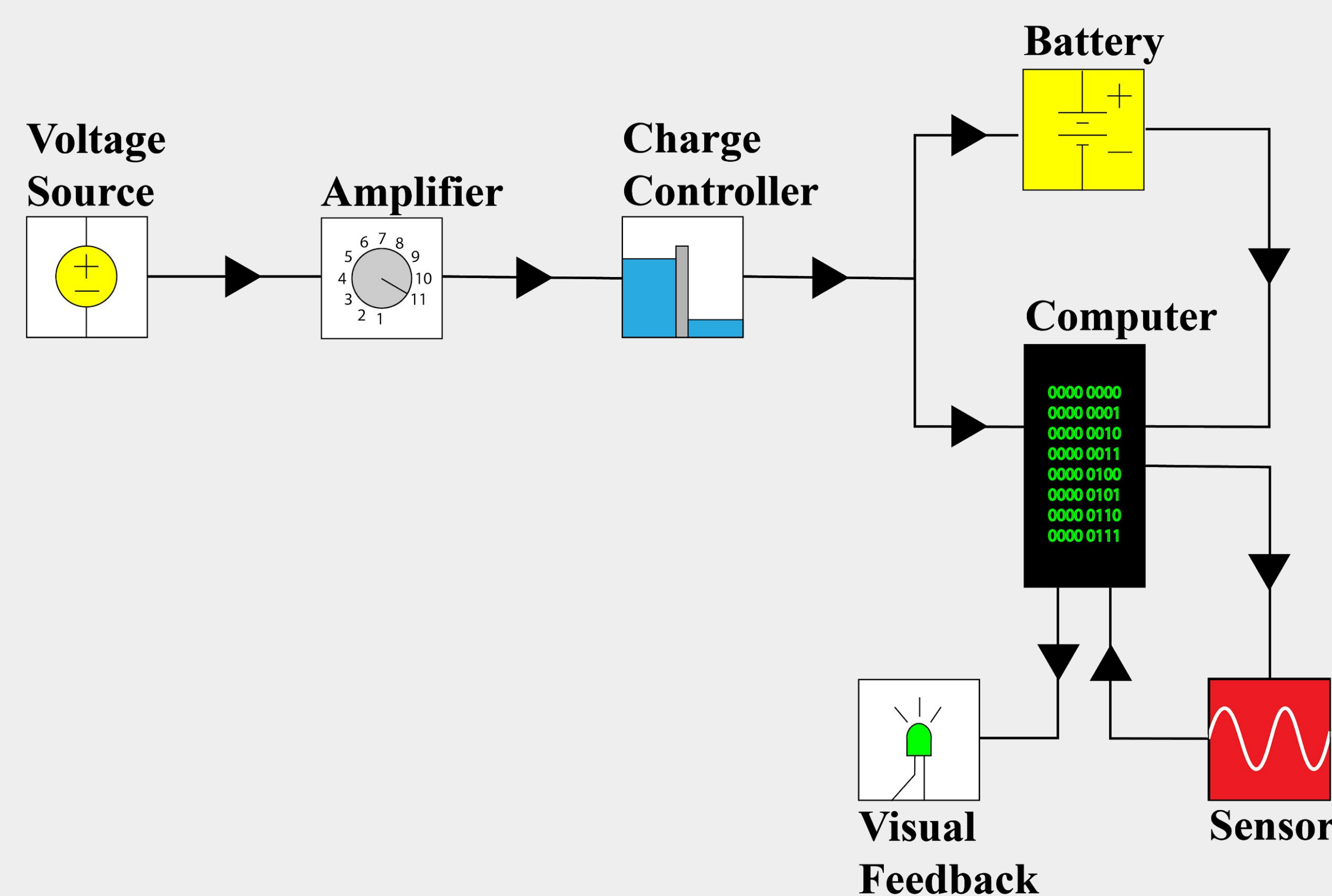


Image 4: TEG integrated wearable circuit schematic

## Introduction

Ultrasonic (US) wedge-wire bonding is a method commonly used for integrated circuit connections that is not fully understood. The main goal of the project is to construct high resolution 3D images of the ultrasonic wedge bonded wire interface from several 2D images obtained through scanning probe microscopy (SPM) for further analysis.

### Current Understanding and SPM

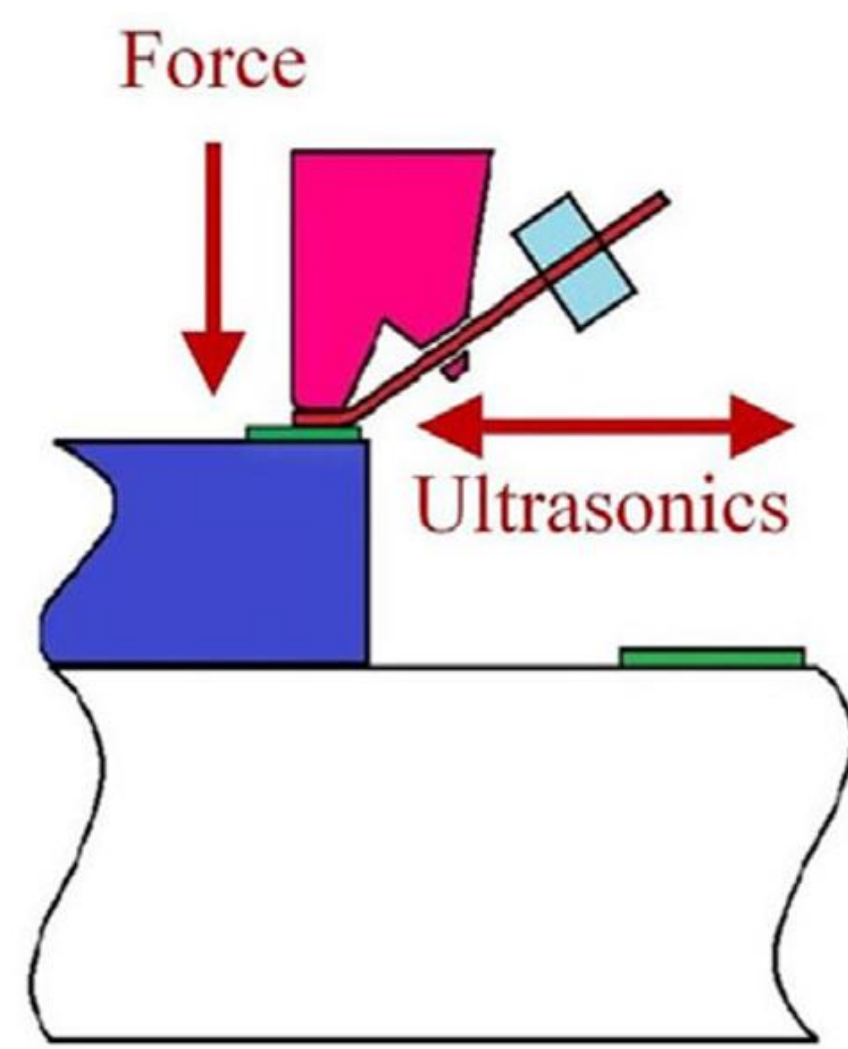


Figure 1: Depiction of US wire bondhead [1]

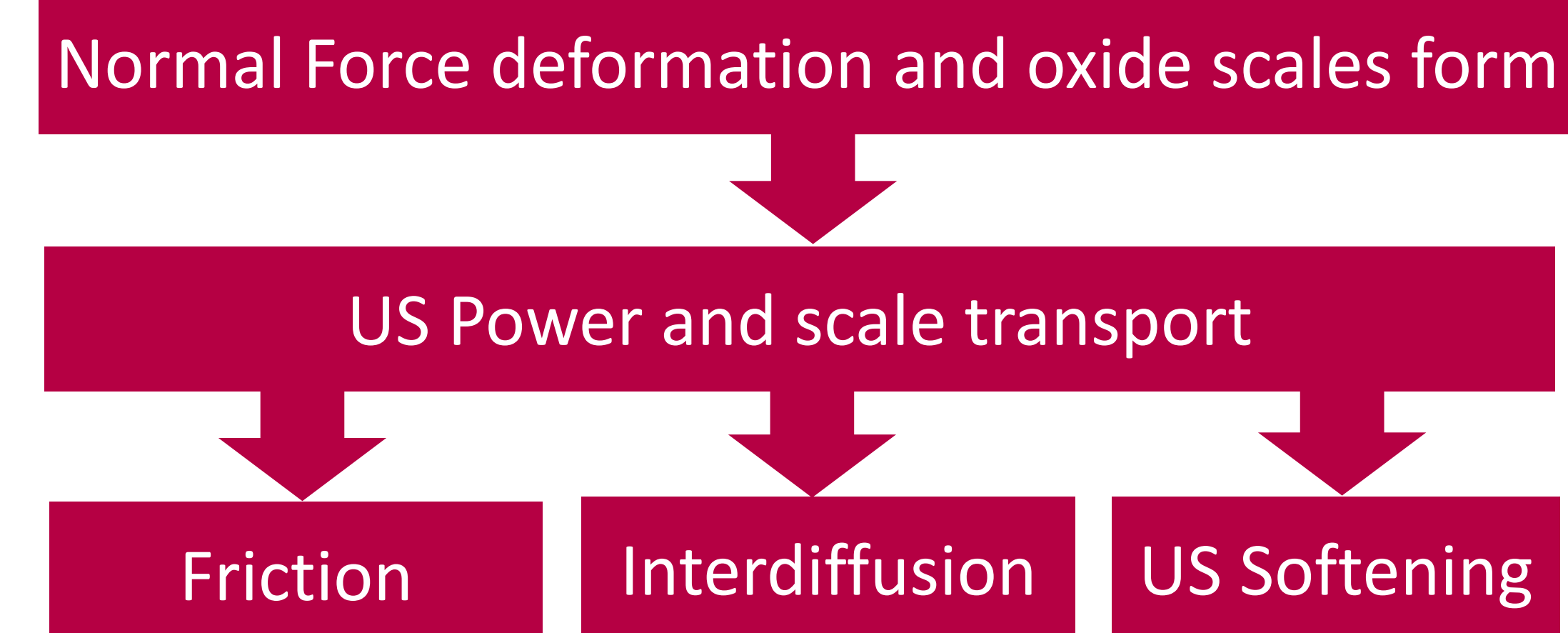


Figure 2: US wire bonding Processes described in [1]

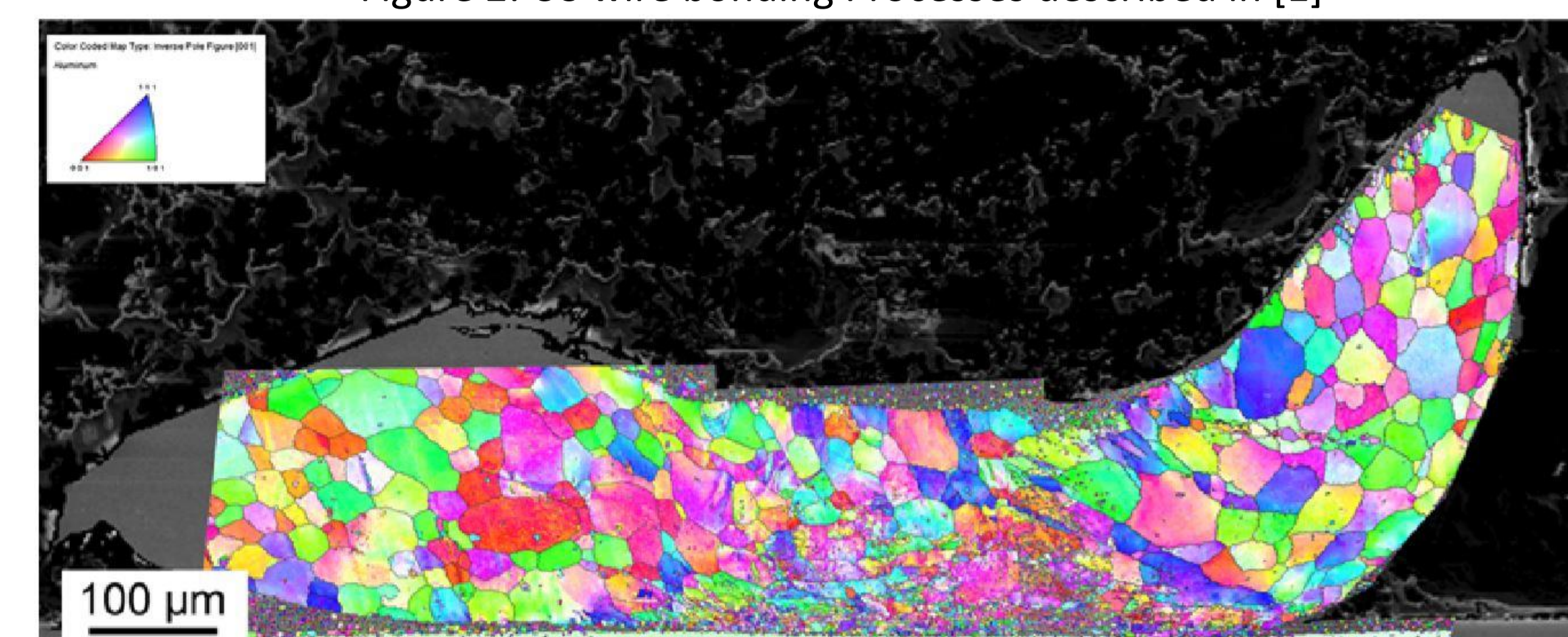


Figure 3: Microstructure closer to interface region contained small equiaxed grains as described in [8] with predominant grain orientation [7]

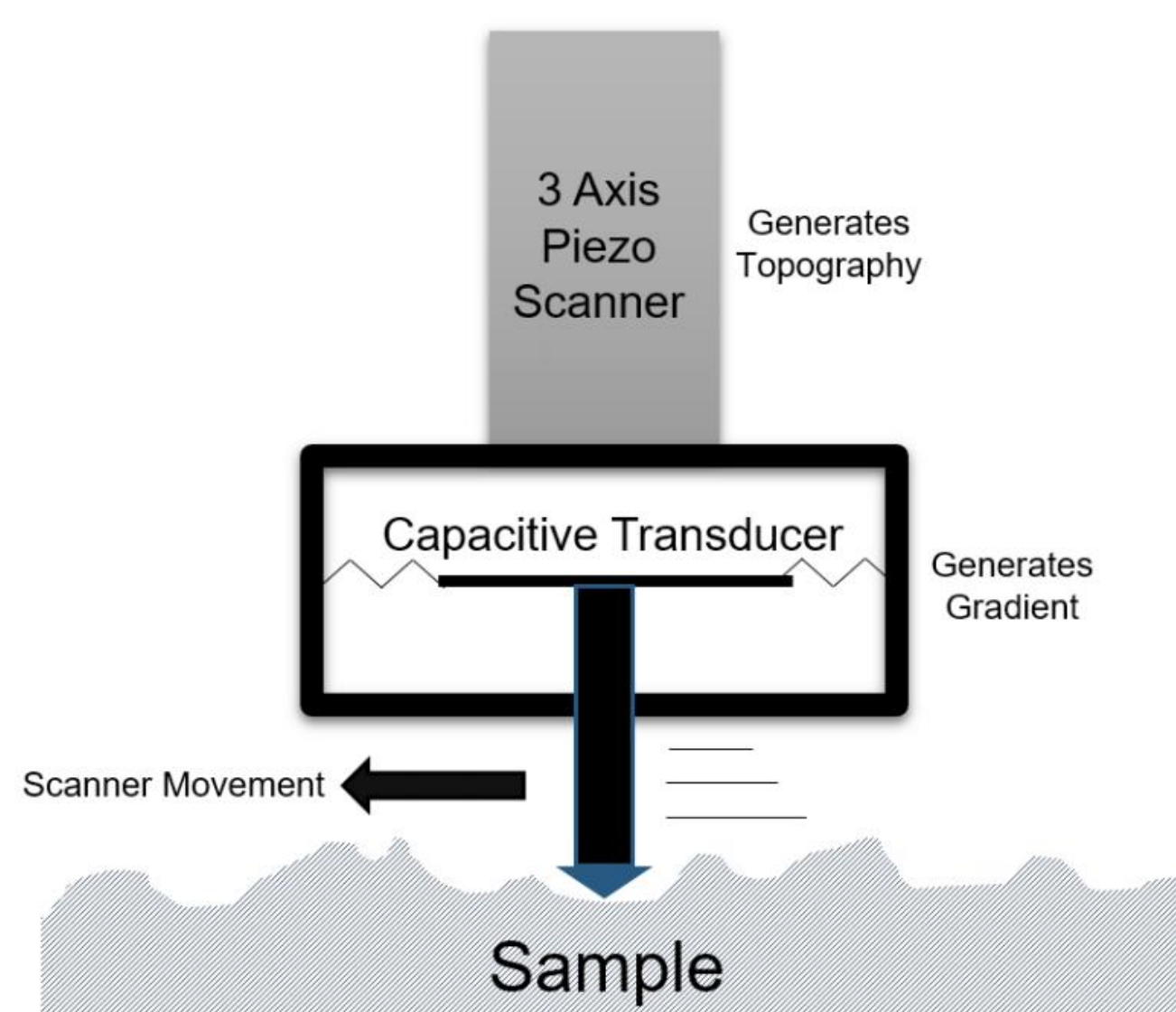


Figure 4: SPM rasters surface with piezo/capacitive sensors[10]

## Importance and State of Research

- 8-9 Trillion US bonds performed in 2008 [9]
- A 3-D representation will increase understanding of mechanisms such as US activation of diffusion quantitatively [2][5]
- Resulting microstructural analysis will allow manufacturers to keep pace with a decrease in IC size [11][3]
- High resolution imaging is key to ensuring reliability/efficiency in connections [7]

### Sample Preparation

- A Series Al wires of 20 mm diameter are bonded on AlSi1 substrate with bond power of 255 arb. units, 30 ms bond time, and on the order of 1000 mN bond force
- After each alumina/diamond polishing step, samples undergo a 10 minute US bath to avoid contamination

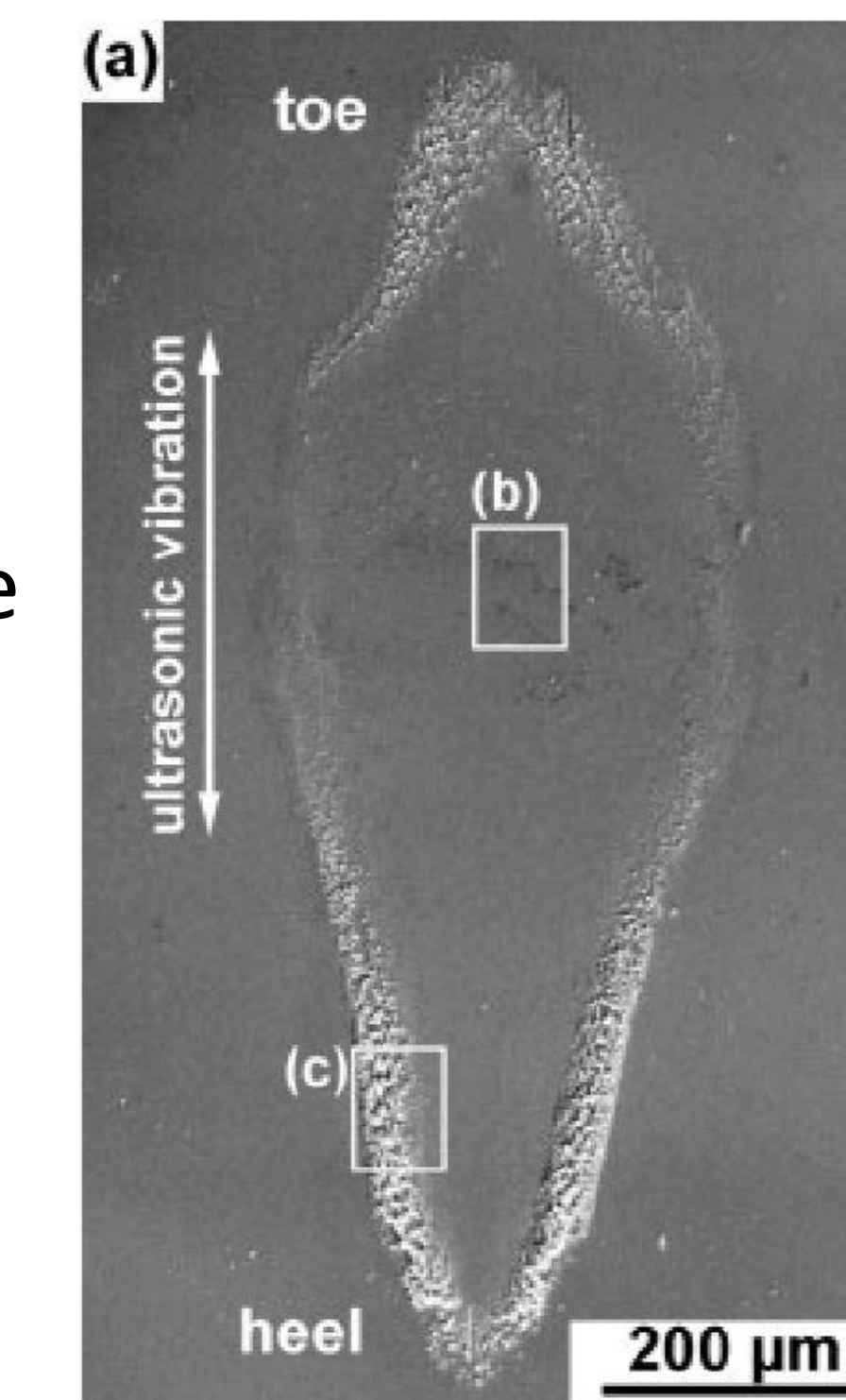
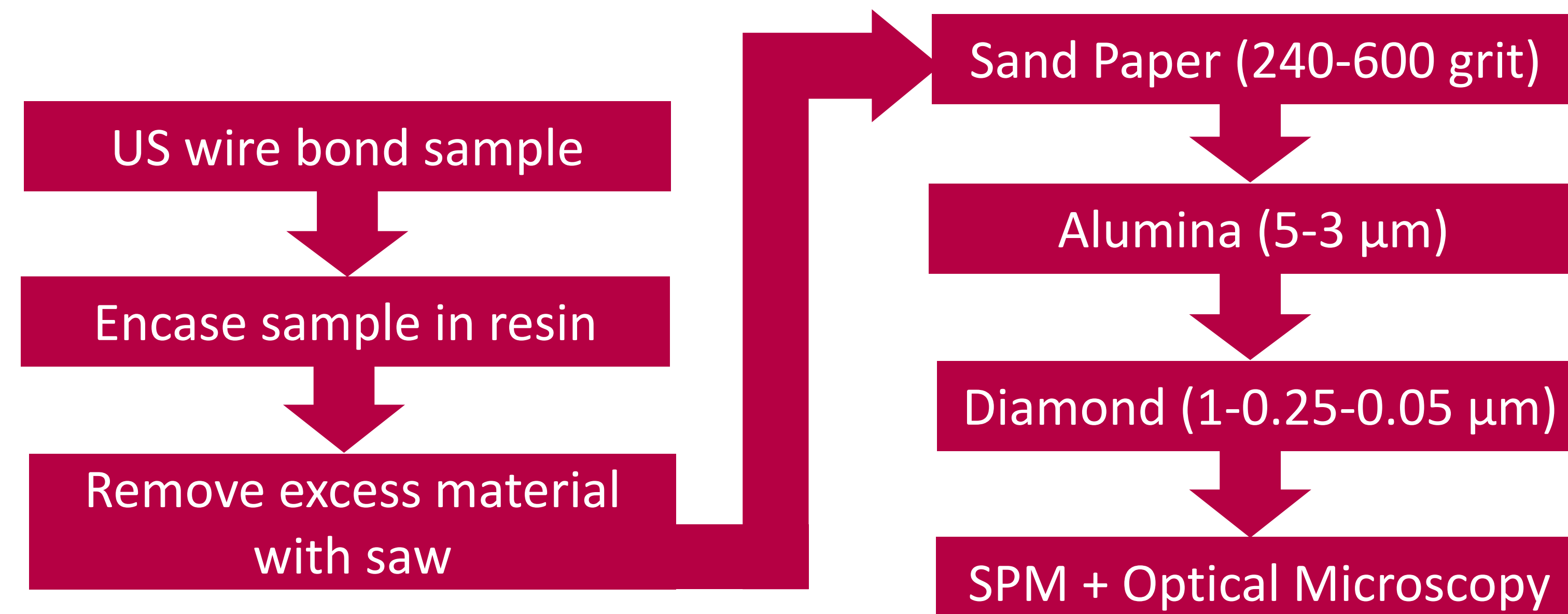


Figure 5: Oxides are more present at the periphery (c) than center (b), evidence of self cleaning mechanism described in [2] could be optimized [4]

### Successes

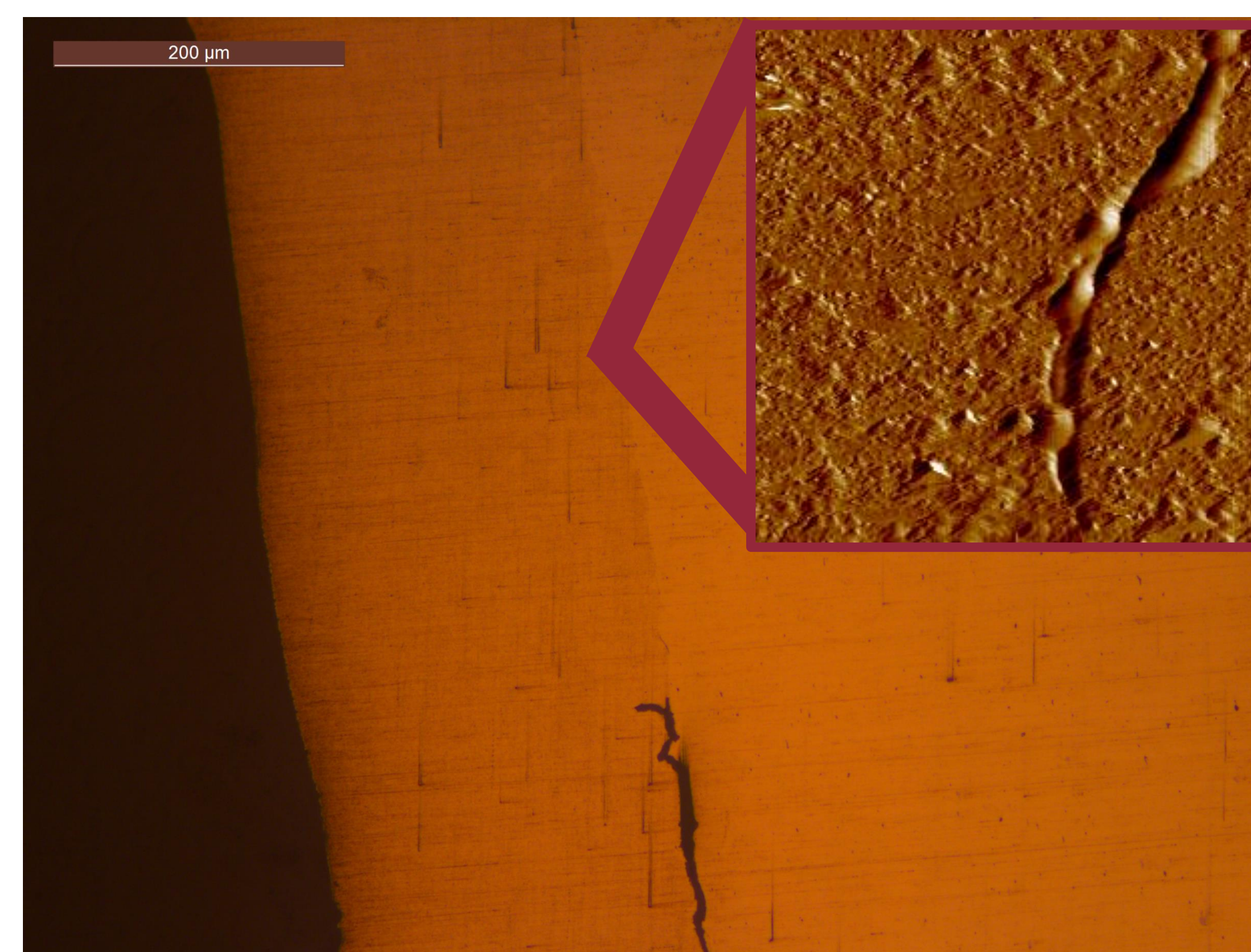


Figure 6: Visible scratches and corrosion still visible on decently polished sample. The SPM image is 10 µm by 10 µm.

- Consistent manual polishing results with supplies on hand
- Located interface region in SPM imaging

### Challenges

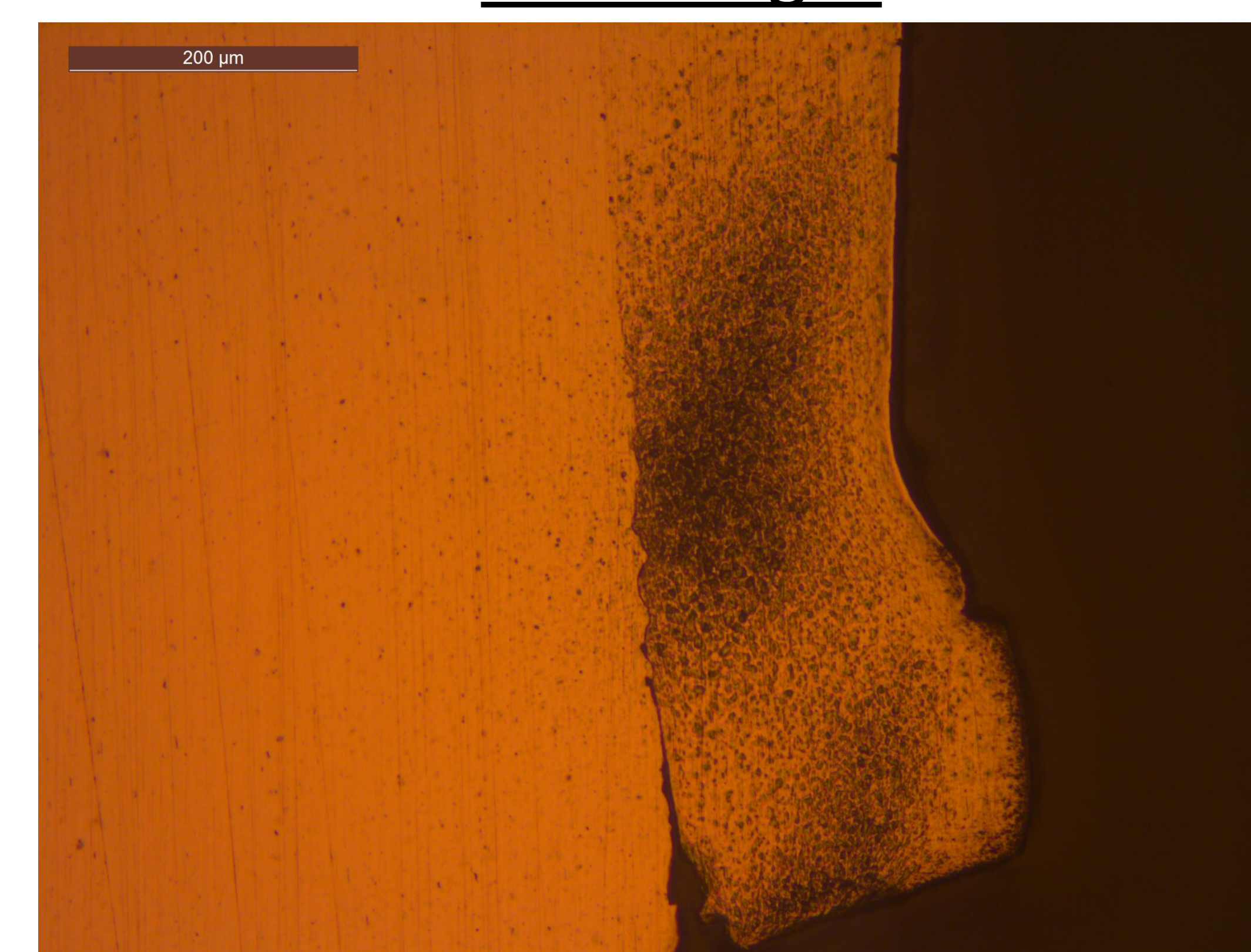


Figure 7: Case of significant corrosion on the pure Al wire

- Corrosion caused by different properties of phases
- Visible Scratches remaining from previous lapping steps at the scale of 3 µm in SPM
- Resolution limits of SPM – thermal drift, resonance [12]

## Future work

Try different polishing abrasives such as silica

Develop control of cutting and new abrasives

Gather several image sets of interfaces and develop/implement algorithm of aligning images with landmarks [6]

Analysis of micro-weld formation

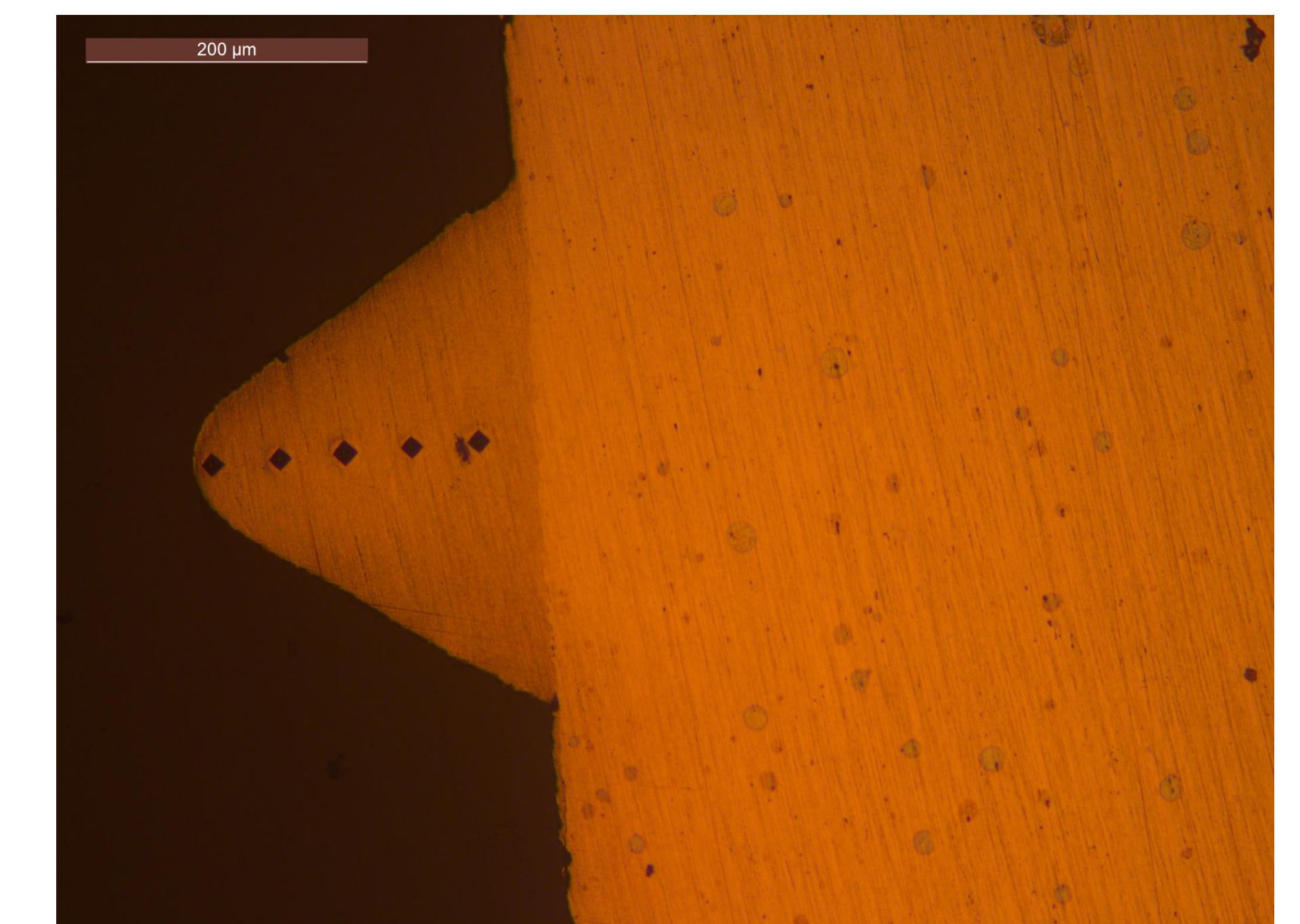


Figure 8: Alternate orientation of wire bonded sample with nanoindentations after rough polish



Figure 9 Wire bonded sample after the first alumina polishing steps

### References

- [1] Long, Yangyang, et al. Journal of Materials Processing Technology, vol. 245, July 2017, pp. 241–258.
- [2] Long, Yangyang, et al. Journal of Materials Processing Technology, vol. 258, Aug. 2018, pp. 58–66.
- [3] Gaul, H., et al. Microelectronic Engineering, vol. 87, no. 4, Apr. 2010, pp. 537–542.
- [4] Hongjun Ji, et al. 2008 International Conference on Electronic Packaging Technology & High Density Packaging, Shanghai, 2008, pp. 1-5.
- [5] Khatibi, G., et al. Journal of Electronic Materials, vol. 41, no. 12, Dec. 2012, pp. 3436–3446.
- [6] Deng, William Nanqiao, et al. Journal of Physical Chemistry A, v 122, n 26, p 5756-5763, July 5, 2018
- [7] Maeda, M., et al. Science & Technology of Welding & Joining, vol. 18, no. 2, Feb. 2013, pp. 103–107.
- [8] Broll, Marian Sebastian, et al. Microelectronics Reliability, vol. 55, no. 6, May 2015, pp. 961–968.
- [9] Harman, G.G. 2010. Wire Bonding in Microelectronics, ed. 3<sup>rd</sup>. McGraw-Hill, NY
- [10] "SPM+ High Resolution Imaging Information Sheet." Bunker Hysitron, St. Minneapolis MN.
- [11] Bonderup Pedersen. Journal of Materials Science: Materials in Electronics, vol 25, No. 7, Jul 2014, pp 2863–2871
- [12] S.D Alekperov. Fizika, Azerbaijan Journal of Physics (English Section), vol. 18, no. 1, March 2012, pp. 3-6

# Comparison of Tapping Mode and Fluid Mode for Membrane Topography using Atomic Force Microscopy



Huong Chau<sup>1</sup>, Alex Hadsell<sup>1</sup>, Maryam Mobed-Miremadi<sup>1</sup>, Unyoung Kim<sup>1</sup> & Richard Barber<sup>2</sup>  
 Department of Bioengineering<sup>1</sup> and Department of Physics<sup>2</sup> at Santa Clara University

## Objective

Intelligent artificial membranes and biofilms can efficiently control the intake of proteins and biomolecules as well as become sturdy vessels for targeted drug delivery. An essential step to synthesizing these biodevices is pore size characterization. This crucial step was our immediate goal for studying the pseudomembranes.

## AFM Background

Imaging was performed via a 3100 Dimension Atomic Force Microscopy machine and subsequent calibrations were performed using a TMZ1 standard. The instrument was operated in tapping mode and fluid mode using a Pyrex-Nitride probe (PNP-TR-20) with triangular cantilever (resonant frequency 17 kHz, force constant 0.08 N/m, thickness 600 nm, length 200 μm, tip radius 7-10 nm).

Figure 1b: AFM Mechanism

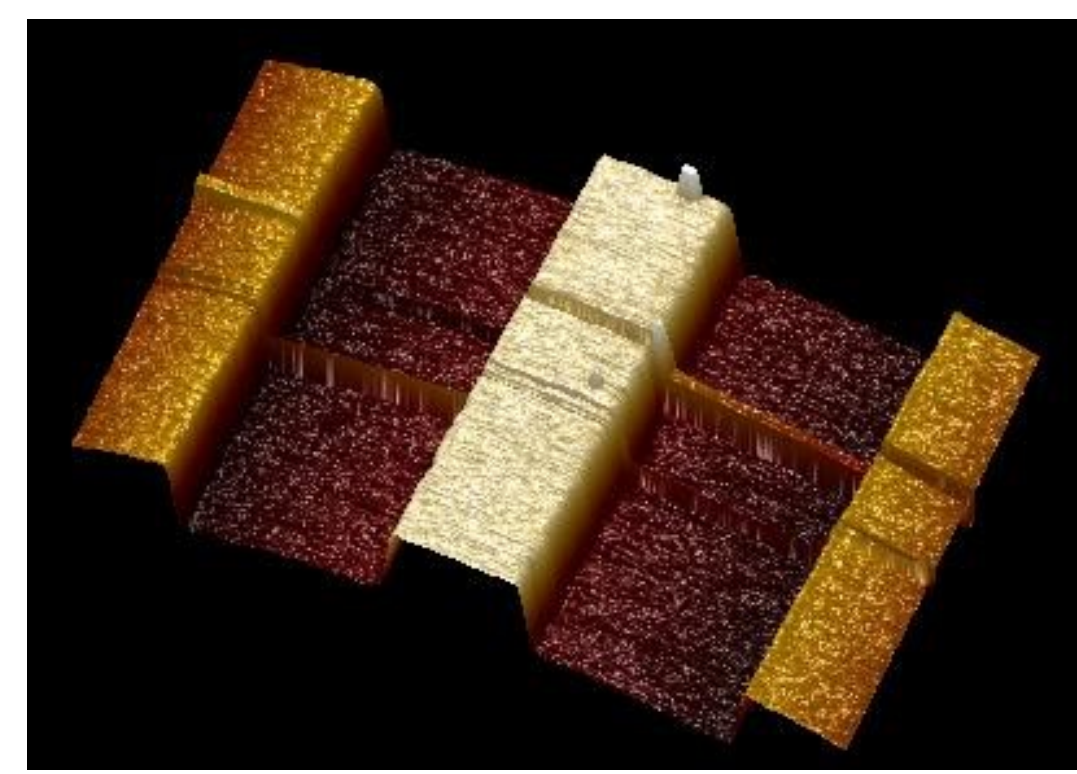
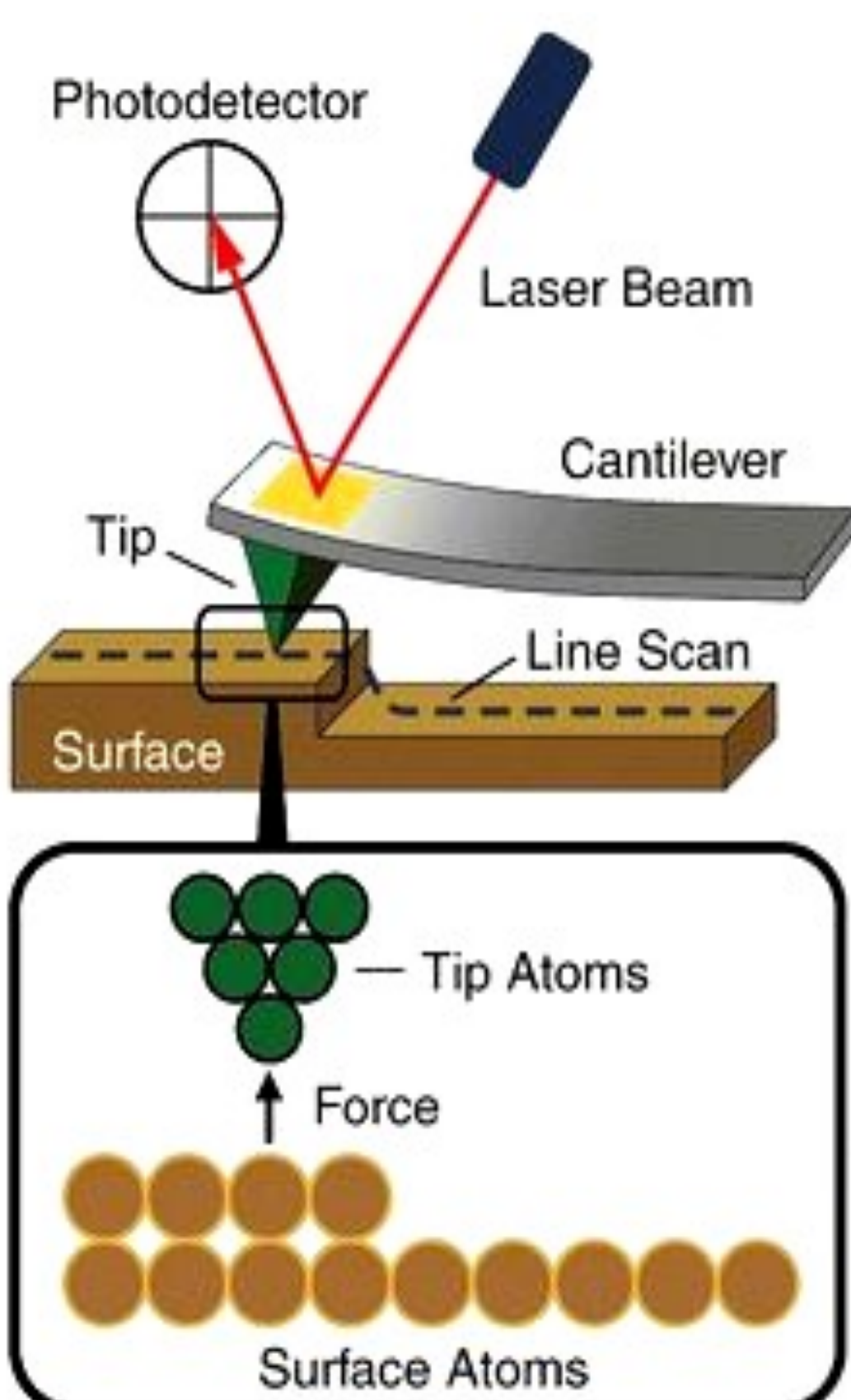
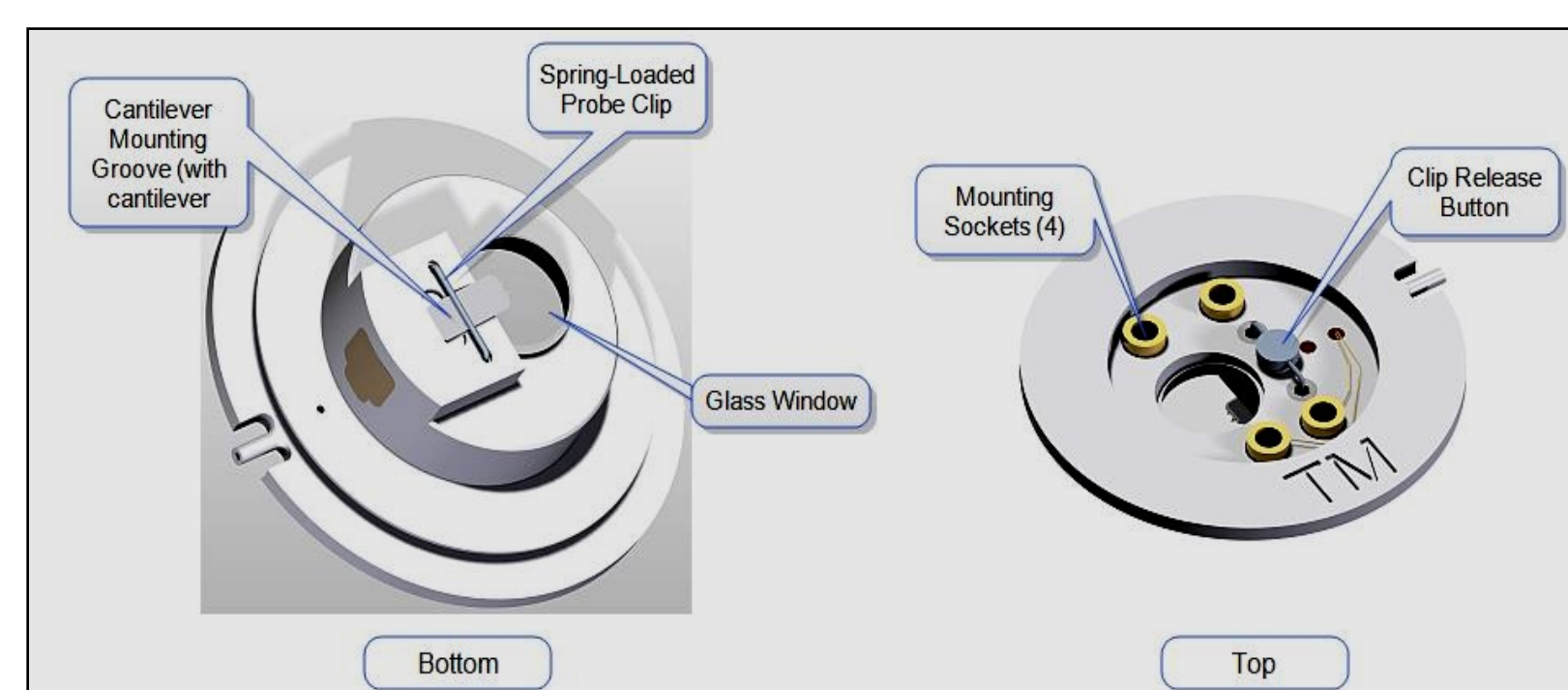


Figure 1a: TGZI Block

The mechanisms of imaging a sample under the AFM probe in tapping mode is portrayed in figure 1b, the AFM image of TGZI calibration block is shown in figure 1a, and the fluid tip holder apparatus is shown in figure 1c.

Figure 1c: Fluid Apparatus



## Materials and Methods

Nanoscope v.6.13, MATLAB 2017a, MATLAB 2017b, Gwyddion v.2.3 were used as qualitative real-time and quantitative image analysis software, respectively. The AFM scan rate was set between 0.1Hz and 0.1658 Hz for samples, and 0.648Hz for standard calibration (TMZ1). The scan area ranged from 0.1 to 10.0 μm with a maximum possible range of 100 μm. The calibrators were 50kDa, 100kDa and 1000kDa dialysis tubing (Cellulose Ester (CE) with molecular weight cutoffs (MWCO) of 50 kDa, 100 kDa and 1000kDa.). Both tapping mode and fluid mode were used.

## Formulas & Equations

$$\text{Stoke's Radius} : \alpha = ((3M\omega) / (4\pi\eta N_a))^{1/3}$$

## Results

A sample AFM tapping scan of a 1000 kDa Dialysis Tubing is presented in Figure 3. The measured radius of the average pore size had a range of 7.2-7.4 nm and can be closely matched to the theoretical Stoke's radius value of 7.3 nm. A sample AFM fluid scan of a 100 kDa Dialysis Tubing is presented in Figure 2. The measured radius of the average pore size had a range of 3.3-3.6 nm and can be closely matched to the theoretical Stoke's radius value of 3.4 nm. The measurements for each calibrator evaluated the strength of discrimination which was based on the area under the ROC curve (AUC).

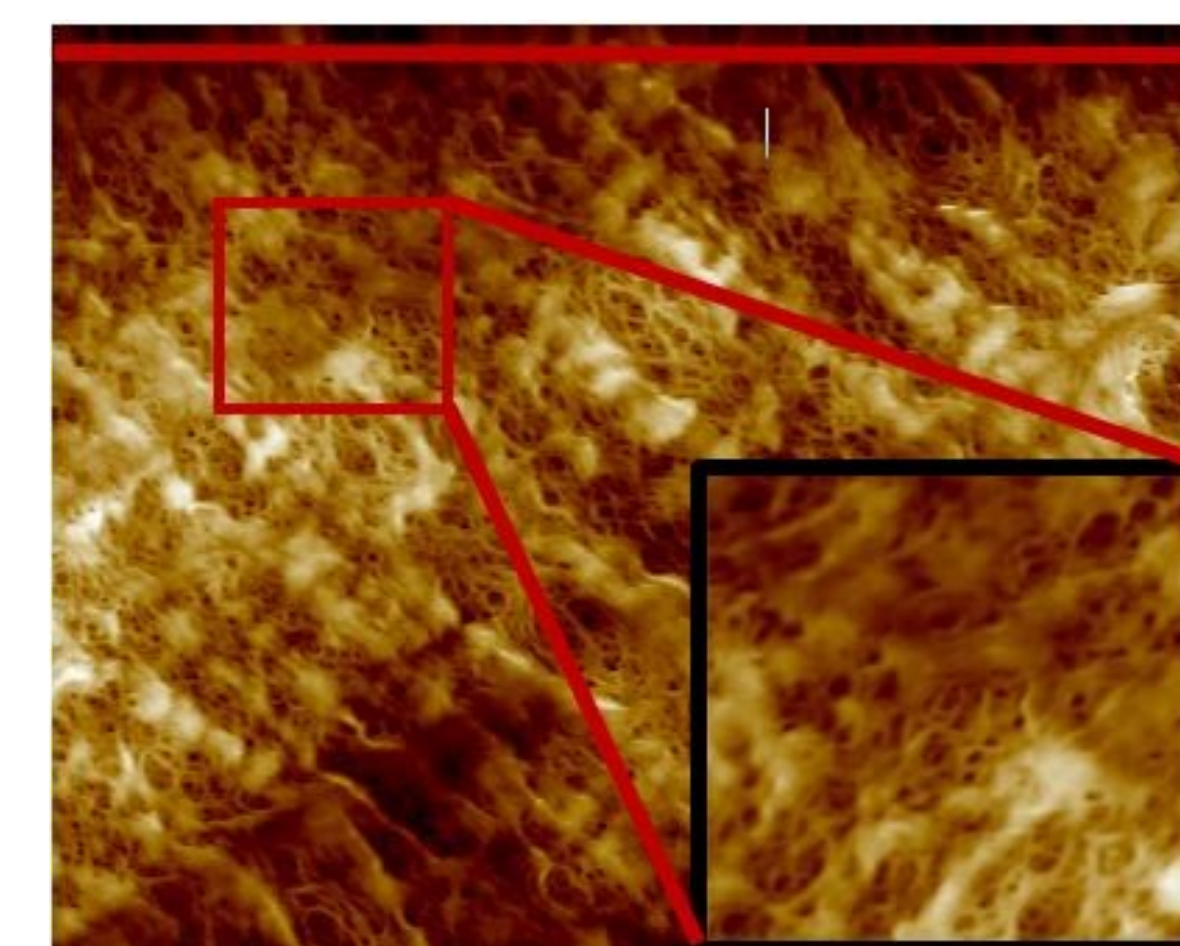


Figure 2: Fluid Mode

8 μm scan area (red bar equals 8 μm) and zoomed in area of 100 kDa Dialysis Tubing via AFM. The measured radius of the average pore size fell in the 3.3-3.5 nm range.

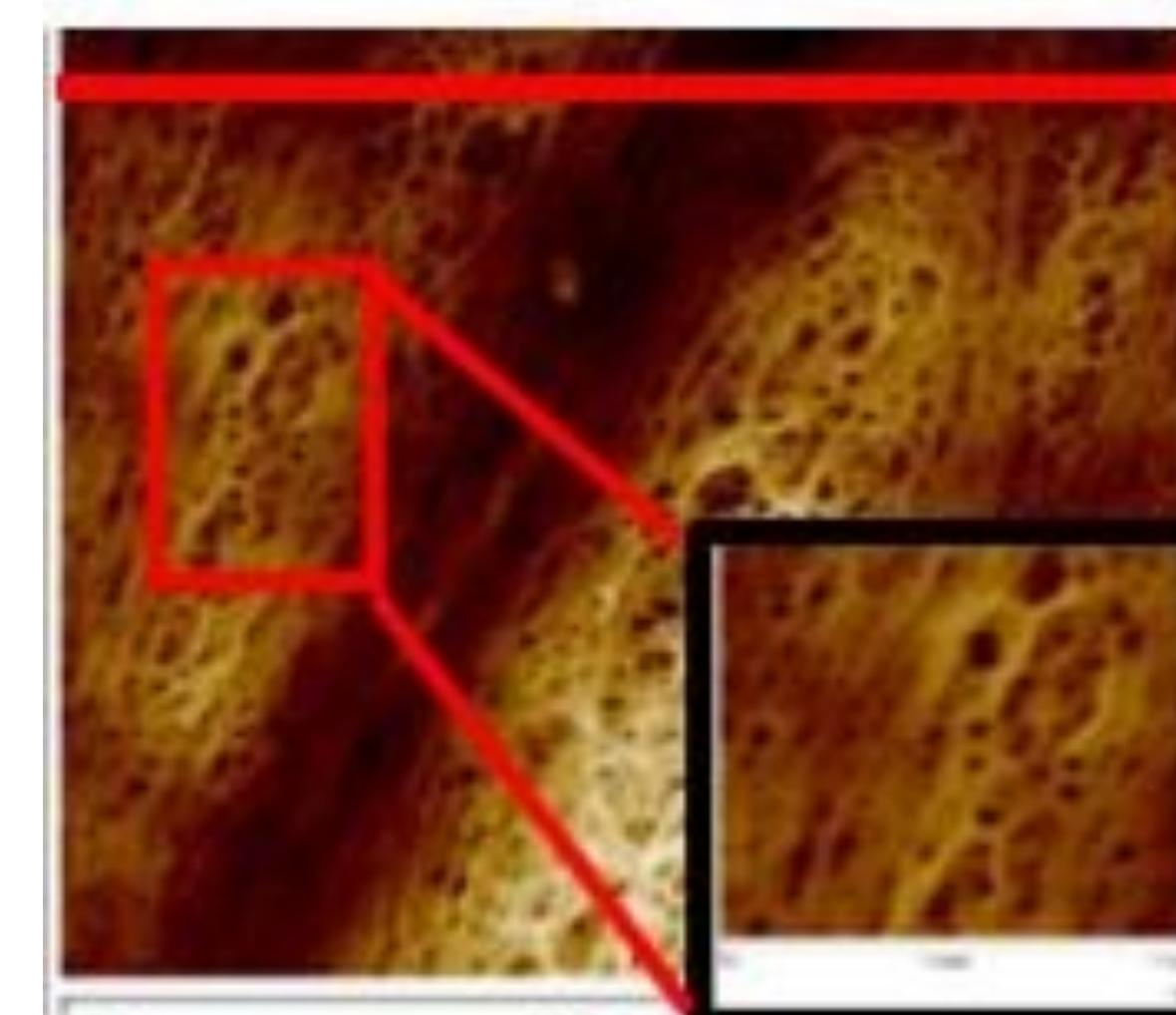


Figure 3: Tapping Mode

6 μm scan area (red bar equals 6μm) and zoomed in area of 1000 kDa Dialysis Tubing via AFM. The measured radius of the average pore size fell in the 7.2-7.4 nm range.

Taping versus Tapping Comparisons	
50 kDa vs 100 kDa	0.5396
50 kDa vs 1000 kDa	0.8406
100 kDa vs 1000 kDa	0.8936

Table 1

Tapping versus Tapping Comparisons	
50 kDa vs 100 kDa	0.5406
50 kDa vs 1000 kDa	0.7079
100 kDa vs 1000 kDa	0.7942

Table 2

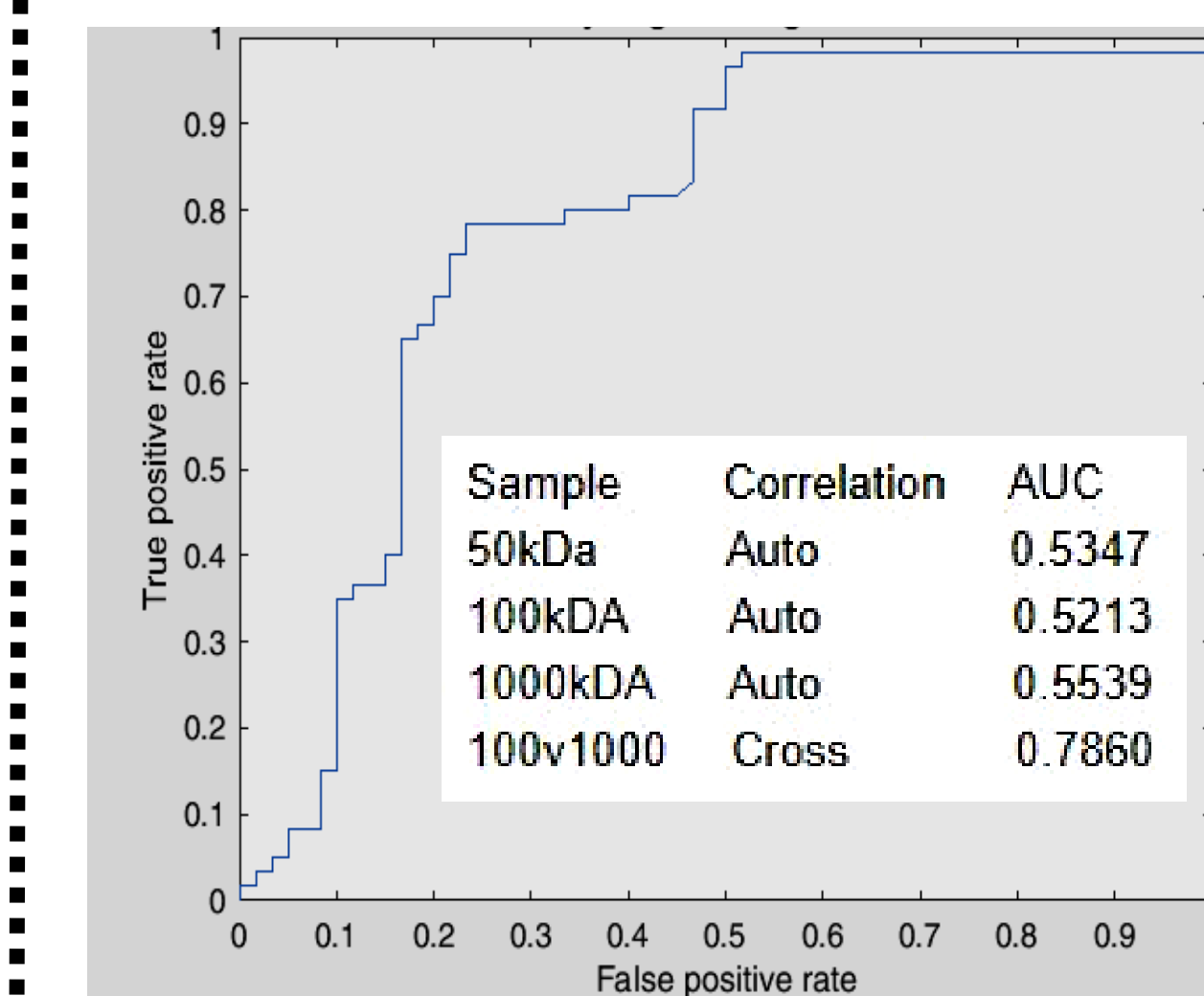
Tapping versus Fluid Comparisons	
50 kDa vs 50 kDa	0.6682
100 kDa vs 100 kDa	0.7029
1000 kDa vs 1000 kDa	0.9294

Table 3

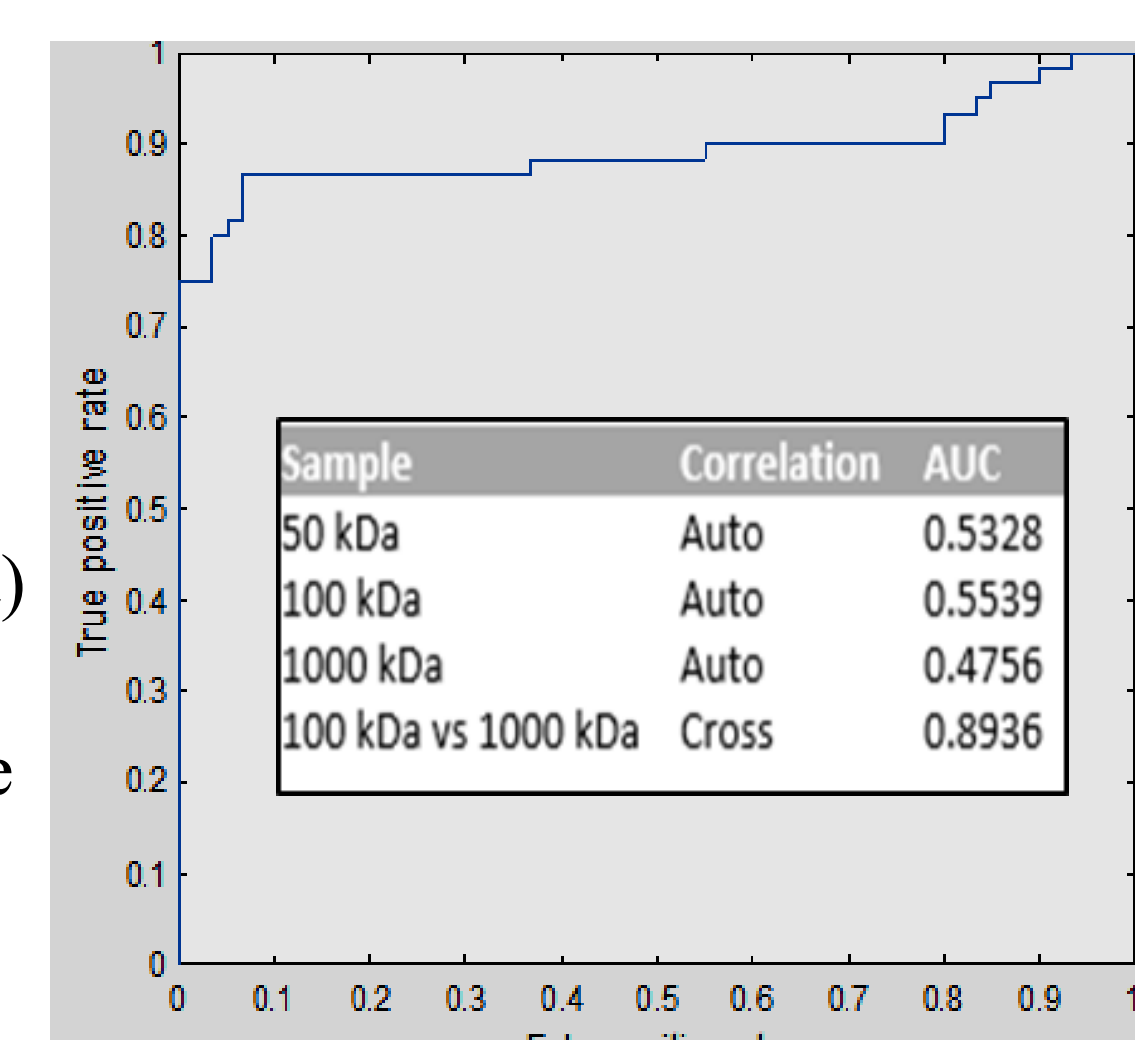
Tables 1, 2 and 3 portray the areas under the ROC curves generated using raw AFM data gathered in both fluid and tapping mode.

## Discussion

Data analysis was further conducted using Matlab2017b to assess the statistical validity of the measurements. A Receiver Operating Curve (ROC) was generated based on results of logistic regression models on unfiltered data. Classifier models can be used on AFM imaging data to discriminate between pore size levels using biopolymer-based calibrators. This classification system establishes the future framework for cross-linked bio-membrane pore size characterization in the nm range.



Calibrator Strength of Discrimination Measurements Fluid mode (Left) and Tapping mode (Right) are shown.



## Conclusion & Next Steps

Our results are essential in moving towards synthesizing intelligent membranes and biofilms that can be geared towards targeted drug delivery, cell encapsulation or exosomal extractions. In our next steps, we will synthesize actual bio-membranes and replicate them for characterization solely in fluid mode to create a more realistic model.

## Citations

- "AFM System - Keysight 5600LS." *Polifab*, www.polifab.polimi.it/equipments/afm/.
- C. Sempliciano, L. Clark, B. Asi, N. Chu, M. Mercado, S. Diaz, M. Goedert and M. Mobed-Miremadi, "Cross-Linked Alginate Film Pore Size Determination Using Atomic Force Microscopy and Validation Using Diffusivity Determinations," *Journal of Surface Engineered Materials and Advanced Technology*, Vol. 3 No. 4A, 2013, pp. 1- 12. doi: 10.4236/jsemat.2013.34A1001.
- "Fluid Imaging ." *NanoPhys--AFM*, Bruker , 2010, www.nanophys.kth.se/nanophys/facilities/nfl/afm/icon/ brucker-help/ Content/Fluid%20Imaging/Fluid%20Imaging.htm.
- Fournier, Ronald L. *Basic Transport Phenomena in Biomedical Engineering*. Taylor & Francis, 2007.
- Vidakovic, Brani. *Statistics for Bioengineering Sciences: with MATLAB and WinBUGS Support*. Springer, 2011.

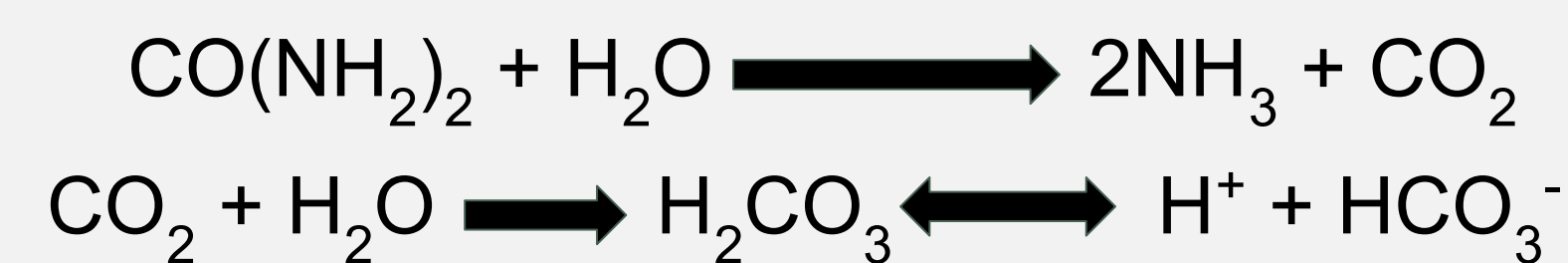
## Acknowledgements

The authors would like to acknowledge the Department of Bioengineering at SCU for its strong commitment to undergraduate research, the Clare Boothe Luce University grant for enabling this research effort, and Ms. Shaun Snyder from the Center of Nanostructures (CNS) for overseeing the measurements and SCU for usage of CNS for conducting measurements and the Engineering Computing Center.

Brandon Lin, Dr. Maryam Mobed-Miremadi  
Power Systems and Sustainable Energy & Department of Bioengineering

## INTRODUCTION

MFCs (microbial fuel cells) are electrochemical devices that take advantage of the metabolic processes of microorganisms to directly convert organic matter such as sugars in industrial effluents and urea from municipal waste into electricity. Compared to other bioenergy conversion processes (i.e. anaerobic digestion, gasification, fermentation), MFCs have the advantage of reduced amounts of sludge production, as well as cost-effective operation, since they operate under ambient environmental conditions [1]. Upon microbial enzymatic hydrolysis, urea forms ammonia and carbon dioxide, the latter is further converted to carbonic acid in equilibrium with carbonate [2].



This hydrolysis is conducted by exoelectrogens at the anode [3], resulting in transfer of electrons and current generation. Much research has been conducted on power generation optimization, namely the design of electrode materials and geometry, the type of proton exchange membrane (PEM), the distance between the electrodes the size of the galvanic cell and genetically-engineered microorganisms [4]. Regardless of the substrate, the most important drawback associated with MFCs are low power generation and the correlation of peak power to microbial growth curve bounding the scope of this research effort [5].

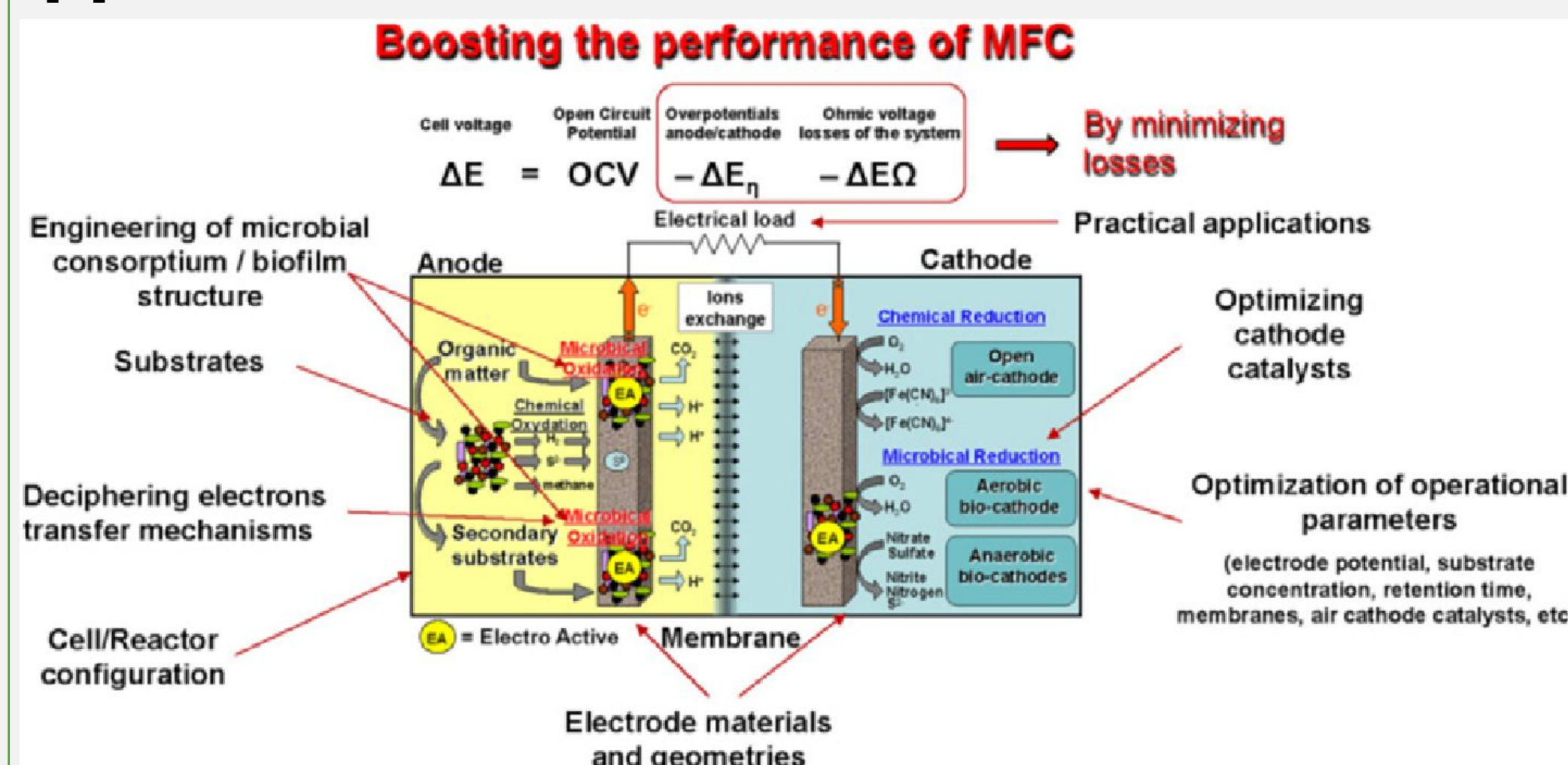


Figure 1: Example of a Microbial Fuel Cell [6]

## OBJECTIVES

- To examine the effect of microencapsulation on partial decoupling of growth rate and current generation due to diffusion limitations using *E. coli* DH5α (pKAU17) and alginate as model organism and membrane material, respectively.
- To simulate power generation by microencapsulated bacteria using an application-based model by incorporating charge transfer kinetics and ohmic losses reported in literature for a specific MFC configuration.

## METHODS

- Urea hydrolysis is simulated in 300 μm microcapsules suspended in a buffered ideal solution. The cofactor NAD<sup>+</sup>/NADH will be co-encapsulated with bacteria in order to eliminate the need for redox mediators and subsequent fluctuations in solubility.
- Equations used are displayed below while the corresponding list of symbols are tabulated.

$$P = \frac{P_{max}[S]}{K_m + [S]} \quad [1]$$

$$P = I_1 I_2 R \quad [2]$$

$$I_1(t) = nFK_c S(t) \quad [3]$$

$$R_s = \frac{dS}{dt} = \left( \frac{-1}{Y_{X/S}} \right) \left( \frac{\mu_{max}[S]}{K_m + [S]} \right) X \quad [4]$$

$$\frac{\partial S}{\partial t} = D\nabla^2 S + R_s \quad [5]$$

$$R_{Smic} = \eta R_s \quad [6]$$

$$\frac{dS}{dt} = Q_b S_b|_x - Q_b S_b|_{x+\Delta x} = (1 - \epsilon_1) \Delta x A_{XS} \eta r_s \quad [7]$$

- Using COMSOL 5.3a, Monod growth kinetics (Eq. 4) and the convective-diffusion equation (Eq. 5) were solved simultaneously to generate the concentration profiles in batch mode illustrated in Figures (2a-3b).

## RESULTS

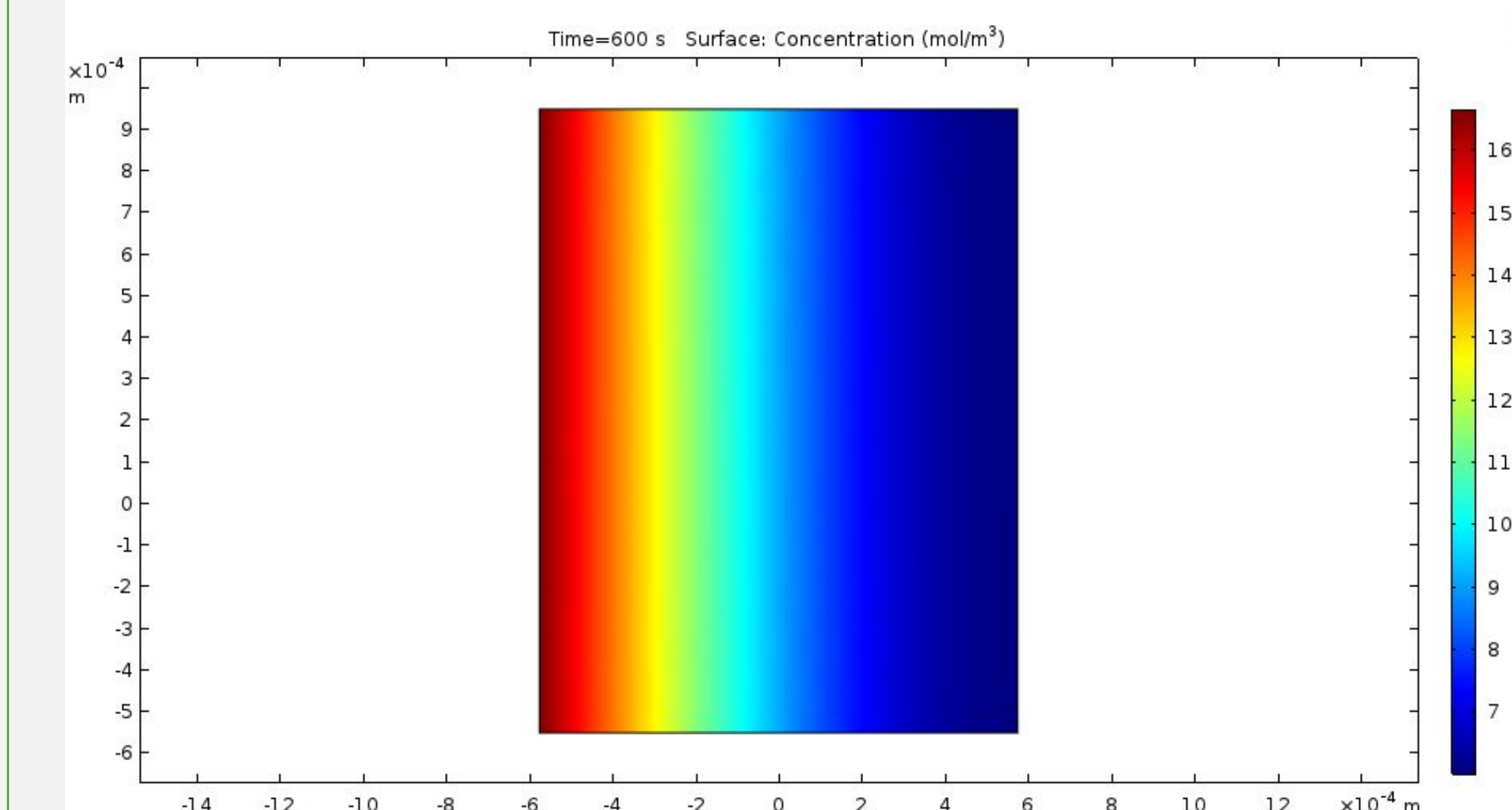


Figure 2a: Plot of the compartment without any capsules present. Plot represents the molar concentration of substrate after 600 seconds.

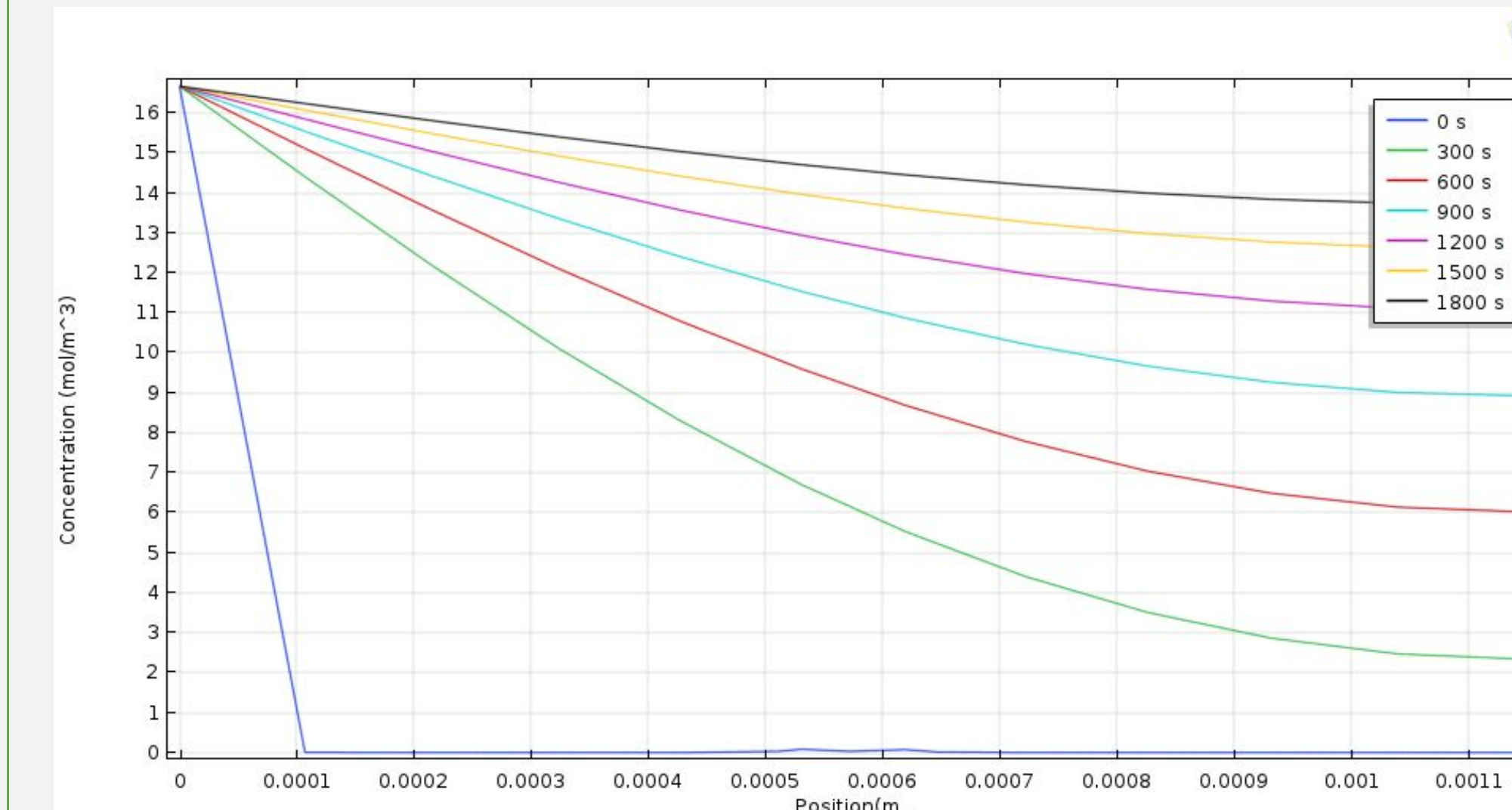


Figure 2b: Line plot of Figure 2a measuring concentration vs. position from left to right of the compartment. A line cut was taken at  $y = 2 \times 10^{-4}$ .

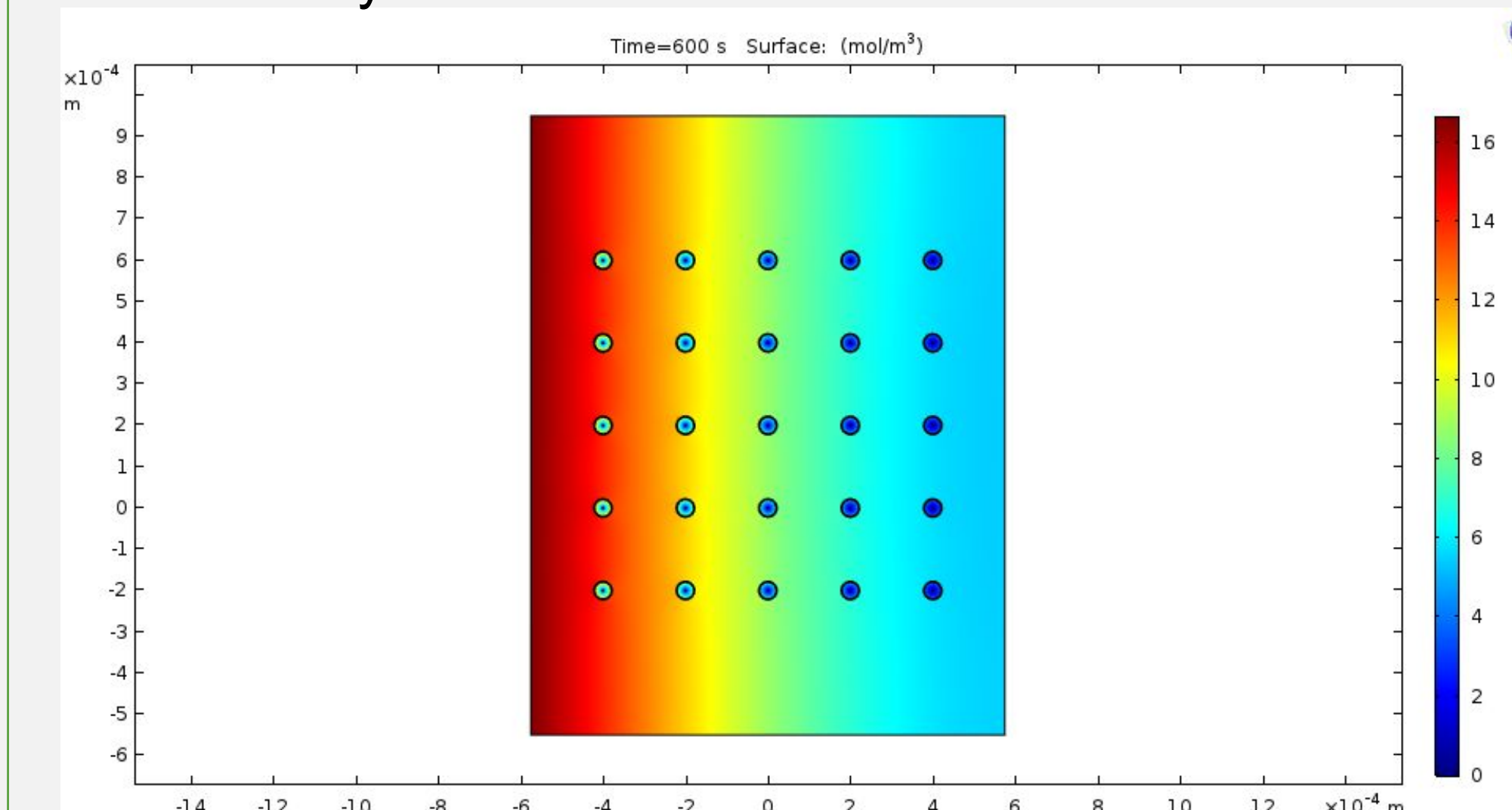


Figure 3a: Plot of the compartment with 25 capsules present and evenly spread out. Like Fig. 2b, plot represents molar concentration of substrate after 600 seconds.

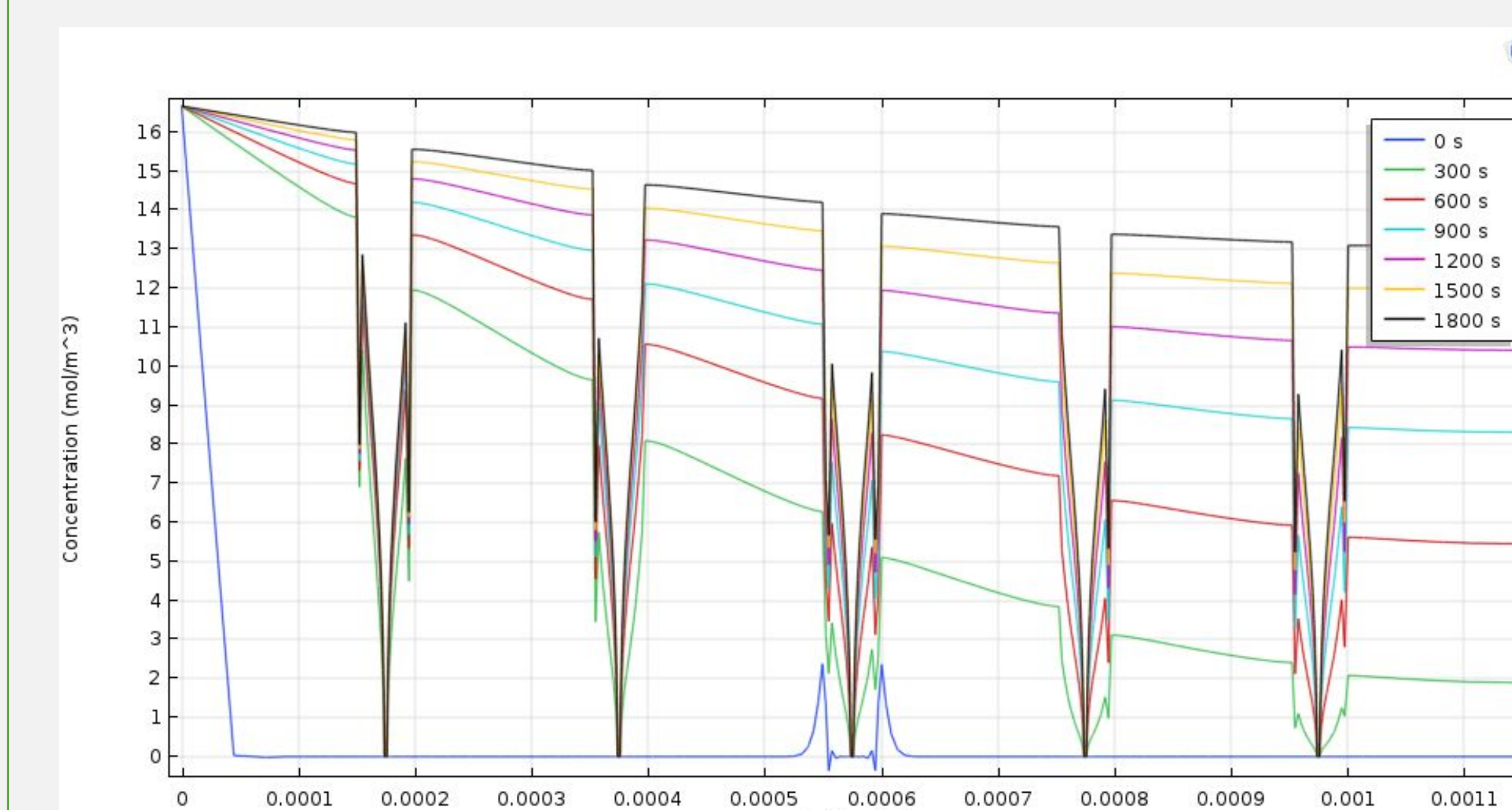


Figure 3b: Line plot of Figure 3a measuring concentration vs. position from left to right of the compartment.

## CONCLUSIONS

As shown by the simulation results (Figure 3b vs. Figure 2b), there is a clear difference between the substrate depletion profiles and thus power generation between the free and encapsulated configurations modeled in batch mode. As a result of microencapsulation, the absolute peak intensity ( $I_{max}$ ) is lowered. However, current density is maintained for a longer period of time.

## FURTHER STUDIES

Efforts include optimizing parameters at the macro and microscales to simulate growth in a Plug Flow Reactor. At the reactor level, the number of microcapsules along with the length and diameter of the reactor will be optimized (Eq. 6). At the microscale, the optimal diameter of the capsules will be determined (Eq. 7) to account for mass transfer limitations. In parallel, integration of this MFC setup into an application-based model for power generation will be considered.

### List of Symbols

Symbol	Unit
P	W
$\mu_{max}$	Maximum growth rate (1/s)
$K_m$	Michaelis-Menten constant (mol/m <sup>3</sup> )
$I_1$	Mass transfer-based current (A/m <sup>2</sup> )
$I_2$	Charge transfer-based current (A/m <sup>2</sup> )
R	Ohmic losses (Ω)
S	Urea (substrate) concentration (mol/m <sup>3</sup> )
n	number of electrons
F	Faraday number (96458 C/mol)
$K_c$	Mass transfer coefficient (m/s)
$R_s$	Substrate depletion rate (mol/m <sup>3</sup> ·s)
X	Biomass concentration (mol/m <sup>3</sup> )
$Y_{X/S}$	Biomass yield coefficient (g/g)
$Q_b$	Volumetric flowrate (m <sup>3</sup> /s)
$\Delta X_s$	Plug/Reactor length (m)
AXS	Reactor cross-sectional area (m <sup>2</sup> )
$\epsilon$	Reactor void volume
$\eta$	Effectiveness factor
$R_{Smic}$	Microencapsulated substrate depletion rate (mol/m <sup>3</sup> ·s)

## REFERENCES

- [1] Chouler J., Padgett G. A., Cameron P. J., Preuss K., Titirici M. M., Ieropoulos I., et al. Towards effective small scale microbial fuel cells for energy generation from urine. *Electrochimica Acta*. 2016, 192, 89–98.
- [2] Duque, R., Shan, Y., Joya, M., Ravichandran, N., et al. Effect of artificial cell miniaturization on urea degradation by immobilized *E. coli* DH5α (pKAU17). *Artificial Cells, Nanomedicine, and Biotechnology*. 2018, 1, 1–10.
- [3] Shreeram, D. D., Hassett, D. J., and Schaefer, D. W. Urine-powered microbial fuel cell using a hyperpilated pilT mutant of *Pseudomonas aeruginosa*. *Journal of Industrial Microbiology and Technology*. 2016, 43, 103–107.
- [4] Xia, C., Zhang, D., Pedrycz, W., Zhu, Y., Guo, Y. Models for microbial fuel cells: a critical review. *Journal of Power Sources*. 2018, 373, 119–131.
- [5] Drapcho, C. M., Nhuon, N. P., & Walker, T. H. (2008). *Biofuels engineering process technology*. New York: McGraw-Hill.
- [6] Santoro C., Arbizzani C., Erable B., Ieropoulos I. Microbial fuel cells: From fundamentals to applications. A review. *Journal of Power Sources*. 2017, 356, 225–244.
- [7] Fournier, R. L. (2007). *Basic Transport Phenomena in Biomedical Engineering*. New York: Taylor & Francis.

## ACKNOWLEDGEMENTS

We would like to thank the SCU Graduate School of Engineering and Dr. Maryam Khanbaghi for their support on this project.



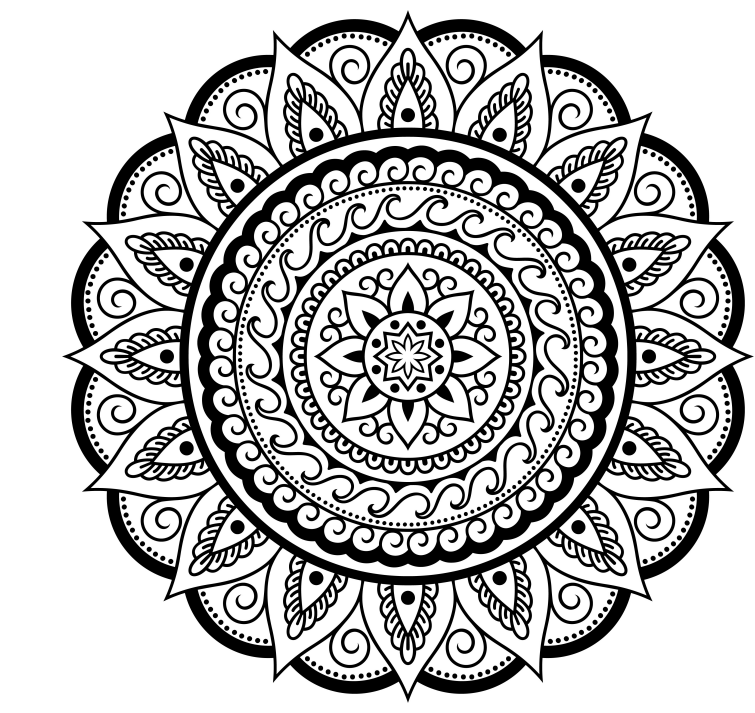


# Brain Computer Interface Development for Virtual Reality Applications

A. Adolfsson<sup>1\*</sup>, J. Bernal<sup>1\*</sup>, M. Breshock<sup>2</sup>, M. Ackerman<sup>1</sup>, J.A. Scott<sup>1</sup>

<sup>1</sup>Computer Engineering and <sup>2</sup>Bioengineering, Santa Clara University, Santa Clara, CA

\*Authors contributed equally



## Objective

**Objective:** Create a brain computer interface (BCI) for a virtual reality (VR) environment that incorporates both feedback and feedforward elements

Neurofeedback translates neural activity into sensory stimuli for the purpose of strengthening self-regulatory ability.

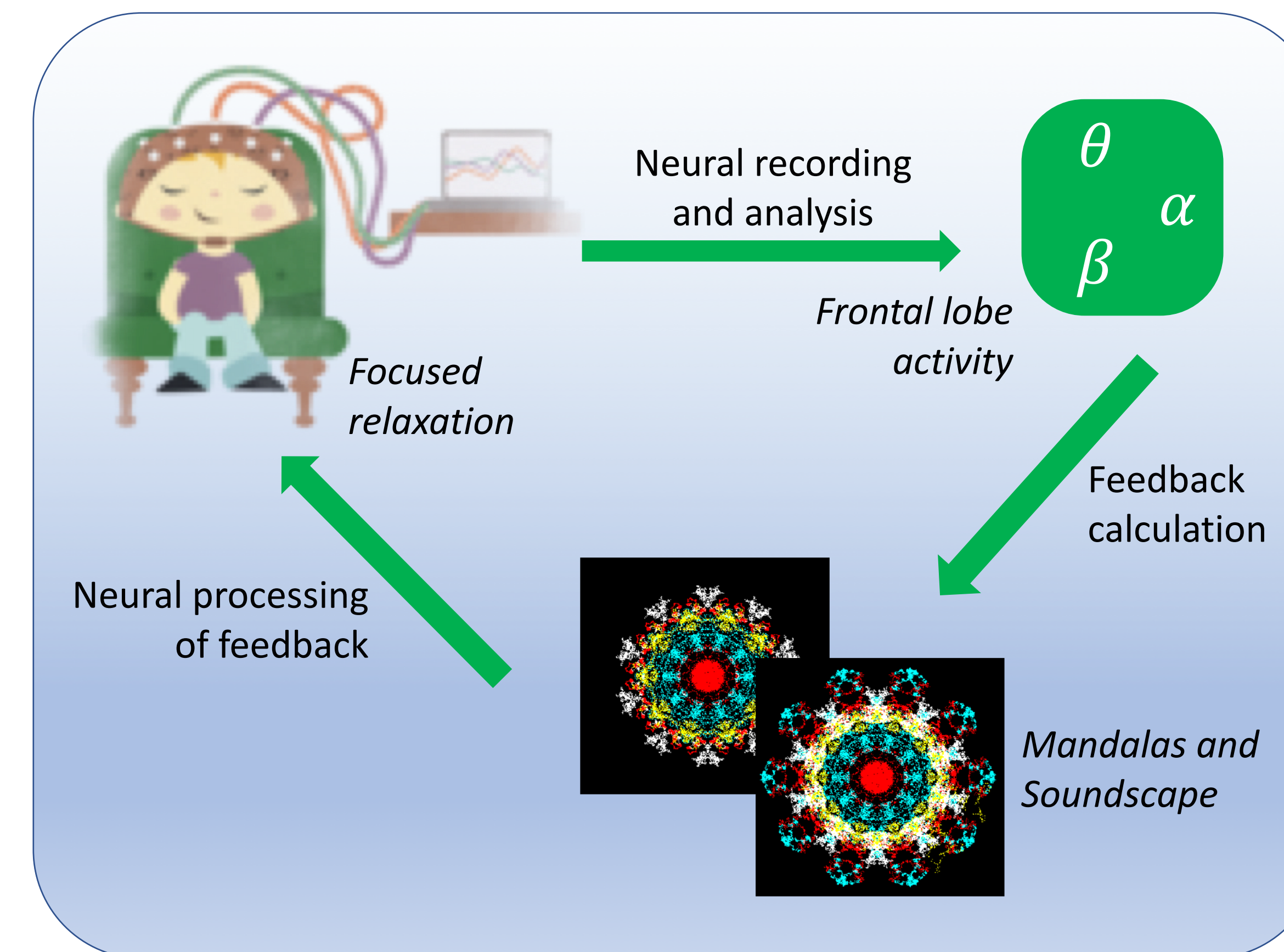
**Problem:** Neurofeedback therapy often fails because the interface lacks in user engagement and the stimuli are missing a feedforward component. Further, cost of in-clinic therapy is prohibitive.

VR enables an immersive and multisensory environment that can potentially overcome hurdles in neurofeedback applications.

**Design criteria** are to create a neurofeedback system that:

- (1) minimizes internal and external distractors,
- (2) applies stimuli that promote the desired mental state, and
- (3) may be used outside of a clinical setting.

## System Overview



## Testing

**Prototype:** A recorded simulation of the experience was run for an event, Night of Ideas 2019. An EEG recording from an experienced user was used as the modulatory input for the environment. Participants watched the simulation in VR and gave qualitative feedback.

**Tuning of feedback:** In a small group of participants, variations of the feedback calculations, duration of training session, and other key parameters will be adjusted to optimize user experience and maximize positive change in alpha power.

**Validation:** Real and sham feedback groups will be compared on the following criteria:

- (1) time-course of change in alpha power,
- (2) pre and post ratings of mental state, and
- (3) autonomic variable reflecting state of relaxation.

## Design

**Overview:** In this proof-of-concept, the purpose of the neurofeedback is to improve focused relaxation. The neural correlate of this mental state is elevated anterior frontal brain activity in the alpha frequency range, measured by scalp EEG. The environment the user is experiencing is a generative mandala and soundscape, both of which are typically associated with focused relaxation. The fluctuations in the EEG signal control parameters of the environment to indicate the direction of change in the signal.

**Virtual Reality Environment:** The visual stimulus is a generative mandala that is created from a random starting point, which procedurally draws repeating arms via random step length and step angle. The auditory stimulus is a layered soundscape composed of an instrumental theme, binaural beats at 10 Hz, intermittent "Om" chant.

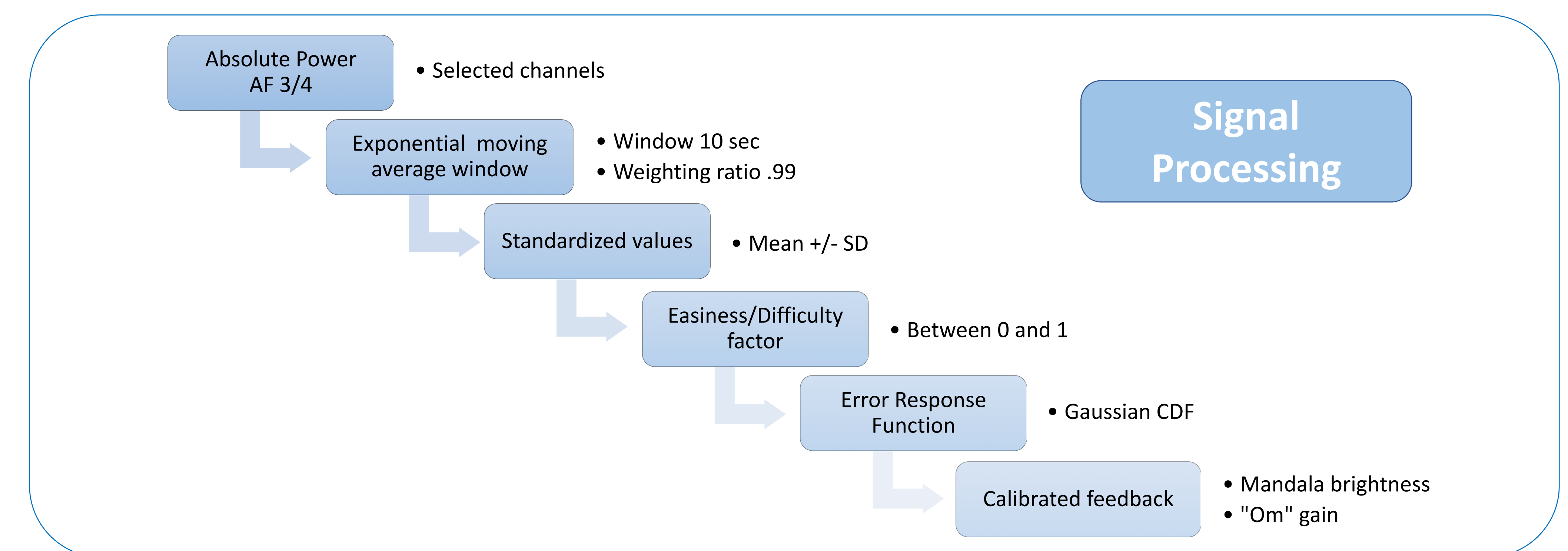
**Feedforward Stimuli:** The continuous generation of the mandala and "Om" promote a state of relaxation. The binaural beats entrain the auditory cortex to oscillate at the specified frequency.

**EEG Recording:** Muse headband is a dry electrode EEG with coverage of standard channels AF3/4 and T7/8. Muse Direct outputs of absolute power for theta, alpha, beta, and gamma frequency bands for each channel are collected.

**Neurofeedback calculation:** The continuous input of absolute power of alpha (8-12Hz) from AF3/4 is converted to a continuous error response function (Figure: Neurofeedback Calculation). This is used to calculate the calibrated modulation of the environment. A directly proportional change occurs in the global brightness of the mandala and gain of the "Om" chant.

### Key Parameters

EEG Channels	AF 3/4
FB: Mandala	Brightness
FB: Om	Gain
FF: Mandala	Generation
FF: Binaural Beat	10 Hz



## Future Directions

### Development Plan:

- (1) test feedback efficacy in recurring sessions,
- (2) integrate adaptive feedback based on previous sessions,
- (3) test efficacy in a clinical population that typically uses alpha feedback, and
- (4) test other types of neurofeedback using more channels and synchrony metrics.

### Virtual Reality Environment:

- (1) redesign of the mandala from procedural to algorithmic version,
- (2) exploration of visual modulation parameters, and
- (3) development of soundscape with more complex feedback.

Work supported by: Bioinnovation and Design Lab, Santa Clara University and the Asian Art Museum of San Francisco